HAL open science

Durability of new metal/rubber assemblies

Kaustubha Kane

To cite this version:

Kaustubha Kane. Durability of new metal/rubber assemblies. Mechanics [physics]. Université de Bordeaux, 2020. English. NNT : 2020BORD0131 . tel-02991790

HAL Id: tel-02991790

https://theses.hal.science/tel-02991790

Submitted on 6 Nov 2020

HAL is a multi-disciplinary open access archive for the deposit and dissemination of scientific research documents, whether they are published or not. The documents may come from teaching and research institutions in France or abroad, or from public or private research centers.

L'archive ouverte pluridisciplinaire **HAL**, est destinée au dépôt et à la diffusion de documents scientifiques de niveau recherche, publiés ou non, émanant des établissements d'enseignement et de recherche français ou étrangers, des laboratoires publics ou privés.

THÈSE PRÉSENTÉE

POUR OBTENIR LE GRADE DE

DOCTEUR DE

L'UNIVERSITÉ DE BORDEAUX

ÉCOLE DOCTORALE

SCIENCES, PHYSIQUES ET DE L'INGÉNIEUR

Par Kaustubha KANE

Durability of New Metal/Rubber Assemblies

Sous la direction de:
Julien JUMEL
Martin SHANAHAN

Soutenue le 07/10/2020

Membres du jury:

M. Creton Costantino,	Directeur de Recherches,	CNRS, ESPCI ParisTech,	Président
M. Verron Erwan,	Professeur,	Ecole Centrale de Nantes,	Rapporteur
M. Laiarinandrasana Lucien,	Directeur de Recherches,	Mines ParisTech,	Rapporteur
Mme. Touzet-Cortina Marie,	Maître de Conférences HDR,	Université de Bordeaux,	Examinateur
M. Marco Yann,	Maître de Conférences HDR,	ENSTA Bretagne,	Examinateur
M. Jumel Julien,	Maître de Conférences HDR,	Université de Bordeaux,	Directeur de Thèse
M. Shanahan Martin E.R.,	Professeur Émérite,	Université de Bordeaux,	Directeur de Thèse

Titre : Endurance de Nouveaux Assemblages Métal/Mélange

Résumé

Les pneumatiques sont des structures composites complexes constituées de nombreux matériaux et renforts de nature différente, textile, fibres polymères mais également câbles et armatures métalliques. Ainsi que pour les matériaux composites stratifiés, la résistance et la rigidité des pneumatiques sont principalement pilotées par celles des renforts. Les câbles métalliques noyés dans la matrice caoutchouc forment un composite élastomère / métal qui constitue le squelette du pneumatique. Usuellement, les câbles d'acier sont revêtus de laiton ce qui permet la formation de liaisons covalentes fortes entre le souffre contenu dans le caoutchouc et le cuivre du revêtement durant le processus de vulcanisation. Ces ponts covalents forment l'interface adhésive qui est soumise en service à des sollicitations mécaniques complexes combinées à une exposition à des environnements physico-chimiques agressifs. Dans ce contexte, accéder à des informations précises sur le comportement mécanique de cette interface métal-caoutchouc est primordial tant pour conduire des développements matériaux que pour dimensionner le système. Traditionnellement, des tests mécaniques standardisés tels que des essais de pelage ou encore d'arrachement sont utilisés à cet effet. Cependant ces tests souffrent de nombreux artefacts expérimentaux et les résultats très globaux mesurés dépendent non seulement des propriétés de l'interface mais également de celles du câble et de la gomme. Ainsi, les tests de pelage ne reproduisent pas la nature axisymétrique du renfort tandis que des phénomènes de friction entre surfaces fissurées compliquent l'analyse des tests d'arrachement. En conséquence, ces tests ne permettent pas d'accéder à des caractéristiques intrinsèques du système adhésif.

Cette thèse a pour objectif la conception et l'analyse d'un essai innovant permettant une évaluation quantitative des performances adhésives entre gomme et renfort pour application pneumatique. Ce protocole d'essai, appelé « Rubber Cord Adhesion Inflation Test » (RCAIT), offre des conditions d'essai maîtrisées et reproductibles réduisant la présence d'artefacts. Le travail mené a porté sur le développement du dispositif expérimental du concept initial jusqu'à la mise en place d'un dispositif industrialisé, mais également sur le développement de modélisations analytiques et numériques permettant de déterminer le taux de restitution d'énergie nécessaire à produire une décohésion complète de l'interface lors du test. En particulier un modèle décrivant le gonflement d'un cylindre épais hyperélastique pressurisé est employé pour effectuer le bilan énergétique nécessaire à la détermination du taux de

restitution critique d'énergie de l'interface, analyse appliquée pour déterminer à partir du RCAIT les performances de différents assemblages métal-mélange pour différentes vitesses de sollicitation. Ce modèle, a été initialement développé pour des comportements matériau de type Mooney-Rivlin et Ogden puis une procédure a été proposée pour mettre en œuvre simplement d'autres types de comportement hyperelastiques et incompressibles. Une technique de suivi de marqueur est proposée pour suivre la propagation de la fissure et permettre de décrire durant le test la réponse contrainte déformation de l'enveloppe de gomme notamment au voisinage du front de fissure. Cette mesure est employée pour évaluer la sensibilité du test à certains paramètres expérimentaux et utilisée avec les modèles mécaniques pour identifier le comportement mécanique du caoutchouc, donnée nécessaire à la détermination du taux de restitution critique d'énergie. Le test RCAIT et les analyses mécaniques développées permettent une détermination fiable des performances adhésives de l'interface en limitant la présence d'artefacts expérimentaux et une détermination *in-situ* des paramètres nécessaires à l'analyse du problème.

Mots clés : adhésion – collage, Elastomères, mécanique expérimentale, pneumatique.

Title: Durability of New Metal/Rubber Assemblies

Abstract

Tyres are complex structures with multiple layers of reinforcement such as fabric, polymers and, most importantly, steel cord mesh. As for laminated composites, both tyre strength and rigidity are largely controlled by properties of the metal cord reinforcements. The steel cords embedded inside the rubber matrix form a cord-rubber composite which acts as the skeleton of the tyre. In modern tyres the steel cords are coated with brass that produces strong chemical bonds between Sulphur from the rubber and Copper from the coating during the vulcanisation process. These bonds act as an adhesive interface and undergo complex mechanical loadings, combined with aggressive environmental exposure during the life of a tyre. In this context, extracting detailed information about the mechanical behaviour of this rubber-cord interface is of great importance, both for materials scientists and tyre designers. Traditionally, standard fracture mechanical tests such as peel tests or pull-out tests are used to extract such information. However, these standard tests suffer from many experimental artefacts, and the test results depend on the rubber and cord properties in addition to those of the interface. The peel test cannot mimic the cylindrical nature of the cords whereas pull out tests suffer from friction effects between the fractured faces. These tests therefore fail to provide an intrinsic value of the fracture energy of adhesion.

This PhD thesis aims to design and develop a novel test protocol for quantitative evaluation of the adhesion between tyre rubber and steel cord reinforcement. With this test protocol, referred to as Rubber Cord Adhesion Inflation Test (RCAIT), reproducible test conditions are achieved, and experimental artefacts are found to be minimal. The thesis work involves development of the RCAIT setup, from its design to its execution stage, analytical and numerical treatment of the problem, and calculation of the fracture energy needed for complete interface separation in the test configuration. A Thick Rubber Tube Inflation Model that describes the deformation of the specimens is proposed, in order to perform the analytical and numerical treatment. This model is used to calculate fracture energy or critical strain energy release rate of various rubber-cord composites at different loading rates. The model is initially developed for Mooney – Rivlin and Ogden rubbers, and then extended to other incompressible hyperelastic models that describe the rubber behaviour. A marker tracking technique is proposed, to monitor the crack propagation and to investigate the rubber deformation in the crack process zone region. This analysis is then extended to study the

effect of certain experimental conditions on the evaluation of fracture energy. Finally, the theoretical model is used in conjunction with the marker tracking technique to estimate the properties of specimen materials and to evaluate fracture energy. Thus, the rubber-cord interface fracture energy evaluated with this technique is found to be more reliable and exhibit minimal experimental artefacts.

Keywords: Tyre, Experimental Mechanics, Elastomers, Adhesion.

Institute de Mécanique et de l'Ingénierie

[I2M, UMR 5295, 351 Cours de la Libération, 33400 Talence]

Acknowledgements

First and foremost, I would like to thank my PhD supervisors Julien Jumel and Martin Shanahan of the University of Bordeaux, and Armel Mbiakop-Ngassa and Francois Lallet of MFP Michelin. Thank you all for believing in my capabilities to carry out this PhD work.

I have received valuable guidance from Julien over the past three years. Working under his guidance has made me step out of my comfort zone and has made me more confident about carrying out complex experimental work required to perform research. His out-of-the-box thinking has always inspired me to do well in my work and it will continue to do so for the rest of my career.

I feel privileged to have worked under Martin's supervision. He has always been very supportive and kind. I will always cherish the technical discussions we had in his office. His valuable guidance about how to present the research work, and his modest and calm demeanour are the things that will stay with me forever.

I am thankful to Armel and Francois for their support and guidance, especially whilst working at Michelin. I have thoroughly enjoyed the technical discussions, debates and high-five moments with Armel. I would like to thank Francois, for bearing with me and being so understanding especially if I was in a difficult situation – not only at work, but also outside of work. I have received a lot of support from both of them whilst moving from Bordeaux to Clermont-Ferrand, for which I am grateful.

I would like to thank the Jury members for taking time to read and evaluate my work: Erwan Verron and Lucien Laiarinandrasana for kindly accepting to review my work, and Costantino Creton, Marie Touzet-Cortina and Yann Marco for the examination.

I would also like to thank MFP Michelin for providing financial support for this PhD project. I am thankful to Jean-Michel Vacherand for his guidance and support throughout this PhD work. Colleagues at MFP Michelin, especially, Fady Mamoud and Celia Martinez are thanked for their help in numerical studies and simulation work. Alexis Luminet, Christophe Schauinger, Guillaume Ballester and Pierre-Yves Boulard are also thanked for their help in setting up the experiments at MFP Michelin. A very special thanks goes to Maxime Daude who sent as many specimens as I requested, even at a short notice. The experimental work would have been incomplete without his generous support.

I am thankful to Jeremy Guitard of I2M laboratory for his help in setting up the experiments and helping in troubleshooting the problems that I faced. His generous help and support made the experimental work at the I2M laboratory possible for which I am truly

grateful to him. I am also thankful to my interns Vaishnavi, Gabrielle, Valmon, Ambroise and Florian for performing experimental and simulation work which has helped me in this thesis. I would like to acknowledge the help and support I received from fellow PhD student Sarah Benart in Bordeaux, in Clermont-Ferrand and while moving between the two towns. Thank you to all the PhD and postdoc researchers at I2M, especially Aditya and Sreedhar, for making my time at the lab an enjoyable experience.

I would also like to thank my friends Siddharth and Omkar for their friendship and their support which made my stay in Clermont-Ferrand very pleasant; and for all those interesting discussions about politics and life which I thoroughly enjoyed.

Finally, I would like to thank my family, especially my parents, who have always been supportive of my decisions. Thank you very much for making me who I am today. I am also thankful to my brother Swaroop and my cousin Ajit who have been my role models since my childhood. Their support and life lessons will always be with me.

I could not have finished this thesis without the support of my wife, Shahana. I cannot thank you enough for showing faith in me, being with me and bringing joy and a sense of satisfaction in my life.

Contents

RÉSUMÉ ..... **II**

ABSTRACT ..... **IV**

ACKNOWLEDGEMENTS ..... **VI**

TABLE OF FIGURES ..... **XII**

CHAPTER I: INTRODUCTION & LITERATURE REVIEW **7**

I.1. A BRIEF HISTORY OF TYRES **8**

I.2. COMPONENTS OF A MODERN TYRE **8**

I.2.1. RUBBER MIXES 9

I.2.1.1. Components of rubber mixes *9*

I.2.1.2. Vulcanisation of rubber *10*

I.2.2. REINFORCEMENT CABLES 11

I.3. CORD-RUBBER ADHESION **13**

I.3.1. RAYON AND NYLON CORD ADHESION 14

I.3.2. POLYESTER CORD ADHESION 15

I.3.3. ARAMID CORD ADHESION 16

I.3.4. STEEL CORD ADHESION 17

I.4. QUANTITATIVE EVALUATION OF ADHESION **21**

I.4.1. SOME NOTES ON FRACTURE MECHANICS 22

I.4.1.1. Linear elastic fracture mechanics *22*

I.4.1.2. Fracture mechanics of adhesively bonded structures *23*

I.4.1.3. Fracture of rubber-like materials *24*

I.4.2. RUBBER-STEEL CORD ADHESION FAILURE 25

I.4.3. FRACTURE TESTS FOR RUBBER-STEEL CORD ADHESION 26

I.4.3.1. Pull-out type tests *26*

I.4.3.2. Peel type tests *29*

I.4.4. NEED FOR A NEW TEST METHOD 30

I.5. AIM OF THE THESIS 33

CHAPTER II: RUBBER CORD ADHESION INFLATION TEST (RCAIT) 35

II.1. INTRODUCTION TO THE RCAIT 36

II.1.1. EXPERIMENTAL SET-UP 36

II.1.2. EXPERIMENTAL RESULTS 39

II.2. THICK RUBBER TUBE INFLATION MODEL (TRTIM) 40

II.2.1. CONSTITUTIVE EQUATIONS 41

II.2.2. BOUNDARY CONDITIONS 42

II.2.3. NUMERICAL MODELLING 46

II.2.4. INFLUENCE OF BOUNDARY CONDITIONS 49

II.3. VIRTUAL CRACK PROPAGATION 52

II.3.1. STRAIN ENERGY RELEASE RATE 52

II.4. IMPROVEMENTS TO THE RCAIT 58

II.4.1. TEST SPECIMENS AND BULK RUBBER CHARACTERIZATION 58

II.4.2. IMPROVED TEST SET-UP AND TEST PROTOCOL 63

II.4.3. CRACK PROPAGATION AND SERR 66

II.4.4. THICK RUBBER TUBE INFLATION MODEL: OGDEN RUBBER 69

II.4.5. SERR: GLOBAL ENERGY BALANCE 74

II.5. RUBBER CORD ADHESION PERFORMANCE CHARACTERIZATION 76

II.5.1. TEST RESULTS 77

II.5.2. POST-PROCESSING 78

II.6. CHAPTER II SUMMARY AND FUTURE STEPS 81

CHAPTER III: EXPERIMENTAL STUDY OF THE RCAIT 82

III.1. INTRODUCTION 83

III.2. EFFECT OF LUBRICATION 84

III.2.1. CHOICE OF LUBRICANT 84

III.2.2. EFFECT OF LUBRICATION ON RCAIT RESULTS 85

III.3. IMAGE PROCESSING 88

III.3.1.-CRACK PROPAGATION MONITORING 89

III.3.2. CHARACTERIZATION OF THE RUBBER 93

III.3.3. EVALUATION OF M AND A USING RCAIT 94

III.4. REPEATABILITY TESTS 98

III.4.1. TEST PLAN 98

III.4.2. REPEATABILITY TEST RESULTS 99

III.4.3. ANALYSIS OF RESULTS 102

III.5. CHAPTER III SUMMARY AND FUTURE STEPS 107

CHAPTER IV: CONSTITUTIVE MODELLING AND ITS EFFECTS ON THE RCAIT 110

IV.1. INTRODUCTION 111

IV.2. THICK-WALLED CYLINDER INFLATION MODEL 111

IV.2.1. GLOBAL ENERGY BALANCE 112

IV.2.2. THEORETICAL MODEL 113

IV.3. APPLICATION TO VARIOUS RUBBER MODELS 118

IV.3.1. UNIAXIAL TEST DATA FITTING 118

IV.3.2. EFFECT OF MODEL ON SERR CALCULATION 123

IV.4. VOLUMETRIC DATA FITTING 125

IV.4.1. DATA FITTING ALGORITHM 125

IV.5. CHAPTER IV SUMMARY & FURTHER DISCUSSION 130

CHAPTER V: PERSPECTIVES AND CONCLUSION 135

V.1. SOME FUTURE APPLICATIONS OF THE RCAIT 136

V.1.1. TESTS ON RUBBER-CABLES COMPOSITES 136

V.1.2. TESTS USING VARIOUS INJECTION FLUIDS 138

V.1.3. CYCLIC TESTS 139

V.2. CONCLUSION 140

REFERENCES 144

APPENDIX A 153

APPENDIX B 155

APPENDIX C 157

Table of Figures

Figure I.2.1: Cross-section of a tyre [4]. 8
Figure I.2.2: Forces on a tyre. 9
Figure I.2.3: Generalised structures in sulphur vulcanised rubber [6]. 10
Figure I.2.4: Components of a steel cord [11]. 12
Figure I.3.1: Schematic of the RFL adhesive system structure [14]. 14
Figure I.3.2: Rayon cord cross-section showing high penetration of RFL adhesive after priming [11]. 15
Figure I.3.3: Two-step polyester to rubber bonding process [13]. 15
Figure I.3.4: p-Aramid to rubber bonding [14]. 17
Figure I.3.5: Schematic of the wire drawing and brass plating process [15]. 18
Figure I.3.6: Schematic of brass to rubber bonding [11]. 18
Figure I.3.7: Depth concentration analysis of a brass-rubber sample [16]. 19
Figure I.3.8: Schematic of the brass-rubber adhesion [18]. 21
Figure I.4.1: The three modes of fracture [21]. 22
Figure I.4.2: Schematic of a DCB Specimen. 24
Figure I.4.3: Crack propagation in rubber-like materials involves cavity formation, chain pull-out and bond breaking [25]. 24
Figure I.4.4: Bond breaking and viscoelastic dissipation near crack tip [25]. 24
Figure I.4.5: TCAT specimen [46]. 27
Figure I.4.6: Injecting pressurised Nitrogen gas at the interface [48]. 27
Figure I.4.7: Coaxial shear pull-out test (CSPT) [49]. 28
Figure I.4.8: Peel testing rig [57]. 29
Figure I.4.9: Blister test- Photograph, Schematic Top View and Schematic Side View [64]. 32
Figure I.4.10: Constrained blister test. The constraint plate restricts the inflation of the blister [65]. 32
Figure II.1.1: The tape adhered around the steel cord creates a barrier between rubber and brass coating. This barrier creates initial crack during the vulcanization process. 36
Figure II.1.2: (a) Test specimen (b) Schematic of the specimen cross-section. The initial debonding length is shown as white tape on the steel cord. (c) Inflated specimen during the test. The ‘fractured and inflated’ length of the rubber envelope is touching the PMMA confinement tube. 37
Figure II.1.3: Schematic representation of RCAIT. 38

Figure II.1.4: RCAIT setup at the I2M laboratory. 38
Figure II.1.5: Schematic of the hydraulic circuit for RCAIT. 39
Figure II.1.6 : (a) Fluid Pressure vs Injected Volume. A nearly constant fluid pressure is observed during the crack propagation stage (ca. 8ml)), (b) Fracture surface of the steel cord. The shining spots (brass-coated steel) may indicate an adhesive failure. 40
Figure II.2.1: Rubber tube deformation stages. P_i is the applied fluid pressure..... 41
Figure II.2.2: Unstable inflation of rubber cylinders. P_{max} is the maximum fluid pressure and the point of instability. 43
Figure II.2.3: (a) Aneurysms in the rubber envelope, (b) and (c) Rubber envelope failure due to absence of a confinement tube. 44
Figure II.2.4: Comparison of unstable and stable inflation of the rubber envelope. Confinement contact comes prior to the point P_{max} thereby avoiding the instability. Results from the FEM simulation closely matches the theoretical model. 45
Figure II.2.5: Schematic of the Rubber Cylinder Inflation modelled in ABAQUS. 46
Figure II.2.6: FE modelling of specimen inflation (a) Overall specimen deformation (b) large deformation is observed near the crack tip region (c) The axial stretch ratio measured along the outer radius of the specimen (d) The circumferential stretch ratio measured along the inner radius of the specimen. 47
Figure II.2.7: Effect of dimensionless radius ($h = w_0/v_0$) and confinement ratio (R/w_0) on Rubber Tube Inflation. Dotted lines represent confinement contact..... 48
Figure II.2.8: Effect of confinement ratio (R/w_0) on Rubber Tube Inflation for a fixed dimensionless radius ($h = w_0/v_0=8$)..... 49
Figure II.2.9: Unconfined Inflation Test. Effect of Axial Stretch Ratios on Cauchy Stresses and P_n..... 50
Figure II.2.10: Purely Confined Inflation Test. Effect of Axial Stretch Ratios on Cauchy Stresses and P_n..... 51
Figure II.3.1: As the crack propagates by an arbitrary small length δa, the rubber envelope inflates and touches the confinement tube. 53
Figure II.3.2: Strain Energy Release Rate as a function of injection Fluid Pressure. 55
Figure II.3.3: Evolution of SERR with applied pressure. Comparison between theoretical model and FE model. 56
Figure II.3.4:Comparison of the energies stored in the fluid and the rubber at crack propagation, calculated for a unit fractured area. G_r is the contribution of the rubber envelope and G_f is of the fluid. G is the SERR, plotted using (II.3.11). 57

Figure II.4.1: (a) Geometry of the tensile test specimen (b) Tensile test specimen under no load (c) Specimen under tension. 59
Figure II.4.2: Tensile test results at 5 strain rates 60
Figure II.4.3: Ogden model fit for Mix B rubber uniaxially loaded at 0.011/s. 61
Figure II.4.4: Ogden Model parameters for Mix A and Mix B. 62
Figure II.4.5: Hydraulic Circuit for RCAIT and the newly designed specimen fixture with glass confinement tube. 63
Figure II.4.6: Improved RCAIT setup 64
Figure II.4.7: Marker monitoring technique used for axial stretch ratio measurement during specimen inflation. 65
Figure II.4.8: RCAIT of Mix A-brass coated cord. Average crack propagation pressure is 90.5 bar. 66
Figure II.4.9: Calculating axial stretch ratio (λ_z) and specimen tip displacement (d) using a particle tracking algorithm. 67
Figure II.4.10: Crack propagation monitoring until it reaches the last marker. 67
Figure II.4.11: Rubber tube deformation stages. P is the fluid pressure. 69
Figure II.4.12: Algorithm to solve the Thick Rubber Tube Inflation problem for Ogden Model. 72
Figure II.4.13: Stable Inflation of an Ogden Rubber tube in the presence of a confinement. Theoretical and FE model follow very precisely the same curve. 73
Figure II.4.14: G vs P for rubber Mix A and Mix B. α and μ are taken as average values from the tensile tests. 75
Figure II.4.15: Effect of rubber properties (loading rate) on G. 76
Figure II.5.1: RCAIT results for rubber Mix A at five different loading rates. 77
Figure II.5.2: RCAIT results for rubber Mix B at five different loading rates. 77
Figure II.5.3: Crack propagation pressure for Mix A and Mix B bonded to brass coated steel cord. 78
Figure II.5.4: Crack propagation rate V_p for Mix A and Mix B bonded to brass-coated steel cord. 79
Figure II.5.5: G_c for 5 loading rates. The specimens consisted Mix A and Mix B bonded to brass coated cord. 79
Figure III.2.1: Effect of lubrication on RCAIT specimen behaviour. 86
Figure III.2.2: Effect of lubrication on specimen axial deformation during RCAIT. 87

Figure III.2.3: Effect of lubrication on mode mixity of fracture. Notice the difference in thickness of the inflated rubber between the two cases. 88
Figure III.3.1: A typical fluid pressure versus injected fluid volume evolution during RCAIT. 89
Figure III.3.2: Marker Monitoring. 91
Figure III.3.3: Target Tracking using IMETRUM® Video Gauge ™. 91
Figure III.3.4: Marker monitoring for specimen axial deformation. 92
Figure III.3.5: Crack propagation length plotted against time. 92
Figure III.3.6: Algorithm to calculate α and μ. 94
Figure III.3.7: Thick Rubber Tube Inflation. Comparison of theoretical model and experimental results. 96
Figure III.3.8: Effect of rubber model parameters on SERR calculation. 97
Figure III.4.1: Repeatability test results for Mix A+ brass coated cord specimens. (a) 5ml/min and (b) 2ml/min. 100
Figure III.4.2: Repeatability test results for Mix B+ brass coated cord specimens. (a) 5ml/min and (b) 2ml/min. 101
Figure III.4.3:Crack propagation pressure for each test. Error bars show standard deviation with respect to the average value per test. 102
Figure III.4.4:Comparison of average crack propagation pressures between Mix A and Mix B. 103
Figure III.4.5: Ogden parameter fitting for the inflation data in Figure III.4.1. 104
Figure III.4.6: Ogden parameter fitting for the inflation data in Figure III.4.2. 105
Figure III.4.7: Average values of evaluated fracture energy for all 4 test cases. 106
Figure III.4.8: Average crack propagation speeds for the 20 tests. 107
Figure IV.2.1: Typical Pressure vs Volume plot of an RCAIT specimen. 112
Figure IV.2.2: Generalised Thick-Walled Cylinder Inflation Algorithm for hyperelastic materials. 116
Figure IV.2.3: Comparison between Thick-Walled Cylinder Inflation algorithms presented in Figure IV.2.2 and Chapter II. 117
Figure IV.3.1: Uniaxial tensile test fit for the five models. 119
Figure IV.3.2: Residuals of the tensile test data fitting. 120
Figure IV.3.3: Thick Walled Rubber Cylinder Inflation behaviour for 10 cases compared with the experimental data. 121

Figure IV.3.4: Evolution of fluid pressure (P) due to increasing deformed inner radius (v_0). 121
Figure IV.3.5: Fluid pressure evolution plotted for all 10 cases and compared with the experimental data. 122
Figure IV.3.6: Evaluation of SERR for all 10 cases. 123
Figure IV.3.7: SERR values evaluated for the test case in Figure IV.2.1. 124
Figure IV.4.1: Comparison between Volumetric Data Fitting algorithms presented in current chapter and Chapter III. 126
Figure IV.4.2: Volumetric data fitting for the specimen in Figure IV.2.1. 127
Figure IV.4.3: Pressure evolution for all 10 cases calculated using the volumetric data fitting. 128
Figure IV.4.4: SERR values calculated for 10 cases using the volumetric data fitting. 128
Figure IV.4.5: SERR values evaluated using the volumetric data fitting for the test case in Figure IV.2.1. 129
Figure IV.5.1: Evolution of circumferential stretch ratio at the inner radius of the inflated rubber tube. Crack propagation pressure for Figure IV.2.1 is shown as a grey dashed line. . 132
Figure IV.5.2: Effect of inner radius on evaluated SERR for five hyperelastic models (a) v_0=1.15mm (b) v_0=1.65mm. 133
Figure V.1.1: Steel cord used in commercial car tyres 136
Figure V.1.2: (a) Test specimen with twisted cable strands bonded to rubber (b) test specimen sealed with epoxy at the end (c) fractured test specimen (d) fractured cable. 137
Figure V.1.3: RCAIT results for specimens with two types of cables bonded to the same type of rubber. 137
Figure V.1.4: RCAIT result for specimen injected with saline water. 138
Figure V.1.5: RCAIT results for specimen injected with ethanol. 138
Figure V.1.6: Cyclic loading and unloading of an RCAIT specimen. 139

Context

Tyres are an integral part of today's road mobility. From bicycles to cars and from trucks to aeroplanes we use tyres to be mobile on the ground. It is estimated that nearly 3billion tyres are produced each year globally. The principle function of tyres is to provide cushion on the hard surface of the ground or road and to reduce rolling resistance of wheels. This toroidal structure forms the outer part of a wheel that rolls on the ground. Pneumatic tyres are capable of absorbing small irregularities on the road and provide a smooth ride. However, tyres were not always pneumatic. Initially they were made out of vulcanised rubber reinforced with several materials like cotton, canvas or steel. However, as the industrial revolution took over Europe, newer technologies were invented to be used in tyre applications that meant filling them with air. The thick toroid of reinforced rubber became two concentric tuber – an inner tube filled with air and an outer tube to protect the inner tube from road friction. Modern tyres are highly engineered rubber composites that are designed to meet the manufacturers' ride, handling, and traction criteria, as well as the quality and performance expectations of the customer. A mid-size car tyre revolves around 500 times per kilometre. Therefore, during a distance of 50,000 km the tyre undergoes nearly 25million load cycles. The tyre has to withstand the changes in temperature, humidity as well as the immense loads arising from the vehicle engine and ground during these millions of cycles. These load cycles not only affect the outer surface of the tyre i.e. tread, but the various components of the tyre as well.

A modern tyre is made up of several components that form the structure of the tyre and help improve the durability of the tyre apart from giving a smooth and safe ride. The millions of cycles that the tyres have to withstand affect these components as well. Therefore, for the safety of the rider and other vehicles on the road, tyres have to pass through multiple tests before, during and after the production phase. These tests are done for three main purposes: (a) Benchmarking, (b) Materials research (c) Safety and regulatory requirements.

From the manufacturer's perspective, it is important to be aware of the competition in the market and the needs of the customers. This is done during the benchmarking process. Tyres of various brands as well as equivalent products produced in-house are tested for their road performance and compatibility with customer needs. Benchmarking helps set short term and long-term goals for tyre production and shapes the direction in which the materials research should be advanced.

During the materials research phase individual components of tyres undergo thorough testing. During this phase, manufacturers test materials, reinforcements as well as the completed design of tyres. This is done by using experimental tests on various materials as well as computer simulation techniques such as Multiphysics modelling, finite element modelling (FEM) and multibody dynamics modelling to accelerate the development process. Computer aided design and manufacturing processes (CAD, CAM) are also used to create bespoke tyre moulds in order to produce optimal tread shape. However, due to the large number of variables present in this process, experimental testing is required to verify the computer-generated projections. These tests are performed on the various components of the tyre such as bead and carcass plies, tread, and bulk rubber material of the tyre. The tests involve wear/rolling friction resistance tests, durability tests on tyre materials such as fracture tests, and effect of harsh environment (temperature, humidity) conditions on various components of the tyre.

Once the tyre is produced, it must pass strong regulatory requirements of the local governing body. These regulations are aimed at making the tyre durable and safe for the riders and other vehicles on the road. These also include effect of tyre performance on fuel efficiency, air and noise pollution. Before selling the tyres, the manufacturer must pass these requirements. However, most tyre manufacturers design tyres that surpass these minimum requirements.

Since modern tyres are made out of anywhere between 60 to 200 ingredients, tyre design and testing take considerable amount of time. The initial development of a new tyre starts with market research and benchmarking. The manufacturer chooses reference tyres of rival brands and its own brands. Competitors' tyres are reverse engineered and tested to determine material performance benchmarks. Using computer modelling, detailed shapes and designs of the tyre's insides and outside are created. These are rough designs based on benchmarking and tyre designers make changes to these designs according to the requirements. Depending on the application of the tyre, the tread arc radius and footprint need to be modified. For vehicles that require maximum grip, the tyre shape must be squarer. However, this might make the ride harsh. Making the arc shape too round will also affect the handling however it will provide a smoother ride. The leading and trailing edges of the tyres should be designed properly to reduce tyre noise during operation. Tyre designers consider an ever-increasing list of parameters while making improvements to the benchmark design. The modified design patterns are then tested using computer simulations to evaluate their rolling resistance, dry and wet traction values, hydroplaning resistance and noise levels.

Once the tyre design procedure is completed, the rubber compound development is started. Several rubber compounds are tested for their dynamic behaviour at changing temperatures. The rubber samples are passed through a dynamic mechanical analyser where the influence of various components of rubber on its dynamic performance is tested. This includes fatigue behaviour, creep behaviour, strain hardening as well as fracture toughness of the rubber compound at various temperatures.

Once the basic tyre shape and structure are designed and the rubber compound design is finished, several tests are performed on these newly designed tyres. These tests can be grouped in two tiers. During the first tier, the profile of the newly designed tyre is verified, and the rubber compound design is also tested. The tyre construction is still based on the generic concept developed during benchmarking. The tests in the first tier involve endurance testing of the tyre in order to pass the regulatory requirements. These tests are aimed at evaluating the maximum loads and load cycles the tyre can withstand before failure. Severe ageing conditions are used to accelerate deterioration of the tyre rubber and the adhesion between various components of the tyre. Tyres are kept at elevated temperature and humidity conditions to accelerate deterioration before testing them for their durability. This process not only speeds up the testing procedure but can imitate extreme environmental conditions the tyres have to withstand in certain regions of the globe.

Tier 1 tests also include testing the rolling resistance of the tyre. This parameter is very important to reduce fuel consumption of the vehicle and is one of the most important regulatory parameters as well. Using the force and deformation data obtained during these tests, machine learning algorithms are developed to understand how various road conditions affect the tyre's performance. These results are very crucial for tyre designers to tune the design for best performance. At the end of the tier 1 tests, the tyre design process is nearly finished.

Tier 2 tests are aimed at testing the tyres performance from the customer's perspective. Tyres are installed on various vehicles and their performance is measured using various parameters such as handling response, precision, road grip, noise levels and breaking. Tier 2 tests are performed on road and often involve various automobile partners in order to test the tyres on different vehicles.

Due to its rigorous nature, tyre development and testing process takes up to three years and it is highly labour and cost intensive. Apart from that, the entire process of producing tyres as

well as testing them impacts the environment at several levels. Tyre production has deep environmental impacts, ranging from deforestation to the extensive use of fossil fuels. Modern car tyres require about 25 litres of crude oil to produce, while truck tyres require nearly 80 litres. Moreover, as the tyre is in operation, the tread rubber wears. This releases plastics/polymers in the environment which eventually end up in the oceans. Tyres are one of the biggest contributors to the ocean microplastic pollution. Tyre production and usage are therefore a big threat to the forest and ocean biodiversity.

Therefore, in line with the Paris Climate Agreement, Michelin Tyres aim at “doing business sustainably while protecting biodiversity”. Michelin started to analyse the environmental impacts of their tyres during the design, research and testing phase to guide the choice of materials, architecture, and manufacturing processes. The aim here is to produce a “clean” tyre which has minimal environmental impact. This heavily affects the R&D process, especially tyre testing. This aim has been at the heart of the broader research project.

Project Goals

For years, Michelin has sought to improve the endurance resistance of tyre materials, in particular for tyres exposed to severe stress conditions. This is the case in particular for emerging markets where non-specification uses (overload, road conditions, etc.) and highly penalising ambient conditions (humidity, heat, etc.) accumulate. Furthermore, in order to reduce the mass of the tyre, which results into a drop in rolling resistance, cost of production as well as fuel efficiency, the tyre complexity and/or material thickness needs to be reduced. Such a strategy supposes being able to make progress in endurance and resistance to aging. In addition, following the “clean” tyre aim, it is important to eliminate any rubber compounds that could potentially have an impact on the environment. The originality of this project is to take into account the impact of the generic modification of all the positions of the tyre simultaneously through new crosslinking and protection chemistries.

This project aims to find generic material solutions to increase endurance and resistance to aging in order to ultimately allow reductions in mass (thickness and / or complexity) and fuel consumption. These solutions must be free from potentially hazardous products in terms of

forest and ocean biodiversity. More precisely, the usefulness of a significant improvement in the resistance to aging of materials is linked to Michelin's desire to make tyres lighter.

PhD Thesis

To achieve the goals of such a huge project, two PhD posts were proposed out of which this PhD thesis is the second one. This PhD thesis aims at performing tests on tyre materials under severe loading conditions. The materials used are in line with the sustainability goals of Michelin. Testing four tyres for a passenger car can cost up to €200,000. Such thorough testing has a huge carbon footprint. Therefore, Michelin aims at developing novel test procedure that minimise the environmental effects of materials testing and research. This is achieved by testing individual components of the tyre instead of testing the entire tyre.

With this aim in mind, this PhD thesis was proposed to devise a new test protocol for tyre component testing which will be focused on testing the tyre materials under severe loading and environmental conditions. The thesis work started as a Research Internship in collaboration with I2M Laboratory of University of Bordeaux in April 2017. The internship was focused on literature review, concept development, test design and feasibility analysis of the test. It was then continued into a PhD thesis from November 2017.

In the first phase of the PhD, the test development continued in parallel to theoretical and numerical development. Near the end of the first year of the PhD, the preliminary results were presented in EURADH/CLBA conference in Portugal in September 2018. In the second year, the experimental development was extended to test several materials under various loading conditions. The results from the first two years were published in literature in the form of two peer reviewed articles. The final year was mainly dedicated to the theoretical and numerical development of the testing and implementation of the test protocol in Michelin's research centre in Ladoux, Clermont-Ferrand. The test equipment's applicability for testing other tyre materials and structures was also evaluated which resulted in promising outcomes.

This PhD thesis is the outcome of such an ambitious collaborative project between the University of Bordeaux and MFM Michelin (Michelin Tyres, France). The thesis is divided into five chapters. The first chapter introduces the state of the art in tyre component testing, literature review of research on materials used in tyres as well as the standard testing

procedures for tyre strength and durability. At the end of the first chapter a novel test protocol referred to as *Rubber Cord Adhesion Inflation Test (RCAIT)* is presented in line with the research project's primary goals described above. The second chapter presents development of this test protocol followed by some experimental and theoretical studies aimed at testing the tyre materials under severe loading conditions. The third chapter continues the experimental work, introduces novel techniques to improve the accuracy of the results. The fourth chapter extends the theoretical and numerical work with the aim of broadening the applicability of the testing protocol along with its implementation in Ladoux, Clermont-Ferrand. The fifth chapter presents future prospects for this test protocol such as applications to testing various tyre components and further research pathways that can be followed to achieve the research projects goals. Finally, the work presented in this thesis is summarised in the form of a general conclusion at the end of the fifth chapter.

Chapter I: Introduction & Literature Review

I.1. A Brief History of Tyres

The earliest record of humans using tyres is from Mesopotamia in the form of leather bands [1]. These leather bands were wrapped around the wheels of a wagon to make the ride smoother. As centuries passed, tyres have been through structural and material changes such as iron/steel on wooden wagon wheels, or rubber cladding on metal wheels. In 1847, the first air-filled (or pneumatic) tyres was patented [2], which consisted a carriage wheel with an air-filled rubber tube around its circumference. There are no records of this tyre going into production. However, in 1888, John Boyd Dunlop developed a tyre to make his son's bicycle ride smooth. This went on to become the first pneumatic tyre successfully produced and used. Since then, tyres have become more and more complex involving an ever-increasing number of components and ingredients. A modern tyre can have up to *60* ingredients [3], which include but are not limited to, Natural Rubber, Synthetic Rubber, Reinforcement Cables (Metallic and Textile), Carbon Black and other chemical agents. Natural rubber and synthetic rubber, which are the main components of the tyre tread form the 'matrix' of the tyre. The reinforcement cables form the skeleton of the tyre. Together, the rubber and the reinforcement cables give the tyre its shape and structure. Some of the remaining ingredients provide the tyre with unique qualities such as low rolling resistance, improved durability and better road grip.

I.2. Components of a Modern Tyre

A modern tyre is a complex mechanical structure that consists of various layers embedded inside an elastomer (*Figure I.2.1*). Since it is the only part of the vehicle that touches the road, a tyre must withstand the road traction and other loads as well as provide safety and comfort. The entire weight of the vehicle, along with the torsional and frictional forces arising from power application, braking and steering are supported by the tyres (see *Figure I.2.2*). They need to be lightweight to reduce the overall weight of the vehicle in order to reduce fuel consumption. At the same time, they must be durable to survive the deleterious environment such has high temperatures and humidity. Striking a balance between all of these factors means

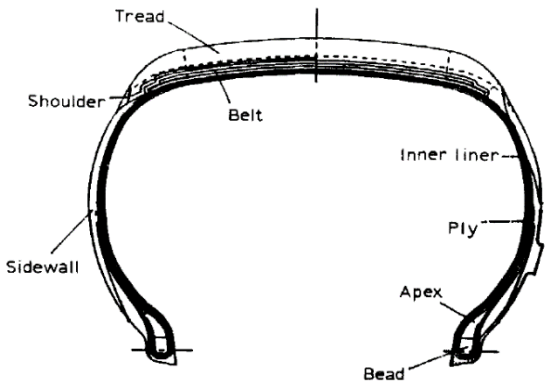

Figure I.2.1: Cross-section of a tyre [4].

that tyre manufacturers have to perform extensive research into how tyres are made, how they perform on and off road, and how each constituent of a tyre affects the tyre's performance. A study of various components inside the tyre and how they affect the performance of the tyre is therefore essential. Some key components (*Figure I.2.1*) of a modern vehicle tyre are as follows [4]:

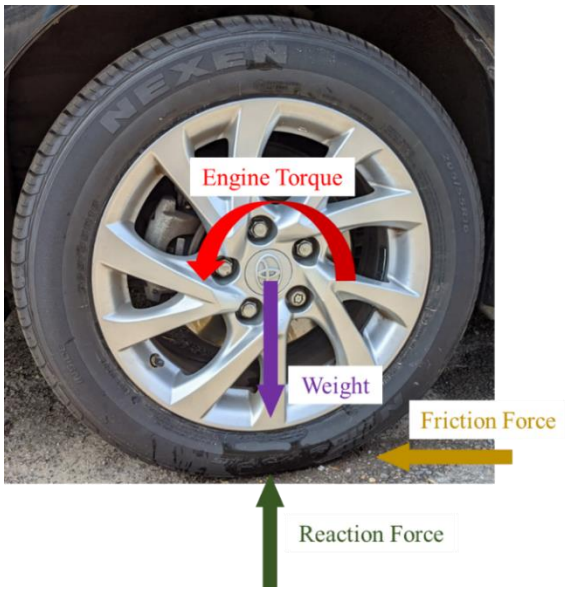

Figure I.2.2: Forces on a tyre.

- Tread – This component comes in direct contact with the road. It must withstand high heat, friction and suppress noise during the ride.
- Sidewall – The sidewalls works as a load transferring member between the wheel and the tread. They also protect the tyre from the damage occurring during turning around corners and kerbs.
- Bead – The beads (1 on each sidewall) keep the inside layers of the tyre structure (the plies) in place and help to secure the tyre on the wheel
- Plies – Plies are the reinforcement members inside the tyre. They consist of various layers of fabric, polymers and metal cables embedded in the rubber matrix. The plies are spread over the entire span of the tyre cross-section.
- Belts – The belts provide additional support to the tyre treads in order to increase their contact stiffness. They are also made out of reinforcement members embedded in rubber.
- Inner Liner – This is a protective layer inside the tyre which acts as an air retaining component in tubeless tyres. For tubed tyres, the inner liner protects the tube from abrasion and wear against the insides of the tyre.

I.2.1. Rubber mixes

I.2.1.1. Components of rubber mixes

The components of the tyre rubber mixes can be further divided into 5 main ingredients [3], *viz*. Polymers, Fillers, Softeners, Antidegradants and Curatives or Vulcanizing Agents. The natural and synthetic rubbers are the polymers which form the matrix of the tyre. Carbon

black and silica are some of the fillers used in tyre rubbers. To aid the processing of the crude rubber mix (un-vulcanised rubber), softeners such as mineral oils, waxes and petroleum oils are used. The antidegradants such as amines, phenols, antioxidants and waxes protect the tyres from heat, oxidisation and ozonation during storage as well as usage of the tyre. The vulcanising agents or curatives such as sulphur create cross-linking between the polymer chains providing strength and rigidity to the rubber, and hence the tyre. This process is explained briefly below.

I.2.1.2. Vulcanisation of rubber

Initially, when raw rubber was used in tyre and other applications, it suffered from many disadvantages such as stickiness which made handling difficult, loss of elasticity at high temperatures and inflexibility at low temperatures. However, as Treloar mentioned in [5], Goodyear's discovery of *Vulcanisation* in 1839 rescued the rubber industry from the difficulties it faced due to some of the properties of raw rubber detrimental to tyre applications. In short, vulcanisation is a process of chemically reacting the rubber with sulphur (or some other agents) to create cross-linking between long rubber molecules. A detailed description of the vulcanisation process is given in [6], which includes several methods of vulcanisation. They are Sulphur Vulcanisation, Peroxide Vulcanisation, Resin or Chlorine Cross-linking and Radiation Induced Cross-linking. Out of these methods, sulphur vulcanisation (applied to natural rubber and SBR) is the most commonly used process especially in tyre applications.

The sulphur vulcanisation requires many reagents, classified mainly as vulcanising agents, accelerators, activators, retarders and inhibitors [6]. The vulcanising agents include elemental sulphur or an organic sulphur donor. Sulphur by itself is a slow reagent, therefore accelerators are added such as sulfenamides, benzothiazoles, thiurams and guanadines which speed up the vulcanisation process and make it cost

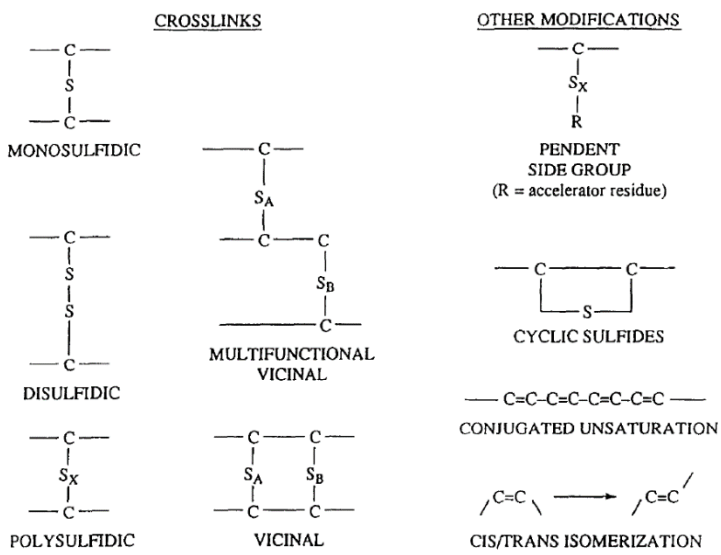

Figure I.2.3: Generalised structures in sulphur vulcanised rubber [6].

effective. The activators aid the accelerators in initiating the vulcanisation. Some commonly used activators are zinc oxide, fatty acids and nitrogen containing bases. The retardants and inhibitors control the speed of vulcanisation in order to elongate the whole process. This is necessary since, during the preparation of the vulcanizates, the crude rubber mix is heated to aid mixing of the components and to mould it into required shape. However, there is a possibility of premature vulcanisation, referred to as 'scorch' or 'cured lumps' in the industry, occurring inside the rubber mix. This affects the processing and handling of the rubber since now it contains areas which are vulcanised and have become hard and stiff. Commonly used retardants and inhibitors are salicylic acid, benzoic acid and N-cyclohexylthiopthalimide (CTP). The crude rubber mix, consisting of the reagents described here is heated in the mould at a certain temperature and for a certain period of time to produce vulcanisation.

The process of vulcanisation has been carried out for over *170 years*, yet, the intricate details of this process are not completely understood. This is partly due to the huge number of ingredients involved in the process. Akiba and Hashim have described various chemical processes involved in vulcanisation in [6]. They have also presented generalised structures present in vulcanised rubber (*Figure I.2.3*) which improve its durability and rigidity as well as impart other physical and chemical changes to the rubber.

I.2.2. Reinforcement cables

The loads and harsh conditions that the tyre has to withstand are shared by the reinforcement cables that form the plies, belt and the beads. They are also important in containing the air pressure inside the tyres. These reinforcements cables, referred to as cords, are made out of various materials. The commonly used cord materials are Nylon (6 and 66), Polyester, Rayon, Aramid and Carbon Steel [3].

Nylon, or aliphatic polyamide cords were initially used for heavy duty trucks due to their high tensile strength [7]. It made its way first into light truck tyres and later into passenger car tyres. The high tensile strength of Nylon is achieved by drawing a polymer with higher molecular weight and at a high drawing ratio. However, polymers with higher molecular weight suffer from dimensional instability. By using the hot stretching method or other ways such as multistep stretching or stretch and relax method, a balance between high tensile strength and dimensional stability can be achieved [7].

Polyesters of the type polyethylene terephthalate are widely used as reinforcement cords in vehicle tyres [7], [8]. This polymer possesses various material properties suitable for a tyre

cord such as low elongation and high modulus during operating conditions. Polyester cords provide the tyre higher resistance against tread wear and better steering abilities thereby improving its high-speed performance. The polyester produced for tyre cord application can have up to *30%* higher molecular weight than regular polyester yarn [7], providing it with higher tensile strength.

Rayon is made from cellulose based fibres and is commonly used in body plies and belt plies. Although rayon cords have very good heat resistance, due to their inferior performance compared to nylon and polyester, they are used for limited applications only. In addition, due to various environmental issues surrounding the production of rayon fibres, they are rapidly being replaced by polyester.

Aramids, or aromatic polyamides, are synthetic fibres with very high tensile strength and better dimensional stability than nylon and polyester [9]. They were initially used as simple aromatic-polyamides [10]. However, later, a newer version of the polymer, called Kevlar or Twaron, which is a para-aramid, was also used due to its excellent material properties. Although these fibres possess superior material properties than other cord materials, the relatively high cost of production has kept their application limited.

As reported in [11], steel cables were first introduced in Europe in 1940s as a new tyre cord material due to the material's high tensile strength. Later, they were used in USA and the rest

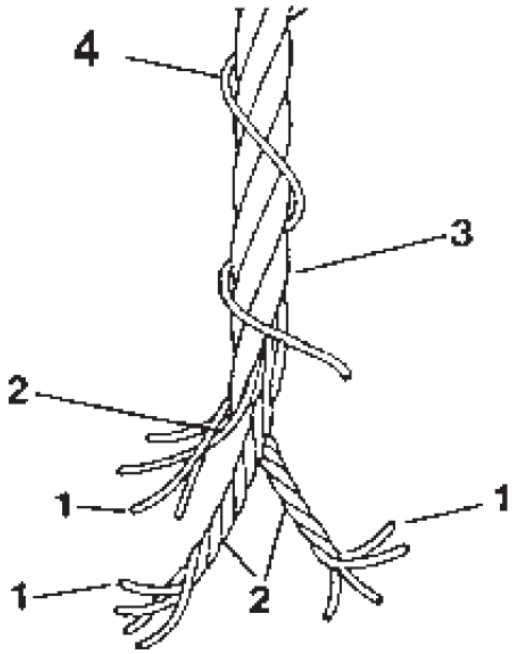

Steel cord components: (1) filaments; (2) strands; (3) cord and (4) spiral wrap

Figure I.2.4: Components of a steel cord [11].

of the world as a common tyre cord material. The steel tyre cords are in the form of twisted cables woven into bundles of multiple filaments (*Figure I.2.4*). Steel cords made by cabling steel filaments have a very high modulus at an affordable cost. They have high compressive as well as bending stiffness, good resistance to fretting fatigue, and good adhesion to rubber. Due to their excellent material properties and low cost, steel cords are used extensively in radial passenger tyres.

The general nomenclature of steel cords presented in [11] is as follows:

- Filaments: it's the single metallic wire of diameter *0.15mm* to *0.38mm*
- Strand: two or more filaments are twisted together to form a strand
- Cord or Cable: single strand on its own or multiple strands twisted together form a cord or cable
- Spiral Wrap: this is a single filament wrapped around the cord to hold the strands together

I.3. Cord-Rubber Adhesion

Durability and safety of tyres depends on that of its constituents. Since the rubber-cord layers form a considerable proportion of a modern tyre, the integrity of these layers is essential for the strength of the tyre. As discussed earlier, the cords possess excellent properties on their own. However, for transferring the loads from the tread and the sidewalls to the individual layers of the tyre effectively, these layers need to be adhered to the rubber matrix firmly. Depending on the type of the cord, the adhesion of the cords to the rubber matrix changes vastly.

McDonel has presented various requisite properties of cord-rubber adhesive systems in [11]. These are:

- Good adhesion to the rubber and the cord
- Intermediate modulus between cord and rubber
- Rapid rate of bond formation
- High fatigue resistance
- No chemical deterioration of cord by the adhesive
- Compatibility with a range of rubber mixes

- No brittleness or flaking in processing

Apart from these properties, the adhesives should also accommodate for the difference in the chemical properties of the rubber and the cords. The polymer cords possess very high polarity whereas the rubber possesses a low polarity. Therefore, the adhesive should act as a layer of intermediate polarity in order to avoid abrupt changes in material parameters of the layers.

I.3.1. Rayon and nylon cord adhesion

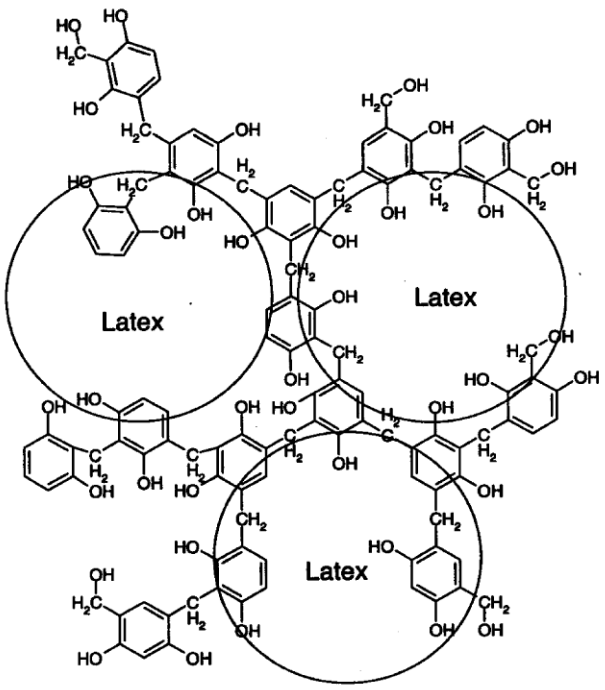

Figure I.3.1: Schematic of the RFL adhesive system structure [14].

In [7], cord-rubber adhesion applied to nylon, polyester and rayon has been reviewed in detail. The study was later updated in [12] to include aramid cord to rubber adhesion. As explained in [7], the first tyre cords ever used were cotton filaments without any adhesives during the late 19th and early 20th century. However, due to the advancements in automobile industry, need for tyres that can withstand higher horsepower carriages kept on growing. Initially, rayon fibres replaced the cotton cords, although without any adhesion. The tyres showed better performance with this new cord, yet they lacked the desired durability. Therefore, a new adhesive system called as resorcinol-formaldehyde-latex (RFL) system was invented (see *Figure I.3.1*). This adhesive system was later also used on nylon cords. As reported in [11], even though the adhesive system was invented over *90 years* ago, it is still being used today as an industry standard.

In [7], the detailed RFL adhesive system preparation is given for rayon and nylon cords. Resorcinol and formaldehyde are first reacted in an aqueous solution of sodium hydroxide. The solution is allowed to rest for six hours at room temperature. Later, the latex is added to the solution; its amount depending on the type of the cord – rayon or nylon. This mixture of RF-latex is then left for maturing for six more hours at room temperature to form the RFL adhesive. The polymer cord is dipped into the RFL adhesive for certain time and heated up to a certain temperature to what is called ‘priming’ of the cord (see *Figure I.3.2*).

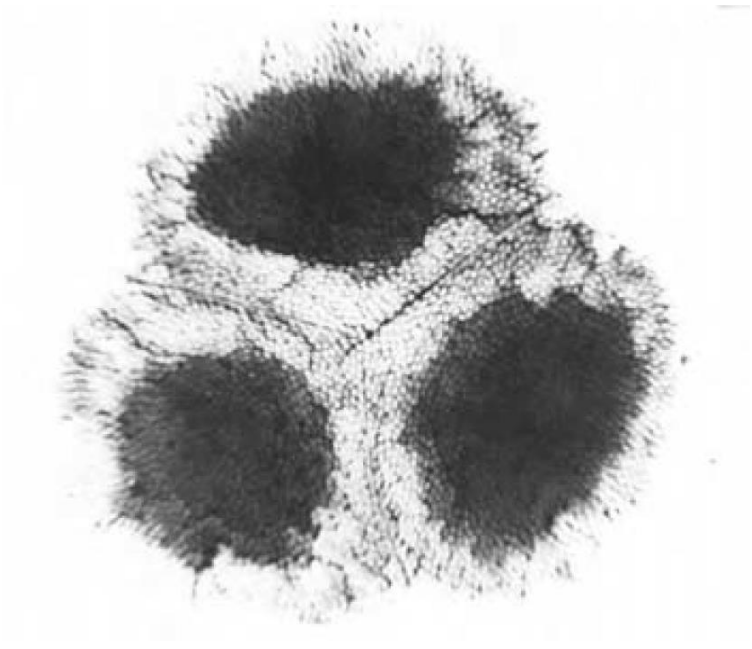

Figure I.3.2: Rayon cord cross-section showing high penetration of RFL adhesive after priming [11].

Some details of this process are also described in [11]. The cord is kept under tension after dipping into the RFL solution. The dip pickup is controlled at up to *6-8%*. For better adhesion, complete wetting of the polymer cord is essential. *2-3* filament layers dipped completely into RFL adhesive is considered as optimal since too much dip pickup or cord wetting will affect the modulus of the cord. During the vulcanisation process of the rubber (or tyre), the RFL layer produces adhesion between the cords and the rubber.

I.3.2. Polyester cord adhesion

In the case of the polyester cord to rubber bonding, significant research has been done since the introduction of polyesters as tyre cord materials. This is partly due to the inability of RFL adhesives to bond to polyesters fibres and partly due to the superiority of polyesters over rayon which meant that polyester cords replaced much of rayon cords in vehicle tyres. In [12], the advances in the polyester to rubber adhesion systems are described in detail.

I. **Two-step process:** In 1967, Shoaf [13] earned a patent for a two-step adhesion process for polyester to rubber bonding (see *Figure I.3.3*). Following that patent, numerous patents have been filed for the two-step polyester to rubber adhesion process, as presented in [12]. In the first step, the cord is coated with an aqueous solution of phenol blocked polyisocyanate, epoxide and a

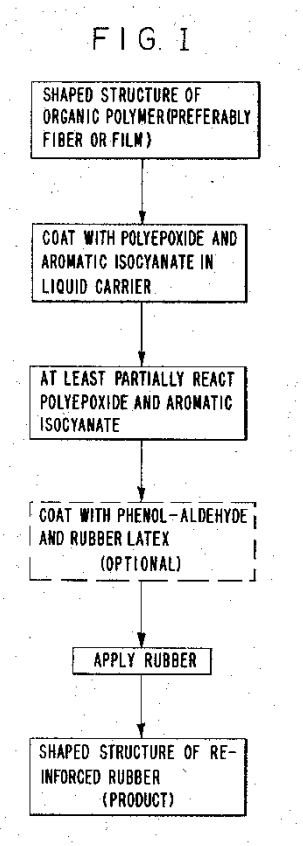

Figure I.3.3: Two-step polyester to rubber bonding process [13].

wetting agent. The cord is then dried and baked at *240°C* followed by application of RFL coating. Most two-step processes such as the one by Shoaf involve chemical activation of the surface of polyester cords in the first step. In the second step, the RFL coating is applied before vulcanising the cord rubber composite.

II. **Single adhesive dip:** According to a patent assigned to Imperial Chemical Industries (Belgian Patent No.688424), a single step procedure can also be followed to activate the polyester cord surface in order for it to adhere to rubber. An aromatic oligomer additive is mixed with the standard RFL solution. The additive, called as H-7, is obtained by condensation of chlorophenol and resorcinol in methylene solution. The phenol group in the adhesive solution penetrates inside the polyester fibre surface which aides in the adhesion to rubber. During vulcanisation, this phenol group bonds with rubber with the help of latex present in the RFL solution.

III. **Fibre surface activation:** By activating the polyester fibre surface during the fibre spinning process, an RFL top coat can be used for polyester cord to rubber adhesion. As Solomon mentions in [12], this process accelerated the use of polyester cords in tyre rubber application. To activate the fibres, an aqueous solution is prepared by mixing sodium carbonate, glycidyl ether, dimethylsiloxane and polyoxyethylene. The undrawn polyester fibres are dipped in this solution and then drawn at a high temperature in order to cure the solution. Following this method, various methods are listed in [12] which describe activation of polyester fibres for cord rubber adhesion.

IV. **Polyester surface modification:** Solomon lists a range of patents in [12], which describe grafting various types of polymer chains onto the polyester surface. These polymer chains can be made up of acrylamides and butadiene, isoprene or vinyl chlorides among others. The polymer chains act as an intermediary between RFL adhesive and the polyester. Solomon also lists several surface modification methods such as treating the polyester fibre surface with amine solutions, preparing the fibres with anionic polymerisation of isoprene and improving hydrophilicity of the cord surface.

I.3.3. Aramid cord adhesion

As reported by Iyengar in [9], the polymer characteristics possessed by Aramids hamper its adhesion capability with rubber. Aramid fibres have large high-temperature moduli due to higher glass transition temperatures ($T_g > 300°C$) compared to nylon and polyesters. However, the adhesive curing occurs at lower temperatures such as *100°C*. Since it is much lower than

the glass transition temperature of aramid fibres, the adhesion of aramids to rubber becomes difficult. The adhesion between aramids and rubber is achieved by primary bonds, specific physicochemical interactions such as H-bonds or diffusion between adhesion and substrate. Trimethylol phenol, epoxides and polyetheleneimine have also been proposed in [12] to promote adhesion of aramid fibres to rubber. By looking at the solubility parameters of these ingredients, Solomon concludes that the adhesion is dominated by hydrogen-bonding mechanisms.

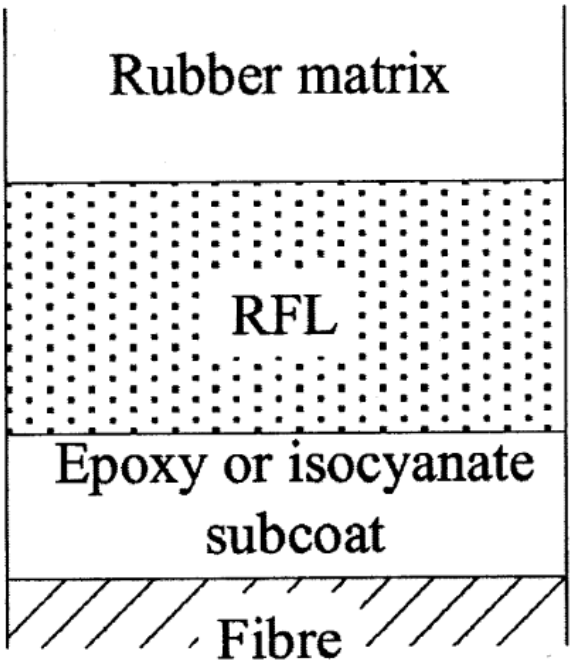

Figure I.3.4: p-Aramid to rubber bonding [14].

Iyengar [9] also proposed a two-step process for aramid to rubber adhesion. A coating of alkaline aqueous solution of epoxide mixed with wetting agents is applied to the aramid fibres in the first step. Later, an RFL coating is applied and the fibres are dried and baked for setting the adhesive. The adhesion between the adhesive and rubber occurs during vulcanisation, similar to other cord-rubber adhesion processes. In addition, adhesion of poly-p-phenylene-terephthalamide or p-aramid fibres to rubber using epoxy or isocyanate subcoat and RFL topcoat is presented in [14].

In [12], several other aramid cord-rubber adhesive systems are also discussed where the subcoat is made out of glycerol diglycidyl ether either by itself or within an alkaline aqueous solution of dioctyl sodium sulfosuccinate and 2-pyrollidone. The topcoat consists of pyridine copolymers or often RFL solution.

I.3.4. Steel cord adhesion

As explained previously, steel cords are extensively used in vehicle tyres due to their low cost and high strength. Therefore, the study of steel cord to rubber adhesion has been an area of research for many years. The steel cords are plated with brass during the wire drawing process, which aides in the adhesion. A typical steel wire drawing procedure is shown in *Figure I.3.5* [15].

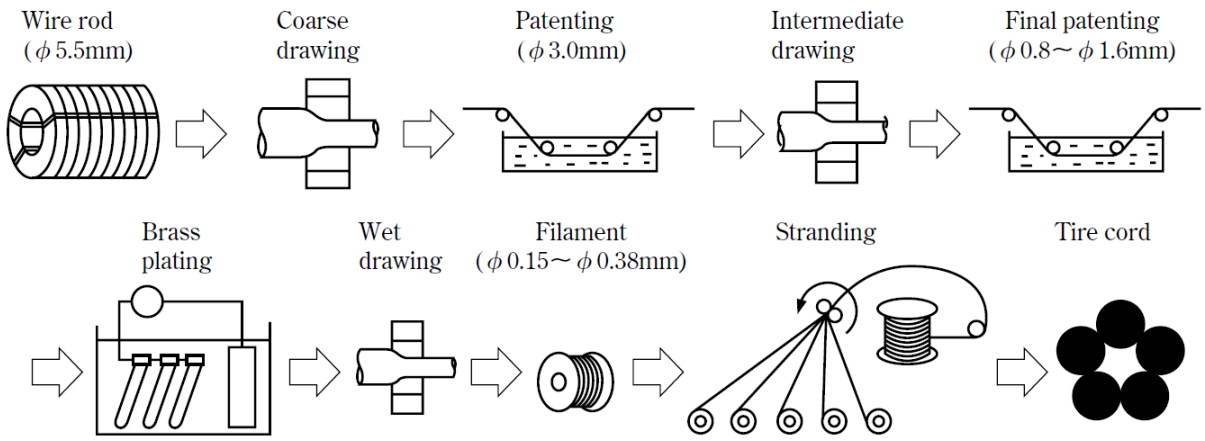

Figure I.3.5: Schematic of the wire drawing and brass plating process [15].

Carbon steel wire rods of the size *Φ5mm-6mm* are coated with lubricants such as borax and drawn into *Φ1mm-3mm* wires. The wires are then annealed or patented to reduce internal strains arising due to the drawing process and to increase their tensile strength. In certain cases, the wires are drawn again through a smaller die to reduce their size to as low as *Φ0.8mm* and annealed subsequently. The next stage is the most crucial step where brass is deposited on the wire via electroplating. After that, it is drawn through a wet drawing process to obtain filaments of size *Φ0.15mm-0.38mm*. Any friction between the dies and the wire can scratch the surface of the filaments making them susceptible to galvanic corrosion due to presence of moisture. Therefore, the dies and the wire are dipped into a lubricant during the drawing process to reduce the friction. Once the filaments are formed, they are twisted and coiled in the form of cables.

During the vulcanisation process, the copper from the brass coating reacts with the sulphur from the rubber, as shown in *Figure I.3.6*. Van Ooij has extensively reviewed this topic in his work [16] - [19]. Although the subject has been an area of research for past *70 years*,

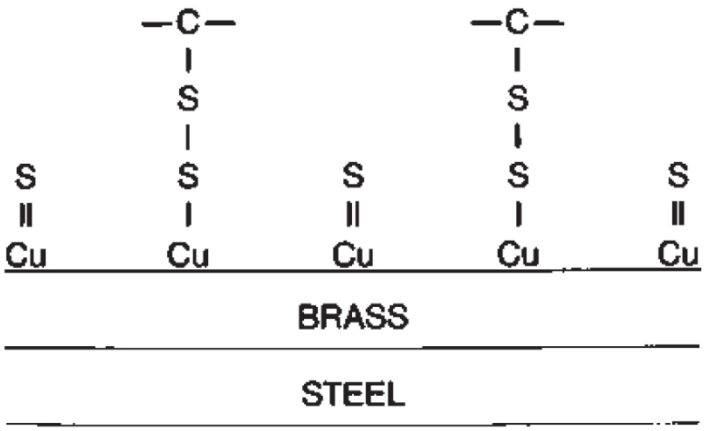

Figure I.3.6: Schematic of brass to rubber bonding [11].

the exact nature of the adhesion is still not known. Nonetheless, van Ooij's work has been regarded as the most comprehensive piece of research and the results presented in his work have been regarded as most detailed and recent.

In [16], van Ooij studied surface characteristics of the brass-rubber interface using XPS analysis. This was one of the first ever reported microscopic studies of the brass-rubber adhesion. In his work, he used lap shear fracture tests to delaminate brass-rubber interface. He then studied the fractured interface using depth profiling. The aim of his work was to investigate the various constituents present at the interface. Using this information, qualitative and quantitative analysis of the adhesion was performed. It is interesting to note that the method used for quantitative study of the adhesion was to perform a fracture mechanical test. This topic will be discussed in detail in following sections (and the rest of this thesis).

In [16], he reported that traces of sulphur were found inside the brass layer and traces of copper and zinc were found inside the rubber layer (*Figure I.3.7*). High concentrations of Cu, Zn, O and S were found inside the rubber near the brass-rubber interface. He concluded that an interfacial zone exists between the rubber and brass consisting copper sulphide, zinc sulphide and zinc oxide. He further discussed the presence of various Cu-S molecules at the interface. In conclusion, he reported that Cu_xS bonds ($x \approx 1.6$) are formed during the vulcanisation which form an adhesive layer between rubber and steel (or brass). He postulated that these bonds are in the shape of dendrites which provide physical adhesion in addition to

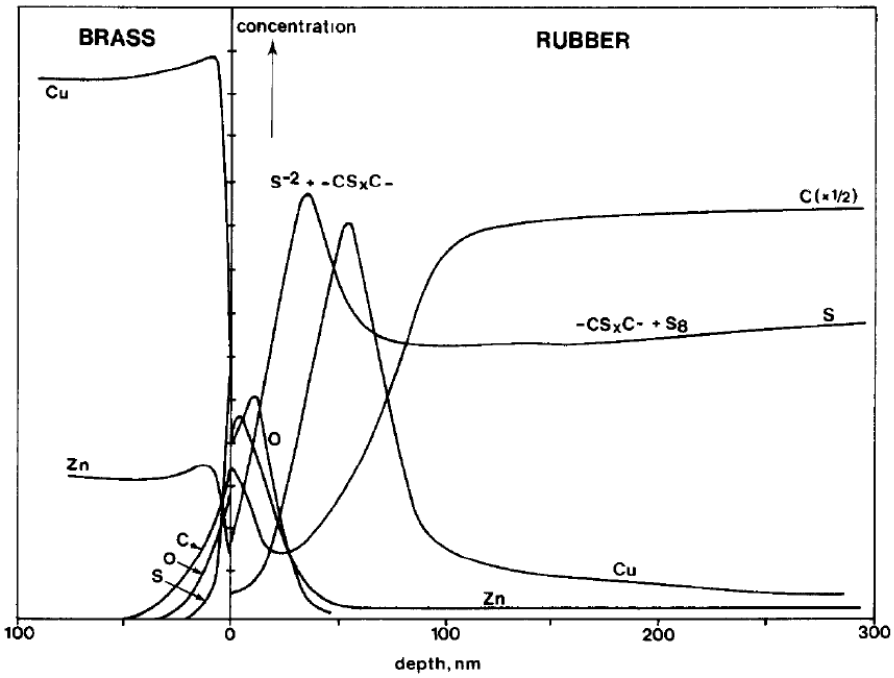

Figure I.3.7: Depth concentration analysis of a brass-rubber sample [16].

the chemical bonds. In addition, due to the reaction of sulphur with copper via this nonstoichiometric Cu_xS bonds, a high concentration of active S_{8-x} fragments is present near the interface. This promotes the free sulphur to react with the rubber to create higher cross-linking density (higher concentration of C-S bonds) near the interface. He also postulated that the Cu_xS films could form chemical bonds with the rubber to further increase the adhesion. However, in a later study [18] he refuted all of these claims.

It is important to note that the results presented in his work are based on rubber samples bonded to solid brass sheets instead of brass coated steel cords. In [17], he reported that these results should be treated with care since the behaviour of rubber to brass sheet bonding is different than rubber to brass coated steel bonding. He listed a few important points to support his claims, which are:

1. Brass sheets have uniform distribution of lattices, whereas brass coated steel cords have deformed lattices containing several defects. This happens mainly due to the drawing process explained previously. Therefore, electroplating a sheet of steel with brass will not result in the same surface characteristics as those associated with a brass coated steel cord.
2. The chemical reactivity of brass sheets is different than that of the brass coated cords due to the presence of steel underneath the brass coating, in the case of brass coated cords.
3. The axisymmetric geometry of the filaments and the cables means that the exposed surface area is likely to be more reactive in terms of corrosion.
4. The size and structures of the brass crystals found in brass sheets and in brass coated steel cords are likely to be different, thereby affecting the chemical and physical properties of the surface.
5. The cord is immersed in a lubricant during the final wet drawing process (*Figure I.3.5*) which leaves residue on the cord surface, affecting its reactivity to corrosive media.

Nonetheless, the results from [16] provide a basis for understanding how brass is adhered to rubber during vulcanisation. Following his work, Haemers [20] also did a study of cord-rubber interfaces using XPS and AES. He also confirmed that the Cu_xS bonds form the adhesive interface between brass and rubber.

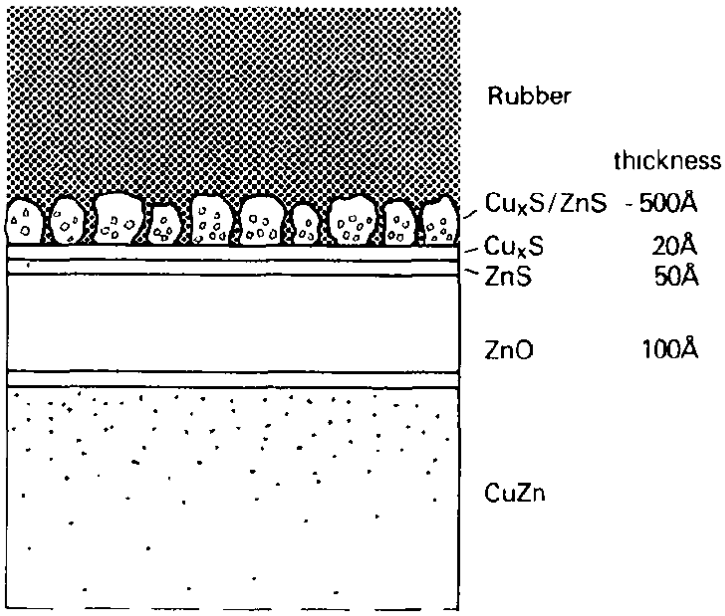

Figure I.3.8: Schematic of the brass-rubber adhesion [18].

In [18], van Ooij performed further analysis of the brass-rubber adhesion to understand the interface better. He showed that Cu_xS dendrites nucleate and grow parallel to the interface during vulcanisation (*Figure I.3.8*). This creates interlocking between the dendrites and the rubber molecules. He concluded that previous claims of the existence of a chemical bond Cu_xS – S_y – NR which link the Cu_xS film to the rubber is not consistent with his results and other literature. He did not comment on whether the brass-rubber adhesion is primarily chemical adhesion or physical adhesion. However, he emphasised that the presence of Cu_xS films on the brass surface is essential for brass-rubber adhesion.

One interesting conclusion from this work is the importance of the ZnO layer and its thickness. van Ooij showed that the ZnO layer promotes the growth of the Cu_xS dendrites during vulcanisation. If the ZnO layer is too thin or too thick, a ZnS film will be formed at the interface, and the Cu_xS formation will be halted rapidly. This suggests that if the cord is treated with acid prior to vulcanisation, the ZnO layer will be removed causing poor adhesive performance.

To summarise, the steel cord to rubber adhesion is primarily caused due to the microporous dendritic film of Cu_xS interlocking with the rubber molecules during the vulcanisation process.

I.4. Quantitative Evaluation of Adhesion

As explained previously, the area of rubber to cord adhesion has been studied extensively, especially the problem of rubber to steel cord adhesion. It is important to develop newer and better adhesive systems as well as improve the older systems to produce durable and safe

tyres. For that reason, it is also important to perform quantitative evaluation of these adhesive systems. The most common method to perform such quantitative evaluation is to use fracture mechanical tests. These tests are also used for qualitative study of the adhesion, such as the lap shear tests used by van Ooij [16]. It is therefore very important for tyre designers to study various fracture mechanical tests and how they evaluate the adhesion performance of rubber-cord composites.

Before moving on to study these tests, their performance as well as their shortcomings, it is worthwhile to have a look at some basic concepts of fracture mechanics and how these concepts are applied in adhesion characterisation.

I.4.1. Some notes on fracture mechanics

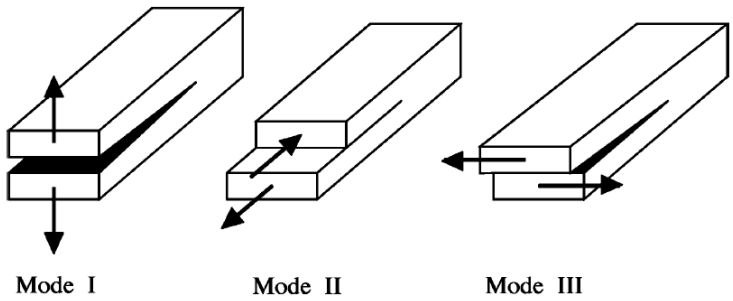

Figure I.4.1: The three modes of fracture [21].

Fracture mechanics is a sub-field of solid mechanics that studies how cracks propagate in materials and structures. Theoretical concepts of continuum mechanics such as airy stress functions and variational methods are used to model the material and structural behaviour in order to calculate the forces or stresses required to propagate the fracture. A fracture or crack propagating in any material or structure is divided into three types, or *Modes* as shown in *Figure I.4.1* [21]. These are called Mode I, Mode II and Mode III, based on the way the cracked faces are opened. Mode I is an opening mode where the crack faces separate after the crack has propagated. Mode II is a sliding mode where the crack faces undergo a shearing motion in the plane of the crack. Mode III is a tearing mode where the crack faces undergo shearing motion causing them to go away from each other.

I.4.1.1. Linear elastic fracture mechanics

The most commonly used fracture analysis technique is called the Linear Elastic Fracture Mechanics (LEFM) where the fracture behaviour equations are assumed to take a linear form. In such a case, the fracture process can be expressed as a linear superposition of the three modes mentioned above. The stress equations derived using the basic principles of continuum mechanics can also be superimposed to simplify the fracture problem. This is an important

step in the fracture mechanical analysis, since most failures observed in materials and structures are a combination of the three modes. In such a case, dividing the problem into simplified subproblems using a technique called Bueckner's principle [22] allows engineers to calculate the stresses that cause the fracture.

According to linear elasticity theory, the stresses that arise near the tip of the crack are infinitely high. However, in practice, no crack tip is perfectly sharp, therefore the stresses and strains occurring near the crack tip have finite values. This can be quantified using a concept called Stress Intensity Factor (SIF) (K_I for Mode I fracture and so on). The stress intensity factor provides a relation between the intensity of stresses occurring near the crack tip and the applied stress in a fracture mechanical problem.

The fracture process is also quantified in terms of the energy released during the creation of unit area of the crack faces, called Critical Strain Energy Release Rate (SERR) or G_c. For pure materials, the energy required to create a unit area of fracture, called the Fracture Toughness or G_{IC}, is a constant value. Similarly, the intensity of stress required to propagate the fracture is defined as the Critical Stress Intensity Factor or K_{IC}. These two terms are used as the defining properties of materials in LEFM. The criterion for failure of materials can therefore be either G_c or K_{IC}. These are referred to as Energy criterion and Stress criterion respectively. There are different opinions in the scientific community over which criterion should be fulfilled in order to propagate the fracture. Recently, a combined energy and stress criterion has been proposed [23], where the fracture process is modelled as an optimisation problem.

Following the superimposition principle of LEFM, any fracture process can be divided into its 3 modes. The energy released during the fracture, and hence G_c, can also be divided into the three modes through superimposition. In such a case, the SIFs are calculated for each mode and the G_{cI}, G_{cII} and G_{cIII} are calculated and superimposed to give G_c.

I.4.1.2. Fracture mechanics of adhesively bonded structures

The LEFM approach is suitable for isotropic elastic materials. Although it is applicable to most engineering problems, as more and more composites and adhesively bonded systems are replacing metals in engineering structures, the need to develop fracture mechanical approaches suitable for such complex systems is growing. An approach called Nonlinear Fracture Mechanics [24] can be used to account for all the nonlinearities arising from material nonlinearities, anisotropy, plasticity and so on. However, often the principles of LEFM are

applied to adhesively bonded structures due to their simplicity as well as compatibility with finite element modelling.

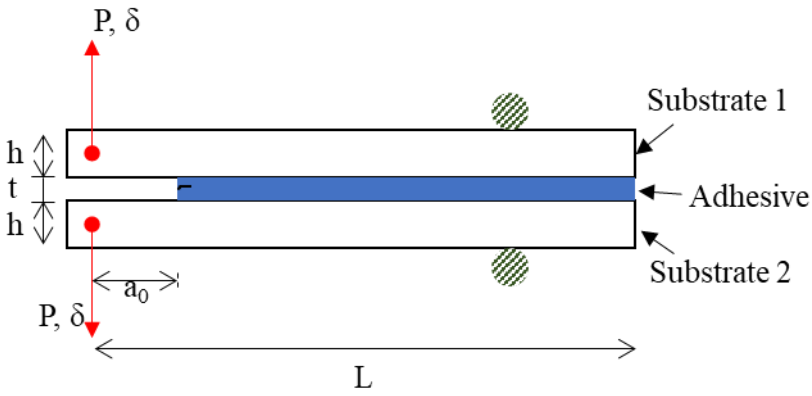

Figure I.4.2: Schematic of a DCB Specimen.

The most commonly used tests for fracture of adhesively bonded structures are the Double Cantilever Beam (DCB) test (*Figure I.4.2*), End Notch Flexure (ENF) test, End Loaded Split (ELS) test, Lap shear test and Single Leg Bending (SLB) test. Upon testing the specimens using one of these tests, the fracture energy is calculated using theoretical equations corresponding to each of these tests. The specimen is also modelled into finite element software such as Abaqus to mimic the crack propagation behaviour using Cohesive Zone Modelling or the Virtual Crack Closure Technique among others. This is necessary since the nonlinear behaviour observed around the crack tip region cannot be modelled accurately by LEFM based equations. As the problem becomes more and more complex, finding analytical solutions for SIF becomes almost impossible. Therefore, with use of FE modelling, the stresses and strains near the crack tip can be evaluated with a better accuracy. The fracture energy of the specimen can also be calculated using a numerical version of the J-integral.

I.4.1.3. Fracture of rubber-like materials

Propagation of fracture in rubber or rubber-like materials is driven by the rupture of adhesion

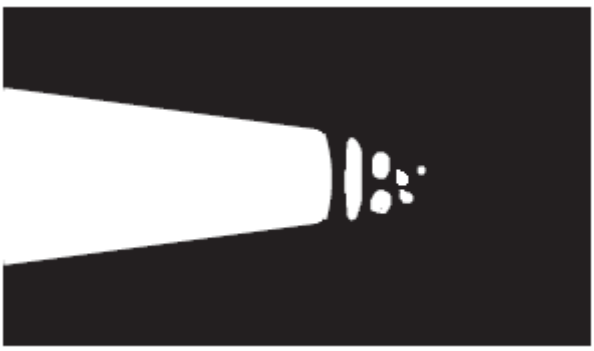

Figure I.4.3: Crack propagation in rubber-like materials involves cavity formation, chain pull-out and bond breaking [25].

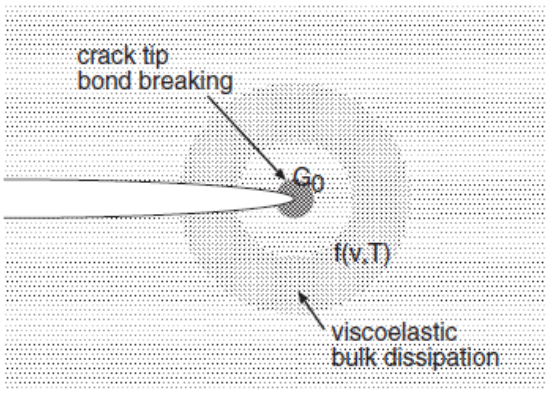

Figure I.4.4: Bond breaking and viscoelastic dissipation near crack tip [25].

and cohesion between the elastomer molecules. The fracture energy (or critical SERR) comprises of the energy required to break the bonds as well as the energy dissipated in the vicinity of the crack tip during crack propagation. This fracture energy, G_c, has been shown [25] to take the form:

$$G_c(v,T) = G_0[1 + f(v,T)]$$

Here, v is the speed of crack propagation and T is the temperature. The function $f \rightarrow 0$ as $v \rightarrow 0$. G_0 is the threshold value, which is the minimum value of fracture energy. The crack propagation involves complex processes such as cavity formation, chain pull-out, stringing as well as bond breaking (see *Figure I.4.3*). These processess are coupled with the viscoelastic dissipation occuring near the crack tip as shown in *Figure I.4.4*. Various fracture mechanical tests are used to study rubber fracture, such as the Trouser Test, Peel Test and Pure Shear Test, where an energy based approach is used to calculate the fracture energy.

However, the study of crack propagation in rubbers suffers from many limitations, such as those detailed in [26]. It is showed that the crack growth is dependant on the specimen dimensions. Modelling the viscoelastic behaviour of rubber in addition to the fracture process is complicated if performed using a theoretical approach. The fracture analysis can also be performed using finite element methods, although, the commercial softwares available have many limitations. XFEM technique has been proposed in [27] for modelling crack propagation in rubber like materials. The original eXtended Finite Element technique is adapted to incorporate the large deformations as well as the asymptotic displacement fields near the crack tip.

I.4.2. Rubber-steel cord adhesion failure

The complex nature of rubber-steel cord adhesion has already been discussed. The incompressibility and hyperelasticity of rubber make the rubber-steel fracture add to this complexity. Moreover, rubber is a viscoelastic material, which means that the crack propagation becomes an even more complex phenomenon. Some of these factors have been studied by Liechti and colleagues in [28] - [31].

In [28], double strip blister test was performed on rubber-steel samples and it was reported that the material model chosen to describe the rubber behaviour significantly affected the evaluated fracture energy (or critical (SERR) or adhesion energy). Since rubber behaviour is highly nonlinear, modelling it accurately using a hyperelastic model is very difficult. The

deformation occurring near the crack tip is very high. Therefore, an appropriate model must be chosen which can describe the rubber behaviour at small as well as large strains. This process of identifying the material model is performed by fitting the rubber data to Cauchy stress equations of the model. Since there is no 'perfect' model that can describe the rubber behaviour accurately at small as well as large strains, tyre designers have to choose a hyperelastic model that gives better fit than other models. This suggests that the fracture energy or critical SERR evaluated for the rubber-steel adhesion will be sensitive to the data fitting performed on the rubber.

The complex viscoelastic nature of the rubber-steel bonding was explored in [31] by Liechti and Wu. Samples of rubber adhered to steel were tested under Mode I and Mode II loading. It was found that, by introducing a nonlinear Kelvin element at the interface, the crack propagation can be modelled in FE using Cohesive Zone Modelling.

The large values of stresses and strains arising at the rubber-rigid substrate crack tip have been studied in detail in [32]-[42]. The analytical treatment involved in these studies is tedious, although it is applied to simple rubber models such as Neo-Hookean. The axisymmetric geometry of rubber-tyre cord composites has never been studied in this aspect. The fracture mechanical study of such a system is very complex and requires a lot of research. Calculating the critical SERR or SIF of the adhesion using analytical models is therefore not explored substantially. Fracture mechanical studies on rubber-steel adhesion mainly focus on performing experimental tests and modelling the macroscopic specimen behaviour using analytical or FE models. The fracture criterion used is usually of the energy kind. This is due to the simplicity of the calculations, as reported by Gent in [43].

I.4.3. Fracture tests for rubber-steel cord adhesion

Various fracture mechanical tests have been used for quantitative evaluation of rubber-cord adhesion. These tests are mainly of two types – Pull-out type tests and Peel type tests. A detailed account of their historical development, discussion of published research and experimental artefacts associated with them is given below.

I.4.3.1. Pull-out type tests

One of the earliest reported cord pull-out tests was the H-Test method presented by Lyons and colleagues in [44], where the cords were made out of cotton. The cords were embedded inside the rubber and were pulled out and the pulling force was measured. Based on the same idea, one of the earliest tests on rubber-steel adhesion, called as the Tire Cord Adhesion Test

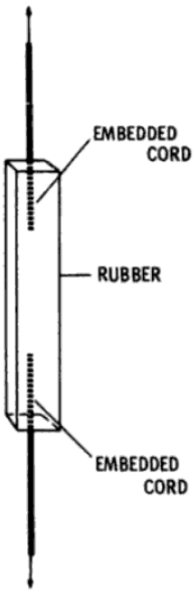

Figure I.4.5: TCAT specimen [46].

(TCAT), was developed by Fielding-Russell and others [45], [46] (*Figure I.4.5*). A simple energy balance was used to associate the pull-out force with the critical SERR of the rubber-cord composite, given by the relation:

$$P = \sqrt{4\pi r E A \alpha}$$

Here, P is the pull-out force required for fracture, r is the cord radius, E is the Young's Modulus of the rubber and α is the critical SERR. The critical SERR evaluated using this test was reported to lie between *14-20kJm*$^{-2}$. In [46], a peel test on rubber-steel samples was also performed to get the adhesion energy of *20kJm*$^{-2}$

Clearly, the quadratic nature of the relation between critical SERR and the pull-out force will not represent the highly nonlinear phenomena occurring during the fracture process. In addition, the rubber is assumed to be elastic and is assumed to not store any energy in the form of elongation. The pulled-out cord must suffer significant friction with the fractured rubber which is not considered in this analysis.

This test was further analysed by Gent and others in [47] to apply Griffith's solution to a penny shaped crack. A new relationship between the pull-out force and the adhesion energy (or critical SERR) was established. The rubber block was assumed to store some energy due to the pull-out force. However, it was assumed to behave elastically. The friction losses occurring during the pulling out were still assumed to be negligible. Although the treatment of the fracture was done with inclusion of the energy stored in the rubber block, the fracture energy value reported, *17±3kJm*$^{-2}$, was nearly the same as the one reported in [40]. This indicates that the addition of stored elastic energy in the rubber into the SERR equation has only a limited effect on the adhesion evaluation of the pull-out test.

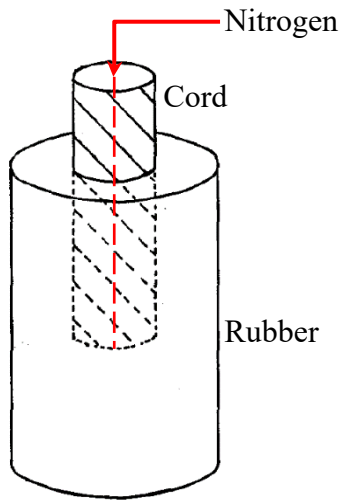

Figure I.4.6: Injecting pressurised Nitrogen gas at the interface [48].

To eliminate the frictional effects present in the pull-out test, Gent and Yeoh presented a gas injection technique in [48] (*Figure I.4.6*). A small axial hole was drilled into the cord and

pressurised Nitrogen gas was injected during the test. The pressure level of the gas was varied from *0bar* to *4bar*. Several tests were carried out each at a unique gas pressure level, and the pull-out force was measured. The gas pressure was believed to have kept the fractured rubber away from the cord thereby reducing the friction. A substantial reduction in pull-out force was measured confirming this assumption. The resulting decrease in G_c value was in the range of *77-90%*. Therefore, the gas injection technique used in this experiment showed very promising results.

However, this test method suffers from a few artefacts as well. Such a huge reduction in adhesion energy value indicates that the effect of friction is rooted much deeper. Calibration of frictional force or energy loss is necessary in order to get a reliable value of adhesion energy. It was assumed that by injecting the gas at higher pressures, the frictional effects were eliminated. However, quantitative study of the frictional effects was not performed. The effect of pressurised gas on rubber in terms of swelling and in terms of strain energy storage was not considered in the analysis. The artificial pull-out force generated by the injected gas was not considered as well. Instead, it was assumed that the reduction in pull-out force must be solely due to the reduction in friction. In addition, to calculate the adhesion energy for only once, a total of *9* tests were performed, and the data was extrapolated to a supposed zero friction condition. Therefore, in order to perform a statistical analysis of the fracture, a huge number of tests will need to be performed which will be time consuming and expensive.

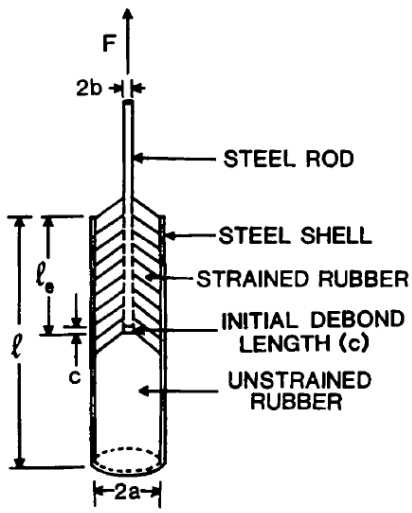

Figure I.4.7: Coaxial shear pull-out test (CSPT) [49].

Ellul and Emerson proposed a new pull-out test in [49], called Coaxial Shear Pull-out Test (CSPT), to eliminate the artefacts associated with the TCAT. The test specimen is a steel cord partially embedded in a cylindrical rubber, that is enclosed in a metal sleeve (see *Figure I.4.7*). The steel cord/rod is pulled out of the rubber, causing a fracture by simple shear. The assumption was that, due to the Poisson's contraction effect (Poisson's ratio=*0.5*), the fractured rubber will not contribute to any friction. It was also shown that the fracture occurs at moderate shear strain values (up to *80%*). This allowed a linear elastic assumption for the rubber behaviour. The results presented in this work seemed promising since there was a good agreement between the theory and the experimental results.

However, the assumption that the strain values are moderate may not be true in all types of rubber-steel cords. Depending on the shear modulus of rubber and the adhesion energy, the strains occurring near the crack tip can be very large, as discussed in [32]-[42]. The effect of the linear elasticity assumption on G_c calculation was not discussed. In addition, for large values of embedment length (*i.e.* l_e in *Figure I.4.7*), larger fluctuation in pull-out force was reported. This could be due to the frictional effects (assumed to be negligible) between the fractured faces. In [50], Gent and Kaang proposed a push-out test in order to eliminate the frictional effects. The test showed promising results; however, it was also reported that, due to buckling of the specimens, carrying out experiments posed a lot of difficulties. They insisted that the pull-out test should be continued to be used as a standard test for rubber-cord adhesion.

Apart from the studies discusses here, some other pull-out tests can also be found in the literature such as [51], [52] and [53]. However, the artefacts associated with these tests are still an issue for tyre designers.

I.4.3.2. Peel type tests

Energy balance for the detachment of adhering tapes used in surgery was first performed by Rivlin [54]. Similar tests were performed by Graham [55], where he used a peeling technique for cleaning metal surfaces before electroplating. Gent and Hamed [56] extended Rivlin's work to investigate peel mechanics applied to flexible strips adhered to rigid substrates. The study was limited only for isotropic elasticity. Results from *90°* and *180°* peel tests on cord rubber samples were presented in [46] and [47], yet no details of the actual tests were given. Cook and colleagues [57] used the same technique for testing rubber-steel cord adhesion for peel angles of *30°*, *60°*, *75°* and *90°*.

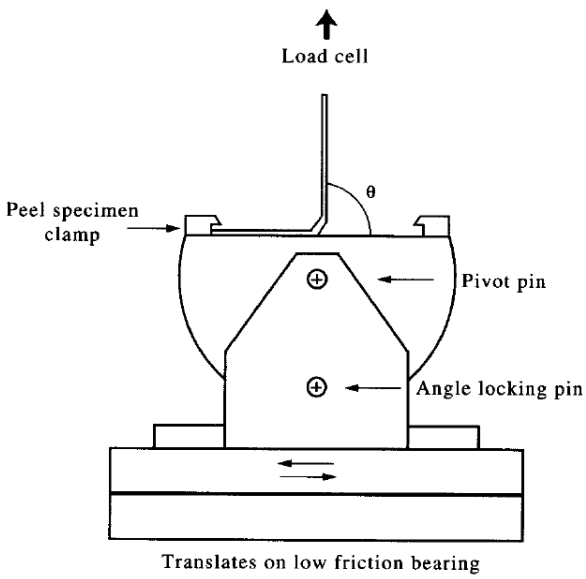

Figure I.4.8: Peel testing rig [57].

The peel test specimen is a thin rubber strip of uniform thickness and width, adhered to a steel plate of similar dimension. The specimen is clamped to the testing rig, as shown in *Figure I.4.8*, and the peeling angle is chosen. The steel plate is fixed on the rig and the

rubber strip is pulled up using a tensile testing machine at a fixed rate. The peel force (F) and the energy of peeling (P) are associated with the relation:

$$P = \left(\frac{F}{b}\right)(\lambda - \cos\theta) - W_\lambda h$$

Here, b is the width of the strip, λ is the extension ratio (or stretch ratio) of the rubber strip, θ is the angle of peeling, h is the thickness of the strip and W_λ is the strain energy stored in the stretched rubber strip. The peel energy comprises of adhesion energy; elastic, plastic and viscoelastic dissipation; and viscoelastic losses due to bending of the strip.

Results presented in [57] show that there is a considerable amount of stick-slip behaviour occurring during the fracture. It was reported that there were distinct peaks and troughs in the peel force. The peel force varied within a range of *20%* causing the peel energy to vary within a range of *32%*. The crack propagation could be of partly static and partly dynamic nature. This artefact associated with peel tests raises questions about the results obtained.

Muhr and colleagues [58] performed peel tests and pull-out tests on vulcanised natural rubber bonded to brass coated steel plates. The adhesion energy calculated using pull-out test was reported to be between $11\text{-}25 kJm^{-2}$. For the same type of specimens, the peel energy was reported to lie between $4\text{-}6 kJm^{-2}$ for *30°* peel tests and $27\text{-}30 kJm^{-2}$ for *90°* peel tests. This considerable difference between peel test results and pull-out test results arises from the frictional effects inherent to the pull-out tests. Although there are no comments about the fluctuation in the peel force, the striation marks are clearly seen on the crack faces which point towards a highly stick-slip nature of the crack propagation.

Apart from the artefacts discussed here, one more disadvantage the peel test suffers from is the geometry of the specimen. As explained previously in §*I.3.4*, the flat geometry of the brass coated steel plates or bulk brass plates in a peel test cannot mimic the behaviour of a cylindrical steel cord plated with brass present in the actual tyre cords. Due to this, the pull-out test is generally favoured in the tyre industry, even though the pull-out test itself suffers from certain artefacts discusses earlier. These tests and their versions are also used as ASTM standards, e.g. [59] - [63].

I.4.4. Need for a new test method

For a reliable evaluation of the critical SERR (or adhesion energy) of the rubber-cord composite, a reliable test procedure is required. The peel test and pull-out tests have already

shown to have many artefacts. In addition, several other important factors need to be considered before choosing the appropriate test method for rubber-steel cord adhesion. Some of these factors are:

1. **Rubber behaviour:** Due to its hyperelastic nature, the rubber undergoes large amounts of strains during fracture. It therefore stores considerable amount of strain energy which needs to be incorporated into critical SERR calculation.
2. **Process zone dissipation:** The fracture process involves energy dissipation in the process zone which should be considered in the fracture analysis of the test.
3. **Quasi-static crack propagation:** In the LEFM approach, the crack is assumed to propagate in a quasi-static way. Therefore, the fracture process occurring in the rubber-cord adhesion test should not be of dynamic nature.
4. **Mode-mixity:** For a comprehensive study of the rubber-cord fracture, mixed-mode failure and control over the mode-mixity are very useful.
5. **Quantitative differentiation between various adhesive systems:** As the tyre and rubber industry evolves, various rubber-cord adhesive systems will need to be tested. The rubber-cord adhesion test should be able to differentiate such systems quantitatively, in terms of the experimental factors such as critical SERR or crack propagation rate.
6. **Effect of environmental parameters:** A rubber-cord adhesion test must be capable of mimicking the harsh environmental factors the tyre undergoes during its life. These could be ageing (humidity and temperature), stress corrosion and environmental fatigue, to name a few.

The standard rubber-steel cord adhesion test protocols cannot incorporate these factors. However, a reliable evaluation of the adhesion is essential for tyre designers to produce safe and durable tyres. Clearly, there is a need to develop a new testing method which can minimise or eliminate the artefacts associated with the standard tests. There is a need to develop a new testing method, which can incorporate the six factors mentioned above in order to provide a reliable alternative to the standard rubber-steel cord adhesion tests.

As mentioned previously, the coaxial shear pull-out test showed promising results since the frictional effects were small and the agreement between the theory and experimental results was good. In addition, the test devised by Gent and Yeoh, in [48], where a pressurised gas was injected to minimize the friction between the fractured faces, possesses capabilities to be

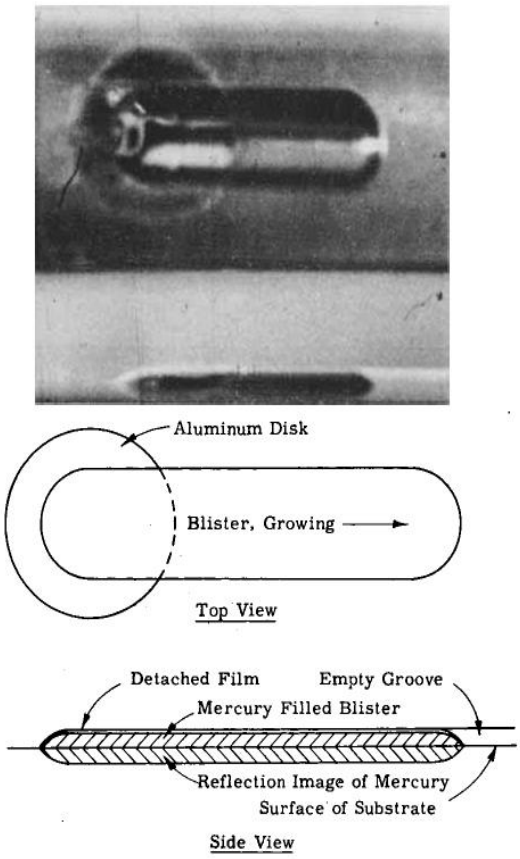

Figure I.4.9: Blister test- Photograph, Schematic Top View and Schematic Side View [64].

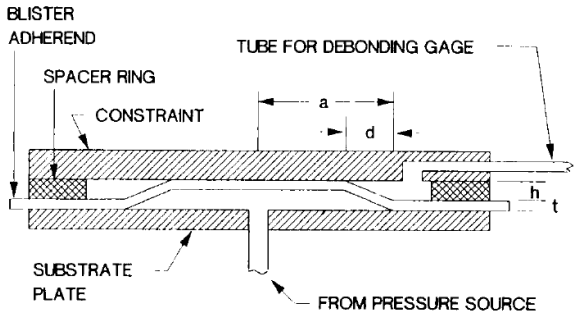

Figure I.4.10: Constrained blister test. The constraint plate restricts the inflation of the blister [65].

a supplementary test method. It was shown in [48] that, after a certain amount of pressure, the crack propagated without any pull-out force. A combination of these two tests would perhaps provide a solution to some of the problems associated with the pull-out test. Moreover, the peel test provides the flexibility of changing the mode-mixity of fracture by changing the peel angle. Such a flexibility can be incorporated in the pull-out tests by controlling the pull-out force in combination with the pressure of the injected gas, or perhaps injected fluid, thereby controlling the angle between crack faces.

A similar concept, applied to a planar axisymmetric geometry, was introduced for delamination of coatings and films bonded to rigid substrates, in [64]. The adhesively bonded films were 'peeled' using a pressurised fluid. The test, called as Blister Test, is shown in *Figure I.4.9*. Later, to restrict the unstable inflation of the blister, a constraint plate (*Figure I.4.10*) was added in [65] and [66]. This technique combines the peel test and the gas injection test [48] for crack propagation. However, as explained previously, due to the flat geometry of the rigid substrate, this test cannot be used directly as an effective alternative. Nonetheless, the advantages of all these tests can be combined to develop a new testing protocol, being the inspiration behind this PhD work.

I.5. Aim of the Thesis

Following the points discussed above, this PhD thesis aims to develop a novel fracture mechanics test protocol for rubber-steel cord adhesion in order to mitigate the shortcomings of the conventional test protocols discussed earlier. This test protocol, referred to as *Rubber Cord Adhesion Inflation Test (RCAIT)*, is an axisymmetric version of the constrained blister test seen above.

The RCAIT test specimen is in the shape of a rubber cylinder with the steel cord embedded along the central axis. The test consists of injecting a pressurised fluid between the rubber and the steel cord to provoke fracture. A coaxial confinement tube restricts the inflation of the rubber allowing the fracture to propagate along the rubber-steel interface. The work presented in this thesis is focused on the development of the RCAIT setup from the concept stage to the execution stage, followed by experimental, theoretical and numerical analysis of the rubber-steel cord adhesion fracture.

In *Chapter II* of this thesis, the RCAIT setup is described in detail along with initial experimental and theoretical development. The rubber-steel adhesion fracture is first evaluated taking into account a Mooney-Rivlin rubber behaviour and later for an Ogden model of the 1st order. Some improvements made to the test protocol are also presented later in the chapter. A *Thick Rubber Tube Inflation Model* is developed to analyse the specimen deformation and to evaluate the fracture energy or critical SERR of the specimen. By incorporating the hyperelastic nature of the rubber in the treatment of the problem, a reliable evaluation of critical SERR is expected.

The experimental development is extended in *Chapter III*, to study the effect of a specific experimental parameter – lubrication between inflating rubber and confinement tube – on the specimen behaviour. A particle tracking technique is presented to study crack propagation as well as process zone deformation. A volumetric data fitting algorithm, applicable to the Ogden model, is used in conjunction with the particle tracking technique for *in-situ* evaluation of the rubber material parameters. A similar concept was used by Ellul and Emerson in [49], to calculate shear modulus of rubber in the CSPT. The fracture energy of the RCAIT specimen is evaluated using these newly calibrated material parameters. This work is followed by a repeatability study on two types of rubber-steel composites. A statistical analysis of the results is also presented.

The theoretical and numerical work is extended in *Chapter IV* to present a generalised Thick-Walled Cylinder Inflation Model. The effect of constitutive rubber modelling on quantitative evaluation of the specimen deformation is also presented. Five hyperelastic models are fitted to the rubber data, and the fracture energy of the rubber-steel adhesion is evaluated considering each of those models. The model is then extended to use the volumetric data fitting technique presented in the previous chapter. The *in-situ* rubber material parameters are evaluated for the same five hyperelastic models and the fracture energy is evaluated.

Finally, along with concluding remarks and discussion, some possible future applications of the test protocol are presented with preliminary results.

Chapter II: Rubber Cord Adhesion Inflation Test (RCAIT)

II.1. Introduction to the RCAIT

The importance of investigating rubber-cord adhesion and the experimental artefacts associated with the traditional fracture mechanical tests to test this adhesion have been discussed in the previous chapter. In that context, the Rubber Cord Adhesion Inflation Test (RCAIT) is perceived as a possible solution to minimise those artefacts. In this chapter the RCAIT protocol is described in detail.

Prior to the development of the theoretical and numerical modelling of the problem, an experimental test campaign was conducted to study the validity of the experimental protocol at the I2M Laboratory at the University of Bordeaux. In the following sections, introduction to the test protocol, details of its working and some preliminary results are discussed. This work forms the basis for the rest of the chapters and the entire thesis.

II.1.1. Experimental set-up

The RCAIT specimen is composed of a *100 mm* long cylindrical rubber envelope of outer radius $w_0 = 4.7mm$ containing a brass coated steel wire of radius $v_0 = 0.65mm$ along its axis (*Figure II.1.1*). The steel wire, or cord, is bonded to the rubber during the vulcanisation process. To ensure reproducible specimen dimensions and accurate cord alignment along the cylinder axis, a specific mould is used.

A crude rubber strip is placed at the bottom of the lower half of the mould. The steel cord is wiped with ethanol to remove any traces of grease and debris, before placing it into the mould. The steel cord is then placed in the mould, along the central axis, and it is tightened under a small tension. If the cord is not aligned perfectly along the central axis, it can bend away from the central line once the mould is clamped. An accurate central alignment of the

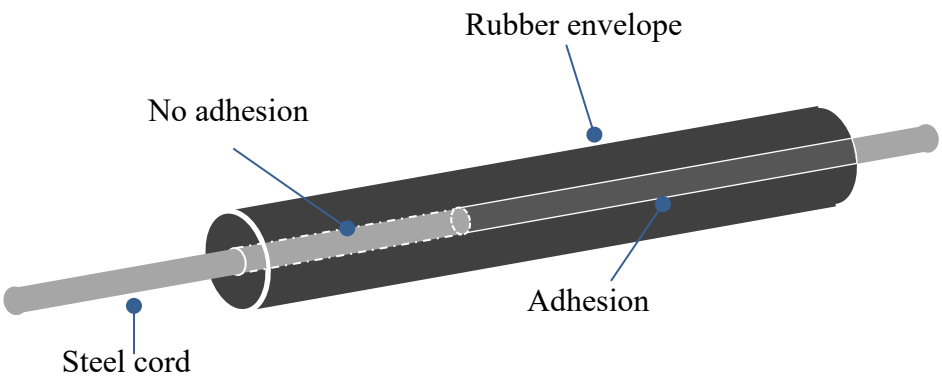

Figure II.1.1: The tape adhered around the steel cord creates a barrier between rubber and brass coating. This barrier creates initial crack during the vulcanization process.

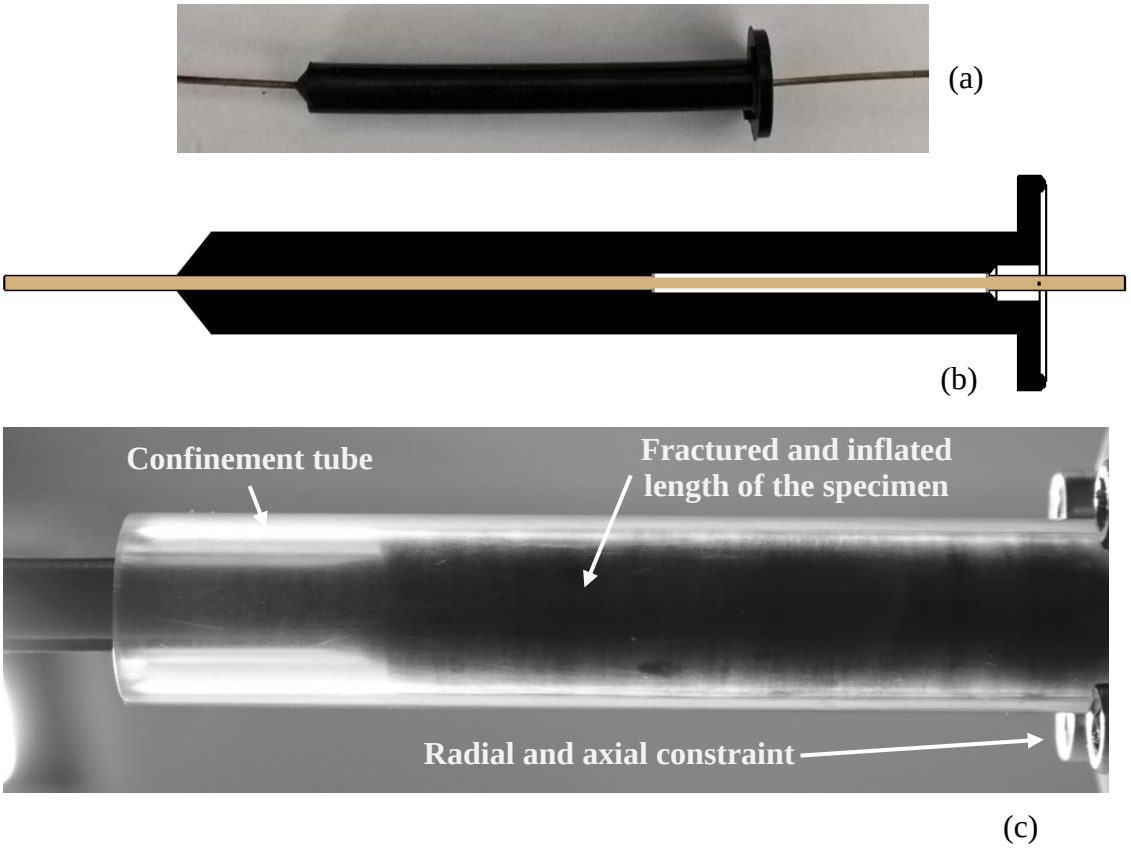

Figure II.1.2: (a) Test specimen (b) Schematic of the specimen cross-section. The initial debonding length is shown as white tape on the steel cord. (c) Inflated specimen during the test. The 'fractured and inflated' length of the rubber envelope is touching the PMMA confinement tube.

cord is essential for the specimen to have acceptable quality. During the vulcanisation process, due to the pressure between the moulds and the high temperature, the cord can buckle away from the central axis. It is therefore essential to keep the cord under small tension, while preparing the mould. Two more rubber strips are laid on top of the cord before placing the other half of the mould on top. The two halves of the mould are then clamped together, under a pressure of *2-3bar*. The mould is then placed in a hot press to produce Cu_xS bonding together with rubber vulcanisation. Copper from the brass coating and Sulphur from rubber create dendritic bonds during vulcanisation, which act as the rubber-steel interface, discussed earlier in.

An anti-adherent PTFE tape covers half of the length of the cord to produce initial debonding (or pre-crack). In addition, specific geometric features are added to the ends of the specimen (*Figure II.1.2 (a)*) such as flange on the fluid injection end and taper on the adhered end. This facilitates clamping of the specimen on the test stand. It also helps to minimise stress concentration, which can potentially cause failure in the rubber envelope before interfacial crack propagation occurs. *Figure II.1.2 (b)* shows a schematic of the specimen. The

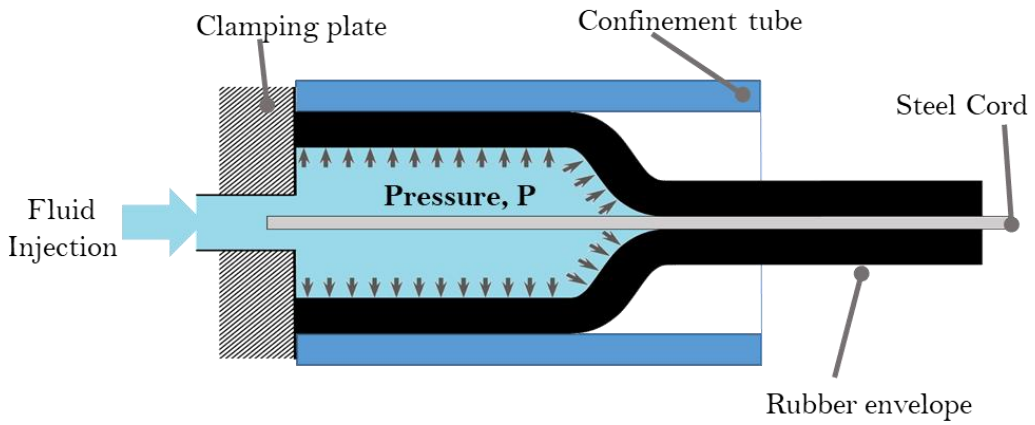

Figure II.1.3: Schematic representation of RCAIT.

debonding length (marked by white tape) is *50mm*. For the preliminary test campaign, the specimen was placed in a climatic chamber and was exposed to 40°C and 60%RH atmosphere for 60 hours to simulate accelerated ageing conditions.

As shown in *Figure II.1.3* a PMMA tube with *10mm* internal diameter and *5mm* thickness was used for radial confinement of the specimen. The importance of this confinement tube and its effect on specimen behaviour are explained in detail in forthcoming sections. Demineralised water was injected at *2ml/min* using a *KD Scientific 410 Series* syringe pump equipped with a *5ml* syringe. During the experiment, the water pressure was recorded using a *Swagelok Model S Transducer* with a capacity of *250bar*. The RCAIT setup installed at the I2M Laboratory, Bordeaux is shown in *Figure II.1.4*. Using a digital camera, the specimen deformation was recorded for post-test analysis.

All the specimens were provided by MFP Michelin and the vulcanisation process was already carried out. The rubber used in the specimens was a natural rubber with *65phr* of carbon black

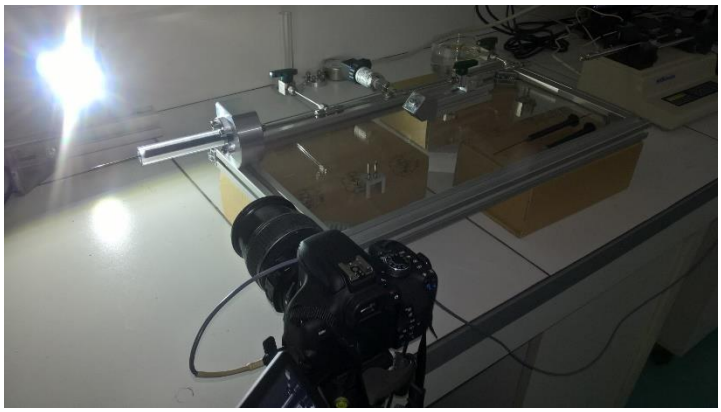

(a) Hydraulic circuit with camera

(b) Syringe pump

Figure II.1.4: RCAIT setup at the I2M laboratory.

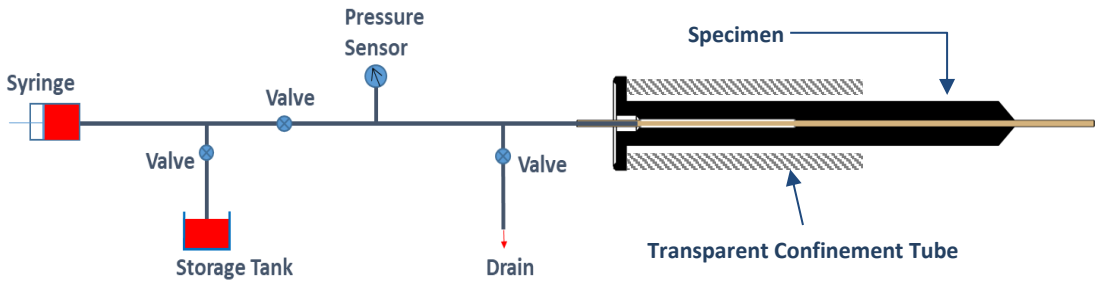

Figure II.1.5: Schematic of the hydraulic circuit for RCAIT.

and *4.5phr* of sulphur. This rubber is an incompressible Mooney-Rivlin material with C_1*=1.6MPa* and C_2*=0.1MPa*. The rubber material data was provided by MFP Michelin and was not cross-checked at this stage of the work. A detailed study of the rubber behaviour and its effect on the test results is presented in later chapters.

After the ageing process, the specimen was attached to the test bench at its fluid injection end, thus imposing radial and axial constraint. Only the rubber envelope was held fixed while the steel cord was free to move axially during the test, allowing the debonded rubber length to inflate freely. Water was injected inside the specimen, using the hydraulic circuit shown in *Figure II.1.5*. The injected water inflated the specimen in radial and axial directions such that the rubber envelope started touching the confinement tube and the water pressure kept rising higher (see *Figure II.1.2 (c)*). After a certain value of fluid pressure had been reached, the injected water initiated and propagated the crack along the rubber-steel interface.

II.1.2. Experimental results

Figure II.1.6 (a) shows the evolution of water pressure versus injected water volume during the test. The test sequence is divided into two phases. Up to ca. *5ml*, the pressure was increasing while the water was being injected in the rubber envelope. No crack propagation was observed during this phase; but the envelope was visibly inflated and could be seen touching the confinement tube. After nearly *8ml* of fluid injection, a pressure of ca. *66.6 bar* was recorded followed by a steady increase in the inflated length of the specimen that corresponded to the crack propagation. Nearly constant pressure was observed during the crack propagation, corresponding to a nearly constant critical Strain Energy Release Rate (SERR), similar to the study by [67].

After the test, the rubber envelope was cut open to observe the cord crack face. As a first observation, almost no remaining rubber was found on the wire surface. The brass-coating can be seen to be shiny on the crack face in *Figure II.1.6 (b)*. This may indicate adhesive failure,

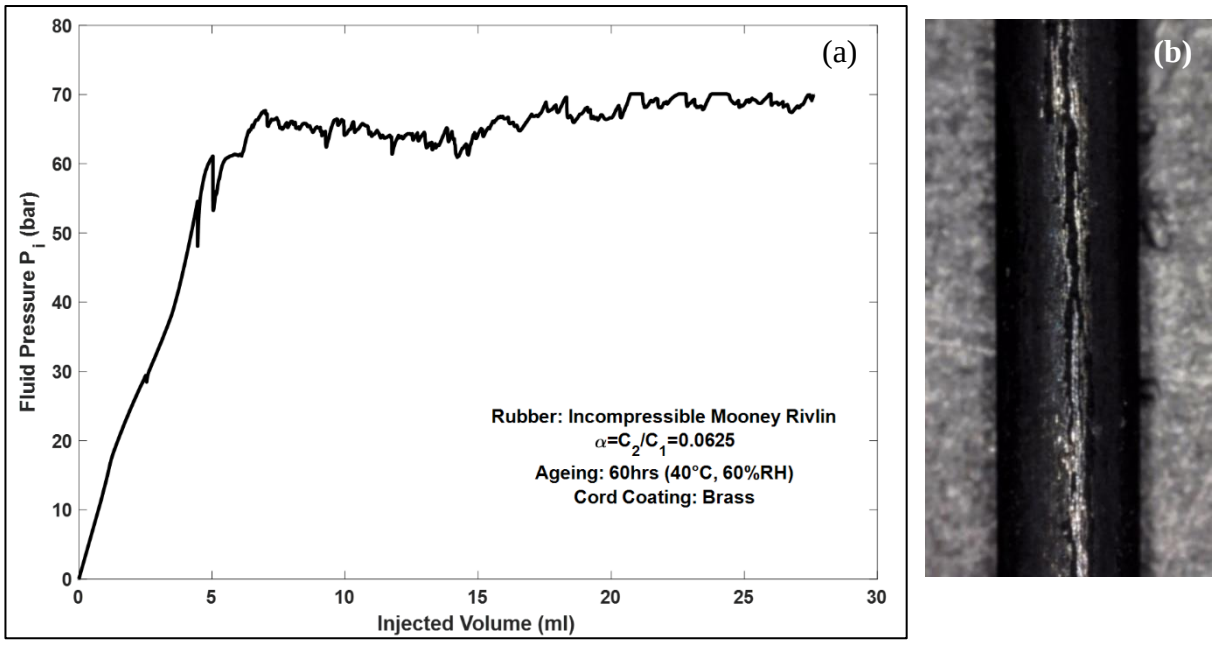

Figure II.1.6 : (a) Fluid Pressure vs Injected Volume. A nearly constant fluid pressure is observed during the crack propagation stage (ca. 8ml)), (b) Fracture surface of the steel cord. The shining spots (brass-coated steel) may indicate an adhesive failure.

although an XPS study of the crack face [68] needs to be carried out to reveal further whether the crack propagated along the adhesive interface or along the rubber surface.

One important observation from *Figure II.1.6 (a)* is that the crack propagation occurred at nearly constant pressure. This leads us to assume that the fracture is self-similar. In other words, the crack propagation is independent of crack length. A global energy balance carried out at any arbitrary crack length will give an average value of critical SERR or Fracture Energy. This hypothesis is the basic assumption used in the quantitative evaluation of the RCAIT. A theoretical model based on this hypothesis can now be constructed to evaluate the critical SERR of the rubber-steel interface.

II.2. Thick Rubber Tube Inflation Model (TRTIM)

The effect of strain energy stored in the rubber on the evaluation of critical SERR was already discussed in *Chapter I*. Before calculating the critical SERR of the rubber-steel interface, it is important to understand the mechanics of the rubber inflation. Once the rubber inflation is modelled, a precise calculation of the critical SERR can be performed. The rubber tube inflation process is intricate, and in §*II.3* it will become clear why nearly eight pages have been allotted to it. In addition, this analysis is required to study the stresses and strains arising

inside the inflated rubber tube. These stress-strain values will aid in making improvements to the test setup in the forthcoming sections. In §*II.2.4*, this point is discussed in detail.

Deformation of a thick elastomeric envelope or tube under internal pressure was previously studied by Skala [69]. The main notations, results and constitutive equations are recalled below before some modification of the boundary conditions are considered to take into account the effect of radial confinement. With these mathematical derivations, the aim is to describe the stress state in the rubber envelope of the specimen as well as the strain energy stored, considering its incompressible hyperelastic nature. In the next section, an energy balance analysis of the water injection process is proposed to determine the critical SERR associated with the crack propagation.

II.2.1. Constitutive equations

Consider a thick hollow elastomer tube with inner and outer radii given by v_0 and w_0 respectively, as shown in *Figure II.2.1*. The problem to solve is axisymmetric in principle, therefore only radial and axial displacements are considered here. The radial and circumferential principal stretch ratios are given by:

$$\lambda_r = \frac{dr}{dr_0} \qquad \lambda_\theta = \frac{r}{r_0} \qquad (II.2.1)$$

with r_0 and r being the radial position in the initial state and deformed state respectively. Taking into account the incompressible nature of the material with the relation $\lambda_r \lambda_\theta \lambda_z = 1$, and considering a constant through-thickness axial stretch, the general expressions of radial

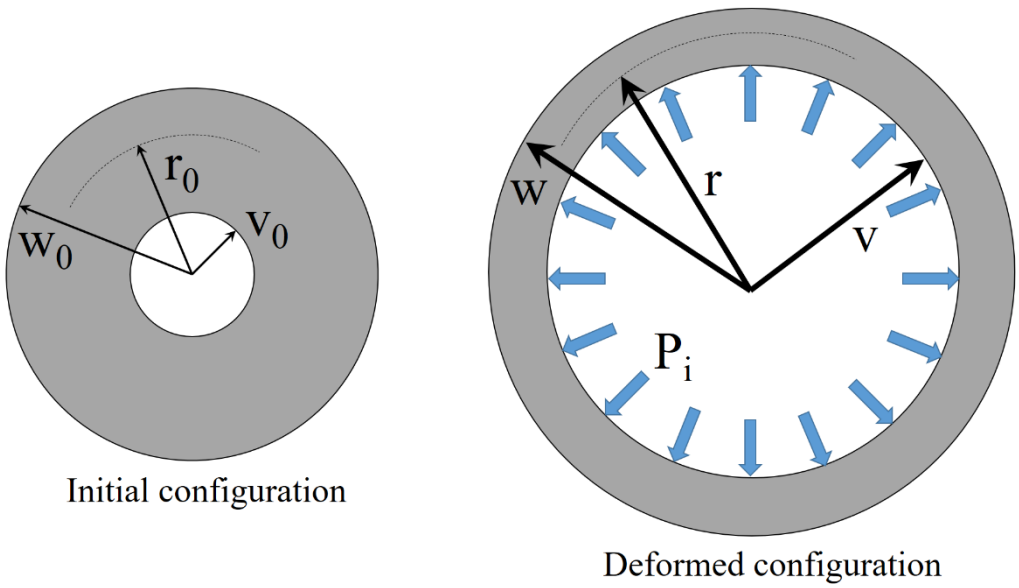

Figure II.2.1: Rubber tube deformation stages. P_i is the applied fluid pressure.

and circumferential stretch ratio in an axisymmetric configuration are found to be [69]:

$$\lambda_r{}^2 = \lambda_z{}^{-1}\left[1 - \frac{1}{cr^2}\right] \qquad \lambda_\theta{}^2 = \lambda_z{}^{-1}\left[\frac{cr^2}{cr^2 - 1}\right] \qquad \textit{(II.2.2)}$$

with c being an integration constant to be determined from constitutive and boundary conditions together with λ_z. Since the general expressions of stretch ratios are known *i.e. (II.2.1)* and *(II.2.2)*, an incompressible hyperelastic Mooney-Rivlin material behaviour [70] can be assumed for the rubber. This assumption stems from the material data provided by Michelin, as explained above. The relation between the Cauchy stresses and stretch ratios is given by:

$$\sigma_i = 2C_1\lambda_i^2 - 2C_2\lambda_i^{-2} + p \qquad \textit{(II.2.3)}$$

with p being the local hydrostatic pressure component of stresses. Under axisymmetric loading, the equilibrium equation gives the relation:

$$\frac{d\sigma_r}{dr} + \frac{\sigma_r - \sigma_\theta}{r} = 0 \qquad \textit{(II.2.4)}$$

Combining equations *(II.2.2)*, *(II.2.3)* and *(II.2.4)* according to the procedure followed in [69], a general expression of the hydrostatic pressure component, p, is found:

$$\frac{p}{2C_1} = \left\{\frac{1}{cr^2} - ln\left(\frac{cr^2}{cr^2 - 1}\right)\right\}\frac{1}{2\lambda_z} - \left\{\frac{1}{2cr^2} + \frac{1}{2}ln\left(\frac{cr^2}{cr^2 - 1}\right) - \frac{1}{cr^2 - 1}\right\}\alpha\lambda_z + d \qquad \textit{(II.2.5)}$$

Here $\alpha = C_2/C_1$ and d is an integration constant. Therefore, the stress distribution in the rubber is fully determined by only three parameters λ_z, c and d, which are obtained by solving the boundary condition equations as described hereafter.

II.2.2. Boundary conditions

Two different sets of boundary conditions should be considered since two stages are observed during the inflation test. Initially, the outer surface of the rubber envelope is free to expand since there is no contact with the confinement tube. This stage is called the Unconfined Inflation Stage (UIS). The following set of boundary conditions is therefore considered.

$$\sigma_{r(r=v)} = -P_i \qquad (II.2.6)$$

$$\sigma_{r(r=w)} = 0 \qquad (II.2.7)$$

$$\int_v^w \sigma_z(r) 2\pi r dr = P_i \pi v^2 \qquad (II.2.8)$$

P_i is the fluid pressure imparted by the injected water. Equation *(II.2.6)* indicates that the radial stress at the inner radius of the inflated rubber tube is the fluid pressure P_i. It is zero at the outer radius as indicated in *(II.2.7)*. The steel cord is not clamped and can move axially freely as the specimen inflates. This means that the axial force exerted on the cord by the fluid is directly transferred to the inflating rubber envelope and is given by *(II.2.8)*.

Solving the boundary conditions as simultaneous equations, and defining two dimensionless quantities $h = w_0/v_0$ and $K=1/(cv_0^2)$, a transcendental relation is found:

$$-2(h^2-1)\left(\lambda_z^3 - 1 + \alpha\lambda_z^2 - \frac{\alpha}{\lambda_z}\right) + K\lambda_z(1-\alpha\lambda_z^2) ln\left[\frac{h^2(1+K\lambda_z)}{h^2+K\lambda_z}\right] = 0 \qquad (II.2.9)$$

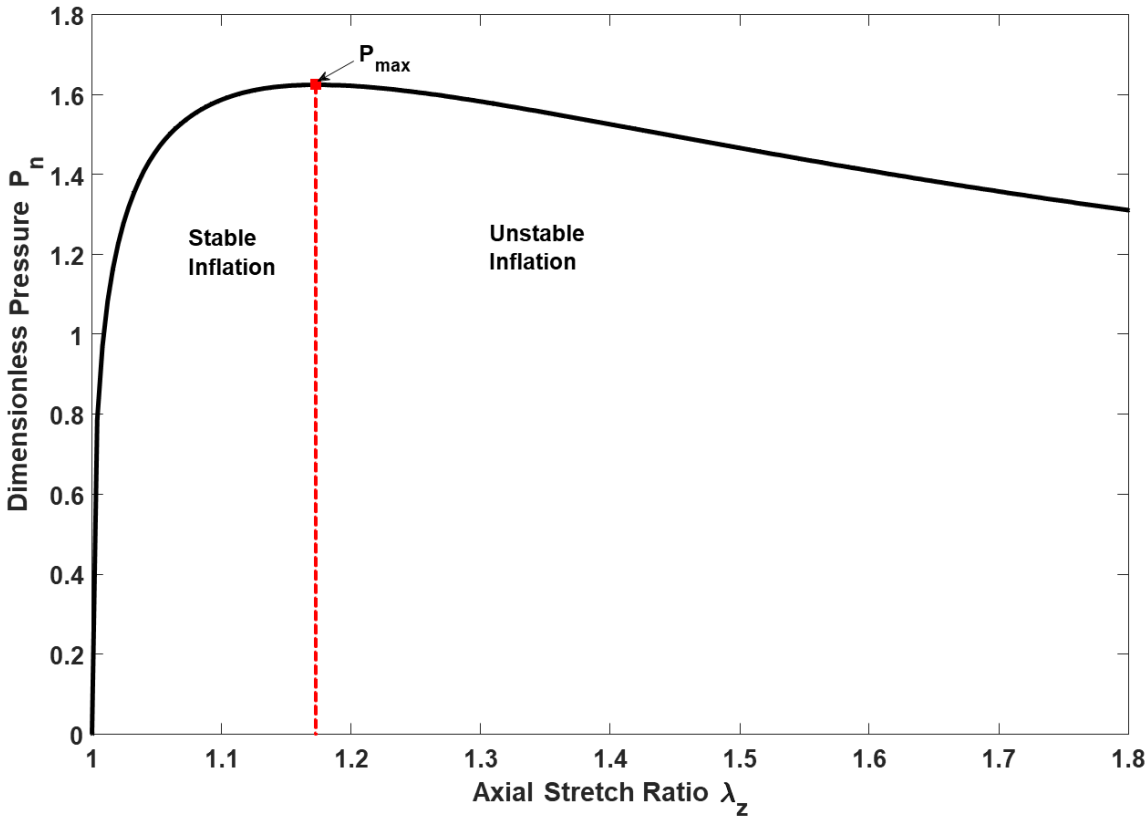

Figure II.2.2: Unstable inflation of rubber cylinders. P_{max} is the maximum fluid pressure and the point of instability.

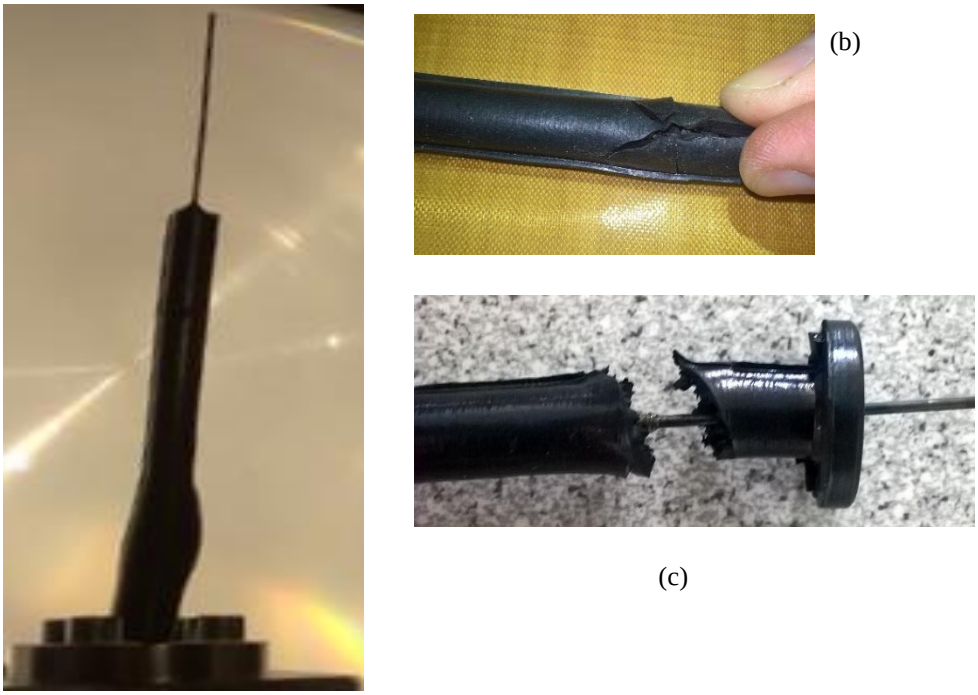

(a) (b) (c)

Figure II.2.3: (a) Aneurysms in the rubber envelope, (b) and (c) Rubber envelope failure due to absence of a confinement tube.

This relation is solved numerically to determine the K versus λ_z evolution from which all stretch ratios and stresses can be found in relation to the dimensionless pressure P_n $(= P_i/2C_1)$ using *(II.2.2)-(II.2.5)*. In *Figure II.2.2* the dimensionless pressure P_n is plotted against λ_z using *(II.2.9)*.

The unconfined cylindrical inflation tests are known to be susceptible to instabilities which must be avoided to keep the present analysis valid [71]; see *Figure II.2.3*. Inflating the cylinder past the instability point P_{max} corresponds to an unstable condition as this causes aneurysms in the rubber envelope. From this point onwards, the injected fluid cannot inflate the rubber homogenously, possibly leading to asymmetric fracture of the interface. As more fluid is injected, these rubber aneurysms explode into fracture, as shown in *Figure II.2.3*. In order to avoid fracture of the rubber envelope under high pressure and to ensure rubber-steel interface separation, a confinement tube is used which prevents excessive deformation of the rubber envelope, as proposed in [72], in planar configuration for the blister test. The radial clearance between the undeformed rubber envelope and the confinement tube is small enough to ensure that the rubber envelope will touch the confinement before reaching the point P_{max} in *Figure II.2.2*. This starts the second stage of the inflation, which is called the Confined Inflation Stage (CIS). It is now important to alter the boundary conditions, which describe the transition from UIS to CIS.

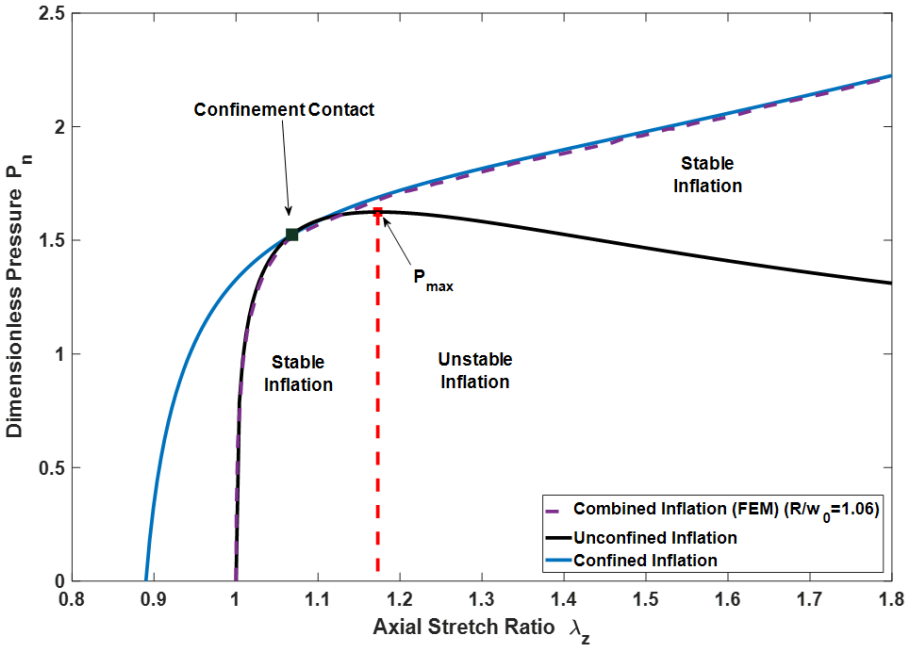

Figure II.2.4: Comparison of unstable and stable inflation of the rubber envelope. Confinement contact comes prior to the point P_{max} thereby avoiding the instability. Results from the FEM simulation closely matches the theoretical model.

The confinement envelope is supposed to be rigid. Therefore, the outer radius of the rubber envelope remains constant. Hence, for the second set of boundary conditions, *(II.2.7)* is changed to:

$$w = R \qquad (II.2.10)$$

with R being the inner radius of the confinement tube. Boundary conditions *(II.2.6)* and *(II.2.8)* remain the same for CIS. *(II.2.10)* leads to the following relation (see *Equation (25)* in [69] for intermediate steps):

$$R^2 = \frac{1}{c} + \frac{{w_0}^2}{\lambda_z} \qquad (II.2.11)$$

Therefore, the constant c is determined directly as a function of the longitudinal elongation λ_z, with the relation:

$$c = \frac{\lambda_z}{\lambda_z R^2 - {w_0}^2} \qquad (II.2.12)$$

Similar to the UIS, combining boundary condition equations *(II.2.6)*, *(II.2.8)* and *(II.2.12)* leads to relations:

$$P_n = -\frac{1}{2\lambda_z}\left\{\frac{2+K\lambda_z}{1+K\lambda_z} - ln(1+K\lambda_z)\right\} + \alpha\lambda_z\left\{\frac{3+2K\lambda_z}{2(1+K\lambda_z)} + \frac{1}{2}ln(1+K\lambda_z)\right\} - d \qquad (II.2.13)$$

$$\begin{aligned}(1+K\lambda_z)P_n = &\left({\lambda_z}^2 - \frac{\alpha}{{\lambda_z}^2} + d\right)(h^2-1) \\ &+ \frac{1}{2}K\lambda_z\left(\frac{1}{\lambda_z} - \alpha\lambda_z\right)ln\left(\frac{1}{h^2}\frac{h^2+K\lambda_z}{1+K\lambda_z}\right) \\ &- \frac{1}{2}\left(\frac{1}{\lambda_z} + \alpha\lambda_z\right)([h^2+K\lambda_z]ln[h^2+K\lambda_z] \\ &- [1+K\lambda_z]ln[1+K\lambda_z]) \qquad (II.2.14)\end{aligned}$$

with $P_n = P_i/2C_1$ being the dimensionless pressure. These two simultaneous non-linear equations can be solved numerically for a given value of λ_z. Finally, all displacements, stresses and stretch ratios are derived using *(II.2.2)* and *(II.2.3)*.

II.2.3. Numerical modelling

The rubber cylinder inflation was modelled in ABAQUS using axisymmetric elements CAX4RH, considering a Mooney-Rivlin material behaviour and contact condition with a rigid confinement envelope as shown in *Figure II.2.5*. The mesh size gradually increased from the inner radius to the outer radius: *0.02mm* at the inner radius (v_0) and *0.1mm* at the outer radius (w_0). A confinement ratio (R/w_0) of *1.06* was chosen as in the experimental conditions. The rubber cylinder was modelled to be of a length of *100mm* and the displacements and stresses were calculated at the middle of the length to avoid any edge effects. Using *Tie* constraint condition, the adhesion between rubber and steel was modelled. An internal pressure of P_i*=66bar* was applied to the specimen and the inflation was simulated. The deformed specimen is shown in *Figure II.2.6*. Uniform inflation of the specimen is observed except near the crack tip region. Large deformation is observed near the crack tip region, along with

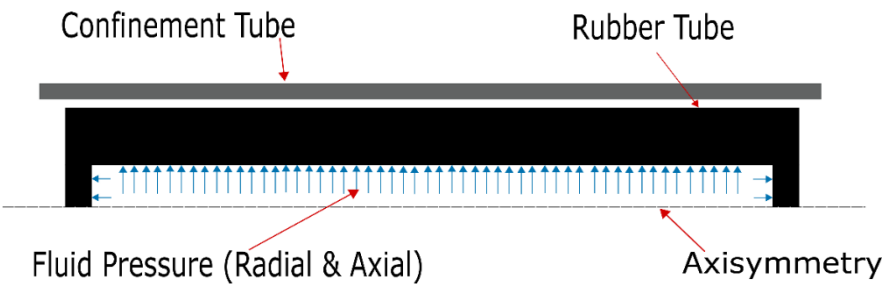

Figure II.2.5: Schematic of the Rubber Cylinder Inflation modelled in ABAQUS.

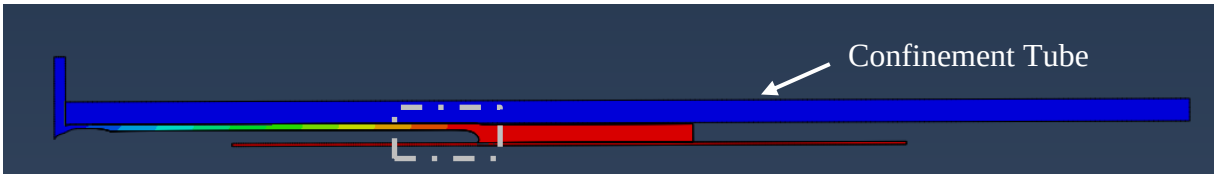

(a) FE modelling of specimen inflation

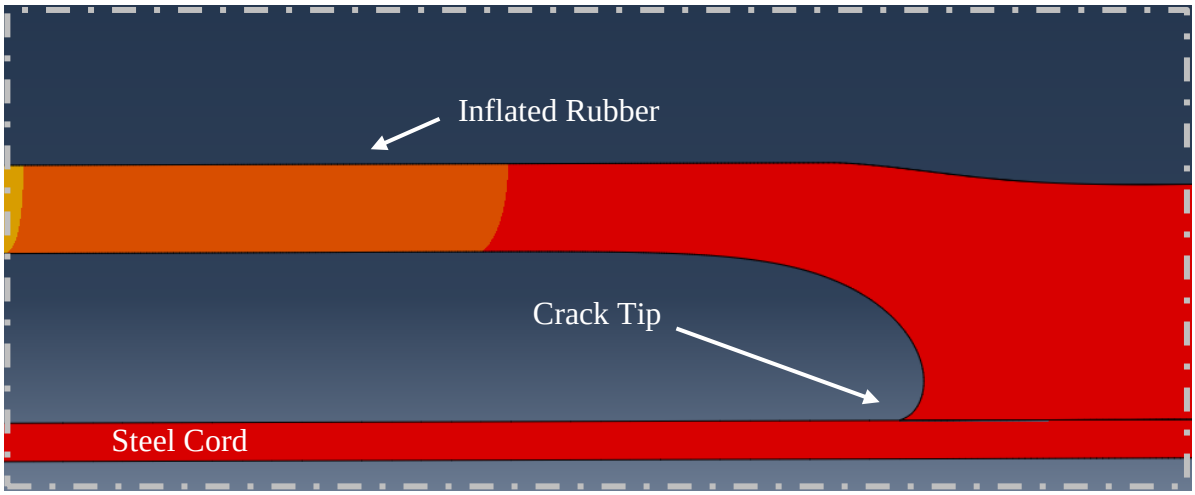

(b) Specimen deformation near crack tip

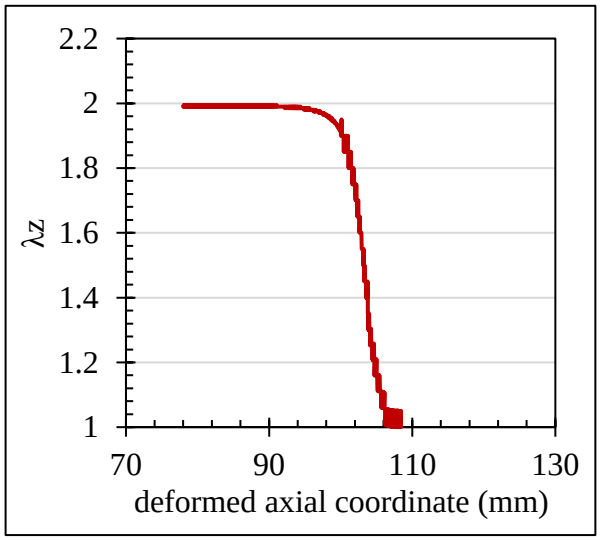

(c) Axial stretch ratio at the outer radius, crack tip region

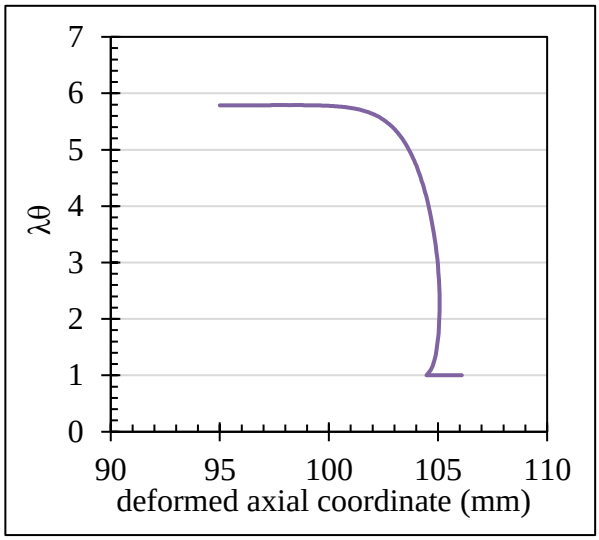

(d) Circumferential stretch ratio at the inner radius, crack tip region

Figure II.2.6: FE modelling of specimen inflation (a) Overall specimen deformation (b) large deformation is observed near the crack tip region (c) The axial stretch ratio measured along the outer radius of the specimen (d) The circumferential stretch ratio measured along the inner radius of the specimen.

rotation of the inflated rubber. The circumferential stretch ratio reached values of up to *5.8* at the inner radius, which needs a further investigation. The complexities related to the fracture mechanical study of the problem pose numerous difficulties, especially modelling the crack propagation behaviour in FE. Some discussion on this topic is presented in *Chapter IV*. At this stage, the FE modelling is limited only to the inflation behaviour. The focus is on

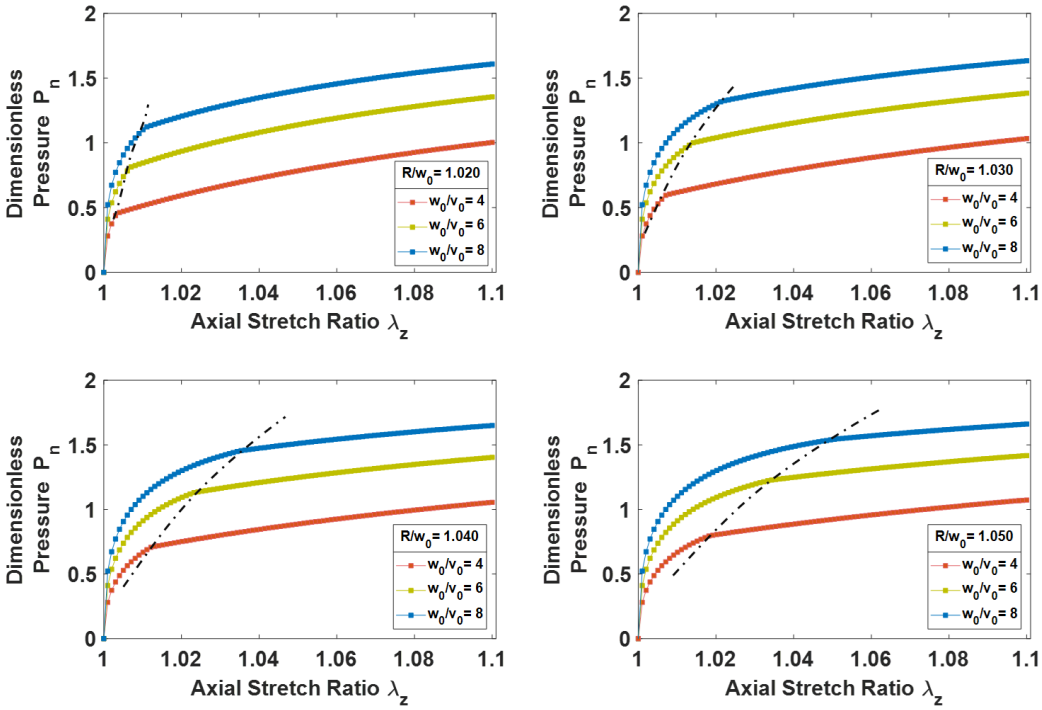

Figure II.2.7: Effect of dimensionless radius ($h = w_0/v_0$) and confinement ratio (R/w_0) on Rubber Tube Inflation. Dotted lines represent confinement contact.

comparing the inflation results obtained by the theoretical model described earlier and the FE results.

Figure II.2.4 shows the comparative results of the inflation tests during the UIS and CIS with a confinement ratio of *1.06*. The UIS (black curve) and CIS (blue curve) are respectively solutions to *(II.2.9)* and *(II.2.13)-(II.2.14)*. After the *Confinement Contact* point, UIS follows unstable inflation whereas CIS follows stable inflation. For the confined configuration with contact, the theoretical model is found to be in very good agreement with the FE model. The transition between the two stages is correctly captured.

Once the analytical model is assessed, parametric investigation can be performed. In particular, *Figure II.2.7* illustrates the effect of the dimensionless rubber envelope radius, h, and confinement ratio R/w_0 on the rubber tube inflation. The overall response is the same, regardless of which geometrical parameters are chosen. Obviously, the evolution of $P_n(\lambda_z)$ does not depend on the parameter R/w_0 during the UIS and the specimen is found to be stiffer when h increases leading to higher values of P_n. Interestingly, the dotted lines indicate the transition from UIS to CIS. It can be observed that there is a risk of unstable inflation for large R/w_0 values since large λ_z values are needed to achieve the contact condition in that case.

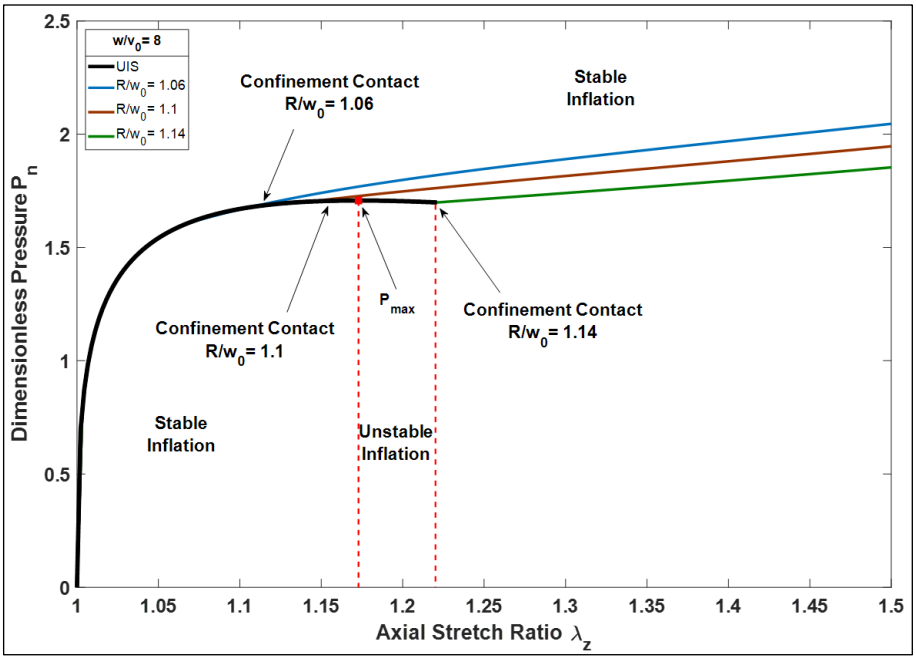

Figure II.2.8: Effect of confinement ratio (R/w_0) on Rubber Tube Inflation for a fixed dimensionless radius ($h = w_0/v_0=8$).

A similar plot for a constant dimensionless radius ($h=8$) and varying confinement ratios is shown in *Figure II.2.8*. The confinement contact is highly sensitive to the confinement ratio. A slightly higher confinement ratio (>1.1) results in unstable inflation.

II.2.4. Influence of boundary conditions

The Thick Rubber Tube Inflation Model explained earlier is based on an important assumption that the Cauchy stresses along the tube radius are not constant. This assumption is similar to the one in the standard Thick Cylinder Inflation Theory for elastic materials. For elastic materials, only engineering (or nominal) stresses are calculated. However, for a hyperelastic material, the Cauchy stresses are calculated due to the large deformations and displacements that lead to geometrical nonlinearities. In this section, the stress variation along the rubber tube thickness owing to the various boundary conditions is studied. The effect of axial stretch ratio (λ_z) on the Cauchy Stresses as well as the Dimensionless Pressure (P_n) is elaborated upon.

In the previous analysis, a series of dimensionless parameters has been introduced which should be recalled here. For a Mooney-Rivlin solid $\alpha = C_2/C_1$ is a material parameter. In this theoretical work, the same value of $\alpha = 0.0625$ which represents the specimen rubber material is used. The dimensionless pressure P_n is considered here as the driving quantity. All stress/stretch evolutions depend on the initial tube dimension as given by the dimensionless radius, $h = w_0/v_0$.

In *Figure II.2.9* the Cauchy stresses (x-axis) are plotted against the deformed rubber tube radius (y-axis) for the UIS (R→∞). Although confinement is absent, a decrease in the rubber tube thickness is observed with an increase in the axial stretch ratio λ_z, due to the incompressibility of the rubber. The horizontal dotted lines in *(b)*, *(c)*, and *(d)* represent the undeformed tube radii (w_0 and v_0). As the inflation enters the unstable region, as shown in *Figure II.2.4*, Cauchy stresses σ_z and σ_θ increase dramatically. A significant variation of σ_r across the tube thickness arises due to the significant thickness of the tube. A thin cylinder tube theory will fail to represent this result. The Cauchy Stress values need to be considered while designing the specimen.

Similar plots can also be obtained for a purely CIS (w_0=w=R). A comparison of the theoretical Cauchy Stress variation and the one from the FE model is shown in *Figure II.2.10.* The stress variation at different axial stretch ratios is virtually identical for both methods of calculation (FE and theory). Again, the horizontal dotted lines represent the undeformed tube radii (w_0 and v_0). During this inflation stage, the confinement tube is loaded with a radial pressure of σ_r. This value of σ_r (up to 4MPa) is far from being negligible and a possible radial expansion of the confinement tube itself may be expected if it is not rigid enough. The Cauchy stress values and their through-thickness variation seen in *Figure II.2.9* and *Figure*

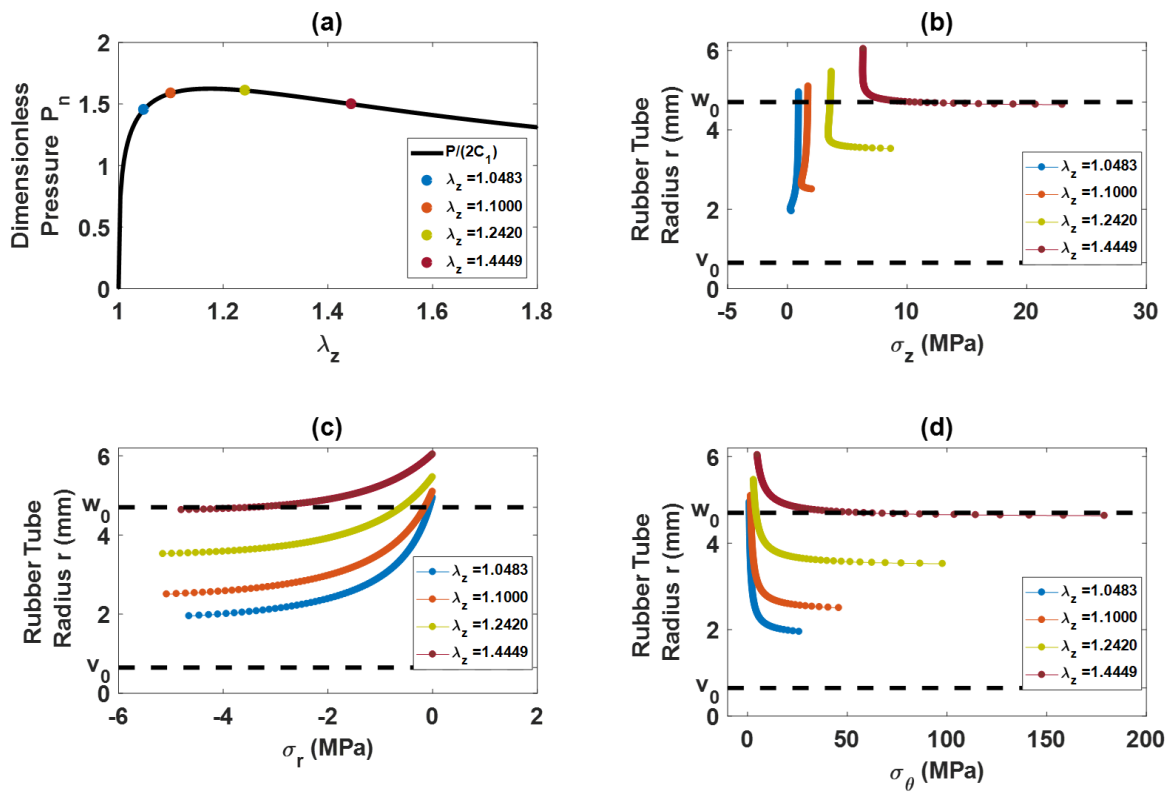

Figure II.2.9: Unconfined Inflation Test. Effect of Axial Stretch Ratios on Cauchy Stresses and P_n.

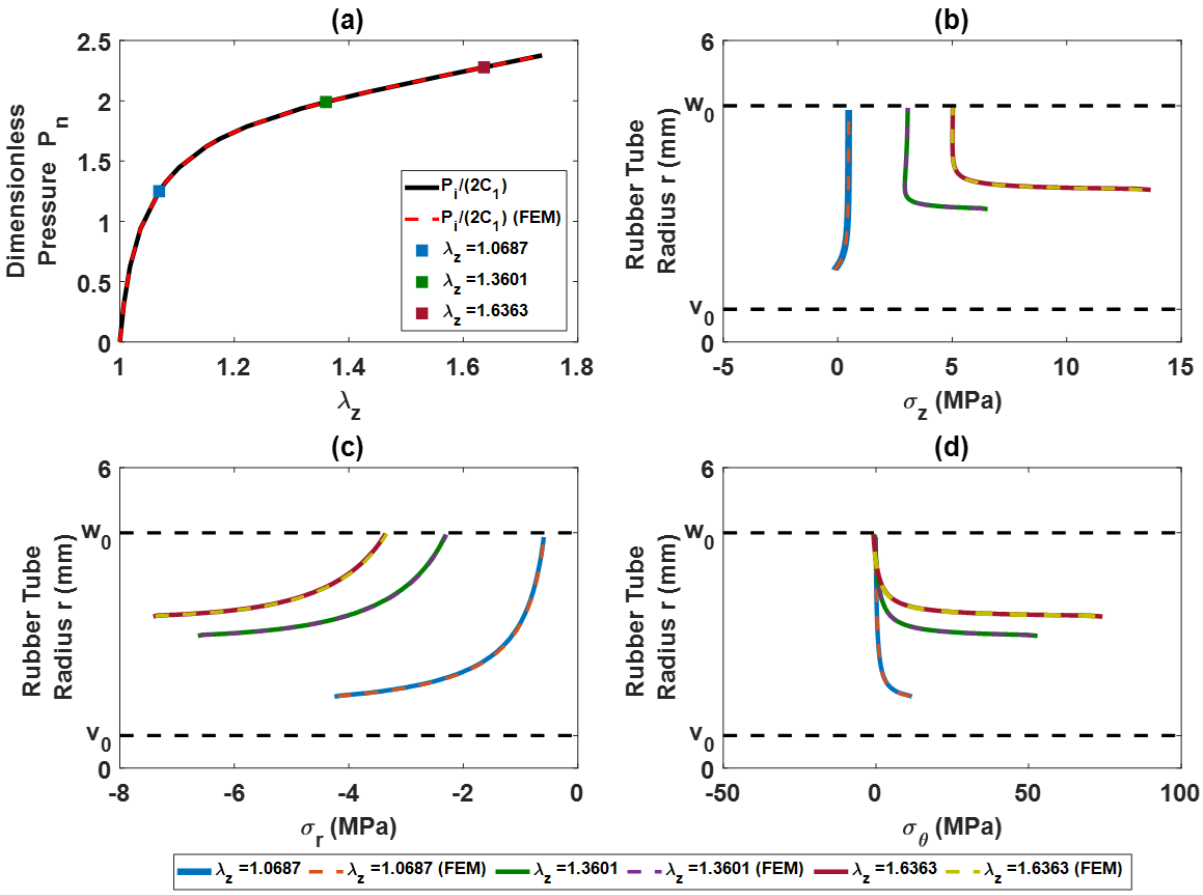

Figure II.2.10: Purely Confined Inflation Test. Effect of Axial Stretch Ratios on Cauchy Stresses and P_n.

II.2.10 are a strong justification for the need to develop a new Thick Rubber Tube Inflation Model instead of using the traditional Thick Cylinder Inflation Theory for elastic materials or assuming that the rubber envelope is a thin membrane. In these traditional models either the nonlinear behaviour of the rubber is not taken into account or the Cauchy Stress variation along the thickness is neglected. This can lead to huge errors in the critical SERR calculation which will be evident from the next section.

Despite the contact pressure, no frictional forces are considered at this stage, since once the contact condition is reached between rubber and confinement envelope, no relative displacement is expected if the inner pressure remains constant. This might not be the case if large pressure fluctuations are measured during the experiment due to, for example, stick-slip phenomena, or if creep behaviour is present. To minimize or eliminate this effect, lubrication would be needed. In the next chapter this topic is studied in detail.

II.3. Virtual Crack propagation

In the previous section, rubber envelope inflation was studied in detail considering the two sets of boundary conditions encountered during the experiments. Theoretical equations were developed for calculating both the axisymmetric deformations and stresses in the rubber. In the current section, these equations are employed for calculation of the energy stored in the rubber during crack propagation. An energy balance equation is subsequently derived to evaluate the crack propagation condition in the framework of linear elastic fracture mechanics (LEFM) theory. Neither a large process zone is supposed to develop ahead of the crack tip nor any plastic deformation in the rubber envelope is assumed to occur. Although LEFM is considered here, the process is expected to be highly nonlinear due to the material and geometrical nonlinearities. All possible additional dissipation mechanisms in the rubber due to viscosity or hardening are neglected at this stage.

II.3.1. Strain energy release rate

The entire test procedure is driven by injecting a pressurized liquid in between the rubber envelope and the steel cord. The overall energy balance can be described as follows. The energy put into the system is due to the work done by the pressurized liquid. This is distributed between the energy stored in the deformed rubber (and a small amount stored in the compressed fluid at high pressures) and the energy required (or released) to cause separation of the rubber-cord interface *i.e.* fracture energy. Once the initial liquid injection (system loading) is finished, the measured pressure remains reasonably constant during crack propagation (see *Figure II.1.6* (a)). The process can therefore reasonably be assumed to be steady state and self-similar.

Once the crack has initiated, a virtual crack extension 'δa' along the interface is considered (see *Figure II.3.1*). Due to the axial deformation, this newly added (δa unit long) length of free, unattached rubber, which is fractured and then inflated, is stretched to length $\lambda_z \delta a$. The corresponding work done in the pressure injection is then simply determined as the product of the constant pressure P_i at which the crack propagates and the injected fluid volume during the crack propagation length δa:

$$W = P_i \pi (v^2 - {v_0}^2) \lambda_z \delta a \qquad (II.3.1)$$

Taking into account the fluid compressibility constant 'χ', the potential energy stored in a compressible fluid during the crack propagation is given by the relation:

$$E_{pf} = \frac{\pi}{2}\chi {P_i}^2(v^2 - {v_0}^2)\lambda_z \delta a \qquad (II.3.2)$$

In this analysis, the incompressible Mooney-Rivlin model is used to describe the mechanical behaviour of the rubber. The strain energy density (energy per unit volume) of such a solid is given by the following relation:

$$\delta W(\lambda_z, \lambda_r, \lambda_\theta) = C_1(I_1 - 3) + C_2(I_2 - 3) \qquad (II.3.3)$$

where:

$$I_1 = \lambda_z^2 + \lambda_r^2 + \lambda_\theta^2 \qquad (II.3.4)$$

$$I_2 = \lambda_r^2\lambda_z^2 + \lambda_\theta^2\lambda_r^2 + \lambda_z^2\lambda_\theta^2 \qquad (II.3.5)$$

Therefore, the total potential energy stored per unit length of the fractured and inflated rubber is obtained by integrating the relation *(II.3.3)* over the tube cross-section as follows:

$$\delta E_{pr} = \int_v^w \delta W . 2\pi r dr \qquad (II.3.6)$$

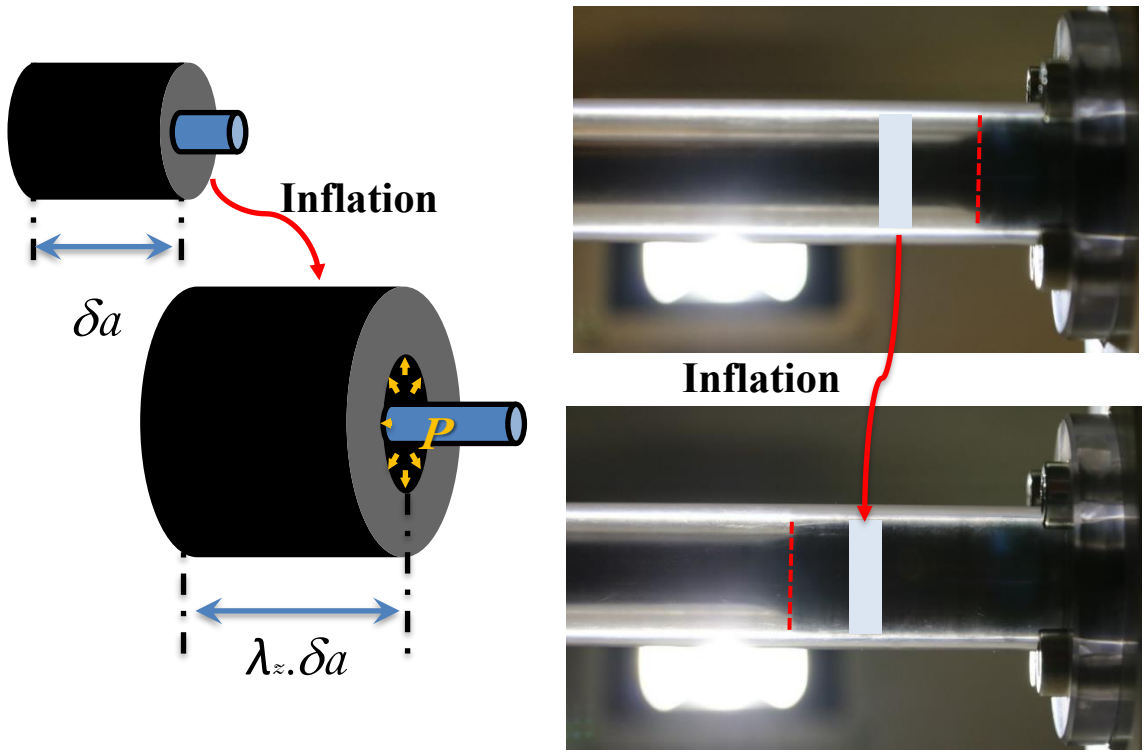

(a) (b)

Figure II.3.1: As the crack propagates by an arbitrary small length δa, the rubber envelope inflates and touches the confinement tube.

Here v and w are respectively the inner and outer rubber envelope radii in the deformed (fractured-inflated) state. Using *(II.2.2)* the integration leads to:

$$\delta E_{pr} = 2\pi\left[\frac{w^2 - v^2}{2}\left(C_1{\lambda_z}^2 + 2C_1{\lambda_z}^{-1} + 2C_2\lambda_z + C_2{\lambda_z}^{-2} - 3C_1 - 3C_2\right) - \frac{C_1{\lambda_z}^{-1} + C_2\lambda_z}{c}\ln\left(\frac{w}{v}\right) - \frac{C_1{\lambda_z}^{-1} + C_2\lambda_z}{2c}\ln\left(\frac{cw^2 - 1}{cv^2 - 1}\right)\right] \qquad (II.3.7)$$

It should be noted again that the integration is performed in the deformed state. Such a procedure naturally takes into account the large displacement effects. For a virtual crack propagation of 'δa' along the interface, the potential energy (E_{pr}) of the deformed rubber tube is increased to $\lambda_z \delta a \delta E_{pr}$ such that:

$$E_{pr} = 2\pi\lambda_z d\alpha[\{C_1(\lambda_z^2 + 2\lambda_z^{-1} - 3) + C_2(\lambda_z^{-2} + 2\lambda_z - 3)\}\left\{\frac{w^2 - v^2}{2}\right\} - \frac{C_1\lambda_z^{-1} + C_2\lambda_z}{c}\{\ln\left(\frac{w}{v}\right) - \frac{1}{2}\ln\left(\frac{cw^2 - 1}{cv^2 - 1}\right)\}] \qquad (II.3.8)$$

Finally, the energy dissipated through the interfacial separation should be considered as given by the relation:

$$D = G.2\pi v_0 \delta a \qquad (II.3.9)$$

where, G is the SERR of the interface and $2\pi v_0 \delta a$ is the area of the fractured face. The fracture propagates when the SERR reaches a critical value such that $G = G_c$; where G_c is the fracture energy or critical SERR.

Applying energy balance to the whole system:

$$W = E_{pf} + D + E_{pr} \qquad (II.3.10)$$

The following expression for the SERR is found:

$$G = \frac{P_i(v^2 - {v_0}^2)\lambda_z}{2v_0} - \frac{\chi}{4v_0}{P_i}^2(v^2 - {v_0}^2)\lambda_z$$
$$- \frac{\lambda_z}{v_0}[\{C_1(\lambda_z^2 + 2\lambda_z^{-1} - 3) + C_2(\lambda_z^{-2} + \lambda_z - 3)\}\left\{\frac{w^2 - v^2}{2}\right\}$$
$$- \frac{C_1\lambda_z^{-1} + C_2\lambda_z}{c}\{ln\left(\frac{w}{v}\right) - \frac{1}{2}ln\left(\frac{cw^2 - 1}{cv^2 - 1}\right)\}] \qquad (II.3.11)$$

In this expression, some terms are known/measurable quantities (P_i, C_1, C_2) and the rest are determined by solving the *Thick Rubber Tube Inflation Model* from the measured fluid pressure, P_i. The value of G does not depend on the initial crack length or debonding length which is consistent with the self-similarity assumption made earlier. However, to avoid edge effects and to facilitate homogeneous inflation of the tube, an initial crack length of *50%* of the total length of the specimen was chosen in the experimental test.

Depending on the rubber material properties, specimen dimensions, radial clearance for inflation (= R - w_0) and the strength of the interface, the crack propagation may occur during UIS or CIS. However, the method followed to calculate the energy balance is unchanged, therefore *(II.3.11)* holds true in both cases.

Figure II.3.2 shows the behaviour of the SERR, equation *(II.3.11)*, *vs* the fluid pressure observed during crack propagation. In the case of *Figure II.1.6 (a)*, the crack propagation

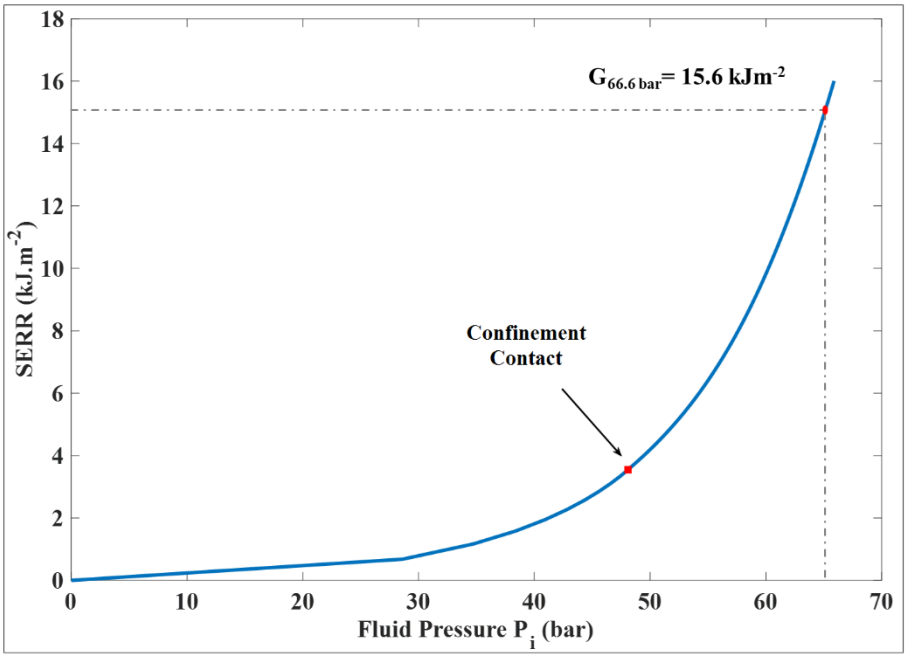

Figure II.3.2: Strain Energy Release Rate as a function of injection Fluid Pressure.

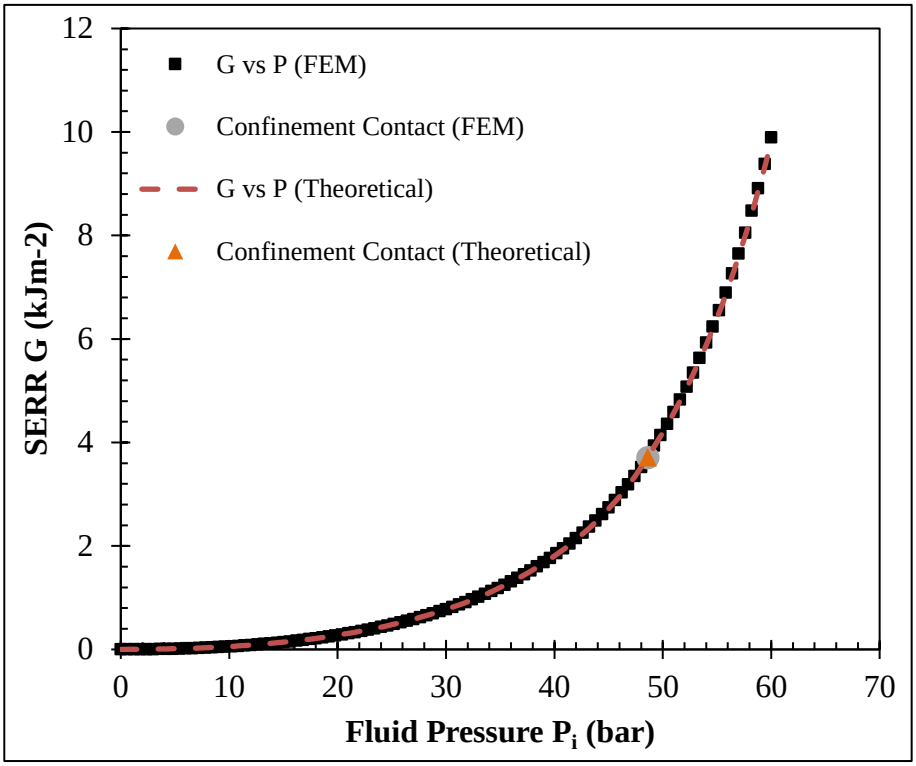

Figure II.3.3: Evolution of SERR with applied pressure. Comparison between theoretical model and FE model.

pressure was *66.6bar* which gives G_c to be 15.6 kJm^{-2}. The critical SERR obtained with an independent *90°* peel test was *21.3 kJ.m*$^{-2}$. A value of ~ *20kJ.m*$^{-2}$ was recorded in [46] for peel tests. Although the values differ by a small amount, experimental conditions from both the tests should be adjusted to match the same loading rates and ageing conditions of the rubber and the interface. Such a detailed comparison would be interesting for future research prospects. However, it is important to note that the order of magnitude (~*kJm*$^{-2}$) of G_c is the same.

For the calculation of *G* using FEM, an approach similar to Virtual Crack Closure Technique (VCCT) [73] was used. Five different crack lengths were modelled, and the specimen was inflated in the FE model up to the same maximum pressure. The difference in the energy stored between the models at any applied pressure gives the energy of fracture or G_c corresponding to that pressure. Similar to previous results, again, the results from the FE model and the theoretical model match almost exactly. *Figure II.3.3* shows comparison of SERR calculated using *(II.3.11)* and the VCCT-like FE approach.

It should be noted that, the calculation of G from *(II.3.11)* is valid only up until the instability point shown in *Figure II.2.4*. Beyond the point P_{max}, as the fluid pressure begins to drop, the contribution of W in *(II.3.11)* simultaneously begins to drop. However, the rubber envelope continues to store potential energy E_{pr} which gives a steadily decreasing value of G. To circumvent such erroneous results, it is imperative to avoid the unstable inflation. A stable inflation prior to the crack propagation can be attained by reducing the ratio R/w_0, such that the CIS starts before the point $P_n=P_{max}$ is reached. The entire test can also be carried out under purely CIS ($w_0=R$) which will certainly avoid the unstable inflation. However, the testing equipment should be designed to work under very high pressures.

A comparison of the contribution of the work supplied by pressure injection (G_f) and that of the potential energy stored in the inflated rubber (G_r) (calculated per unit fracture area) in comparison with the SERR (G) is shown in *Figure II.3.4*. The contribution of the potential energy stored in the fluid compressibility is negligible (<1%) for nearly incompressible fluids such as water. The nonlinear behaviour of the function G is directly attributed to the nonlinear behaviour of rubber.

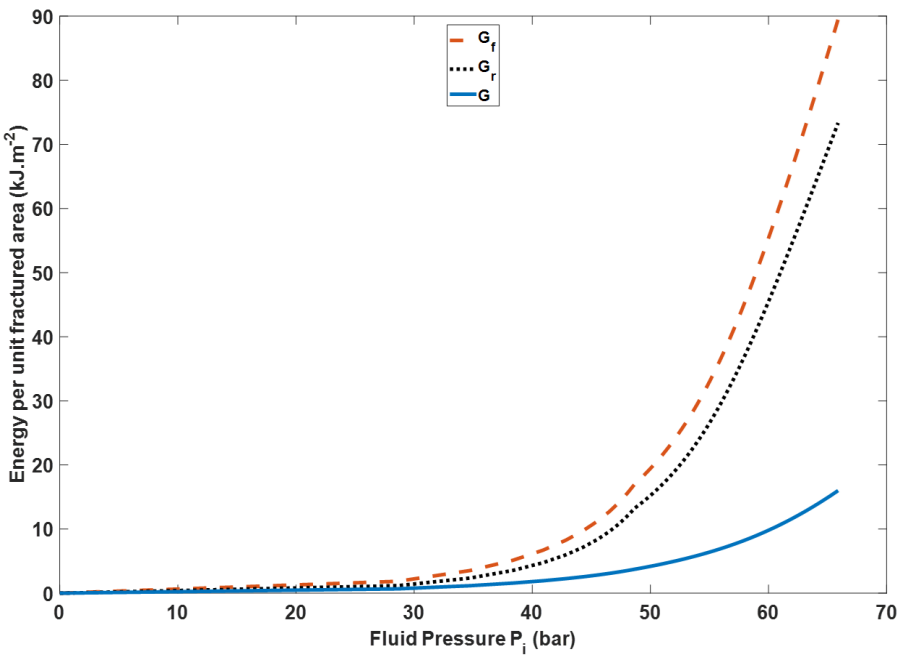

Figure II.3.4:Comparison of the energies stored in the fluid and the rubber at crack propagation, calculated for a unit fractured area. G_r is the contribution of the rubber envelope and G_f is of the fluid. G is the SERR, plotted using (II.3.11).

II.4. Improvements to the RCAIT

In §*II.2* the Thick Rubber Tube Inflation Model (TRTIM) was developed for Mooney-Rivlin rubber. The choice of the hyperelastic model was based on the data provided by MFP Michelin. The theoretical model and experimental results presented in the previous sections provide strong evidence that the RCAIT can be performed for quantitative analysis of rubber-steel adhesion fracture. It is now of interest to focus on individual parameters of the test protocol: improvements to the theoretical model and test protocol and the effect of various experimental factors on the test results. By focusing on each of these parameters, an in-depth analysis of the rubber-cord adhesion will be possible.

In the following sections, improvements to the theoretical model and its application to the Ogden model as well as improvements to the test protocol are discussed.

II.4.1. Test specimens and bulk rubber characterization

The test specimen is composed of a *100 mm* long cylindrical rubber envelope of outer radius w_0*= 4.7mm* containing a steel wire of radius v_0*=0.65mm* along its axis. Two different types of coatings (brass and bronze) are deposited on the steel cord during the wire drawing process. In actual tyres, the steel cord is brass coated. The bronze-coated specimens are used in this work only for comparative purposes. The average thickness of the coating is in the range of *0.05 to 0.1μm*. All specimens are made out of vulcanized virgin rubber with no ageing performed. Two different types of rubber mixes are used, having different mechanical and adhesive behaviour. In the following, these two rubber materials are designated as *Mix A* and *Mix B. Mix A* is a natural rubber containing *60phr* of carbon black and *7phr* sulphur. Rubber *Mix B* is a natural rubber containing *65phr* of carbon black and *4.5phr* of sulphur. Their detailed compositions and curing conditions remain subject to industrial confidentiality.

The material properties of these two mixes have been evaluated separately by performing tensile tests on custom designed dumbbell specimens (*Figure II.4.1*). To obtain the tensile test specimens, *2.5mm* thick rubber sheets are cured for vulcanisation. The dumbbell specimens are produced by pressing a mould, whose dimensions are shown in *Figure II.4.1(a)*, onto the cured sheet. The specimens are attached to a *Zwick/Roell® Z010* tensile testing machine equipped with a *10kN* load cell and loaded under a constant traverse displacement rate. Five different displacement rates are used in the range of *1mm/min* to *25mm/min* (or $4.4\ x10^{-4}/s$ to $110\ x10^{-4}/s$) to evaluate the influence of strain rate on the rubber mechanical behaviour. To measure elongation, white marks are drawn on the specimen. Pictures of the specimens are

acquired periodically during the test, and *MATLAB*® and *ImageJ*® [74] scripts are used to determine longitudinal elongation of the specimens. The resulting *nominal* stress (calculated per unit original area) *vs nominal* strain are represented in *Figure II.4.2* for both *Mix A* and *Mix B* and for five loading rates. The effective elongation rate for each specimen is calculated from the elongation *vs* time evolution.

Overall, rubber *Mix B* shows relatively low strain rate sensitivity, even at 100% strain. Rubber *Mix A* seems to exhibit more pronounced strain rate sensitivity as slightly stiffer behaviour is observed at higher strain rates. However, the variations in the tensile behaviour remain relatively small considering the range of strain rates tested. Also, due to limited availability of the raw material samples for this study, the tests could not be repeated for each loading rate. Therefore, it is difficult to distinguish possible material/specimen variability from loading rate effect.

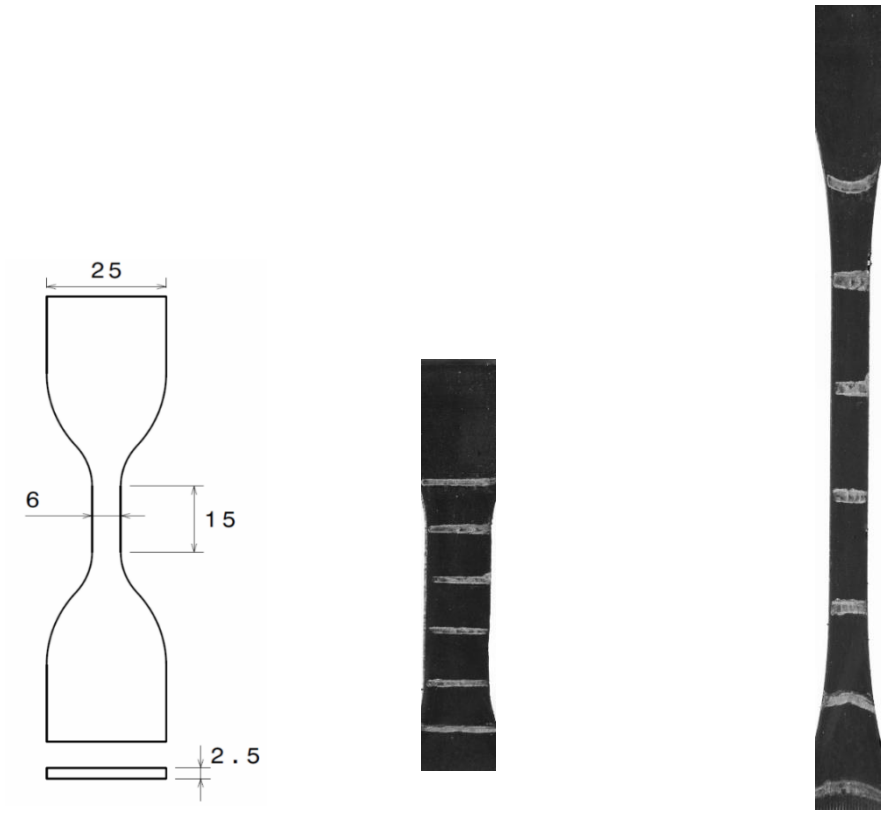

(a) (b) (c)

Figure II.4.1: (a) Geometry of the tensile test specimen (b) Tensile test specimen under no load (c) Specimen under tension.

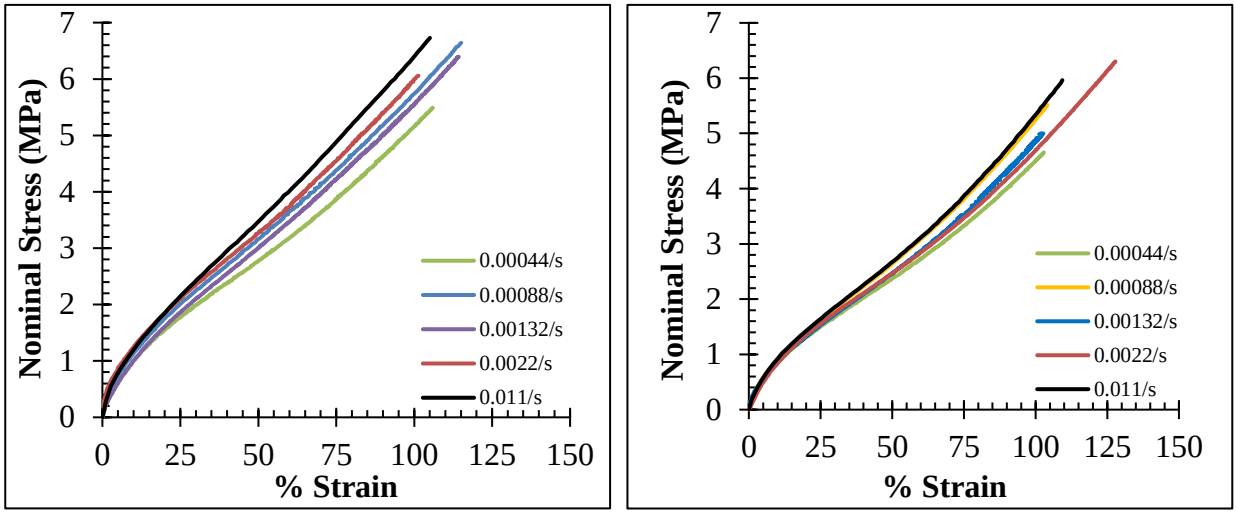

(a) Mix A (b) Mix B

Figure II.4.2: Tensile test results at 5 strain rates

In the present contribution, simple hyperelastic models are considered. The viscoelastic contribution is not taken into account explicitly. Separate material parameters are identified for each tensile test. The variability will account for both material properties variability and strain rate sensitivity. Several hyperelastic models can be used to describe the monotonic loading sequence of the virgin rubber, such as Mooney-Rivlin, Ogden, Yeoh or Gent.

Amongst these different standard models, the best fit is obtained with the Ogden model, which will therefore be used in the following analysis. Only the first order terms are needed in the series to achieve reasonable accuracy for the model, as seen in *Figure II.4.3*. The uniaxial Cauchy stress can therefore be given as $\sigma = \mu(\lambda^{\alpha} - \lambda^{-\frac{\alpha}{2}})$. As a result, the mean values of the material constants (α and μ) for rubber *Mix A* and *Mix B* in the strain rate range tested are considered. The standard deviation in the present context accounts for both specimen variability and possible strain rate effect.

The parameter α governs the behaviour of the rubber at large strains (it becomes stiffer). This is because it is present as an exponent in the Cauchy stress equation. The parameter μ, on the other hand, dictates overall increase or decrease in the Cauchy stress value, regardless of strain (or stretch ratio λ). A higher value of μ thus indicates a stiffer material overall, whereas a higher value of α indicates increased stiffness at large strains. Values of α and μ for the two mixes and various loading rates are given in *Figure II.4.4*.

It is impossible to mimic the loading conditions of an inflation test on a uniaxial dumbbell specimen. The inflation test is multiaxial, and the loading histories are different along both the

radial and axial directions. Therefore, in this work, average values of α and μ based on the five tensile tests are used. They are $\alpha=2.435$ and $\mu=2.293MPa$ for *Mix A* and $\alpha=2.785$ and $\mu=1.502MPa$ for *Mix B*. The variation of the rubber properties with strain rate is of use for evaluating the uncertainty in the calculation of the interfacial critical SERR due to a poor description of the exact material behaviour. More complex envelope inflation modelling would correspond to a completely different research topic as a future prospect.

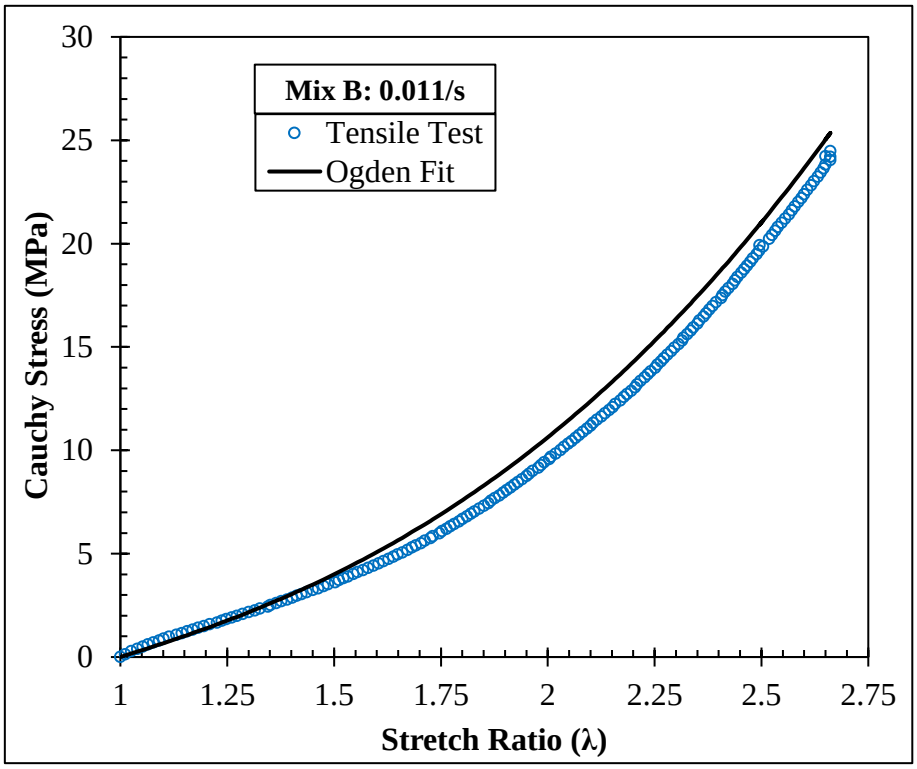

Figure II.4.3: Ogden model fit for Mix B rubber uniaxially loaded at 0.011/s.

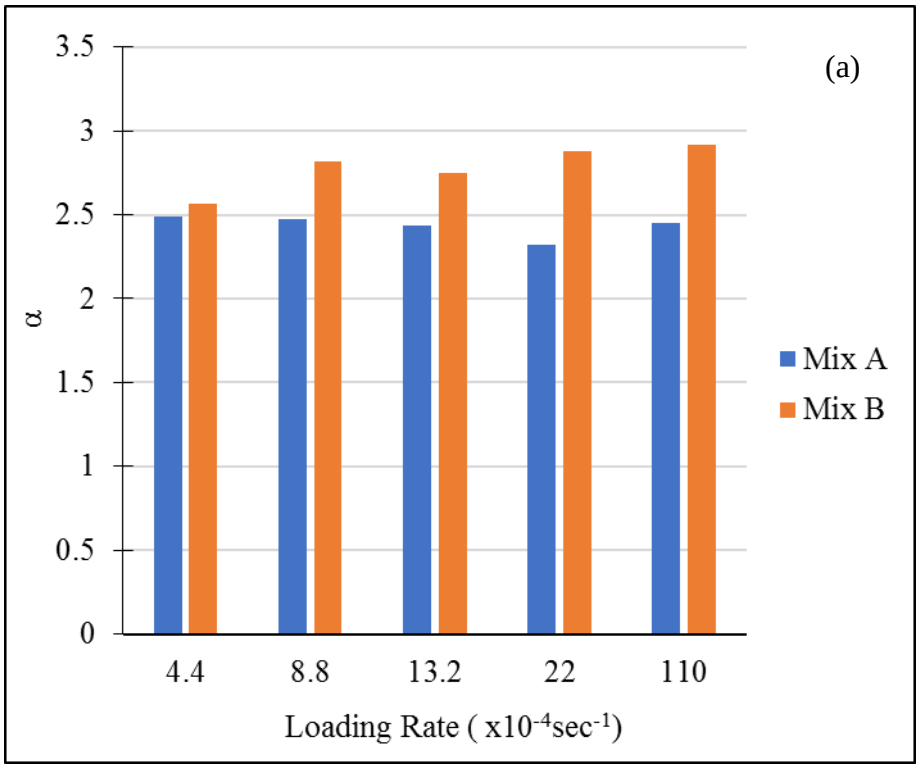

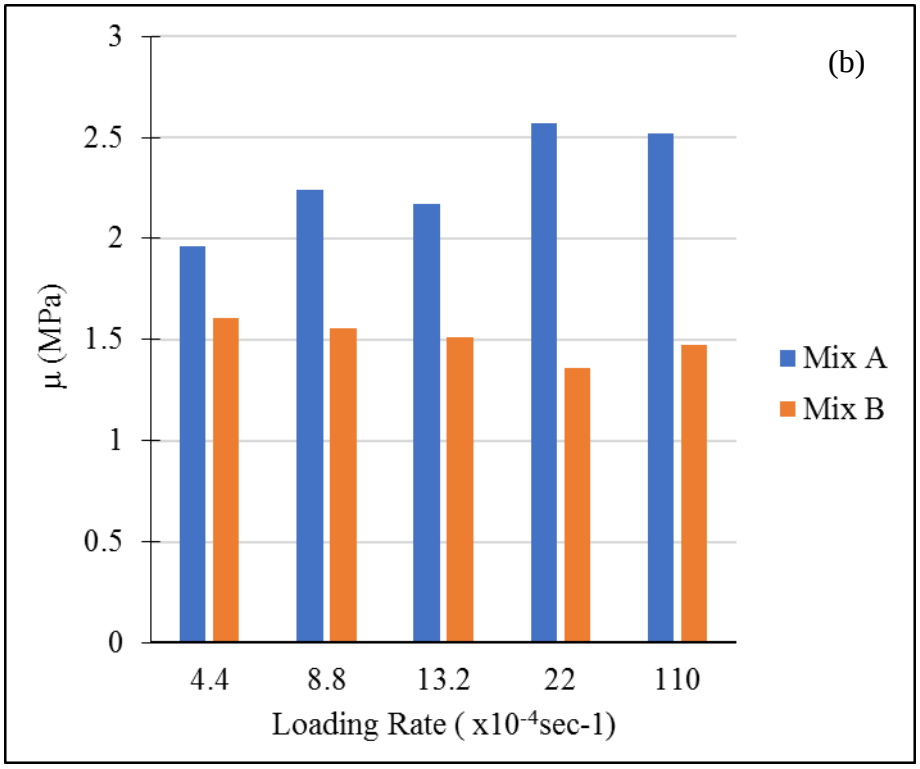

Figure II.4.4: Ogden Model parameters for Mix A and Mix B.

II.4.2. Improved test set-up and test protocol

During the initial stage of this study a few practical issues regarding the test protocol were discovered. The confinement tube was insufficiently long to encase the inflated specimen completely. After a certain length of the rubber envelope had been inflated and axially stretched, it started extruding from the open end of the confinement tube. The syringe used for fluid injection had a very small capacity (*5ml*) compared to the amount of fluid required to be injected until complete interface fracture (*10-15ml*). This meant frequent refilling of the syringe during the entire test. As the syringe is being refilled, the inflated rubber starts to relax, and the fluid pressure decreases. This is not an ideal situation and it creates discrepancies between the theoretical assumptions and the test conditions. Replacing the current syringe with a large capacity syringe is important but it meant using a syringe with a bigger diameter. This creates a reaction plunger force of up to *3kN* on the syringe pump that can only handle a maximum force of *800N*. Therefore, the whole test bench was adapted to be used on a tensile test machine. A new specimen fixture was designed with a *300mm* long confinement tube (see *Figure II.4.5*). The PMMA confinement tube, initially used, underwent immense radial loads and deformed at certain locations after several tests were performed. It was therefore replaced with a clear glass tube of *10mm* inner diameter. The glass tube can carry heavy internal pressures and it is scratch resistant. This is essential for the image processing technique that is described in following sections. The improved test setup is shown in *Figure II.4.6*.

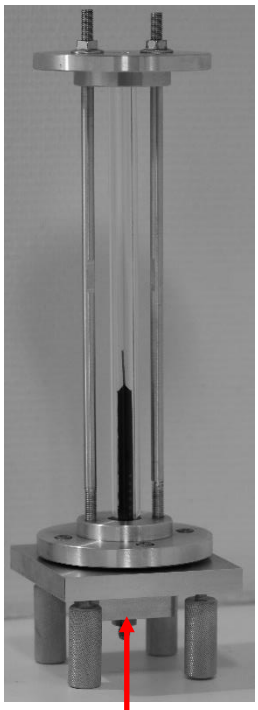

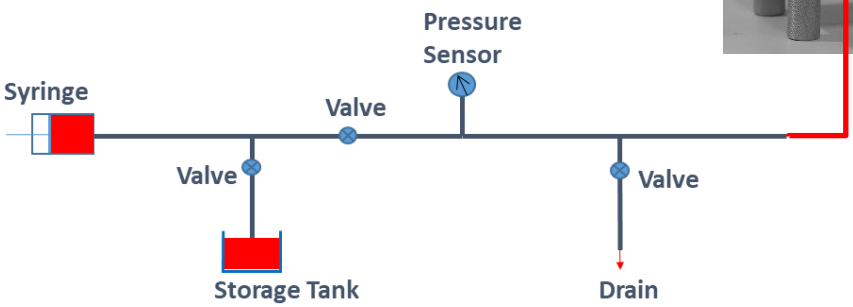

Figure II.4.5: Hydraulic Circuit for RCAIT and the newly designed specimen fixture with glass confinement tube.

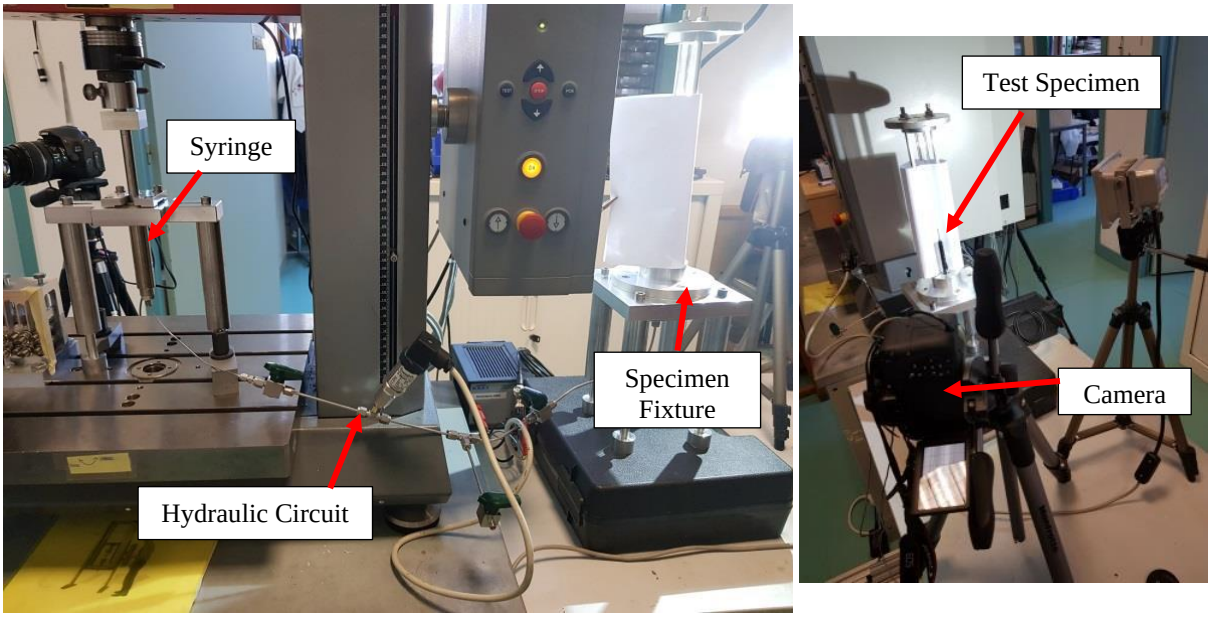

Figure II.4.6: Improved RCAIT setup

In the new test setup, the specimen side fixture is connected to a *20 ml Swagelok®* stainless steel high-pressure syringe using hydraulic tubes, valves and connectors as shown in *Figure II.4.5*. The syringe is filled with the pressurizing fluid *i.e.* demineralised water. A *250bar* pressure sensor (*Swagelok® Model S-Transducer*) is used to measure the injection pressure during the test. The piston of the syringe is attached to the load cell of a *Zwick/Roell® Z010* tensile testing machine. The experiments are performed under constant displacement rate of the syringe piston (or constant volume injection rate). To ease the sliding of the rubber inside the confinement tube during inflation, lubricating oil is applied in the tube prior to the experiment. The fluid pressure, force and piston displacement are recorded during the experiment with the tensile testing machine control and in-built software. A *CANON® EOS 800D* camera is used to capture images of the specimen during the experiment. During the test, image capture and pressure measurement is done simultaneously at a chosen rate by the tensile testing machine. This ensures that each data point (time, pressure, force and piston displacement) corresponds to a unique image in the camera. Multiple white spots are drawn on the exterior surface of the specimen along the longitudinal direction whose positions during the experiment are monitored using a particle tracking script coded with *ImageJ©* freeware (see *Figure II.4.7*). The particle tracking assists in calculating rubber elongation (axial stretch ratio) and monitoring the crack propagation.

Before starting the test, the fluid is injected at a slow rate (*~0.1ml/min*) up to a low pressure (*~2-3bar*). The drain valve is then opened to remove air trapped in the circuit, allowing the pressure to drop to zero again. The desired volume injection rate (*ml/min*) is converted into

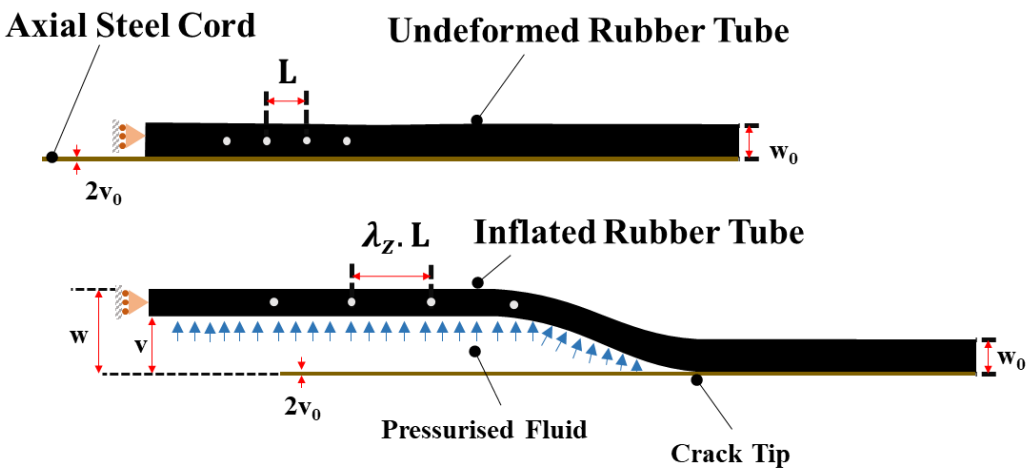

Figure II.4.7: Marker monitoring technique used for axial stretch ratio measurement during specimen inflation.

piston displacement rate (*mm/min*) and entered into the machine software. Image acquisition rate and data storage rate are also fed to the software. Prior to the start of the test, calibration of injected volume *vs* machine crosshead displacement is performed by injecting the fluid while the specimen side valve is kept closed. It was observed that the pressure increased up to *100 bar* very quickly (negligible injected volume). This confirms that the overall system stiffness is sufficiently large not to influence the RCAIT results. As a result, the crosshead displacement is a reliable measurement to evaluate injected volume.

Figure II.4.8 shows the evolution of fluid pressure during inflation of the rubber tube and subsequent crack propagation as a function of injected volume, calculated using the crosshead displacement of the machine. Similar to the results shown in §*II.1.2*, first UIS and then CIS are observed. Once a critical pressure is reached, fracture initiates and propagates along the rubber - cord interface. During the crack propagation stage, self-similar and stable crack propagation associated to a constant pressure is observed. Finally, unstable, catastrophic failure is observed when the crack tip approaches the end of the specimen (the conical part at the right end of the specimen in *Figure II.1.2 (a)*).

The results are following the same trend seen earlier in *Figure II.1.6 (a)*. The specimen in *Figure II.4.8* is *Mix A* rubber bonded to a brass coated steel cord. The fluid is injected at a rate of *1ml/mm*. The crack propagated at a mean pressure of *90.5 bar*. It is important to note that the injection pressure is not controlled, instead the rate of injection (volume) is controlled and pressure is recorded.

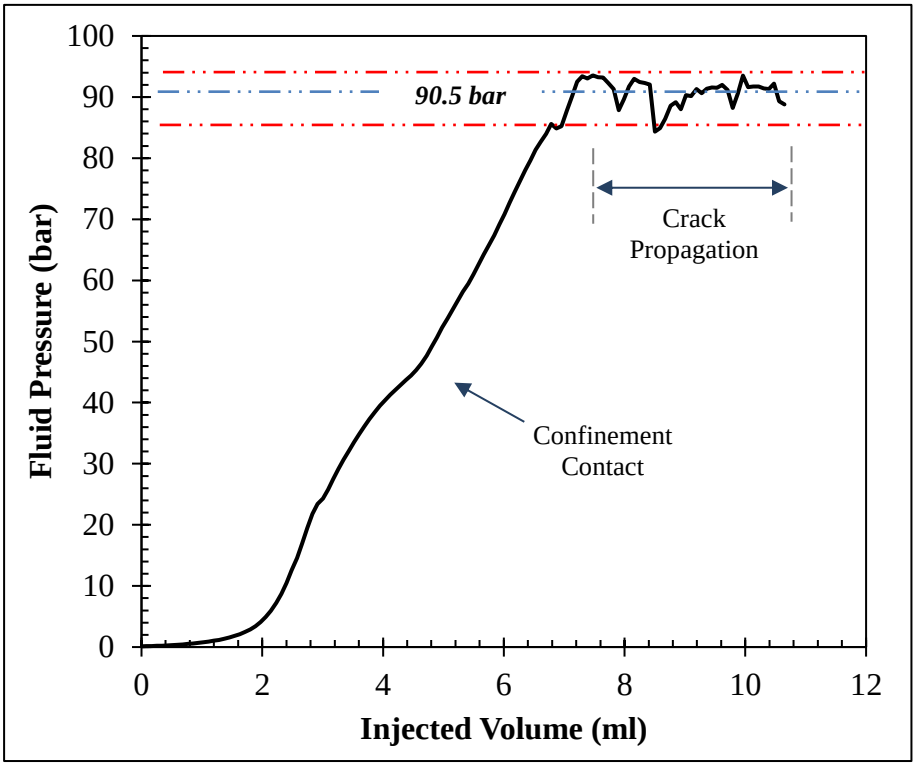

Figure II.4.8: RCAIT of Mix A-brass coated cord. Average crack propagation pressure is 90.5 bar.

II.4.3. Crack propagation and SERR

To evaluate the fracture energy of the interface (or critical SERR), a simple energy balance analysis is used as described previously. Using the standard definition of SERR, fracture energy can be calculated from the experimental data. If the energy balance is carried out for a small length of crack propagation, then the fracture energy is simply the energy released per unit area of the propagated crack. The released energy can be calculated using the work done on the pressurised fluid and integration of the strain density function of the rubber. To do so, the experimental data can be directly used.

The quantities measured during the test or calculated from the test data are fluid pressure, injected fluid volume, elapsed time and axial extension of the tube (or axial stretch ratio). From a practical perspective, measurement of fluid pressure is straightforward. It is done by simply recording the voltage output from the pressure sensor. The injected volume and elapsed time during the test are also readily found.

However, monitoring crack propagation is difficult since the interface separation front is hidden due to the axisymmetric nature and opacity of the specimen (see *Figure II.4.7*). Crack propagation is therefore monitored by constructing a simple model of the specimen

deformation. It is assumed that the extent of the process zone around the crack tip is negligible. For the test case shown in *Figure II.4.8* the displacement of the tip of the specimen (un-inflated end) is equal to:

$$d \approx (\lambda_z - 1)a$$

where d is the displacement of the specimen tip (or the topmost marker in *Figure II.4.9*), λ_z is the axial stretch ratio of the inflated part of the specimen and a is the crack propagation length (excluding the initial debonded length of *50mm*). The displacement d is measured as soon as the crack has reached the first marker in the adhering region. Therefore, the crack propagation length is zero in the inflation regime (up to ca. *7ml*) of *Figure II.4.10*.

Considering purely hyperelastic behaviour of the rubber envelope and constant pressure self-similar crack propagation, two regimes can be considered. During the inflation regimes (both UIS and CIS), crack length a remains constant (zero) and λ_z can be evaluated from the specimen end displacement (see *Figure II.4.7*). During the crack propagation regime, since the inflation pressure remains constant (theoretically), so does λ_z, therefore the crack propagation increment, Δa, is determined from the relation:

$$\Delta a = \frac{\Delta d}{\lambda_z - 1}$$

To ensure reliable measurement of λ_z, marks are also drawn on the pre-cracked part of the specimen so that λ_z is measured during the specimen inflation regime. This measurement is likely to be unaffected by the process zone development near the crack tip region

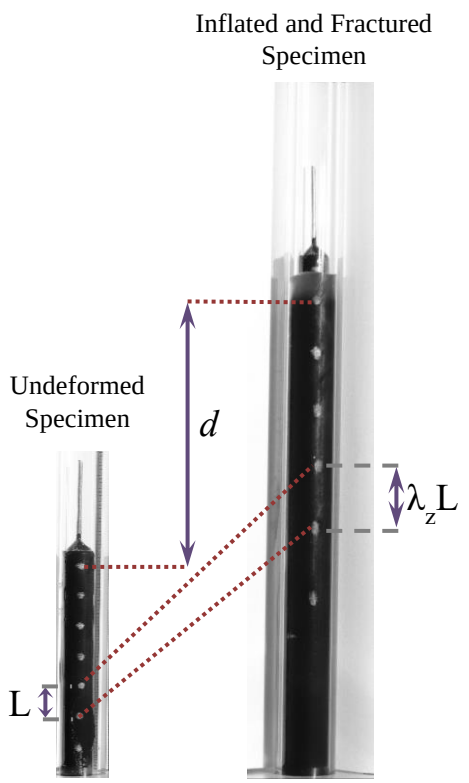

Figure II.4.9: Calculating axial stretch ratio (λ_z) and specimen tip displacement (d) using a particle tracking algorithm.

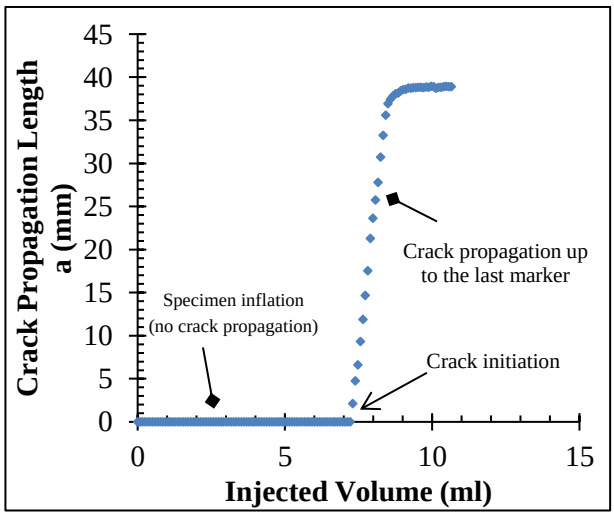

Figure II.4.10: Crack propagation monitoring until it reaches the last marker.

(*Figure II.4.9*). It is important to note that the exact time of the crack initiation is not necessary in this analysis as the propagation is self-similar. The key factor is the increment of crack propagation distance Δa between two points in time. These time points can be arbitrarily chosen during the crack propagation regime.

Using the crack propagation length calculated with this method, critical SERR can be calculated from the experimental results following the definition of energy release rate. The fluid pressure energy, ΔE, supplied for an arbitrary length of crack propagation, Δa, is

$$\Delta E = P\Delta V$$

where P is the average crack propagation pressure and ΔV is the fluid volume injected during propagation of Δa. This energy is partly stored in the inflated rubber (ΔE_r) and partly released during creation of the fracture surface $2\pi v_0 \Delta a$, where v_0, is the initial inner rubber envelope radius. Critical SERR is therefore:

$$G_c = \frac{P\Delta V - \Delta E_r}{2\pi v_0 \Delta a}$$

It is assumed here, that the fluid does not store any significant amount of energy in the form of fluid compressibility. This is pertaining to the fact that the share of energy stored in the fluid compressibility is less than *1%* even at pressures up to *100bar*.

For a hyperelastic rubber with strain energy density W, ΔE_r is defined as:

$$\Delta E_r = \lambda_z \Delta a \int_v^R 2\pi r W dr$$

where v is the deformed inner radius of the rubber tube and R is the confinement tube inner radius. Using the marker tracking technique described here (*Figure II.4.7*, *Figure II.4.9*) λ_z is calculated for the test case shown in *Figure II.4.8*. For the *Mix A*-brass specimen with the Ogden model, using the material properties described in §*II.4.1*, ΔE_r is calculated to be *17.8J*. Therefore, the critical SERR for the *Mix A*-brass specimen is $80.2 kJm^{-2}$ for a fluid injection speed of *1ml/min*.

It might appear from this result that developing the theoretical model is not necessary. The critical SERR is evaluated by using the experimental data only. However, one important reason for developing the theoretical model is to eliminate the sensitivity of the image processing associated with various experimental conditions, such as the effect of lighting, that of glare from the confinement tube and various others. These factors affect the accuracy of image processing as well as the time required to perform it and are difficult to control and/or

eliminate. They also affect the value of critical SERR calculated above. However, the critical SERR and crack propagation length calculated with image processing provide a basis for comparison.

II.4.4. Thick rubber tube inflation model: Ogden rubber

In §*II.2* a Mooney-Rivlin rubber model was used. However, in the present work the Ogden model is used since it reproduces the results from the uniaxial tensile tests more accurately. The constitutive equations of the *Thick Rubber Tube Inflation Model* and the solution method are derived below. A few steps in the derivation are similar to the ones described in §*II.2*. However, they are included here again for clarity and continuity of the derivation.

Constitutive Equations:

Consider a thick, hollow, elastomeric tube with inner and outer radii of v_0 and w_0 respectively as shown in *Figure II.4.11*.

In the deformed configuration, the radii become v and w. Due to the axisymmetric configuration, the radial and circumferential stretch ratios are given by:

$$\lambda_r = \frac{dr}{dr_0} \qquad \lambda_\theta = \frac{r}{r_0} \qquad (II.4.1)$$

with r_0 and r being the radial position in the initial state and deformed state respectively. Taking into account the incompressible nature of the material with the relation $\lambda_r \lambda_\theta \lambda_z = 1$ and assuming a constant axial stretch λ_z throughout the thickness, the general expressions for

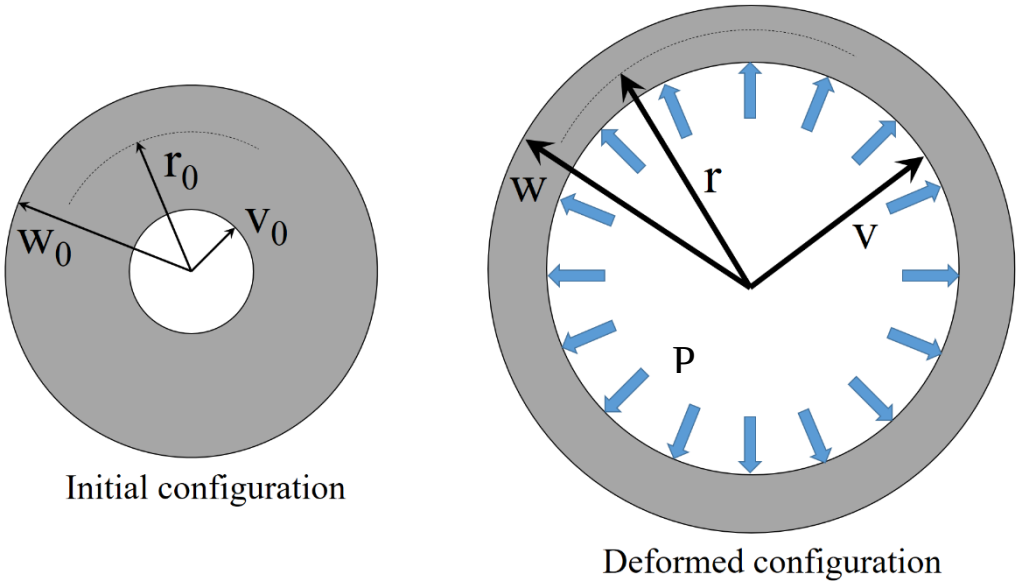

Figure II.4.11: Rubber tube deformation stages. P is the fluid pressure.

radial and circumferential stretch ratio are [69]:

$$\lambda_r{}^2 = \lambda_z{}^{-1}\left[1 - \frac{1}{cr^2}\right] \qquad \lambda_\theta{}^2 = \lambda_z{}^{-1}\left[\frac{cr^2}{cr^2 - 1}\right] \qquad \textit{(II.4.2)}$$

with c being an integration constant to be determined from boundary conditions together with axial stretch ratio, λ_z. The following relations give three-dimensional Cauchy stresses for an Ogden rubber:

$$\sigma_z = p + \mu\lambda_z^\alpha \qquad \textit{(II.4.3)}$$

$$\sigma_r = p + \mu\lambda_r^\alpha \qquad \textit{(II.4.4)}$$

$$\sigma_\theta = p + \mu\lambda_\theta^\alpha \qquad \textit{(II.4.5)}$$

where μ and α are the Ogden rubber coefficients (*Figure II.4.4*) and p is the hydrostatic pressure due to incompressibility (not to be confused with fluid pressure P). The equilibrium equation for an axisymmetric loading is

$$\frac{d\sigma_r}{dr} + \frac{\sigma_r - \sigma_\theta}{r} = 0 \qquad \textit{(II.4.6)}$$

Then, substituting *(II.4.3)-(II.4.5)* into *(II.4.6)* we get

$$\frac{dp}{dr} = -\mu\left[\frac{\lambda_r^\alpha - \lambda_\theta^\alpha}{r} + \alpha\lambda_r^{\alpha-1}\frac{d\lambda_r}{dr}\right] \qquad \textit{(II.4.7)}$$

Boundary Conditions:

During the Unconfined Inflation Stage (UIS), the rubber tube expands freely both radially and axially. Since the specimen is closed at both ends (fixed at one end and adhering to the cord at the other), an axial force is also exerted on the envelope by the internal pressure leading to the three boundary conditions as seen previously:

$$\sigma_{r\ |(r=v)} = -P \qquad \textit{(II.4.8)}$$

$$\sigma_{r\ |(r=w)} = 0 \qquad (II.4.9)$$

$$\int_{v}^{w} \sigma_z(r) 2\pi r dr = P\pi v^2 \qquad (II.4.10)$$

P is the pressure imparted by the injected fluid. A detailed explanation of these boundary conditions has already been given previously in §*II.2.2*.

Using equations *(II.4.4*) and *(II.4.8)* the hydrostatic pressure *p* can be calculated at the inner radius *v* of the inflated rubber tube. Similarly, *p* can be calculated at the outer radius *w* using *(II.4.4*) and *(II.4.9)* for UIS.

$$p_{|(r=v)} = p_v = -P - \mu \left[\frac{cv^2 - 1}{\lambda_z c v^2}\right]^{\frac{\alpha}{2}} \qquad (II.4.11)$$

$$p_{|(r=w)} = p_w = -\mu \left[\frac{cw^2 - 1}{\lambda_z c w^2}\right]^{\frac{\alpha}{2}} \qquad (II.4.12)$$

For CIS, the boundary condition *(II.4.9)* is changed to

$$w = R \qquad (II.4.13)$$

with *R* being the inner radius of the confinement tube. The equation *(II.4.13*) can be used to write *c* in terms of λ_z (see *Equation (25)* in [69] for intermediate steps) as

$$c = \frac{\lambda_z}{\lambda_z R^2 - {w_0}^2} \qquad (II.4.14)$$

The inflation behaviour of the rubber tube can be described for an Ogden rubber by solving *(II.4.8)-(II.4.10)* for UIS and *(II.4.8)*, *(II.4.10)* and *(II.4.14)* for CIS. By solving the equations to get λ_z, rubber tube deformation and Cauchy stresses can be calculated. It will be used further to calculate the energy stored in the inflated rubber.

Solving for λ_z:

While an analytical solution was found for the UIS and CIS configuration for a Mooney-Rivlin rubber previously, a numerical resolution technique is preferred here for the sake of simplicity and also to make the procedure adaptable to other types of rubber models. A step-by-step numerical solution is found, by considering an incremental increase of the internal

radius and determining the hydrostatic pressure *p(r)*, so that boundary conditions *(II.4.8)*, *(II.4.10)* and *(II.4.9)* or *(II.4.14)* are satisfied. The numerical procedure is summarized in *Figure II.4.12*. The same procedure can be followed for any rubber model if the equations for three-dimensional Cauchy stresses *(II.4.3)-(II.4.5)* are known.

The reason for choosing the deformed inner radius *v* as the driving parameter for the algorithm can be deduced from *Figure II.4.13*. The easiest parameter to measure during the experiment is the fluid pressure. Therefore, it is logical to keep *P* as the driving parameter in the algorithm. However, it is possible that the rubber tube inflation will become unstable due to either a large confinement radius or absence of a confinement tube. In certain cases, this may result in decreasing fluid pressure [71] or nearly constant fluid pressure, as seen in

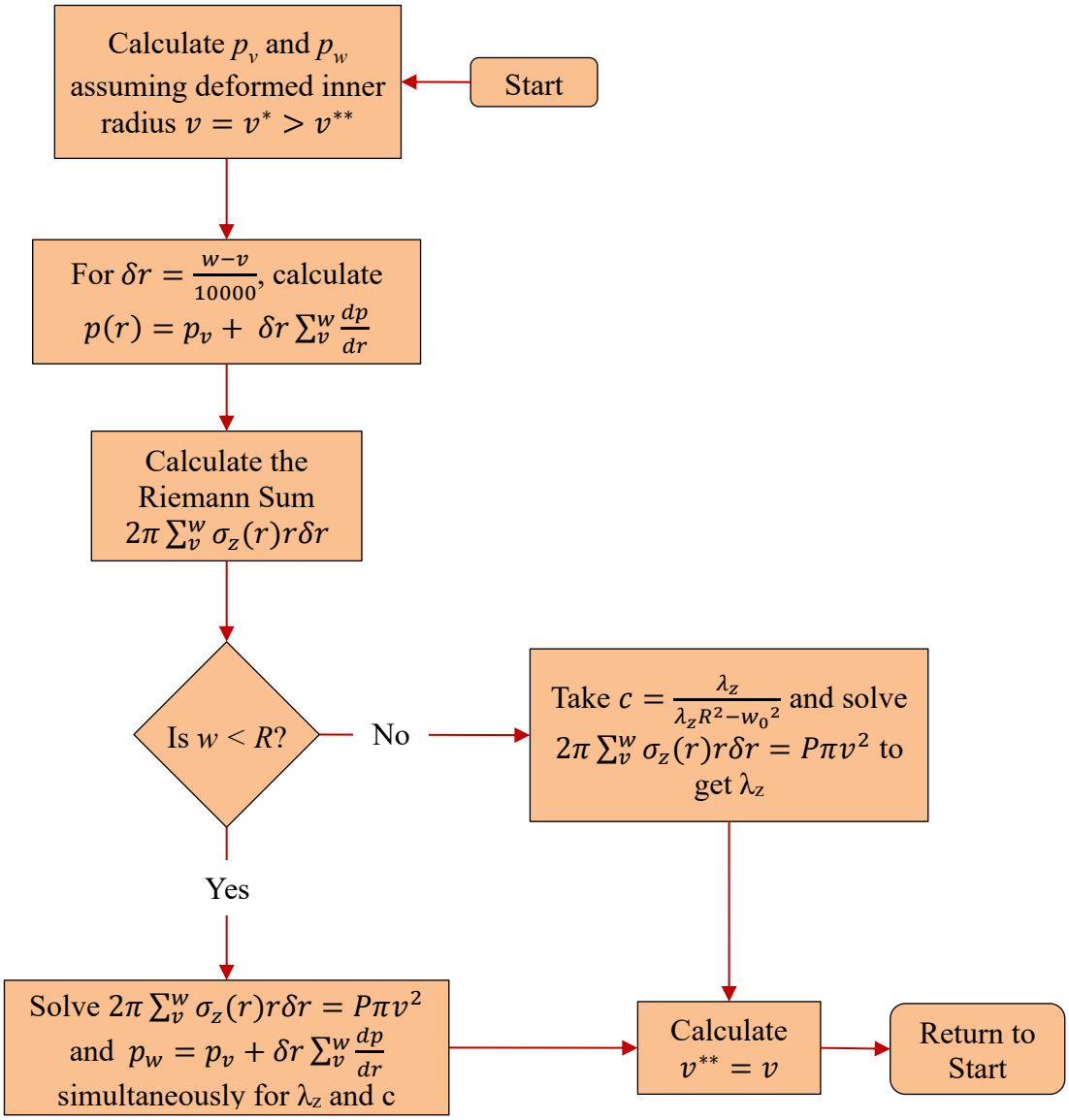

Figure II.4.12: Algorithm to solve the Thick Rubber Tube Inflation problem for Ogden Model.

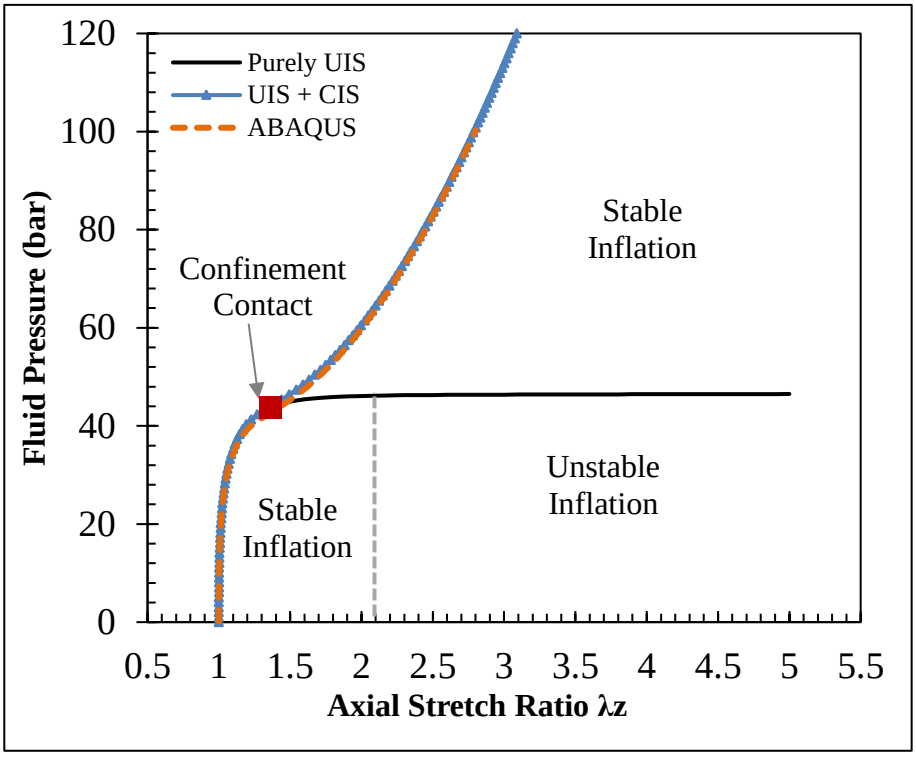

Figure II.4.13: Stable Inflation of an Ogden Rubber tube in the presence of a confinement. Theoretical and FE model follow very precisely the same curve.

Figure II.4.13. This phenomenon is already described in §*II.2.2*. In such a case, keeping *P* as the driving parameter will lead to erroneous results. Similarly, in certain cases it is possible that the axial stretch ratio of the rubber tube, λ_z, will initially decrease below unity, *i.e.*, retraction occurs. This depends on the properties of the rubber (or the model). However, the inner radius *v* is the only parameter that consistently and monotonically increases during inflation.

In a purely UIS regime for *Mix B* (see *Figure II.4.13*), the rubber tube will undergo unstable inflation giving rise to aneurysms. After the point $P \sim 46bar$ ($\lambda_z \sim 2.1$), the gradient of the curve stays very close to zero. This phenomenon has already been discussed in §*II.2*. However, by choosing a tight confinement tube, *i.e.* smaller radius, *R*, higher pressures can be attained whilst maintaining stable inflation. Such a situation is shown by the blue line in *Figure II.4.13*. The confinement contact occurs well before the instability point and inflation stays in a stable region even for a very large axial stretch ratio.

Thick rubber tube inflation can also be modelled in ABAQUS using the same Ogden parameters and specimen dimensions (see *Figure II.4.13)*. It can be seen that the theoretical model and FE model follow the same curve very precisely. However, the theoretical model provides greater flexibility over the FE model when it comes to changing the inflation

parameters such as material properties, specimen dimensions or fluid pressure. Moreover, the theoretical model can be extended to compute SERR for a given fluid pressure in just a few lines of code. Another advantage of the theoretical model over the FE model is the time required for convergence. Where the theoretical model can compute the curve shown in *Figure II.4.13* in a matter of a few minutes, with the FE model it takes nearly one hour.

II.4.5. SERR: Global energy balance

In §*II.3.1*, equation *(II.3.11)* was calculated for Mooney-Rivlin rubber. The general procedure followed is similar for any type of elastomeric material. By performing an energy balance of the system, the SERR can be calculated as following:

$$W = \Delta U_e^{fluid} + \Delta U_e^{rubber} + D \qquad (II.4.15)$$

with W being the energy supplied to the system by the pressurised fluid. ΔU_e^{fluid} is the energy stored due to fluid compressibility. Both quantities can be calculated in exactly the same way as described in §*II.3.1*. ΔU_e^{rubber} is the energy stored in the deformed, inflated rubber and D is the energy released during crack propagation. In this work, the SERR equation is derived for an Ogden rubber with two coefficients (μ and α). The strain energy density function for an Ogden rubber (W_e) can be written as:

$$W_e = \frac{\mu}{\alpha}({\lambda_z}^{\alpha} + {\lambda_r}^{\alpha} + {\lambda_\theta}^{\alpha} - 3) \qquad (II.4.16)$$

Therefore, the energy stored in the crack length, δa, of the rubber can be written as:

$$\Delta U_e^{rubber} = \lambda_z \delta a \int_v^w 2\pi r \delta w_e dr \qquad (II.4.17)$$

Using the *Thick Rubber Tube Inflation Model* described earlier, λ_z, c, v and w can be calculated for the crack propagation pressure observed during the RCAIT. The integration can then be solved numerically by converting it into a Riemann Sum.

For an infinitesimal crack length, δa, the energy released during fracture is:

$$D = G.2\pi v_0 \delta a \qquad (II.4.18)$$

Therefore, the SERR can be calculated from equations *(II.4.15)*, *(II.4.17)* and *(II.4.18)* as:

$$G = \frac{\lambda_z P(v^2 - v_0^2)}{2v_0} - \frac{P^2 \lambda_z (v^2 - v_0^2)}{2\chi v_0} - \frac{\lambda_z}{2\pi v_0}\left[\int_v^w 2\pi r \delta w_e dr\right] \qquad (II.4.19)$$

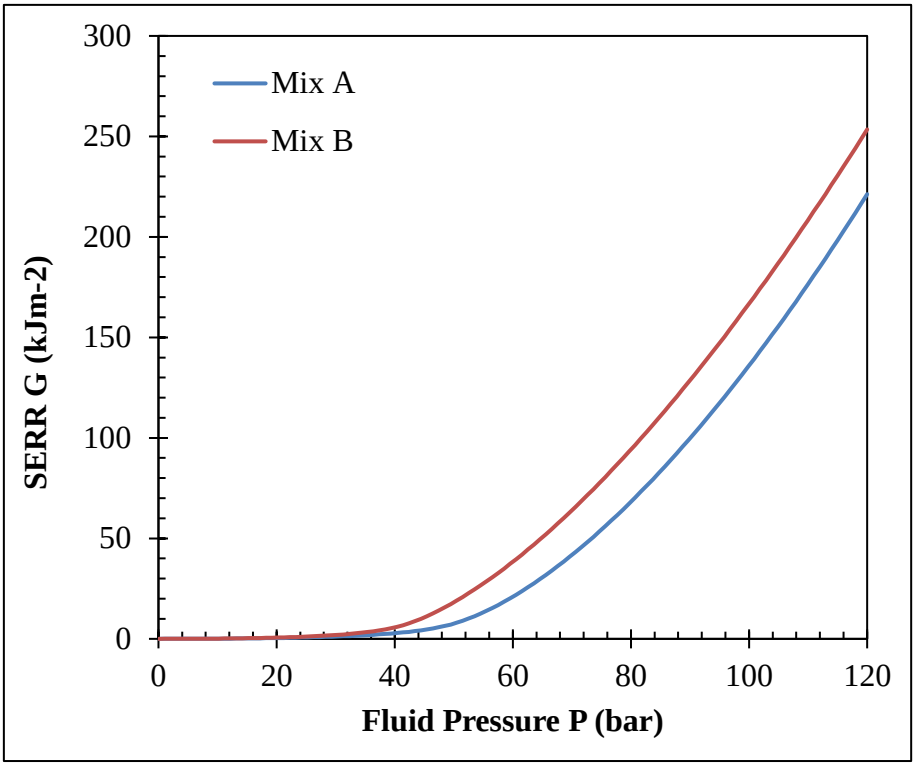

Figure II.4.14: G vs P for rubber Mix A and Mix B. α and μ are taken as average values from the tensile tests.

Using the *Thick Rubber Tube Inflation Model* described earlier (*Figure II.4.12*), λ_z can be calculated for a given value of *P*. *G* is therefore a function of fluid pressure (*P*), rubber material coefficients (μ and α) and specimen dimensions. The fracture propagates when $G=G_c$. *G* is independent of the initial crack length, which is consistent with the self-similar nature of the crack propagation and constant pressure measured during the test.

Figure II.4.14 shows *G* vs fluid pressure *P* for both *Mix A* and *Mix B*. The Ogden parameters are calculated as average values from the tensile tests at five loading rates (see §*II.4.1*). For pressures of up to *30bar*, *G* is nearly the same for both rubber mixes. Material nonlinearity as well as large deformation during inflation result in nonlinear behaviour of *G*. For the case shown in *Figure II.4.8*, the crack propagated at an average pressure of *90.5 bar*. The critical SERR (G_c) is therefore $100.6\ kJm^{-2}$.

Comparing *Figure II.4.14* in this section to the *SERR vs* P_i curve in *Figure II.3.2*, it is clear that calculation of *G* is sensitive to the quality of fit of the rubber model. In §*II.3.1* for rubber *Mix B* bonded to brass coated steel, the crack propagation pressure was recorded as *66.6bar* and, using a Mooney-Rivlin model, G_c was found to be $15.6\ kJm^{-2}$. However, fitting an Ogden model to the same rubber mix results in a G_c value of $54.7\ kJm^{-2}$. Since a significant amount of the work provided by the fluid injection is transferred to the rubber, it is important to

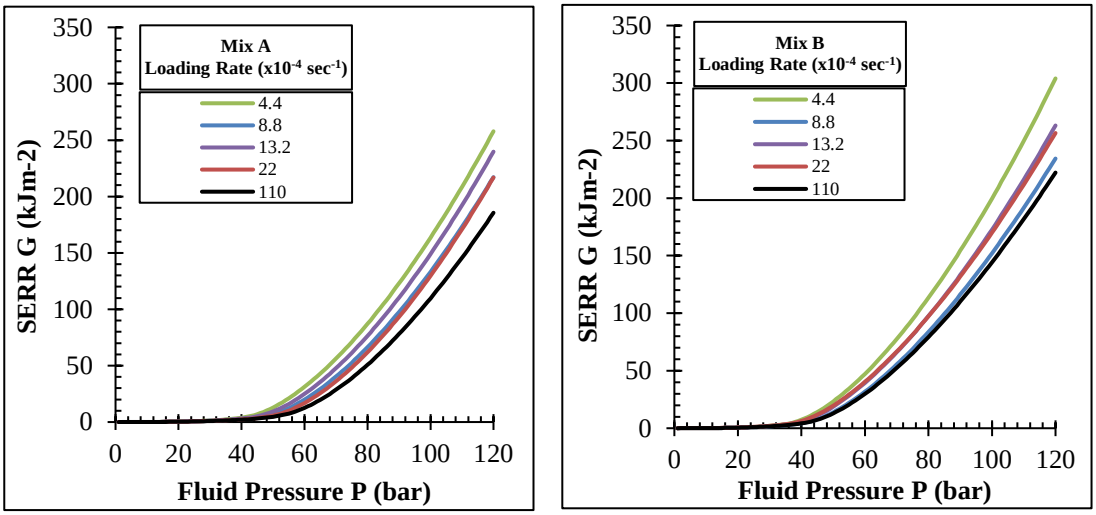

Figure II.4.15: Effect of rubber properties (loading rate) on G.

identify its mechanical behaviour properly to achieve a reliable evaluation of G_c. In addition, the stresses and strains occuring near the crack tip will also be predicted accurately. This will pave the way to investigate the fracture from a theoretical and numerical perspective.

The effect of the strain rate on the calculation of G is clear from *Figure II.4.15*. As in the tensile test results shown in *Figure II.4.2*, there is considerable spread in the curves, especially at higher crack propagation pressures. This result can be further investigated by performing the RCAIT at various loading rates.

For a large crack propagation pressure, the energy stored in the rubber is higher and so is the energy stored in the fluid. Therefore, by neglecting the energy stored in the fluid compressibility in *(II.4.19)*, G is the output of a competition between the energy stored in the rubber and that stored in the fluid.

II.5. Rubber Cord Adhesion Performance Characterization

With the improvements to the test protocol and theoretical model presented in the previous section, it is now important to focus on performance of the rubber-steel cord adhesion under various experimental conditions. To investigate the effect of various experimental parameters such as volume injection rate, crack propagation rate and strain rate on rubber inflation behaviour, *20* tests were carried out. The test campaign included two rubber types, *Mix A* and *Mix B*, two cord coatings, brass and bronze, and five volume injection rates – *0.1ml/min* to *5ml/min*. The results are presented as follows.

II.5.1. Test results

The pressure-volume evolution for *Mix A* is represented in *Figure II.5.1* for bronze and brass coated steel. *Figure II.5.2* shows similar plots for *Mix B*. The effect of volume injection rate or loading rate can be seen clearly in the figures. Higher loading rates (or injection rates) cause greater energy dissipation in the rubber and particularly near the crack tip, allowing the pressure to mount higher before the onset of crack propagation. Fluid penetration at the

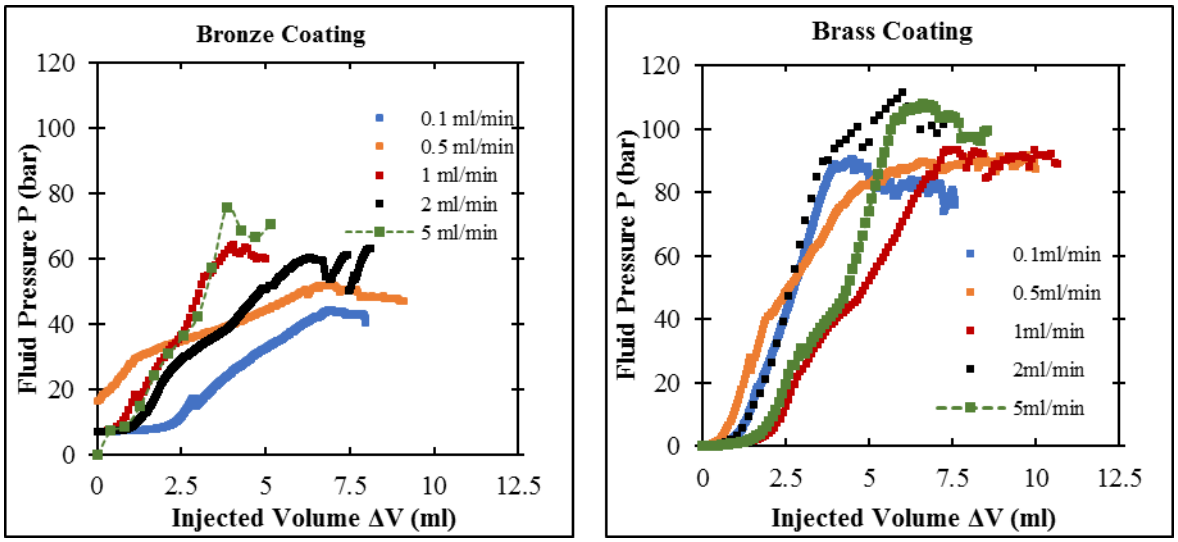

Figure II.5.1: RCAIT results for rubber Mix A at five different loading rates.

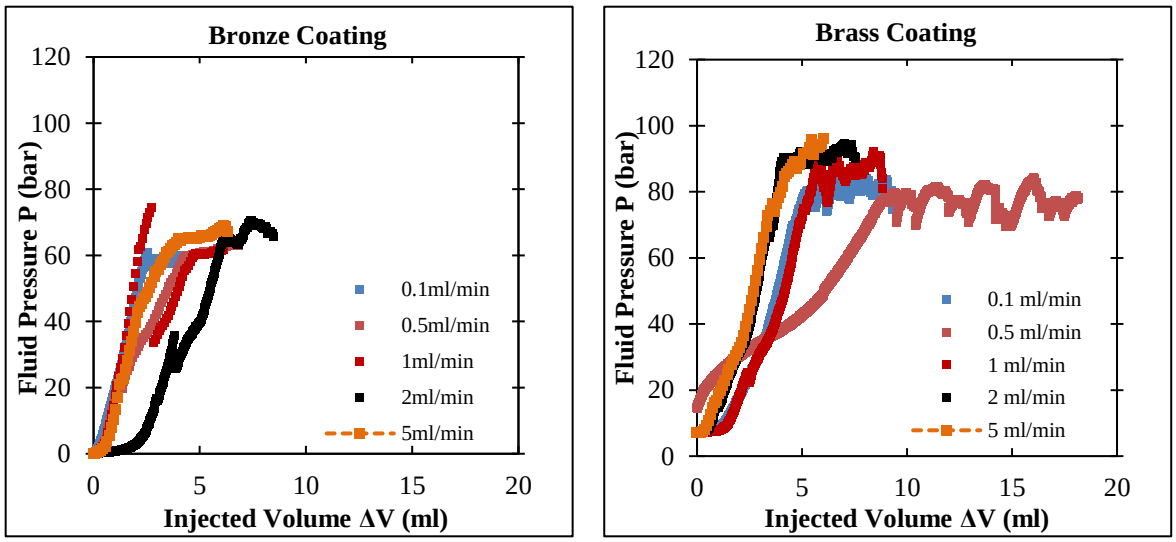

Figure II.5.2: RCAIT results for rubber Mix B at five different loading rates.

interface can be seen in the form of fluctuations in the crack propagation pressure.

Overall, for both *Mix A* and *Mix B*, specimens with brass coated cords show higher crack propagation pressure than specimens with bronze coated cords. This difference in pressure

levels is much greater for *Mix A* specimens than *Mix B*. For any given rubber mix, the fluid volume injected during the test is slightly larger for bronze coated cords than for brass coated cords.

II.5.2. Post-processing

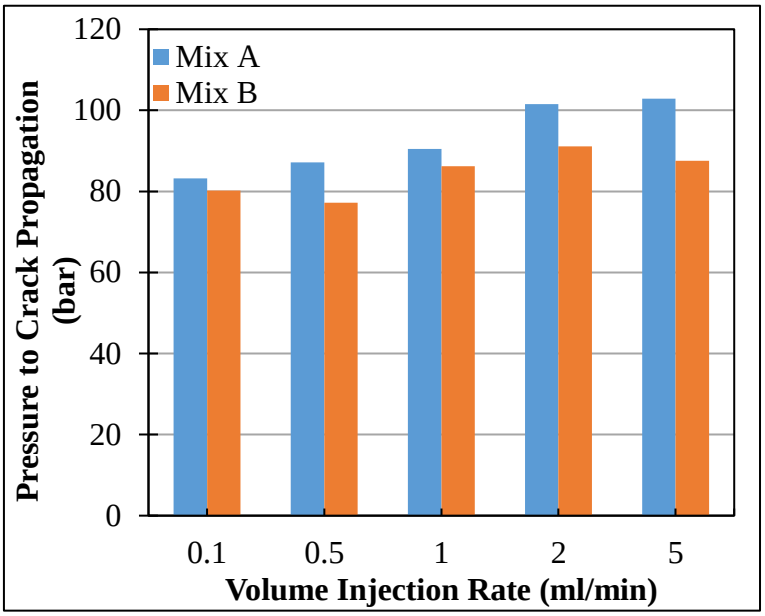

Figure II.5.3: Crack propagation pressure for Mix A and Mix B bonded to brass coated steel cord.

Only the specimens with brass-coated cords are considered for post-processing. Bronze coated cords were used for demonstration purpose only.

A small variation in the crack propagation pressure can be observed in *Figure II.5.3* for both rubber mixes. For rubber *Mix B* the pressure varies within a narrower gap than Mix A. This variation could be a mixture of dissipation at the interface as well as in the rubber. However, the dissipation in the rubber is assumed to be minor and virtually constant, based on the tensile test results. The inflation tests show similar trends to the tensile tests for both types of rubber. The rate effect is significantly smaller for *Mix B*. To separate the effects of the rubber from those of the interface, one should investigate the effect of volume injection rate on the crack propagation rate (V_p). The crack propagation process is a self-similar process. Therefore, the behaviour of rubber during crack propagation can be assumed as repetitive. The different phenomena observed can therefore be a result of fluid-interface interaction.

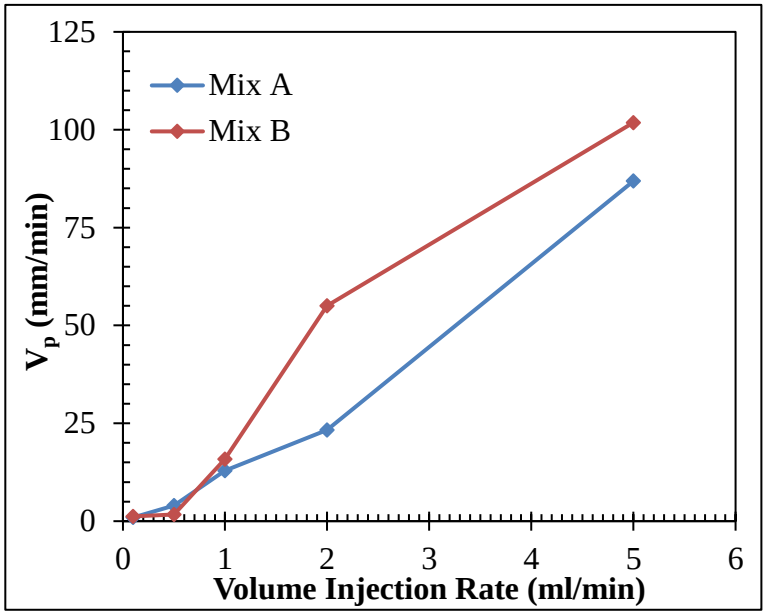

Figure II.5.4: Crack propagation rate V_p for Mix A and Mix B bonded to brass-coated steel cord.

For self-similar crack propagation, calculating the rate of crack propagation is straightforward. In *Figure II.4.8* the time required to propagate a crack of *50mm* was *3.86min*, giving an average crack growth rate of V_p*=12.95 mm/min.*

The same procedure is followed for all the tests to calculate V_p. The trend visible in *Figure II.5.4* clearly indicates the effect of volume injection rate (or in other words, fluid penetration rate). Here, an almost linear trend is observed between fluid injection and crack propagation rate. Due to the incompressible nature of the fluid (water) and a high stiffness of the test

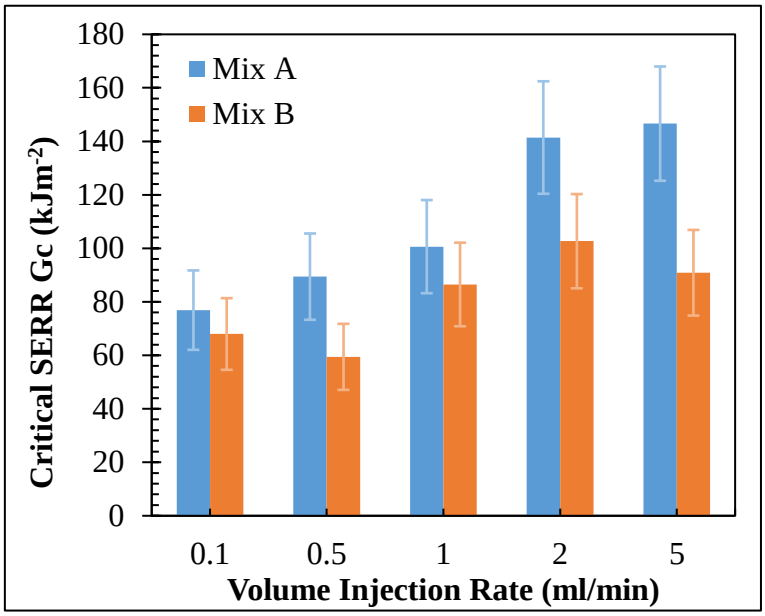

Figure II.5.5: G_c for 5 loading rates. The specimens consisted Mix A and Mix B bonded to brass coated cord.

G_c (kJm^{-2})	Experiment	Theory
	80.2	100.6

Table II.5.1: Comparison of G_c calculated using experimental data and theoretical model.

equipment, for a given system (rubber mix + cord coating type) and critical pressure value, the crack propagation rate is essentially controlled by the injection rate.

Mix B-brass coated cord specimens show higher crack propagation rates than *Mix A*-brass coated cord specimens (*Figure II.5.4*), which is reflected in *Figure II.5.5* as lower G_c values. The error bars in *Figure II.5.5* correspond to the standard deviation of G values based on the material parameters for five strain rates (*Figure II.4.15*).

Higher crack propagation rate is followed by greater fluid penetration. For rubber *Mix A*, the value of G_c doubles between the two extreme volume injection rates. There is a steady rise in the G_c values for *Mix A* specimens. This rise seems contradictory to the rise in V_p seen in *Figure II.5.4*. Fluid penetration is greater for large injection rates but G_c is higher as well. This suggests that the viscous dissipation at the interface is at play for higher injection rates. In the case of *Mix B* rubber, this effect is much weaker. In addition, if the error bars are considered, the effect of fluid injection rate on G_c for *Mix B* rubber specimens is even smaller.

For the rubber *Mix A*-brass cord specimen loaded at *1ml/min* volume injection rate, G_c was calculated as $80.2kJm^{-2}$. For the same case, the *Thick Rubber Tube Inflation Model* predicts $G_c = 100.6kJm^{-2}$ (see *Table II.5.1*). The agreement is good, but the difference could be attributable to the variability of G_c related to the quality of fit to the rubber model. It is also important to note that the value calculated using a more general definition of critical SERR ($80.2kJm^{-2}$) does not consider various macro/microscopic phenomena such as dissipation in rubber, dissipation due to process zone, fluid-rubber interaction (e.g. swelling), etc. On the other hand, the values shown in *Figure II.5.5* are calculated based on average values of Ogden parameters obtained from the uniaxial tensile tests. Therefore, a disagreement between values of G_c calculated using the two methods is understandable.

II.6. Chapter II Summary and Future Steps

One of the most important aims of this research work was to develop a new type of rubber-cord adhesion test that eliminates or minimizes the experimental artefacts associated with the standard tests used widely in the industry. The novel test protocol referred to as *Rubber Cord Adhesion Inflation Test* (RCAIT) was introduced in *Chapter I* with this very aim.

In this chapter the RCAIT protocol was described in detail in §*II.1.1*. Test results were presented for one representative case and a theoretical and numerical analysis of the test was carried out. Based on the key hypothesis of self-similar nature of the crack, the rubber inflation and subsequent interface fracture problem was investigated in §*II.2* and §*II.3*. An analytical relation was developed between the various parameters of the test conditions as well as the specimen rubber and the fracture energy of the rubber-steel interface. A simple FE model was used to validate the analytical results. Following those results many improvements were suggested in the RCAIT protocol in §*II.4*. The *Thick Rubber Tube Inflation Model* first introduced in §*II.2* was extended to Ogden rubber. The test setup was redesigned to eliminate many practical problems encountered during the first stage of the test development.

Finally, in §*II.5* a detailed experimental study was performed to investigate the effect of loading rate on the RCAIT results. Many interesting conclusions were drawn which will lead to further investigation in forthcoming chapters. The RCAIT is now one step closer to providing a reliable evaluation of critical SERR of the rubber-steel interface.

In the forthcoming chapters, further analysis of the test protocol will be presented. The experimental investigation will be taken further along with the theoretical modelling. The intention behind developing such a test is to use it as a supplementary test. Therefore, a repeatability study is also presented to discuss consistency of the RCAIT results and how the test can be used in practice in the industry.

Chapter III: Experimental Study of the RCAIT

III.1. Introduction

In *Chapter II* a global energy balance analysis was proposed for a quantitative evaluation of the fracture energy of the RCAIT. The main difficulty in the analysis concerns the determination of the energy needed to inflate the rubber envelope which was evaluated using a semi-analytical model. In §*II.2*, a Mooney Rivlin rubber behaviour was considered whereas the Ogden model was used in §*II.4*, which results in different evaluation of the critical Strain Energy Release Rate (SERR). *In-situ* rubber characterization and/or model corroboration is therefore required to improve test reliability.

Another important modelling hypothesis concerns the contact condition between the confinement envelope and the rubber, assumed to be frictionless until now. It is known from previous rubber tube expansion analysis that a significant axial force is applied to the envelope due indirectly to the pressure exerted on the inner surface. This results in a longitudinal expansion and sliding of the rubber on the confinement surface. A lubricant is used to reduce the friction between the rubber envelope and the confinement tube, thus friction is assumed to be negligible in the model. The efficiency of lubrication has not yet been quantified. However, dissipation due to friction or adherence may drastically modify the boundary conditions applied to the specimen as well as the critical SERR evaluated.

In this chapter, the effect of lubrication on RCAIT results and its subsequent modification of the evaluated critical SERR are studied. Having chosen a lubricant, the work is then extended to introduce an improved marker tracking technique. This technique is used to monitor the longitudinal extension of the rubber during the inflation and crack propagation regimes, thereby calculating crack propagation speed. Using the theoretical model proposed in §*II.4* and this marker tracking technique, the rubber material parameters are calculated during the inflation regime. This helps to improve the accuracy of the critical SERR evaluation of the rubber-steel adhesion.

Finally, equipped with this new technique, a repeatability study is carried out on two types of rubber-cord composites. Each type of specimen is tested in the same experimental conditions multiple times and the consistency of the results is studied. In this context, the effect of loading rate on the specimen behaviour is studied again.

III.2. Effect of Lubrication

During preliminary tests it was observed that, despite the fluctuation present in the pressure during crack propagation (*~10bar* in *Figure II.4.8*), variability of the axial stretch ratio, λ_z, was very small. This strongly suggests that there is non-negligible friction between the inflated rubber and glass confinement tube. To investigate this, several tests were carried out using commercially available lubricants on rubber *Mix B* and brass coated steel cord specimens. Below is a short summary of the findings.

III.2.1. Choice of lubricant

Various traditional lubricants such as machine oil and grease were initially used in RCAIT. However, the λ_z values recorded were found to be very low, considering the very high pressures recorded during the tests. It was also found that these lubricants penetrated the outer surface of the rubber, as the surface stayed tacky even after a thorough wash with ethanol. Thus, it is suspected that the lubricant might be affecting rubber material properties, at least on the surface (perhaps a new line of research to look into). There is a possibility that the outer surface of the rubber is adhering (though relatively weakly), to the confinement tube thereby affecting the specimen behaviour during the test.

Upon trying several commercially available lubricants, it was found that, for the particular elastomer used in the tests (*Mix B*), silicone greases gave the best lubrication performance without apparent modification of the rubber. The rubber outer surface was found to be completely dry after wiping the lubricants with cotton.

The three lubricants tested were *LOCTITE® LB8021*, *Ambersil® AMS4* and *CRC Silicone Grease*. At a fluid injection rate of *5ml/min*, three identical RCAIT specimens were tested using one lubricant per specimen. The main criterion used to choose the lubricants was the maximum axial stretch ratio (λ_z) of the rubber envelope recorded during the test. As is clear from *Table III.2.1*, *CRC Silicone Grease* showed a slightly higher λ_z value than the other two

Lubricant / Parameter	LOCTITE LB8021	Ambersil AMS4	CRC Silicone Grease
λ_z	1.83	1.89	2.06
$\Delta\dot{a}$ (mm/sec)	1.47	1.19	1.08

Table III.2.1: Comparison of lubricant performance. Larger values of λ_z represent lesser friction.

lubricants.

The effect of lubrication on crack propagation rate, $\Delta\dot{a}$, can also be observed. In *Table III.2.1*, $\Delta\dot{a}$ is calculated for each test using a general definition of crack propagation rate. The total length of the crack (*50mm*) is divided by the time required to propagate the crack to give $\Delta\dot{a}$. In the presence of friction, the axial extension of the specimen is restricted. However, the fluid is injected at a constant rate. The fluid injected must occupy the space generated by either expanding the rubber tube radially and axially or by propagating the crack. Radial expansion will itself result in more axial extension due to the incompressible nature of rubber. However, due to the presence of friction, axial extension is restricted. This results in faster crack propagation to accommodate for the injected fluid. Therefore, it is clear from *Table III.2.1* that *CRC Silicone Grease* is again the best performer out of the three as it allows for the slowest $\Delta\dot{a}$.

Finally, a few practical issues also need to be considered before choosing the lubricant. For example, for the image processing to work efficiently, the lubricant needs to be transparent or at least translucent. For the test case with *LOCTITE® LB8021* lubricant, the markers drawn on the specimen were partially dissolved by the lubricant. This created complications during processing the images as the markers became smudged during the test. Although *CRC Silicone Grease* performed better than the other lubricants it would not have been chosen if it had caused these practical problems.

Having chosen the lubricant, it is now of interest to test to what degree the lubrication affects the RCAIT results. It should be noted here that the tests on the lubricant performance were carried out only for *Mix B* specimens. However, both the rubber mixes are natural rubbers with fillers which suggests that the lubricants will show similar performance when used in the tests. Moreover, the *CRC Silicone Grease* is nearly transparent which makes it a preferred lubricant.

III.2.2. Effect of lubrication on RCAIT results

To investigate the effect of lubrication (or lack thereof) on RCAIT results, two tests were carried out using rubber *Mix B* and brass coated steel cord – one without any lubricant and one with *CRC Silicone Grease*. Fluid injection rate was kept at *5ml/min* with an image and data acquisition frequency of *3Hz*. The results are shown in *Figure III.2.1*.

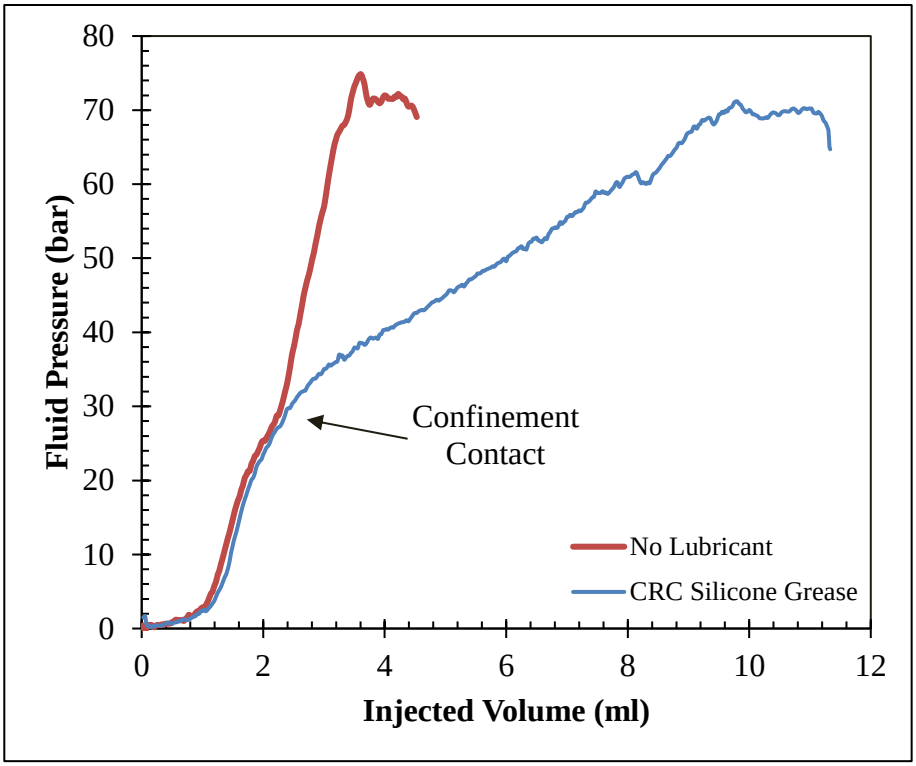

Figure III.2.1: Effect of lubrication on RCAIT specimen behaviour.

Several silver dots are drawn along the specimen length using a *Schmidt® 700 Silver* pen. During the experiments, the specimen deformation and inflation is recorded using an *IMETRUM® PDT* camera connected to *IMETRUM® Video Gauge™* software. The dots on the specimen are assigned as targets in the software. During the test, the software tracks these targets and displays their position in each frame of the video. This data is later used to calculate axial displacement of the specimen. Using a *Swagelok® Model S Transducer*, the fluid pressure is measured during the test. Parallel to the recording of the video, the voltage output from the pressure sensor is also recorded in the video capturing software. This ensures that, for a given pressure value measured by the pressure sensor, there is a unique frame recorded in the camera. This synchronisation is the key to the image processing and subsequent crack monitoring.

In *Figure III.2.1*, the two curves are almost identical until confinement contact occurs (at ca. *28bar*). As the inflated specimen touches the confinement tube, contact friction between the specimen outer surface and the confinement tube inner surface comes into play. From this point onwards, the two curves bifurcate, and the inflation behaviour is influenced by lubrication.

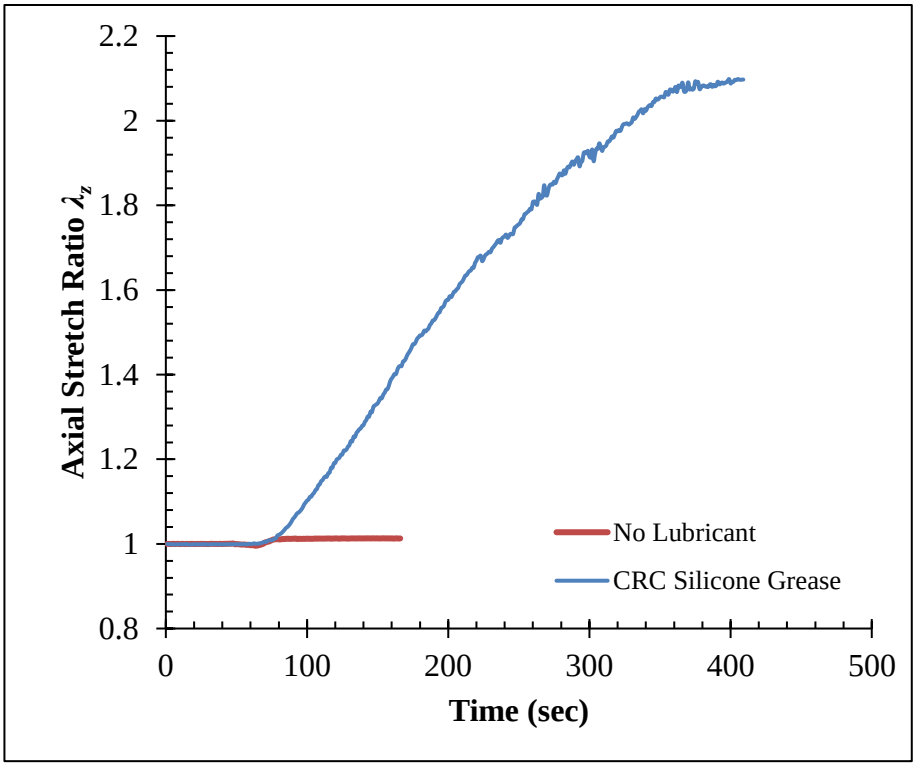

Figure III.2.2: Effect of lubrication on specimen axial deformation during RCAIT.

The effect of lubrication (or lack thereof) is reflected in the curves in the form of crack propagation pressure and total volume injected until complete interface fracture. The specimen with no lubrication undergoes fracture at a somewhat higher pressure than the lubricated specimen. However, the total volume of liquid injected into the latter is more than twice than that of the former. This huge difference can be explained by looking at the axial stretch ratios of the two specimens (see *Figure III.2.2*). In the first case (no lubricant), the specimen inflates only until it touches the confinement tube. The axial stretch ratio (λ_z) increases from *1* to *1.012* during the unconfined inflation stage (UIS). Once the specimen touches the confinement tube, λ_z stays nearly constant at *1.012* during the CIS and subsequent crack propagation. This indicates that the confinement contact condition is essentially that of no-slip. As the specimen's axial extension is restricted due to no-slip contact, total specimen deformation is also restricted due to incompressibility. This results in a smaller inner volume of the inflated specimen.

A small value of λ_z and only slightly higher crack propagation pressure means that the energy stored in the fractured-inflated rubber for the no lubrication case will be lower. In terms of the global energy balance, this means that the fraction of the overall fracture energy will be higher.

On the contrary, in the lubricated case, the lubricant allows the specimen to extend more than twice its original length ($\lambda_z = 2.08$), thereby changing the volume of the rubber cone (pointed annulus) ahead of the crack tip (see *Figure III.2.3*). Therefore, the effect of lubrication and no-slip contact on interface fracture is to change the relative proportion of *Mode I* and *Mode II* during crack propagation. For a specimen with no lubrication, *Mode II* fracture will dominate. Due to the domination of *Mode II* and the fact that the strain energy stored in the rubber will be smaller (as explained above), the critical SERR may be expected to be higher for the specimen with no lubrication.

Use of *CRC Silicone Grease* leads to greater axial stretching of the specimen due to minimal friction. Therefore, the boundary conditions experienced by the specimens are approximately the same as those assumed in the theory described in §*II.2.2*. The inflation process can now be assumed to be ideal, to a good approximation, and the experimental data can be processed with better accuracy. The specimen deformation is close to the theoretical value, therefore some improvements to the image processing can now be discussed.

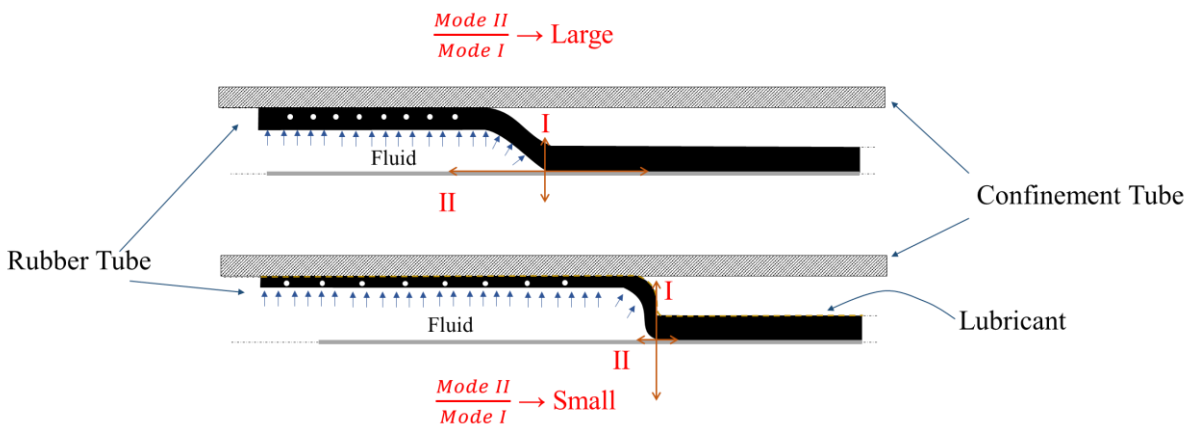

Figure III.2.3: Effect of lubrication on mode mixity of fracture. Notice the difference in thickness of the inflated rubber between the two cases.

III.3. Image Processing

Due to the axisymmetric nature of the rubber inflation, there are limitations to the information that can be extracted from the specimen. Using the traditional methods, only the fluid pressure and volume are recorded during the tests. However, more intricate behaviour is occurring during crack propagation that is not reflected in the Pressure vs Volume curve- *Figure II.4.8*. The self-similar behaviour or steady quasi-static nature of the crack under the multi-axial inflation loading and its effect on the SERR calculation are important factors that need to be

studied. Extracting data about specimen deformation using image processing can reveal a lot. In this section, a novel image processing technique is applied to the RCAIT to study crack propagation and rubber material behaviour under inflation loading.

III.3.1. Crack propagation monitoring

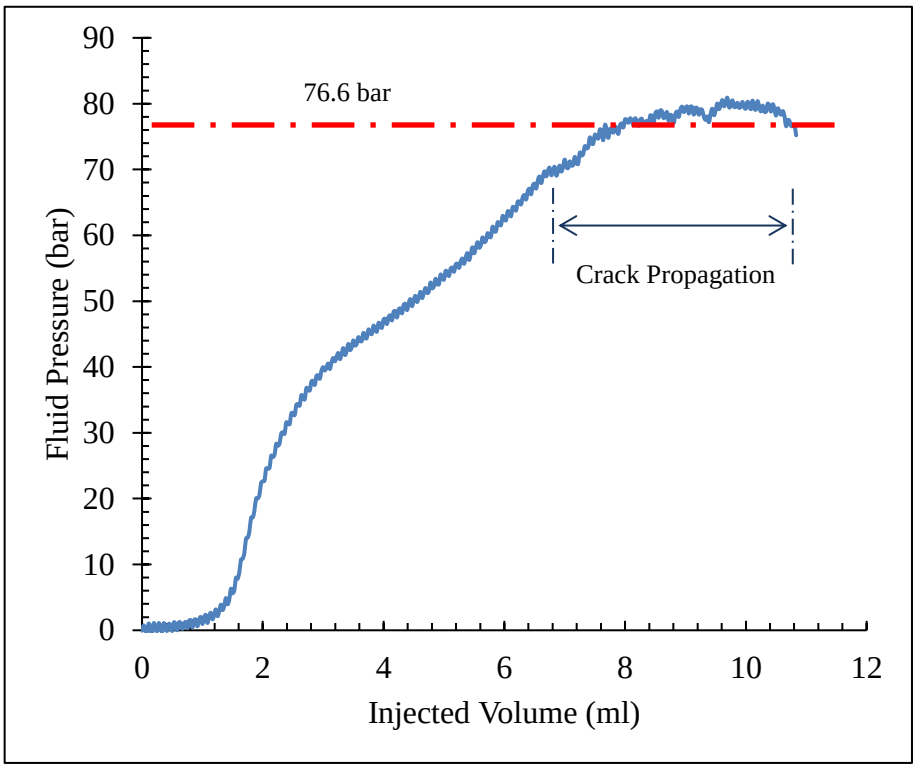

Figure III.3.1: A typical fluid pressure versus injected fluid volume evolution during RCAIT.

A typical pressure evolution recorded during the RCAIT is presented in *Figure III.3.1*. The specimen is a *Mix B* rubber envelope bonded to a brass coated cord. *CRC Silicone Grease* is used as the lubricant between the specimen and the confinement tube. Water is injected into the specimen at *5ml/min* to inflate the rubber. The inflation is followed by crack propagation at a nearly constant pressure of *76.6 bar*. The curve can be divided into three regimes- UIS, CIS and crack propagation. Stick-slip behaviour is observed within a small range of pressure (*~10bar*). To monitor crack propagation during the RCAIT, a marker monitoring technique is used. Due to the cylindrical geometry of the specimen and its inherent opacity, the crack tip is invisible, therefore an indirect method of measurement is necessary. Silver markers (or spots) are drawn on the outer surface of the specimen along its axis. These markers are visible through the transparent glass confinement tube (see *Figure III.3.2*). At the start of the test, one image is taken with a ruler placed next to the specimen. Using the scale markings on the ruler, the pixel units are converted into *mm* during data processing.

Deformation of the specimen (displacement of the markers) is captured with an *IMETRUM®* *2D PDT* camera at a chosen frame rate. Using *Video Gauge™* software from *IMETRUM®*, the markers can be tracked during the test for each frame (see *Figure III.3.3*). The voltage signal from the pressure sensor is also recorded simultaneously at the same rate in the software. This gives a unique frame or image for a given value of fluid pressure at a given time. The synchronisation of data is essential for data processing that follows from this point onwards.

In *Figure III.3.2*, the markers *A*, *B* and *C* are drawn along the bonded length of the rubber envelope. As the test begins, the pre-cracked length of the rubber envelope inflates in the radial as well as the axial directions. The markers *A*, *B* and *C* follow a rigid axial motion, seen in *Figure III.3.4*, linear with time. As the crack approaches the markers one after another, the rubber disc corresponding to that point inflates, and touches the confinement tube. As the crack propagation pressure is nearly constant, the axial displacement of the points reaches a plateau value.

The crack tip position itself cannot be observed, but the crack propagation step, Δa, can be measured at any chosen instant during crack propagation. The rubber envelope elongation can be reasonably considered as homogeneous in the cracked region. The elongation of the rubber in the bonded part is zero. Therefore, the longitudinal displacement of the bonded part is given by the relation:

$$d \approx (\lambda_z - 1)a \qquad \textit{(III.3.1)}$$

In this equation, d is the displacement of marker *C* measured after the crack has passed marker *A*. λ_z is the axial stretch ratio of the fully fractured and inflated part of the specimen, shown in *Figure III.3.4*. For a self-similar fracture, as shown in *Figure III.3.1*, this value stays nearly constant during the crack propagation. Distance a is the length of the crack propagation. If the exact instance of crack initiation is known, a can be calculated with a good accuracy. However, since the crack front is hidden from the camera this is not possible. A crack propagation step corresponding to a finite growth in the current value of crack length can still be calculated with reasonable accuracy using the following procedure.

A minimum of three markers are needed in the initially bonded length of the specimen to monitor the experiment (see *Figure III.3.2*). The first two markers (*A* and *B*) are used to measure the axial stretch ratio λ_z. The third marker (*C*) is placed near the end of the specimen

to measure the end displacement. During the crack propagation stage, the value of λ_z stays nearly constant, which is consistent with constant crack propagation pressure. The crack propagation step, Δa , is then determined from the change in displacement of marker C, Δd, using the relation:

$$\Delta a = \frac{\Delta d}{\lambda_z - 1} \qquad (III.3.2)$$

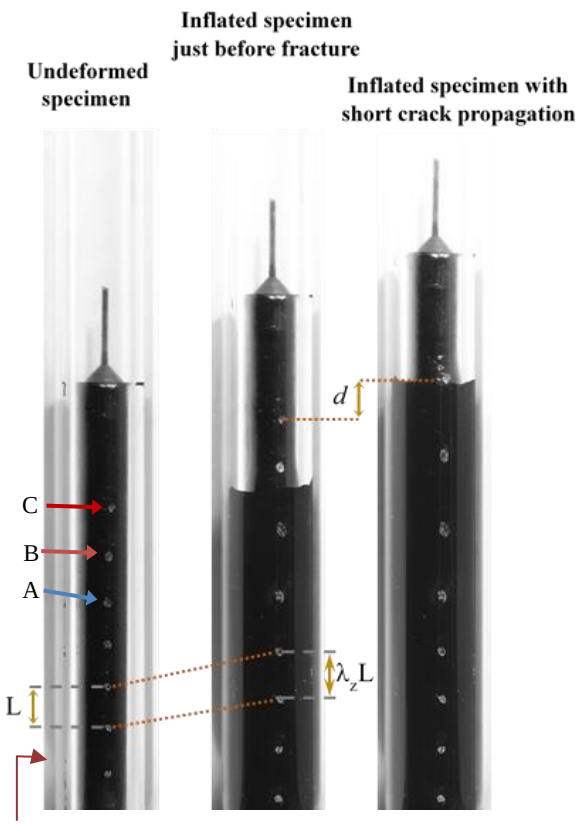

Figure III.3.2: Marker Monitoring.

Figure III.3.3: Target Tracking using IMETRUM® Video Gauge ™.

Figure III.3.4 shows axial displacement of three markers *A*, *B* and *C* (shown in *Figure III.3.2*) spanning the entire duration of the test. The axial stretch ratio, λ_z, is the ratio of the distance between markers *A* and *B* in the deformed and undeformed states. At the start of the test, some time is required (ca. *25sec*) for the fluid to enter the specimen pre-crack length. Once the pre-cracked length is filled with water, the pressure starts mounting. As the pre-cracked rubber inflates, the whole specimen is displaced axially. The injected fluid enters the specimen at a fixed rate; therefore, the slope of the marker displacement is constant. As the crack reaches the marker *A*, the envelope inflates radially and axially starting at ca. *97sec*. From this point, the axial deformation of marker *C* is measured as *d*. The gradient of the straight line slowly

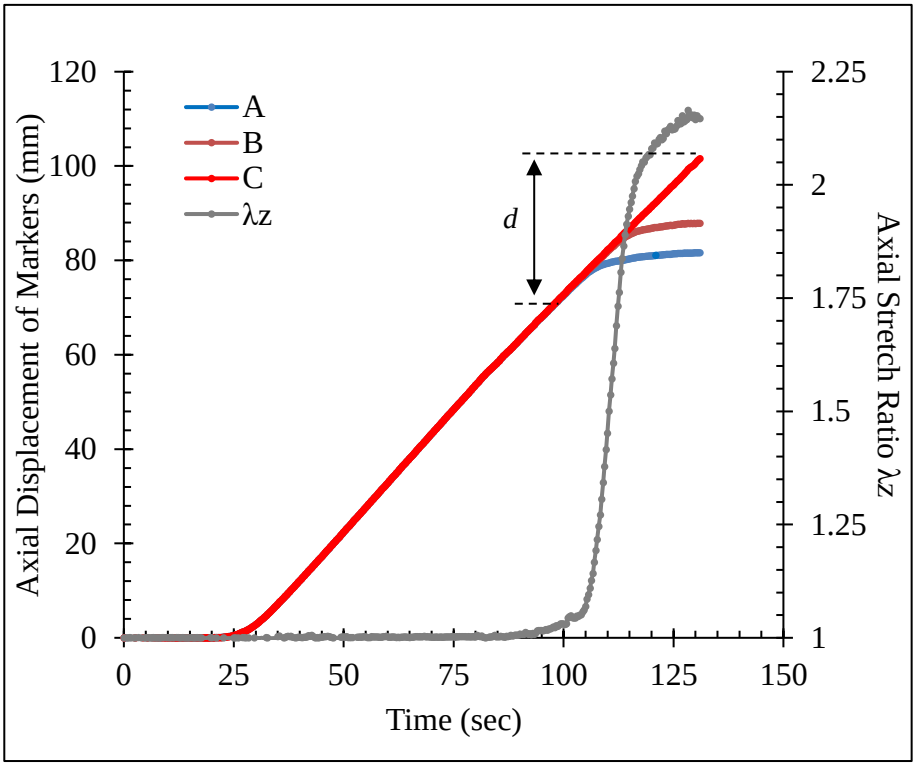

Figure III.3.4: Marker monitoring for specimen axial deformation.

decreases towards zero as the crack propagates beyond marker *A*. The crack then reaches marker *B* which exhibits the same behaviour. After the crack has crossed marker *B*, λ_z reaches a steady value between *A* and *B*. Once the crack has reached the marker *C*, its displacement value remains constant and it can no longer be used for data processing. Therefore, crack propagation monitoring is limited by the position of marker *C* on the specimen.

For the case shown in *Figure III.3.1*, the axial stretch ratio (λ_z) is found to be *2.16* during crack propagation. Using this information and the equations developed before, crack propagation can be plotted against time as shown in *Figure III.3.5*.

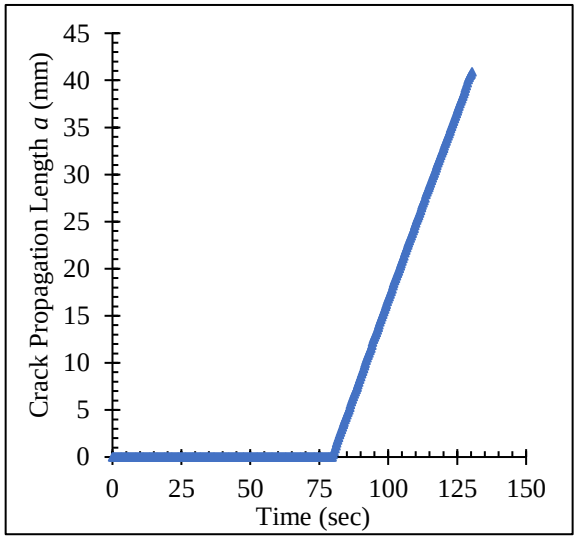

Figure III.3.5: Crack propagation length plotted against time.

During the initial inflation regime, there is no crack propagation and the fluid is injected into the specimen at a constant rate (*5ml/min*). As the pressure increases and reaches a certain level (crack propagation pressure), every increment in volume of fluid will aid in crack propagation. Injecting a quantity of fluid, ΔV,

will result in a certain crack extension, Δa. As crack propagation is self-similar and occurs at constant pressure, the two quantities are directly proportional, resulting in the following equation:

$$\Delta V = \pi(v^2 - v_0^2)\Delta a \lambda_z \qquad \textit{(III.3.3)}$$

where $\Delta a \lambda_z$ is the fractured-inflated length of the crack produced by injecting volume ΔV, v is the inner radius of this fractured-inflated crack and v_0 is the un-deformed inner radius of the rubber tube. Dividing both equations by time yields:

$$\Delta \dot{V} = \pi(v^2 - v_0^2)\Delta \dot{a} \lambda_z \qquad \textit{(III.3.4)}$$

where $\Delta \dot{V}$ is the rate of volume injection (*5ml/min*) and $\Delta \dot{a}$ is the speed of crack propagation. The linear behaviour of crack propagation visible in *Figure III.3.5* can be explained by this relation. Relation *(III.3.4)* can be used to calculate *v* using:

$$v = \sqrt{\frac{\Delta \dot{V}}{\pi \Delta \dot{a} \lambda_z} + v_0^2} \qquad \text{(III.3.5)}$$

to give *v=3.94mm* for the crack propagation shown in *Figure III.3.1*.

III.3.2. Characterization of the rubber

For accurate calculation of the critical SERR during fracture, it is important to choose an appropriate model to describe the hyperelastic behaviour of the rubber. Due to the highly nonlinear behaviour of the material, fitting the material data to get accurate values of material parameters is essential. In §*II.2* a Thick Rubber Tube Inflation Model was developed for a Mooney-Rivlin rubber. In §*II.4* the model was applied to an Ogden Rubber. In this section, the same rubber, *Mix B*, is used for the tests, therefore the Ogden model is fitted to uniaxial tensile test data from rubber sheet samples (see *Figure II.4.3* and *Figure II.4.2*).

In §*II.4* it was shown that the Ogden model with only first order terms fits the tensile test data well. A small rate dependence of Ogden parameters (μ and α) was found (see *Figure II.4.4*). It is important to note that the tensile test is a planar test on 2D rubber sheets, whereas in RCAIT the rubber envelope is a cylindrical geometry undergoing multi-axial inflation loading. Although the Ogden rubber model fits well with tensile test data at various linear strain rates, the μ and α values calculated from tensile tests will not truly depict the inflation

behaviour of the cylindrical rubber loaded at a volumetric strain rate. Therefore, the μ and α values calculated in *Figure II.4.4* will result in inaccuracies in the SERR calculation.

III.3.3. Evaluation of μ and α using RCAIT

To obtain reliable values of μ and α which depict the inflation behaviour accurately, the Pressure *vs* Volume data from *Figure III.3.1* can be used in conjunction with the results from the image processing described earlier. In the Thick Rubber Tube Inflation Model described in §*II.4*, the pressure values from the RCAIT along with μ and α calculated from tensile tests were used to calculate the axial stretch ratio, λ_z. However, λ_z can be obtained directly using image processing, and the value of the fluid pressure is readily available from the test data. Therefore, the Thick Rubber Tube Inflation Model can be inversed to treat μ and α as unknown variables, and fluid pressure and λ_z can be treated as the driving quantities. In this fashion, the material properties can be obtained from the test itself at the chosen fluid volume injection rate before the onset of the crack.

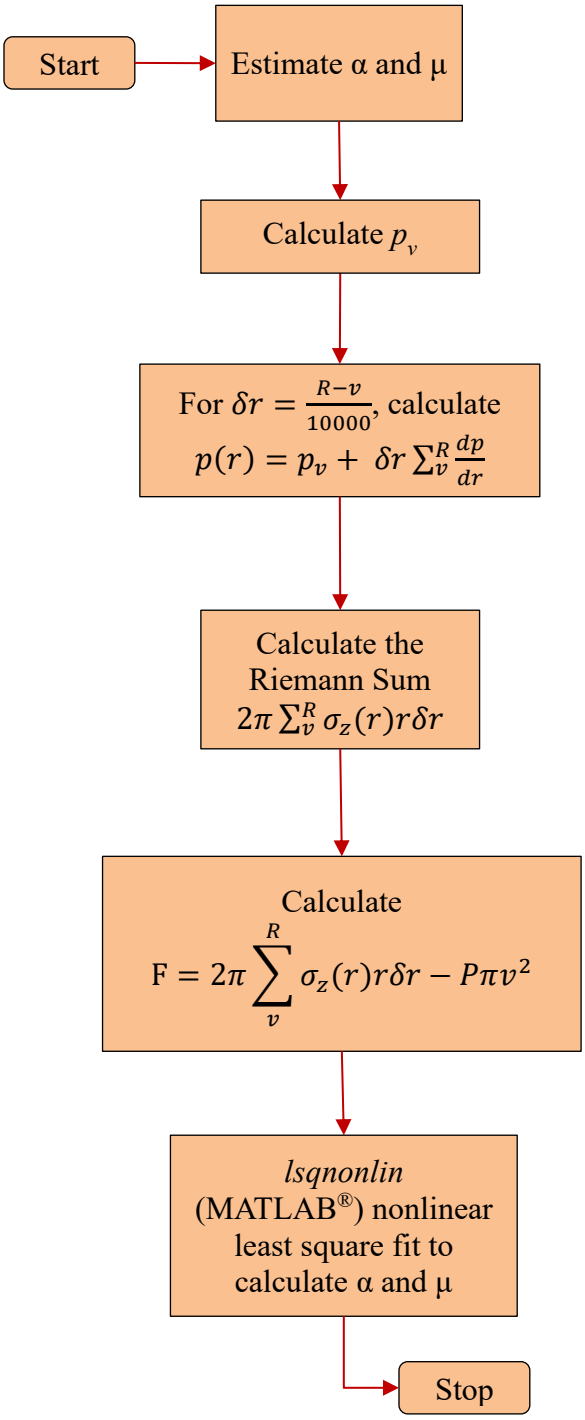

Figure III.3.6: Algorithm to calculate α and μ.

During the CIS regime of the test, the outer surface of the rubber tube is in contact with the inner surface of the confinement tube. However, the crack has not yet initiated. During this phase of the test, the axial forces on the specimen are balanced at each data point, giving rise to a set of nonlinear equations. The number of equations is equal to the number of data points during the confined inflation phase. The test data are then to be

used in these equations, applying nonlinear regression analysis to get μ and α.

The equations and intermediate steps used for this work are the same as described in equations *(II.4.1)-(II.4.14).* Inserting P and λ_z values from the experimental data into *(II.4.10)* yields a set of nonlinear equations with μ and α as the variables. Using a nonlinear least square fit algorithm such as *lsqnonlin* of MATLAB®, μ and α values can be calculated for the rubber at the chosen volume injection rate. The algorithm to solve these nonlinear equations is described in *Figure III.3.6*.

For the specimen shown in *Figure III.3.1*, the Ogden parameters found with this method are, $\alpha=3.25$ and $\mu=1.19MPa$. It is important to note that these values are very different from those calculated using tensile tests (*Figure II.4.4*). It is clear that the 2D uniaxial tensile test alone is insufficient when it comes to modelling axisymmetric inflation of the rubber. Apart from that, the Ogden model seems to be incapable of describing the rubber behaviour completely. Perhaps a more advanced rubber model may be used in the future that can capture the inflation behaviour of rubber using results from tensile tests or other planar tests alone.

By inserting these parameters in the Thick Rubber Tube Inflation Model, λ_z values for any given fluid pressure P can be calculated. The P *vs* λ_z values obtained by the three methods, *viz*. (a) experimental data (through image processing), (b) Ogden parameters mentioned above, and (c) uniaxial tensile test data (*Figure II.4.2*) can then be used for comparison. This comparison is shown in *Figure III.3.7*. The curves for experimental data and the Ogden parameters mentioned above match very closely except in the range of *20bar* to *40bar* when the rubber tube is not touching the confinement tube. However, crack propagation occurs at much higher pressures when the rubber tube is touching the confinement tube. Therefore, for the global energy balance of the fracture, this slight disagreement between the two methods at lower pressures is believed to be unimportant.

The curve for uniaxial tensile test data is plotted using average values of μ and α from *Figure II.4.4*. It is clear from *Figure III.3.7* that the uniaxial tensile test alone is insufficient for modelling axisymmetric inflation of the rubber. As explained previously, the limitations of the Ogden model can also be responsible for the huge difference in the two curves.

Uniaxial tests, however, are very important to fit the data to a rubber model out of the numerous choices available by using only the Cauchy stress and strain. Fine tuning of the

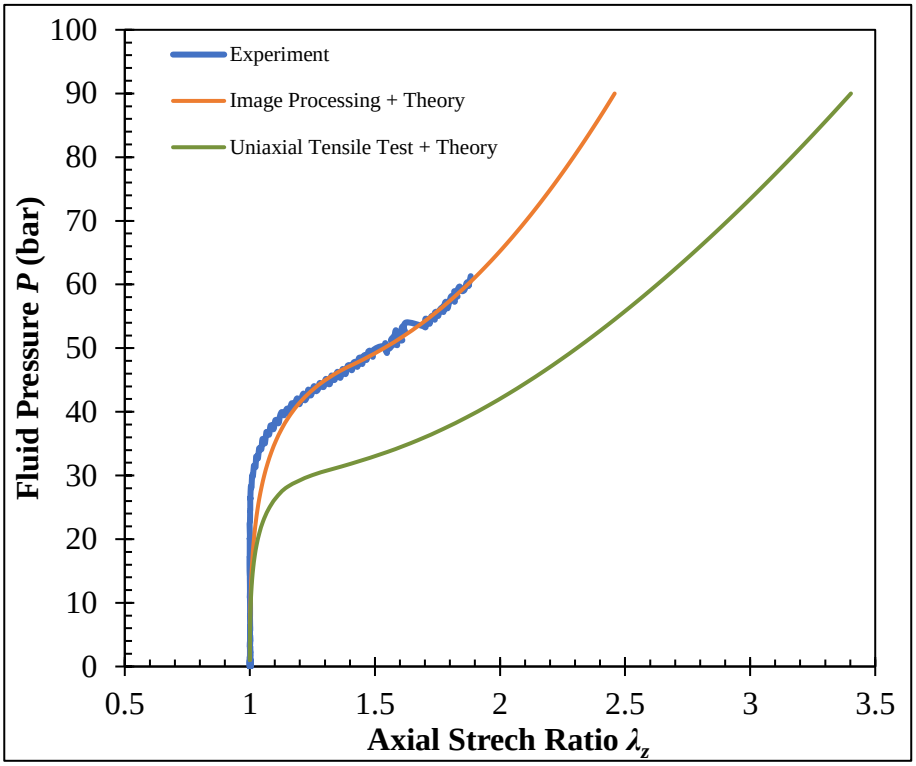

Figure III.3.7: Thick Rubber Tube Inflation. Comparison of theoretical model and experimental results.

model parameters can then be done for the chosen rubber model using the algorithm in *Figure III.3.6*.

A quantitative verification of the material parameters mentioned above would be to consider the deformed inner radius. For the test shown in *Figure III.3.1*, the deformed inner radius of the rubber tube was calculated as $v=3.94mm$ using the experimental data (equation *(III.3.5)*). The value calculated using the Ogden parameters mentioned above is $v=3.91mm$.

The Ogden parameters obtained from the tensile tests fail to mimic the inflation behaviour. Therefore, it is interesting to investigate what effect those parameters have on the SERR calculation. From *Figure III.3.8* it is evident that there is a considerable difference in SERR values computed using the two methods. The image processing technique coupled with the theoretical model is a powerful tool to study the fracture behaviour of the RCAIT.

To improve accuracy of the results obtained by image processing, it was important to control various factors affecting the whole process. One important factor that affects specimen deformation, and indirectly influences the fracture mode, is lubrication between the rubber and confinement tube. Using *Figure III.3.8* and *Figure III.2.1* the critical SERR (G_c) values calculated for the no lubrication and 'perfect' lubrication case (*CRC Silicone Grease*) are given in *Table III.3.1*. In the no lubrication case, the crack propagation pressure was found to

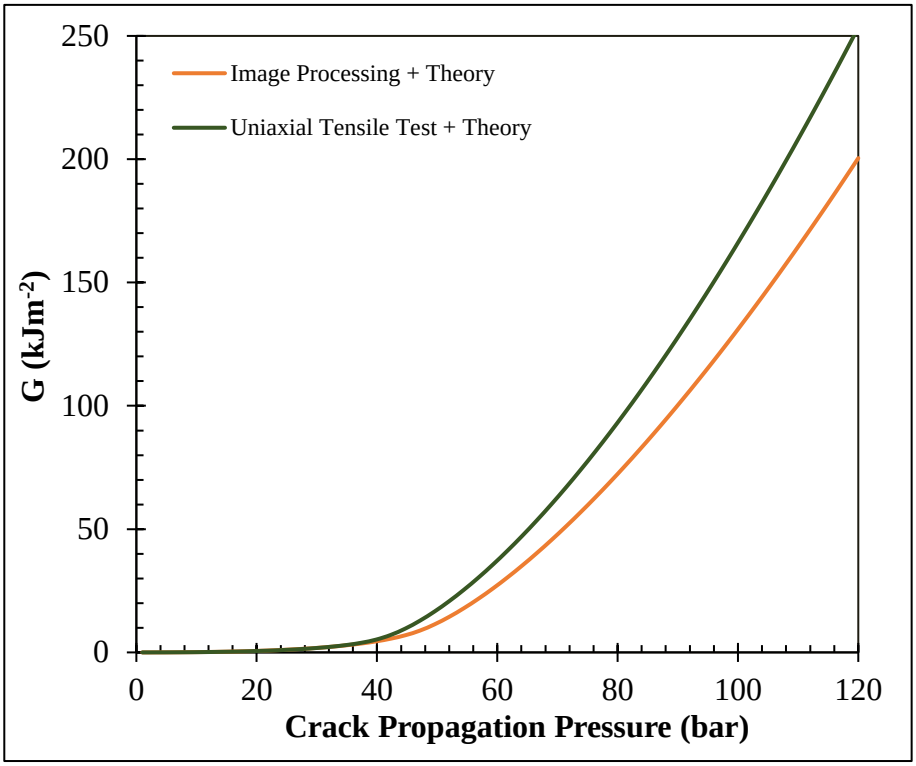

Figure III.3.8: Effect of rubber model parameters on SERR calculation.

be *71.5bar* in *Figure III.2.1*. Therefore, locating this pressure value on the orange curve in *Figure III.3.8* gives a G_c value of *60.6kJm*$^{-2}$. As postulated previously, the no lubrication case has a somewhat higher value of G_c compared to the lubricated case, ca. 8%. This is of some interest. Whilst experimental error and such effects as (very) slight departure from strict axisymmetry of the specimen may account for some of the difference, the result is believed to be significant. Friction will change the fracture mode mixity to an extent which is, at present, difficult to assess quantitatively. The relative fraction of *Mode I* and *Mode II* will almost certainly be changed by the absence or presence of lubricant, thus influencing the overall value of fracture energy. In addition, the shape of the deformed zone of the rubber ahead of the crack tip will be more limited geometrically without lubrication; however, the average state of strain therein will consequently probably be higher. The overall effect cannot presently be apportioned to lubrication only. At this stage, the effect of lubrication on G_c is merely a basic investigation. The effects of lubrication on mode mixity (G_{CI}/G_C) merit further research.

	No Lubricant	***CRC Silicone Grease***
G_c (kJm^{-2})	60.6	56.2

Table III.3.1: Critical SERR for two extreme cases.

The key here is to understand that the effect of lubrication is not limited to the axial stretch ratio or rubber inflation only. It also affects the angle of the pointed rubber annulus ahead of the crack tip. The relative axial displacement of the rubber envelope and the cord is affected as well. At this stage it is impossible to comment on how these factors affect the mode mixity; although they all seem to be interdependent. Perhaps a detailed finite element analysis of the effect of the friction coefficient on the deformation of the rubber envelope might reveal more details.

At this point, a good lubricant for the RCAIT has been identified for future tests. The image processing technique equipped with marker tracking system has also been developed for crack position monitoring as well as the identification of rubber material parameters. In summary, more reliable evaluation of the fracture energy or G_c is now possible. This experimental study can now be extended to investigate the consistency of RCAIT results and to perform statistical study based on the experimental data. This will be the focal point of the forthcoming sections.

III.4. Repeatability Tests

The motivation behind developing a novel rubber-steel cord adhesion test was to minimize or eliminate unwanted artefacts present in the traditional fracture mechanical tests. The Rubber Cord Adhesion Inflation Test comes out as a strong candidate to replace these traditional tests. The aim of MFP Michelin behind supporting this project was to develop a reliable test protocol that can be implemented at their Ladoux Research Centre for future projects. Therefore, it is important to do a statistical study of the results and to establish the repeatability of the test results. Such a repeatability study will serve as a stepping stone and will give tyre designers and engineers in Michelin confidence in using the test protocol as a supplement for the standard tests.

III.4.1. Test plan

This repeatability study is carried out on *Mix A* and *Mix B* and brass coated cords. Rubber sheets (*2.5mm thick*) and brass coated cords were produced internally at MFP Michelin Ladoux Research Centre. The specimens were formed using a specific mould and cured at respective temperatures and curing times. Since all specimens have brass coated cords, the

two types of specimens are identified based on the rubber only. They are referred to as *Mix A* and *Mix B* from here onwards.

Each of the two specimen types was tested at *5ml/min* and *2ml/min* volume injection rates. Each such test was repeated five times. The entire test campaign was carried out at the Ladoux Research Centre using a Promess® tensile test machine. Details of the test equipment setup and the hydraulic circuit have already been described in *Chapter II*.

III.4.2. Repeatability test results

Figure III.4.1 and *Figure III.4.2* show the pressure-volume plots for all ten tests. Overall, the spread between the curves is small except for *Mix B* specimens at the injection speed of *2ml/min* – a maximum spread of nearly *3ml* at the crack initiation. However, some of those specimens were made out of a rubber sheet of different thickness (*2mm*) and came from a different batch. This could have influenced the behaviour of the rubber and produced a spread in the pressure-volume curve. Apart from this result, the specimen behaviour seems to be repeatable. The total volume of fluid injected until complete fracture for each test remains within a small range of *1.5ml*. All the tests seem to follow a self-similar fracture with nearly constant crack propagation pressure for individual tests. This hypothesis can be investigated further by looking at the standard deviation for each test.

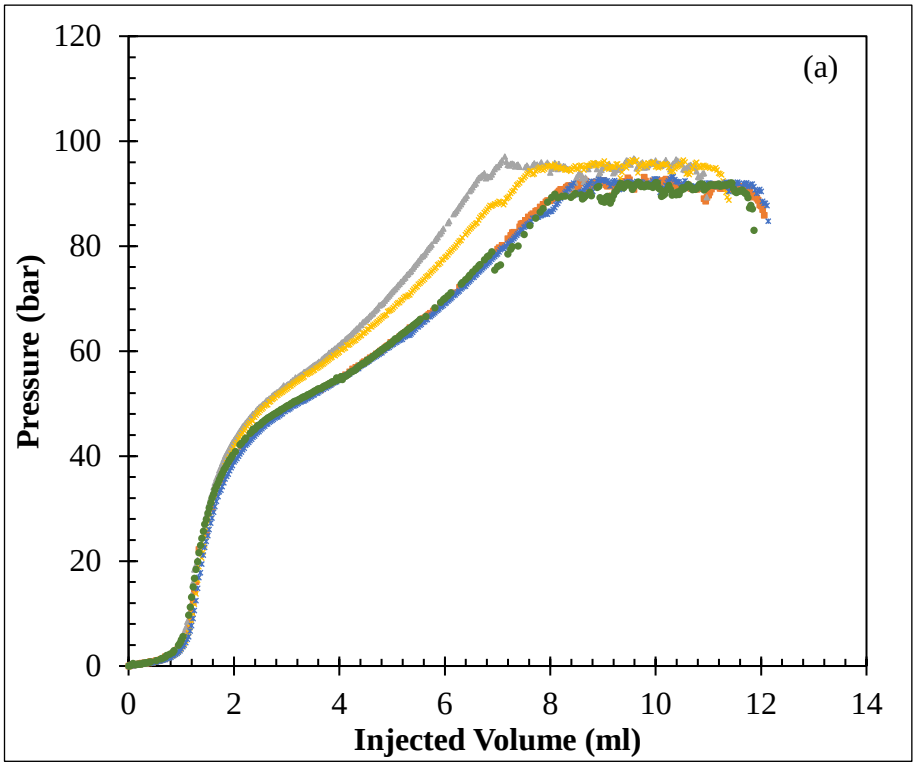

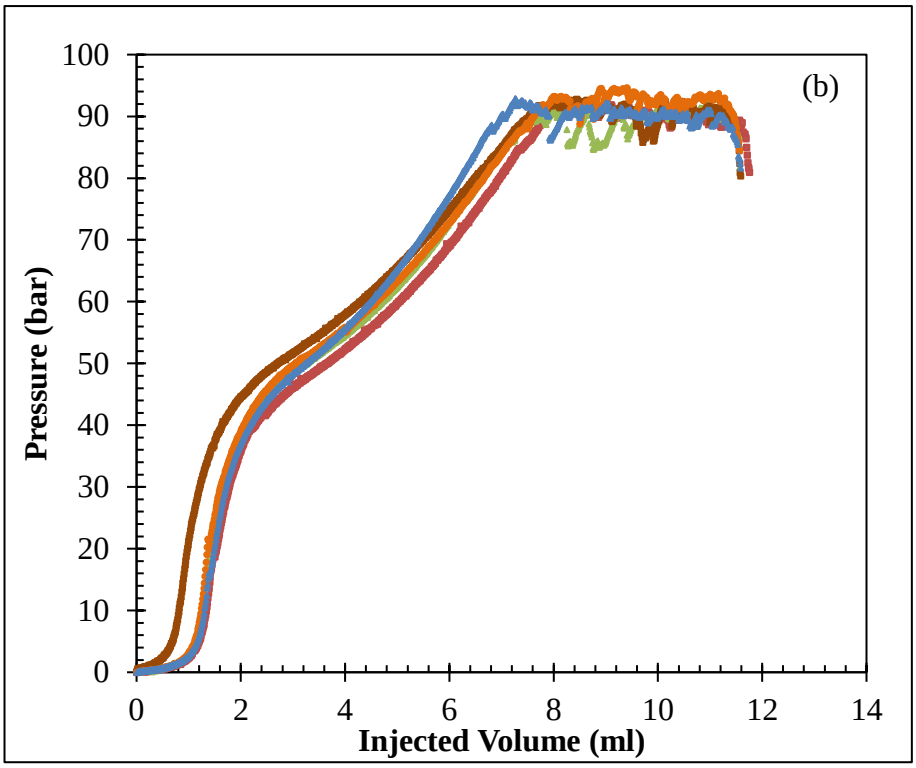

Figure III.4.1: Repeatability test results for Mix A+ brass coated cord specimens. (a) 5ml/min and (b) 2ml/min.

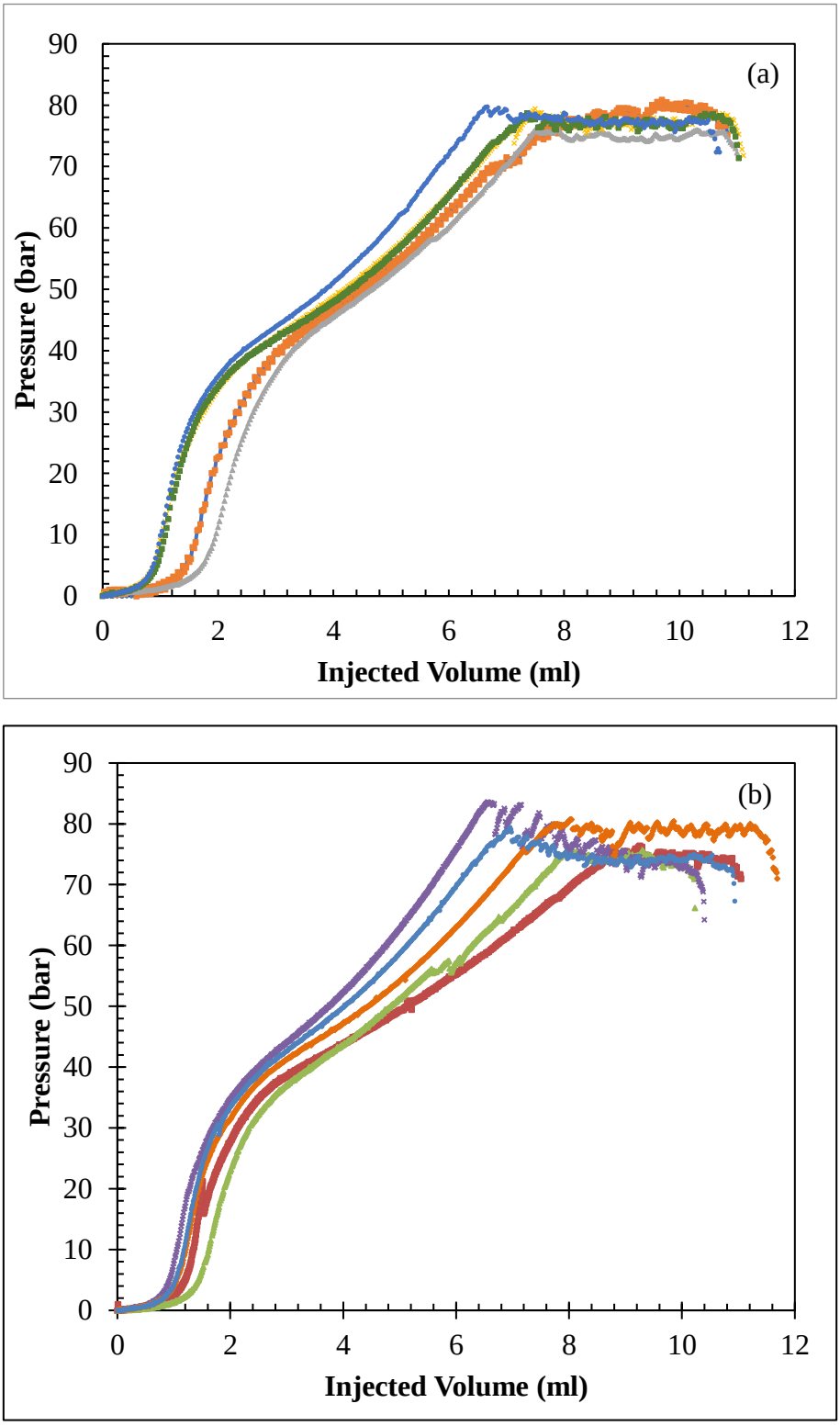

Figure III.4.2: Repeatability test results for Mix B+ brass coated cord specimens. (a) 5ml/min and (b) 2ml/min.

III.4.3. Analysis of results

In *Figure III.4.3* the crack propagation pressure recorded during each of the *20* tests is shown with individual error bars. Each error bar represents the standard deviation of the pressure

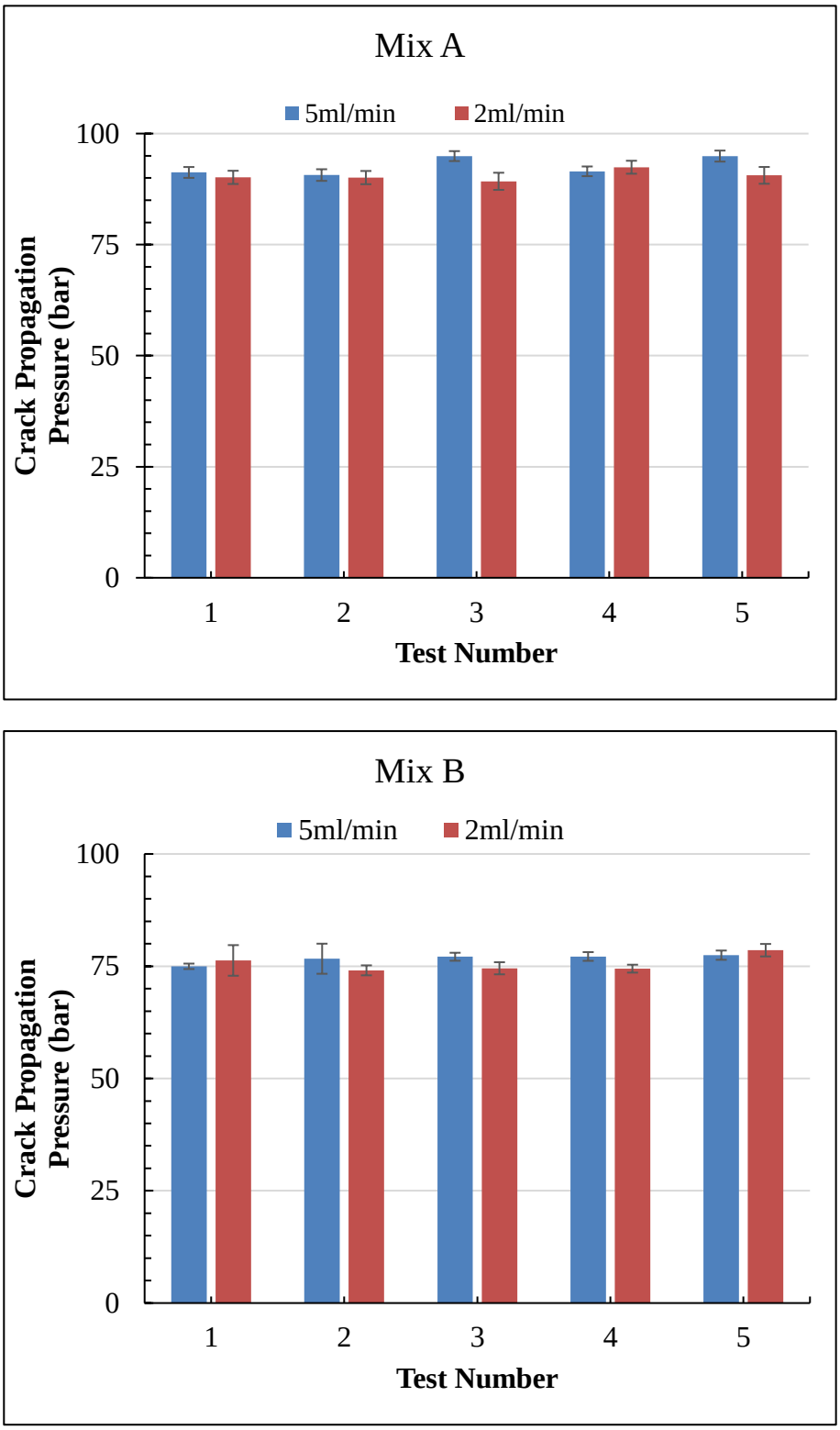

Figure III.4.3:Crack propagation pressure for each test. Error bars show standard deviation with respect to the average value per test.

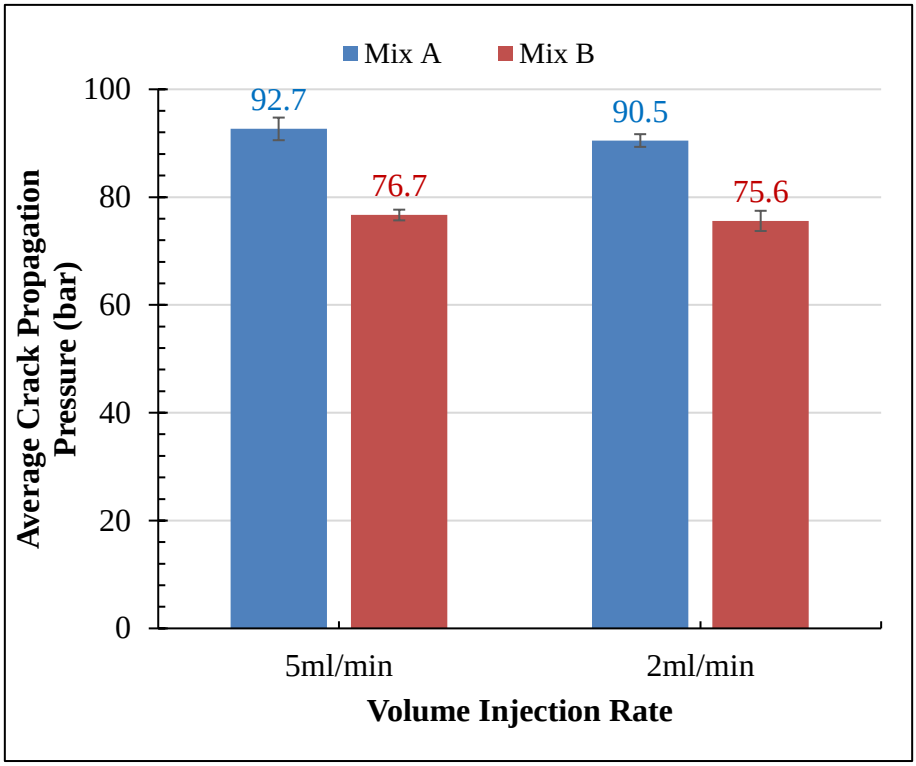

Figure III.4.4:Comparison of average crack propagation pressures between Mix A and Mix B.

fluctuation recorded during the entire specimen crack propagation with respect to the average crack propagation pressure during that test. These error values vary within *5%* of the average crack propagation pressure for all the tests. This is considered to be a small fluctuation.

A clear distinction between the two rubber mixes in terms of the average crack propagation pressure is seen in *Figure III.4.4*. The ordinate shows the average value of the five crack propagation pressures shown in *Figure III.4.3* for each type of 'specimen-loading rate' combination. The error bars show the standard deviation of the average value, which stays within *3%*; again, considered to be small. *Mix A* and *Mix B* are vastly different mixes designed for different adhesion performance. A variation of nearly *15bars* in the average crack propagation pressure values between the two specimen types shows that the RCAIT can quantitatively differentiate between different specimen types. The sensitivity of SERR calculation to the crack propagation pressure will reveal further how the RCAIT can be used to distinguish between various rubber-metal composites.

Before moving on to calculate SERR for the tests, it is important to find material parameters using the volumetric data. Using the image processing described earlier, the 1st order Ogden model can be fitted to each of these *20* tests to evaluate α and μ. This in itself constitutes a repeatability test on the specimen rubber.

The results are shown in *Figure III.4.5* and *Figure III.4.6*. Values of α and μ for both rubbers vary considerably between each test and between the two fluid injection rates. Considering the nonlinear nature of the specimen deformation, drawing parallels between material parameter variation and the spread in the pressure-volume curves is impossible. However, it is

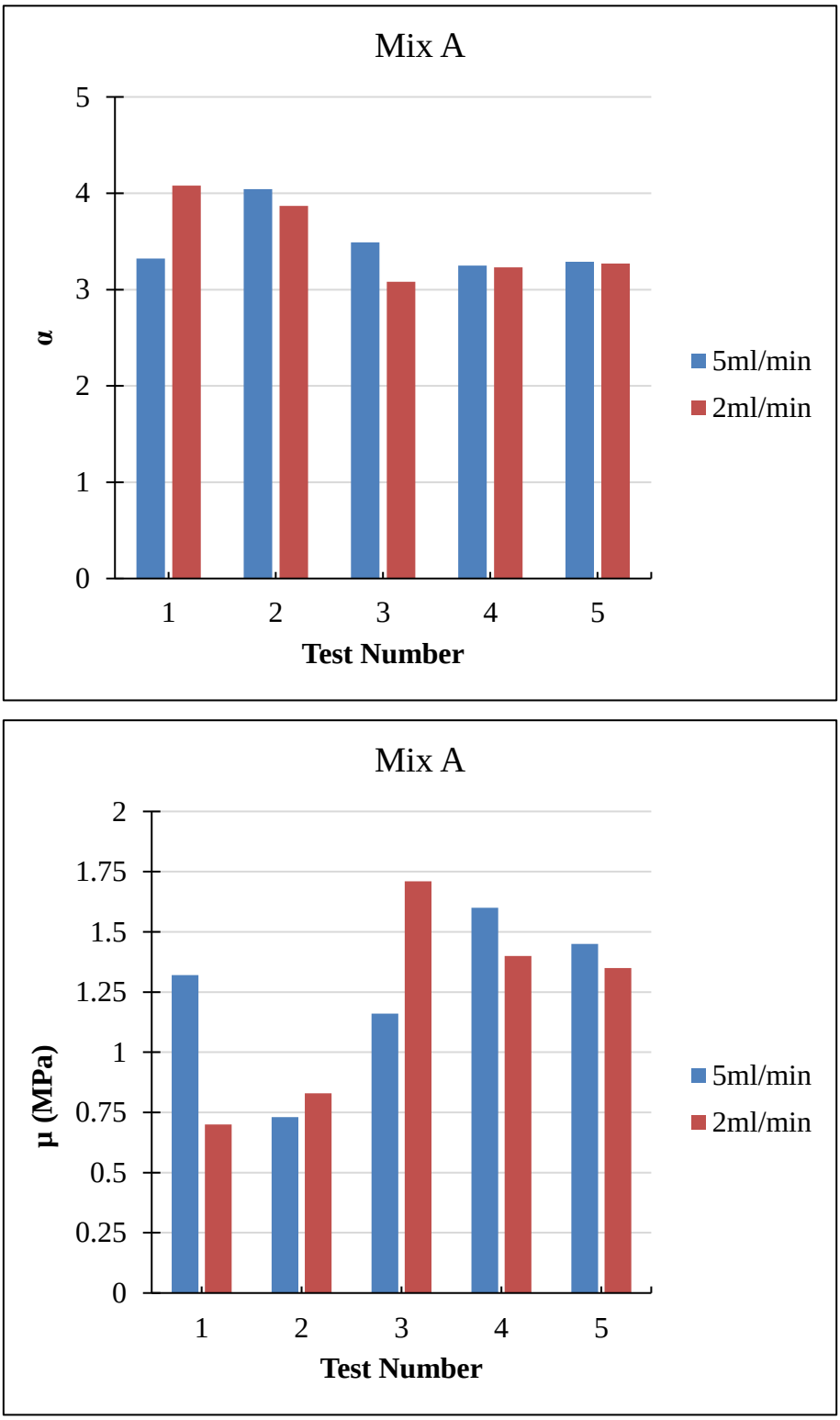

Figure III.4.5: Ogden parameter fitting for the inflation data in Figure III.4.1.

interesting to note that there is a relatively larger variation in μ values than α values.

The material parameters calculated here are an outcome of (nonlinear least-square) curve fitting. The P-λ_z values from the experimental data corresponding to the CIS are used to fit the boundary condition equation *(II.4.10)*. The lubrication is assumed to be perfect for both *Mix A*

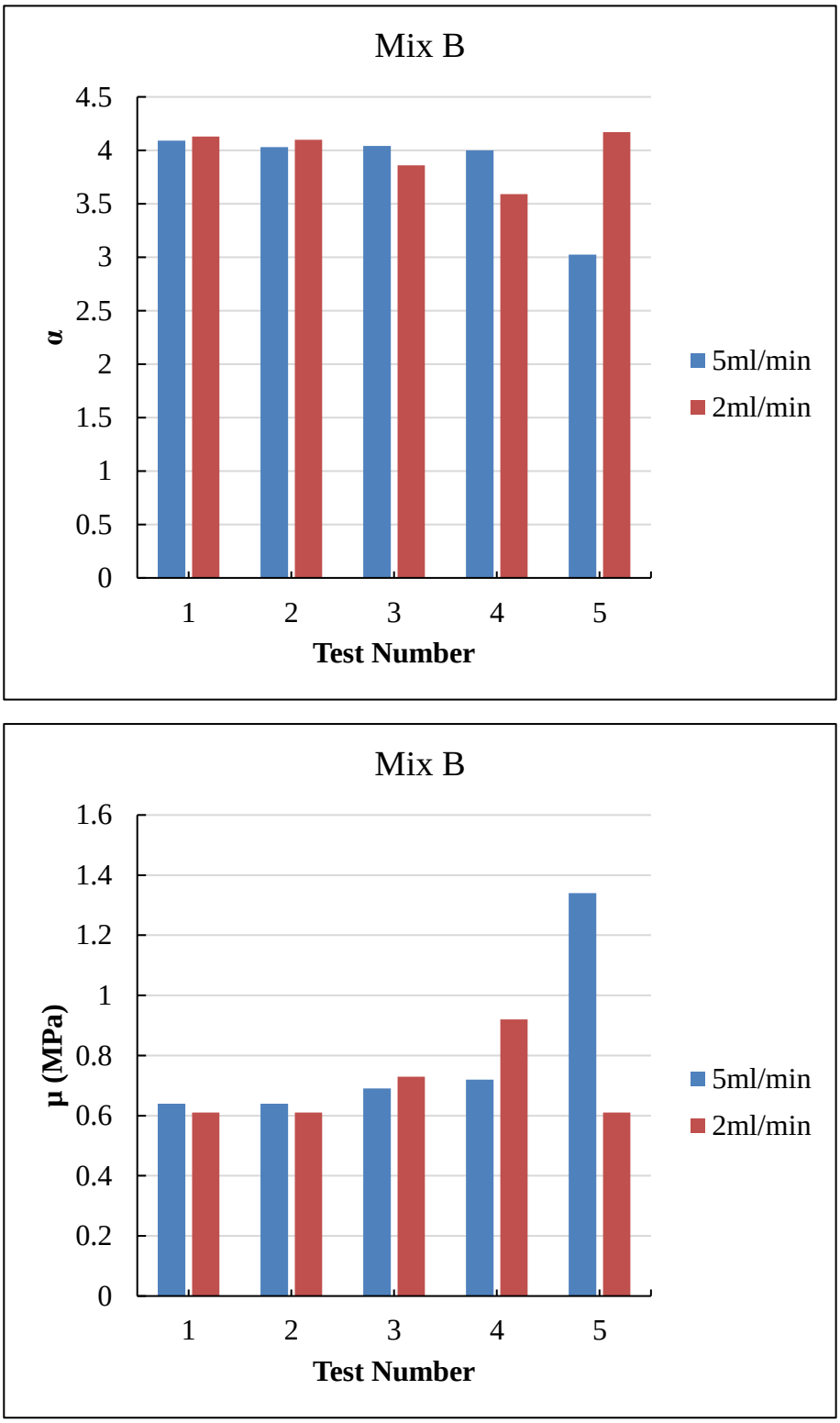

Figure III.4.6: Ogden parameter fitting for the inflation data in Figure III.4.2.

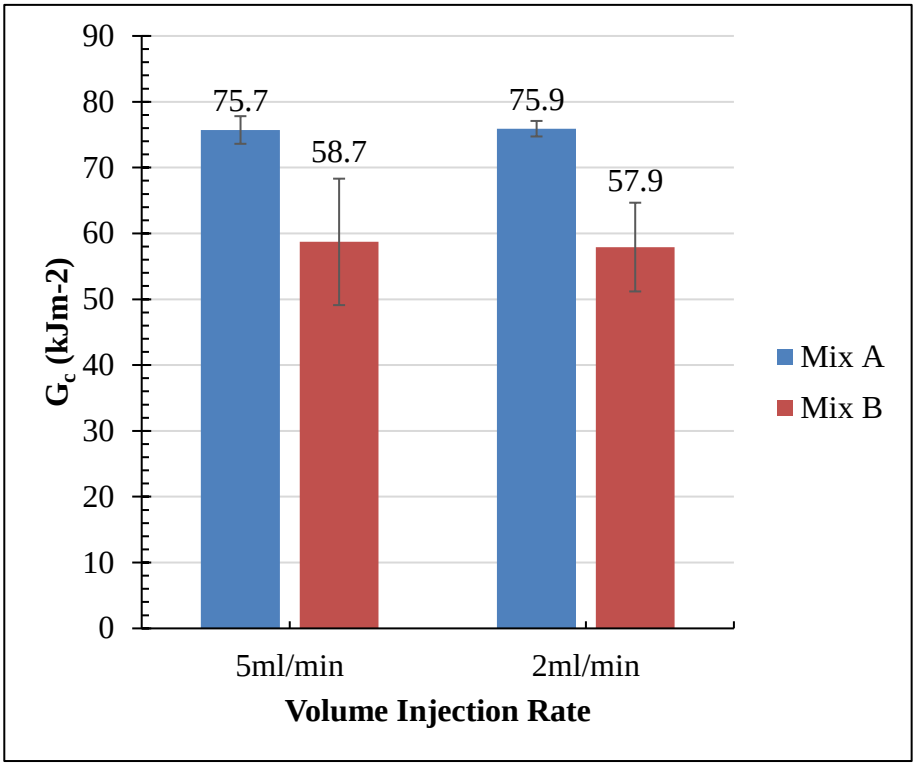

Figure III.4.7: Average values of evaluated fracture energy for all 4 test cases.

and *Mix B* rubber specimens though in the previous section only *Mix B* was studied for the effect of lubrication. A variation in the rubber properties of *Mix B* may be expected due to there being two different batches. All of these factors can affect the material parameters evaluated for each test.

Now, the fracture energy or critical SERR (G_c) can be evaluated for all tests using the material parameters from *Figure III.4.5* and *Figure III.4.6*, as shown in *Figure III.4.7*. The error bars represent standard deviation from the average values. They represent the deviation in G_c corresponding to the variability in α and μ seen earlier. The standard deviation stays within *6-17%*, which is considered not small, but reasonable. A clear distinction between the two specimen types, as was seen in *Figure III.4.4* is visible in *Figure III.4.7* again. This result suggests that the RCAIT can distinguish successfully between various rubber-cord adhesive systems.

One more interesting study could be to look at the crack propagation speed (V_p) for the tests, as shown in *Figure III.4.8*. It was shown earlier that the crack propagation speed is influenced and to some extent, controlled by the fluid injection rate (see equation *(III.3.4)*). This again becomes clear when looking at the difference in the crack propagation speeds. V_p for the *5ml/min* specimens are nearly *2.5* times that for the *2ml/min* specimens. However, the difference is much smaller between the two rubber mixes. This indicates that the interfacial

fracture speed can be controlled by RCAIT protocol. This should enable tyre designers to test the strength of the rubber-steel adhesion over a wide range of crack propagation speeds. Mixed-mode rubber-metal debonding has been studied previously, such as [75] and [76]. It is shown that the crack propagation incorporates viscoelastic dissipation at the interface. Therefore, having the ability to influence the crack propagation speed using the experimental parameters will give tyre designers control over viscoelastic dissipation at the interface as well. Moreover, this dissipation at the interface will dominate the evaluated fracture energy. This opens a new avenue for testing.

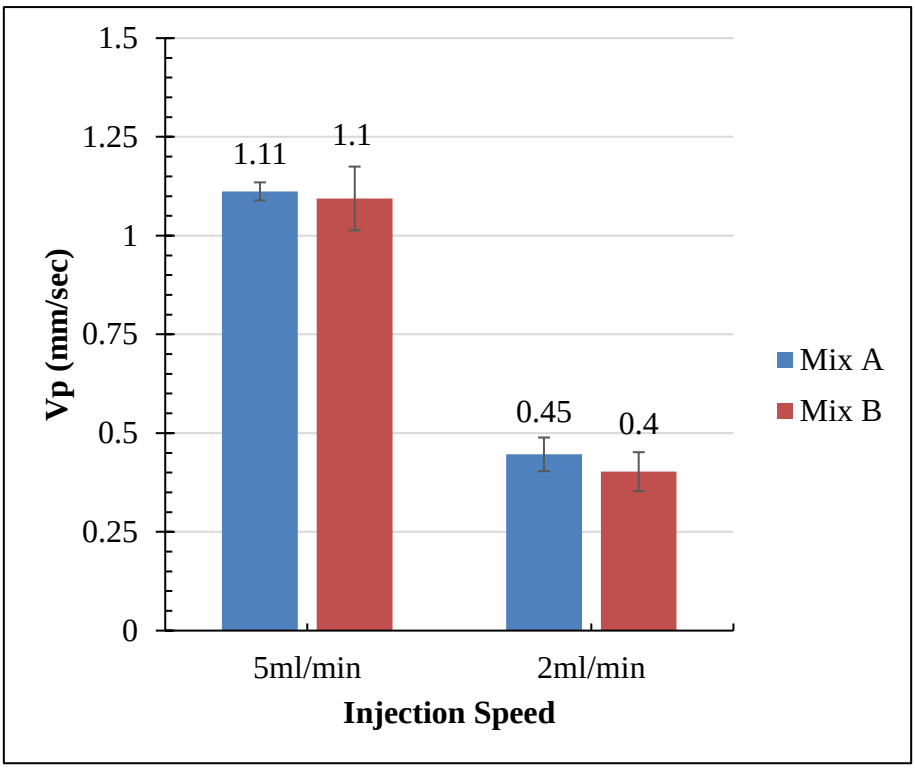

Figure III.4.8: Average crack propagation speeds for the 20 tests.

III.5. Chapter III Summary and Future Steps

In this chapter, the initial conception and theory of the RCAIT presented in *Chapter I* has been extended, mainly in terms of experimental test development. In §*III.2* the effect of lubrication on specimen inflation was studied in detail. It was found that *CRC Silicone Grease* reduces friction between the rubber and glass and allows for larger axial stretch ratios. In addition, being nearly transparent, it does not hinder the image processing. After choosing the lubricant, the effect of friction on RCAIT results was studied. It was found that lack of lubrication reflected in the test results by decreased values of λ_z and higher fracture energies.

It is speculated that the lubrication (or lack thereof) affects the shape of the inflated rubber near the crack tip, thereby affecting the mode mixity of the crack propagation. This hypothesis would benefit in the future from a detailed analysis using theoretical and finite element modelling. The image processing technique can be used in conjunction with finite element modelling to investigate the mode mixity in further detail. The stresses and strains occurring near the crack tip, and how the lubrication affects their magnitudes, will be an interesting topic for further research.

During the literature review (*Chapter I*), it was found that there has been much work done investigating fracture modes involving rubber materials with examples being found in references [32]-[42]. However, none of them were found to deal with such a complex problem involving incompressible hyperelasticity, bi-material (rubber-metal) adhesion, axisymmetric geometry and considering crack face traction (pressurised fluid) simultaneously. The problem seems yet to be tackled considering its limited application and high complexity. In most cases in the literature, the rubber is assumed to follow neo-Hookean behaviour which puts limitations on its applicability. Indeed, studying the mode mixity problem by incorporating all of these factors deserves its own dedicated research work. This aspect merits its own investigation, perhaps as a separate study.

A novel image processing technique introduced in §*III.3* could be used for many other testing procedures. The technique is extended to compute material parameters of the rubber and to simulate the inflation behaviour. This procedure is found to give results with better accuracy compared to established methods. Equipped with this new image processing technique, the RCAIT set-up could be used to perform various other tests, such as cyclic tests taking into account the Mullins effect [77] and viscoelastic dissipation. It could also be used to perform creep tests on rubber or the rubber-metal interface.

At this point, the RCAIT protocol is established with detailed experimental, theoretical and numerical development. To take this work beyond a PhD thesis and to implement it in industry is a very important step to make the RCAIT as a supplementary test protocol to the standard rubber-cord fracture mechanical tests. To achieve this, repeatability tests were performed on two types of specimens and two loading rates. All the tests were performed at Ladoux Research Centre of MFP Michelin in Clermont-Ferrand. It was found that the RCAIT can clearly distinguish between different adhesive systems represented by different rubber-cord combinations. The results were repeatable with small standard deviations.

One interesting result stemming from these repeatability tests is the crack propagation speed V_p. The material parameters α and μ are calculated at the chosen injection speed using the inflation data (pressure-volume). This technique eliminates the necessity to quantify the viscoelastic effects prevalent in the rubber as the material parameters are calculated from 'instantaneous' deformation and not from planar tests such as uniaxial/biaxial tests. Therefore, the only viscous dissipation that needs to be addressed is near the crack tip (process zone) and the interface itself. RCAIT gives control over the crack propagation speed thereby the dissipation at the interface as well. This way the fracture energy or critical SERR can be separated from the viscous dissipation at the interface, giving the tyre designers precision in SERR evaluation. At this stage, this is just a hypothesis; nonetheless it shows the capabilities of the Rubber Cord Adhesion Inflation Test.

The experimental part of the RCAIT has now been developed completely and the test can be implemented in the Ladoux Research Centre of MFP Michelin. In the next chapter, the theoretical and numerical study will be extended for various phenomenological hyperelastic models. A more general rubber inflation model will be developed and applied to RCAIT results.

Chapter IV: Constitutive Modelling and its Effects on the RCAIT

IV.1. Introduction

For a quantitative analysis of the rubber-steel adhesion by RCAIT, a global energy balance was proposed in *Chapter II*. It was shown that the energy stored in the pressure-inflated rubber constitutes a major part of the fracture energy evaluation. This energy was calculated for a Mooney-Rivlin rubber and then for an Ogden rubber. It was found that the fracture energy evaluation is sensitive to the energy stored in the rubber during crack propagation. With this result in mind, this chapter presents an investigation into the influence of various rubber models on predicting the energy stored in the rubber, and subsequently how this affects the evaluation of the fracture energy for RCAIT. A similar study of various rubber models and how well they fit to the tensile and shear test data has been carried out in [78] and [79]. In addition, in [80], [81] and [82] a review of various hyperelastic models, their stress-strain relations and some experimental results are presented.

In the first section of this work, a generalised Thick-Walled Cylinder Inflation Model is constructed, which can be applied to any phenomenological hyperelastic model. A generalised critical Strain Energy Release Rate (SERR) equation is then presented, based on this theoretical model. Furthermore, following the framework of *Chapter II*, the critical SERR of the rubber-steel interface is evaluated using five different hyperelastic models.

This analysis is extended by introducing a generalised volumetric data fitting technique, applicable to any phenomenological hyperelastic model. The results obtained with this fitting method are presented along with evaluated SERR for each of the hyperelastic models.

IV.2. Thick-Walled Cylinder Inflation Model

Results from RCAIT on a specimen are shown in *Figure IV.2.1*. The specimen was made of a rubber envelope of inner radius *0.65mm* and outer radius *4.7mm* adhered to a brass coated, steel cord of diameter *1.3mm*. The rubber envelope was *Mix B* (natural rubber with *65phr* of carbon black and *4.5phr* of sulphur). Water was injected inside the specimen at a rate of *5ml/min*. Confinement contact was observed at ca. *50bar* causing the gradient of the *Pressure vs Volume* curve to change. Eventually, the fluid pressure reached a plateau value and the crack propagated at ca.*74.9bar*.

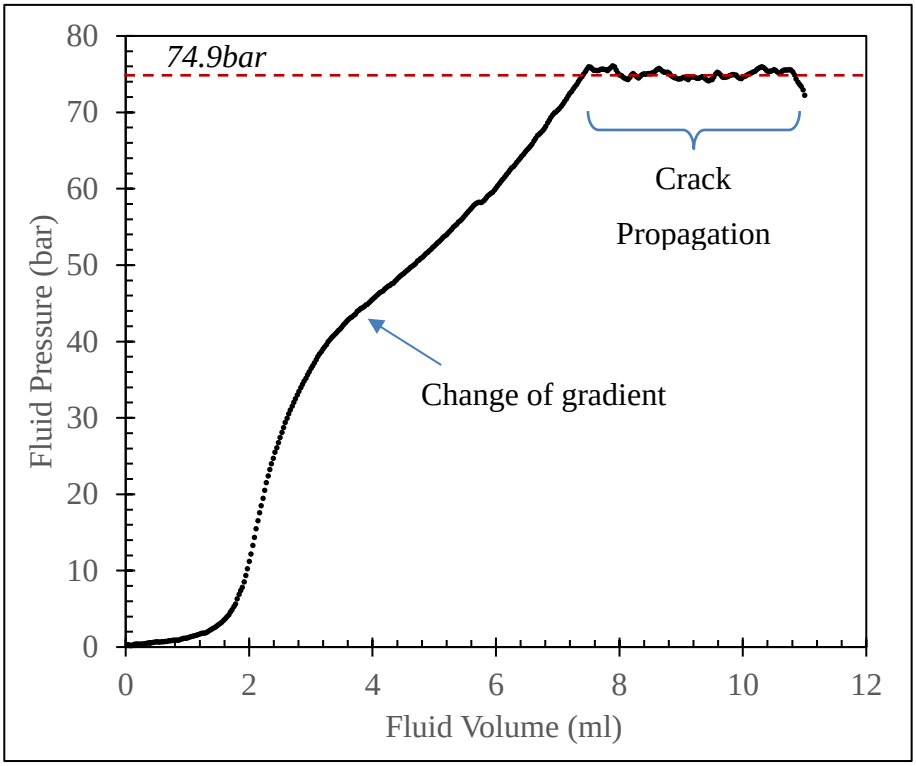

Figure IV.2.1: Typical Pressure vs Volume plot of an RCAIT specimen.

IV.2.1. Global energy balance

It was already shown in *Chapter II* that the fracture energy, or critical SERR, is directly proportional to the energy stored in the inflated rubber and in the pressurised fluid. Therefore, to evaluate the critical SERR or G_c, it is important to evaluate the energy stored in the rubber as accurately as possible. The test results can then be treated without any experimental artefacts. This task is, in fact, complex since the rubber undergoes complex loading conditions. Measured elongation can be as high as *250%*, and the closed tube geometry combined with confined configuration leads to large stress/strain gradients across the thickness (see *Figure II.2.10*). Not all rubber models are able to capture these phenomena in a reliable manner. Therefore, a preliminary analysis should be performed to identify which models are more likely to capture the real rubber response.

The work presented in forthcoming sections focuses on evaluating the energy stored in the rubber and investigating its effect on the calculation of G_c. The Thick Rubber Tube Inflation Model proposed previously in *Chapter II* for an Ogden type rubber can be extended to various phenomenological hyperelastic models. In the following section, an alternative semi-analytical resolution technique is proposed which is applicable to a large variety of rubber models. The results from *Figure IV.2.1* are then processed using this model and the effect of various constitutive rubber models on the evaluation of G_c is studied.

The usual approach to evaluation of strain energy consists of selecting a suitable hyperelastic model and identifying its parameters from a series of mechanical tests under various loading conditions ([78]-[82]) such as uniaxial tensile tests or biaxial tests. The model is then used to simulate the rubber envelope inflation process. However, multiaxial loading conditions are experienced by the rubber envelope during the inflation test. These conditions may not be correctly captured by simple models such as those identified with standard uniaxial tensile tests. This study reveals whether the G_c evaluation is sensitive to the chosen rubber model or not. Although precise identification of rubber material parameters may not be possible with only tensile test data, this study of how various rubber models predict the outcome of RCAIT is of great interest for future work at MFP Michelin. In the next section, some important equations to describe the thick-walled cylinder inflation are presented, followed by a generalised algorithm that is programmed in *MATLAB*®.

IV.2.2. Theoretical model

A short review of a few incompressible hyperelastic models applied to monotonic loading conditions is proposed here. Their applicability to the present tube inflation problem is also evaluated. In a fracture mechanics context, the objective is to adapt the stress-elongation relations for each of these models to the tube expansion conditions, thereby evaluating the strain energy density function. The strain energy density function will then be used to evaluate the energy stored in the rubber envelope. This review is not exhaustive since a large number of complex hyperelastic models can be found in the literature. Only a few of them have been applied since the test data available for the rubber is limited. Similar analysis has been proposed in a different context in [78] and [79].

Considering an isotropic, incompressible material, the strain energy density function depends on only two invariants I_1 and I_2. I_3 remains constant due to the constant volume condition. Therefore, these invariants are given by relations:

$$I_1 = {\lambda_1}^2 + {\lambda_2}^2 + {\lambda_3}^2 \qquad (IV.2.1)$$

$$I_2 = {\lambda_1}^2{\lambda_2}^2 + {\lambda_2}^2{\lambda_3}^2 + {\lambda_1}^2{\lambda_3}^2 \qquad (IV.2.2)$$

$$I_3 = {\lambda_1}^2{\lambda_1}^2{\lambda_3}^2 = 1 \qquad (IV.2.3)$$

where λ_i are the principal stretches of deformation. For incompressible materials, the true principal (Cauchy) stresses are related to the stretches and invariants by the relations:

$$\sigma_i = 2\left(\lambda_i{}^2 \frac{\partial W}{\partial I_1} - \frac{1}{\lambda_i{}^2}\frac{\partial W}{\partial I_2}\right) - p \qquad \textit{(IV.2.4)}$$

$$\sigma_i = -p + \lambda_i \frac{\partial W}{\partial \lambda_i} = -p + \sigma_i{}^{dev} \qquad \textit{(IV.2.5)}$$

where $\sigma_i{}^{dev}$ is the deviatoric part of the stress, W is the strain energy density function of the rubber in consideration and p is the hydrostatic pressure arising due to incompressibility.

The following procedure is used to determine all quantities describing inflation of the cylindrical rubber envelope under confined or unconfined conditions. Firstly, internal and external radius values are set as the driving parameters so that c and λ_z are determined with the relations:

$$\lambda_z = \frac{w_0^2 - v_0^2}{w^2 - v^2} \qquad \textit{(IV.2.6)}$$

$$\frac{1}{c} = \frac{v^2 w_0^2 - w^2 v_0^2}{w_0^2 - v_0^2} \qquad \textit{(IV.2.7)}$$

All symbols have their usual meanings, as explained in *Chapter II*. Then, using *(II.2.1)* and *(II.2.2)*, the radial and circumferential stretch ratios are determined so that the deviatoric part of the Cauchy stress becomes:

$$\sigma_i{}^{dev} = \lambda_i \frac{\partial W}{\partial \lambda_i} \qquad \textit{(IV.2.8)}$$

Then, the equilibrium equation *(II.2.4)* is used to introduce the hydrostatic pressure evolution as:

$$\frac{dp}{dr} = \frac{d\sigma_r{}^{dev}}{dr} + \frac{\sigma_r{}^{dev} - \sigma_\theta{}^{dev}}{r} \qquad \textit{(IV.2.9)}$$

For a given inner and outer radius, the deviatoric part of the stress is known throughout the thickness, and the hydrostatic pressure must be determined using the following integral formulation:

$$p(r) = \sigma_{rr}{}^{dev}(r) - \sigma_{rr}{}^{dev}(v) + \int_v^r \frac{\sigma_{rr}{}^{dev}(u) - \sigma_{\theta\theta}{}^{dev}(u)}{u} du + p(v)$$

$$= \delta(r) + p(v) \qquad \textit{(IV.2.10)}$$

The hydrostatic distribution $\delta(r)$ can be determined numerically using trapezoidal integration. The hydrostatic constant $p(v)$ can then be determined by combining *(II.2.6)* and *(II.2.8)* as follows:

$$F_z = -p(v)\pi(w^2 - v^2) + 2\pi \int_v^w [\sigma_{zz}{}^{dev}(u) - \delta(u)]udu = \pi v^2 P \qquad (IV.2.11)$$

The fluid pressure P is given by

$$P = -\sigma_{rr}(v) = p(v) - \sigma_{rr}{}^{dev}(v) \qquad (IV.2.12)$$

Therefore:

$$p(v) = \frac{v^2}{w^2}\sigma_{rr}{}^{dev}(v) + \frac{2}{w^2}\int_v^w [\sigma_{zz}{}^{dev}(u) - \delta(u)]udu \qquad (IV.2.13)$$

Using the $\delta(r)$ value calculated by the trapezoidal integration, *p(v)* is determined numerically using the trapezoidal rule again.

For an open-end condition, the axial force is zero. Therefore:

$$F_z = -p(v)\pi(w^2 - v^2) + 2\pi \int_v^w [\sigma_{zz}{}^{dev}(u) - \delta(u)]udu = 0 \qquad (IV.2.14)$$

Therefore:

$$p(v) = \frac{2}{w^2 - v^2}\int_v^w [\sigma_{zz}{}^{dev}(u) - \delta(u)]udu = 0 \qquad (IV.2.15)$$

Once the total hydrostatic pressure function *p(r)* is evaluated for a given choice of inner and outer radii, the stress distribution in the entire rubber thickness can easily be obtained. Finally, the inner and outer pressure values are determined by the relations:

$$P_{int} = P = -\sigma_{rr}(v) \qquad P_{ext} = -\sigma_{rr}(w) \qquad (IV.2.16)$$

In the UIS, an iterative procedure is used to adjust the outer radius *w*, so that the stress-free outer surface condition $P_{ext}=0$ is satisfied. In the CIS, the $P(\lambda_z)$ evolution is obtained directly by imposing $w = R$ (*(II.2.10)*) and using the above integration procedure.

The algorithm to calculate the stress-elongation state of the rubber cylinder at any specified deformed state (*v* value) is described in *Figure IV.2.2*. The term *v* is the only parameter increasing monotonically during inflation. Therefore, it is chosen as the driving parameter.

To apply the algorithm presented in *Figure IV.2.2* to a chosen rubber model, stress *vs* stretch ratio relations *(IV.2.4)* and *(IV.2.5)* must first be derived. Then, using the algorithm, the through thickness stress – strain distributions must be found so that specimen overall deformation can be expressed as a function of applied fluid pressure. In *Figure IV.2.3*, theoretical evolution of $P(\lambda_z)$ is given for the experimental condition presented in *Figure*

IV.2.1 considering a Mooney-Rivlin model as well as a 1st order Ogden model. These results are compared with the results presented in *Chapter II* using the Thick Rubber Tube Inflation Model specific to the rubber models (*(II.2.13), (II.2.14)*) and *Figure II.4.12*). The rubber material parameters are found by fitting uniaxial tensile test data to the Mooney-Rivlin and Ogden models. The Mooney-Rivlin parameters are $C_1 = 1.34MPa$ and $C_2 = 0.37MPa$, whereas the Ogden parameters are $\alpha = 2.64$ and $\mu = 1.89MPa$. The two curves plotted using previous work and this work follow the same path for both material models. In *Chapter II*, the semi-

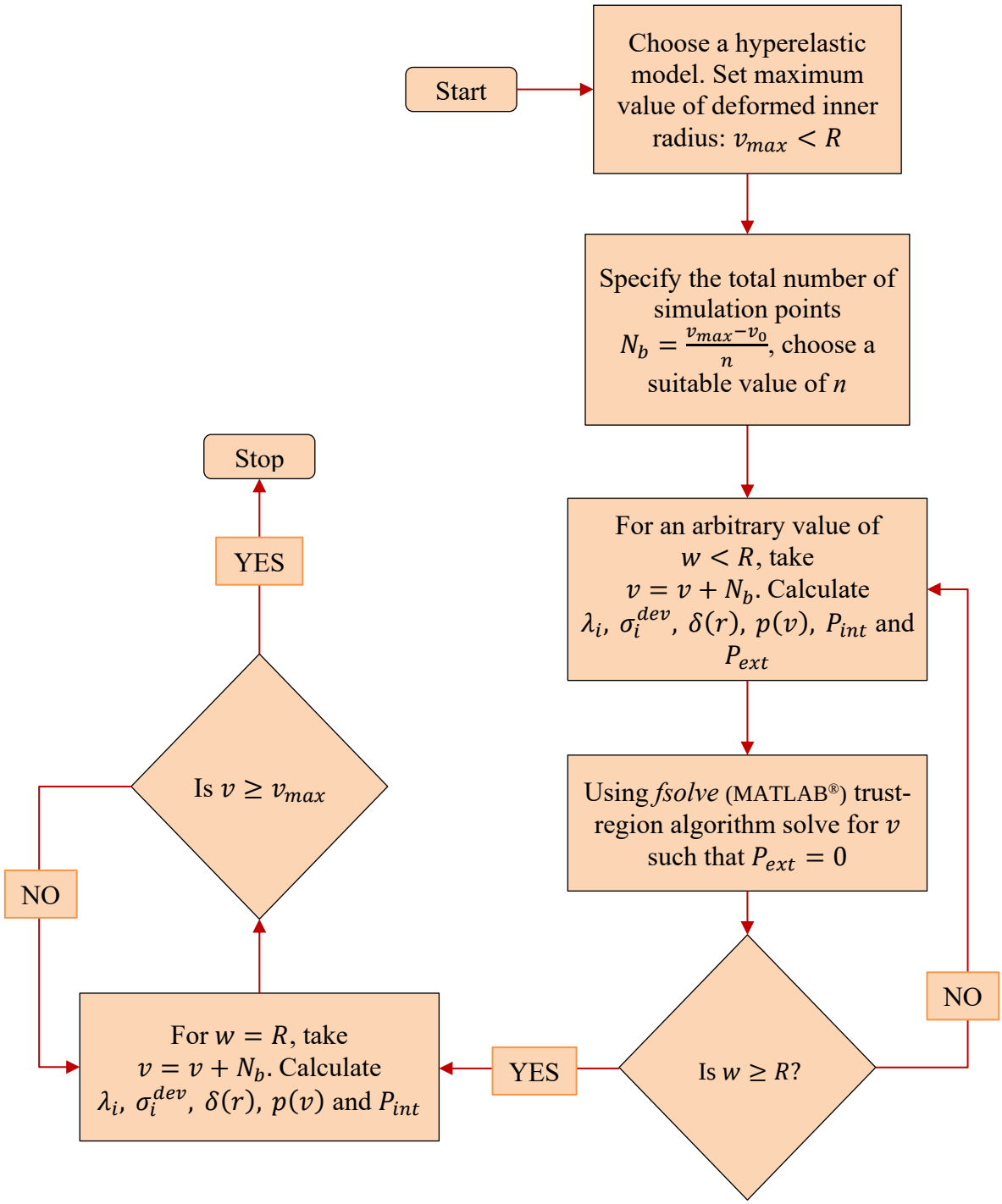

Figure IV.2.2: Generalised Thick-Walled Cylinder Inflation Algorithm for hyperelastic materials.

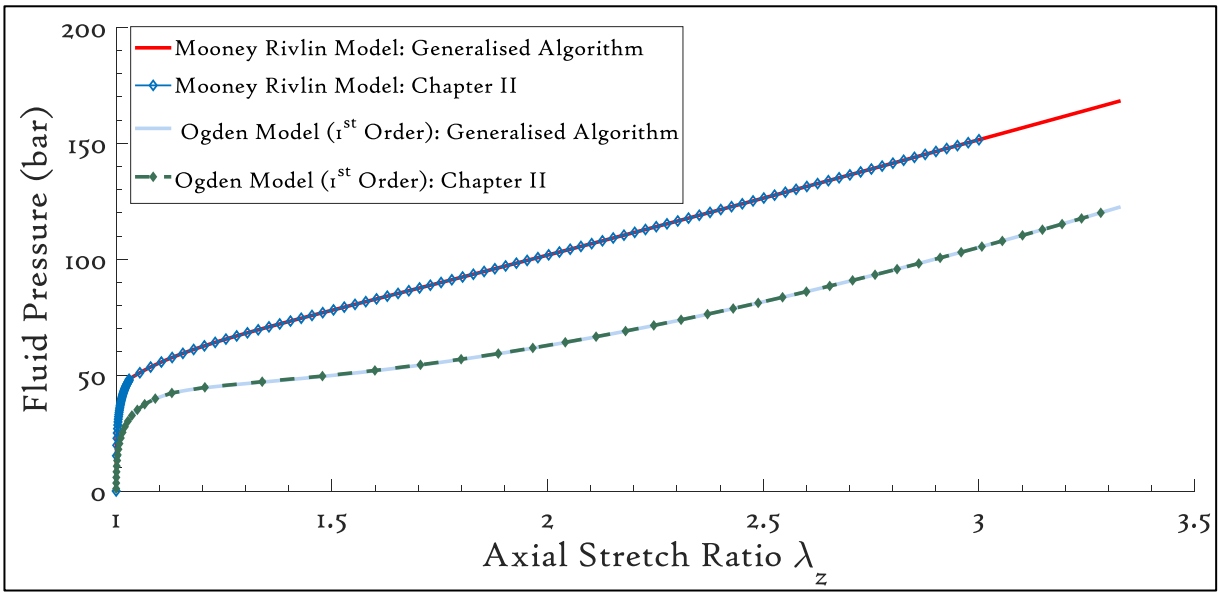

Figure IV.2.3: Comparison between Thick-Walled Cylinder Inflation algorithms presented in Figure IV.2.2 and Chapter II.

analytical model (Mooney-Rivlin) and the algorithm (Ogden model) were cross-checked using finite element models and were found to be virtually identical. Therefore, *Figure IV.2.3* constitutes strong evidence for the results obtained using *Figure* IV.*2.2*.

Having established the validity of the equations and the algorithm, the specimen fracture energy can now be computed by performing global energy balance analysis as explained in §*II.3* and §*II.4.5*. However, it is important to note that the extent of the process zone ahead of the crack tip is not known exactly. Also, the specimen envelope deformation controls the stress/strain distribution in the near crack tip vicinity and consequently the damage process. Viscous dissipation will be present ahead of the crack tip in the process zone, which will induce some coupling between crack propagation energy and ΔU_e^{rubber}terms. G_c can then be considered as an effective critical energy release rate term for the whole specimen. Its intrinsic nature must be demonstrated by evidencing a constant value irrespective of the rubber envelope dimensions. Equation *(II.4.19)* can be rearranged to get

$$G_c = \frac{\lambda_z}{v_0}\left[\left(\frac{P_{int}}{2} - \frac{P_{int}^2}{4\chi}\right)(v^2 - v_0^2) - \int_v^w \delta w_e(u)udu\right] \qquad (IV.2.17)$$

(IV.2.17) holds true for any hyperelastic model (neglecting dissipation mechanisms) applied to the rubber cylinder. By following the procedure described earlier, the stress-elongation state of the rubber cylinder can be calculated for any type of hyperelastic material. It can then be used to solve the integral $\int_v^w \delta w(u)udu$ using a Riemann Sum, Trapezoidal Rule or any other numerical integration method.

IV.3. Application to Various Rubber Models

Since proper evaluation of the deformation of the rubber is fundamental for reliable determination of G_c, correct identification of the rubber behaviour is also essential. Therefore, it is interesting to investigate how various rubber models can be used to describe the complex inflation problem and how they affect the value of critical SERR (G_c) evaluated using *(IV.2.17)*. In [78] and [79] a similar study was done on various hyperelastic models to compare their performance on uniaxial, biaxial and pure shear data, reported by Treloar in [83].

IV.3.1. Uniaxial test data fitting

Out of the numerous hyperelastic models available in literature, *10* different models were fitted to the tensile test data of the rubber and it was found that five models show the least residual values signifying a good fit. These models are: Mooney-Rivlin [70], Ogden [84], Yeoh [85], Lopez-Pamies [86] and ExpLn [87]. Of these, Mooney-Rivlin model and Ogden model (1st order) were already used in *Chapter II*, to describe the thick wall cylinder inflation of the rubber under consideration. They are included here again since they are one of the most commonly used hyperelastic models in the literature. A short summary of these models, their strain energy density functions and corresponding deviatoric stress relations are given in *Appendix A*.

For the tensile test data, a dumbbell specimen was cut from a sheet of *Mix B* rubber. It was loaded under tension at a constant displacement rate of *5mm/min* or a constant strain rate of $0.22x10^{-2}/s$. Using the *lsqnonlin* algorithm of *MATLAB*®, the Cauchy stress *vs* stretch ratio data was fitted to the five models. It should be recalled that the Ogden, Yeoh and Lopez-Pamies models are expressed as a series sum. The strain energy density terms can be written as 1st order, 2nd order, 3rd order, etc. In this work, only the first 3 orders of the strain energy density functions are considered for Ogden and Lopez-Pamies models. The Yeoh model is used in its 2nd and 3rd order only. The 1st order Yeoh model is equivalent to a Neo-Hookean solid which shows a very poor fit due to the absence of a strain hardening factor, as well as I_2 independence. Hence it is omitted in this work. Therefore, in total there are 10 hyperelastic Cauchy stress functions to be fitted to the tensile test data; referred to as *10 cases* from here onwards.

The uniaxial tensile data fitted to these 10 stress functions are shown in *Figure IV.3.1*. Due to the absence of a strain hardening parameter, the Mooney-Rivlin model does not fit well at

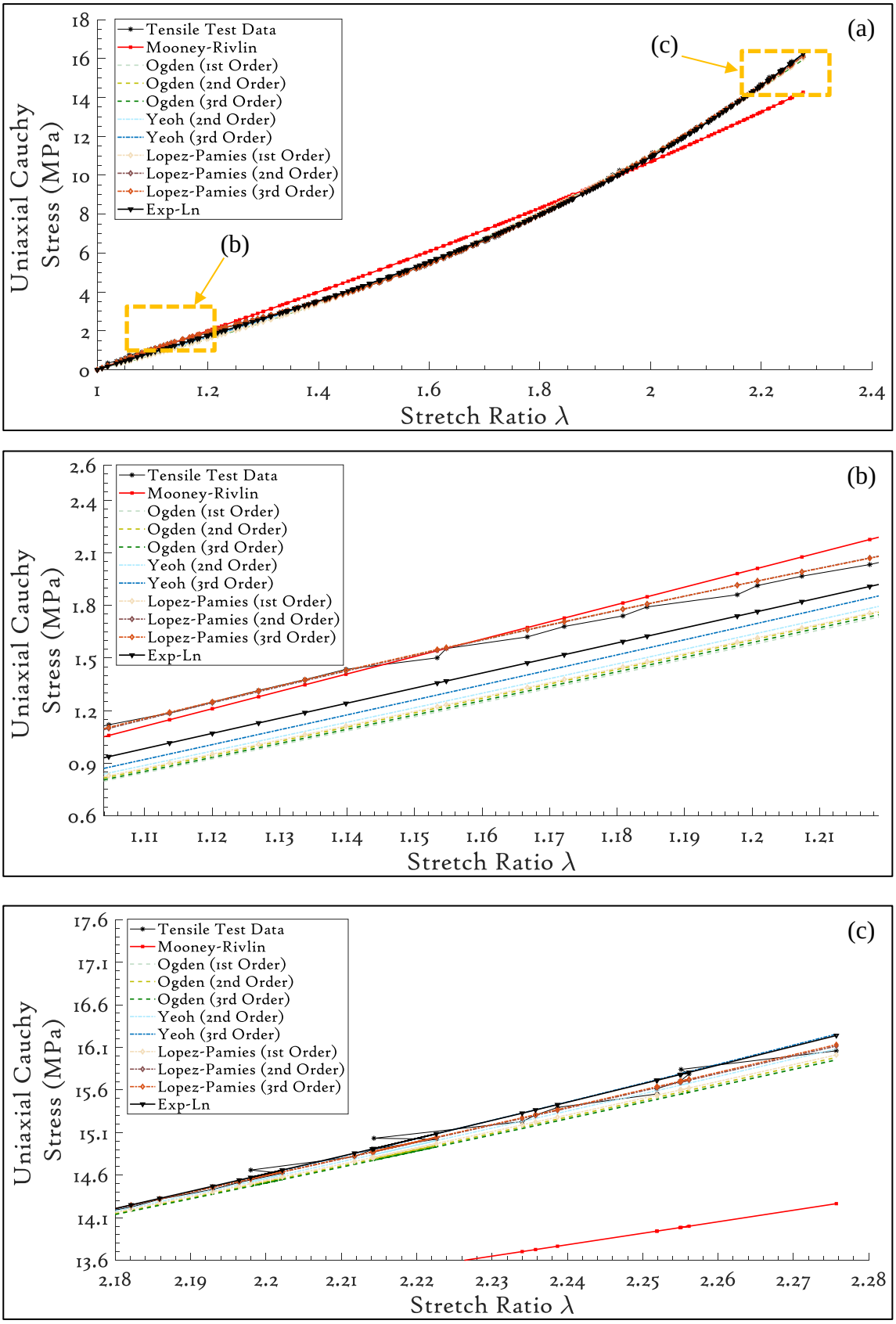

Figure IV.3.1: Uniaxial tensile test fit for the five models.

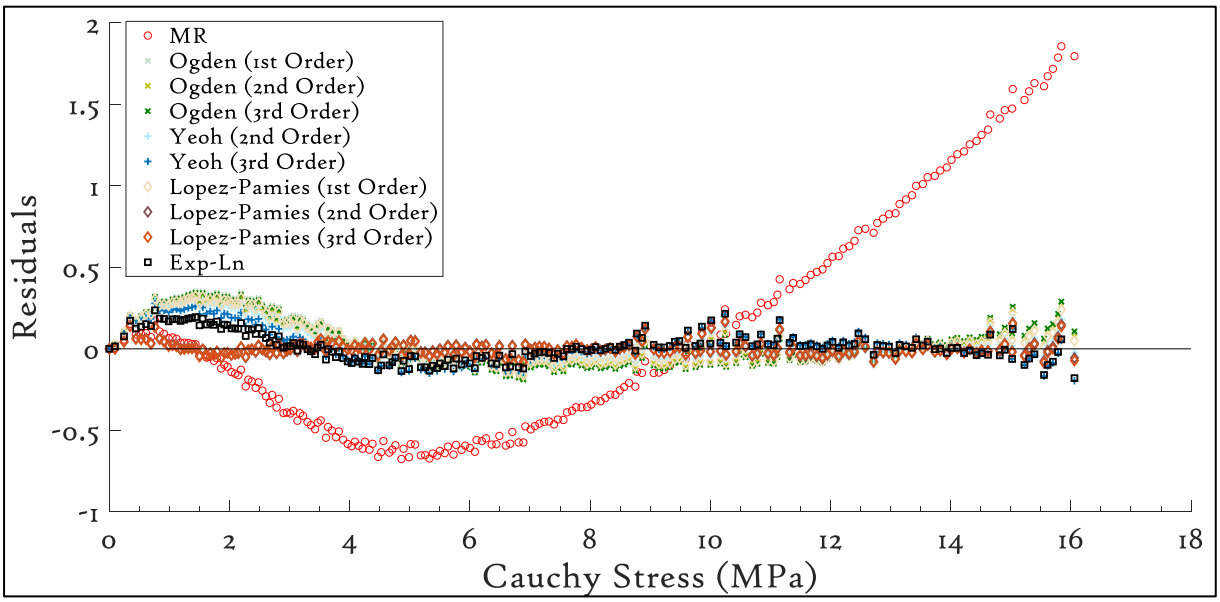

Figure IV.3.2: Residuals of the tensile test data fitting.

moderate and large strains. Overall, the other four models seem to fit to the data well at small as well as large strains. The residual values seen in *Figure IV.3.2* show that the Lopez-Pamies model of the 2nd and 3rd order fit closely to the data. The residual is an absolute value, calculated as $residual=\sigma_{data} - \sigma_{fit}$. Except for the Mooney-Rivlin model, all other models show a residual of ±0.4MPa or less. The strain energy density parameters calculated for each of the 10 cases are tabulated in *Table B.I.*

Planar uniaxial tests are not a true representation of the multi-axial inflation loading that the rubber undergoes in RCAIT. However, this study of different hyperelastic models and how they predict inflation behaviour highlights the importance of choosing the appropriate model. The small difference in the residual values between these models may result in a considerable degree of variability in the SERR evaluation which will be clear below.

Before moving to the SERR evaluation, the Thick-Walled Cylinder Inflation evolution for each of these models based on the data from *Table B.I* should be considered. Following the algorithm described in *Figure IV.2.2* this data can be converted into a *fluid pressure vs specimen axial stretch ratio* evolution. Such a plot is shown in *Figure IV.3.3* compared with the experimental results. The fluid pressure is readily measured during the experiments, whereas the axial stretch ratio is calculated using image processing as presented in *Chapter III*. The Ogden models seem to follow the experimental data quite well until the confinement contact. However, upon close observation, it is revealed that the confinement contact pressures for the Ogden models lie between *40-45bar*, which, for the experimental case is nearly *57bar*. This indicates that the close agreement of the curves and the experimental data

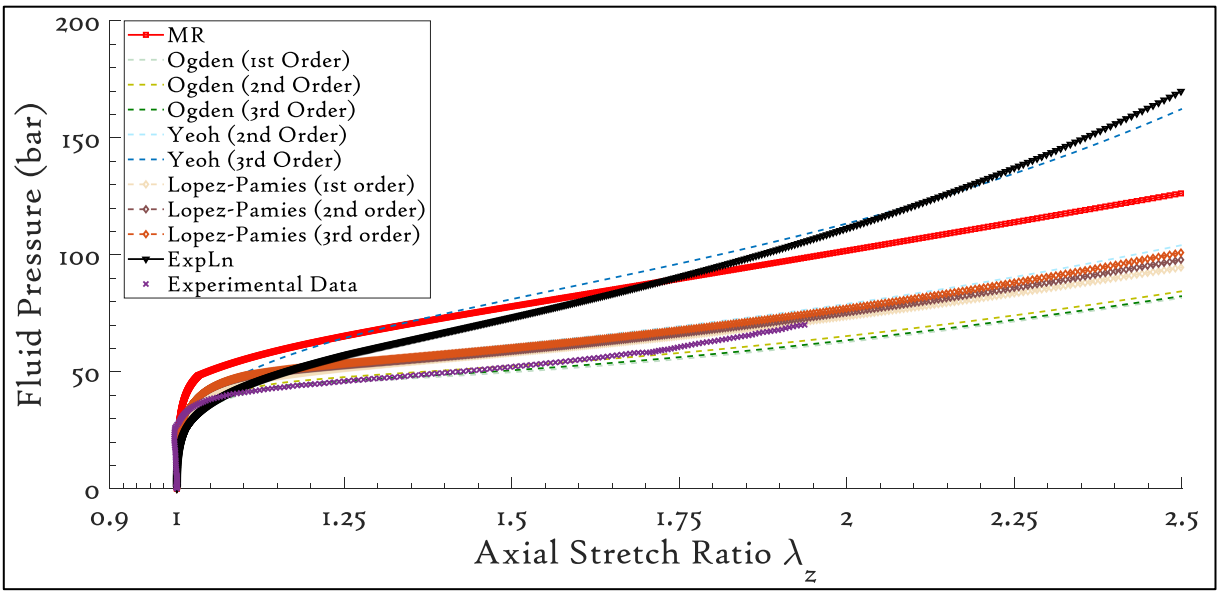

Figure IV.3.3: Thick Walled Rubber Cylinder Inflation behaviour for 10 cases compared with the experimental data.

is merely a coincidence. In fact, none of the five models predict the confinement contact pressure correctly. This result is not favourable, but it is indeed interesting and important.

Overall, after a strain of as little as *5%* (λ_z*=1.05*), all the curves start diverging. The ExpLn and Yeoh model (3rd order) show considerable strain hardening, especially after *100%* strain. All 3 orders of the Lopez-Pamies model follow a parallel trend in the CIS, as do the Ogden model curves. It is interesting to note that in *Figure IV.3.2* all models except Mooney-Rivlin shown similar values of residuals at large strains (*~200%*). This indicates that these models can predict the rubber behaviour precisely even at large strains. However, the behaviour of these models is very different in *Figure IV.3.3* at large strains. This could be due to the

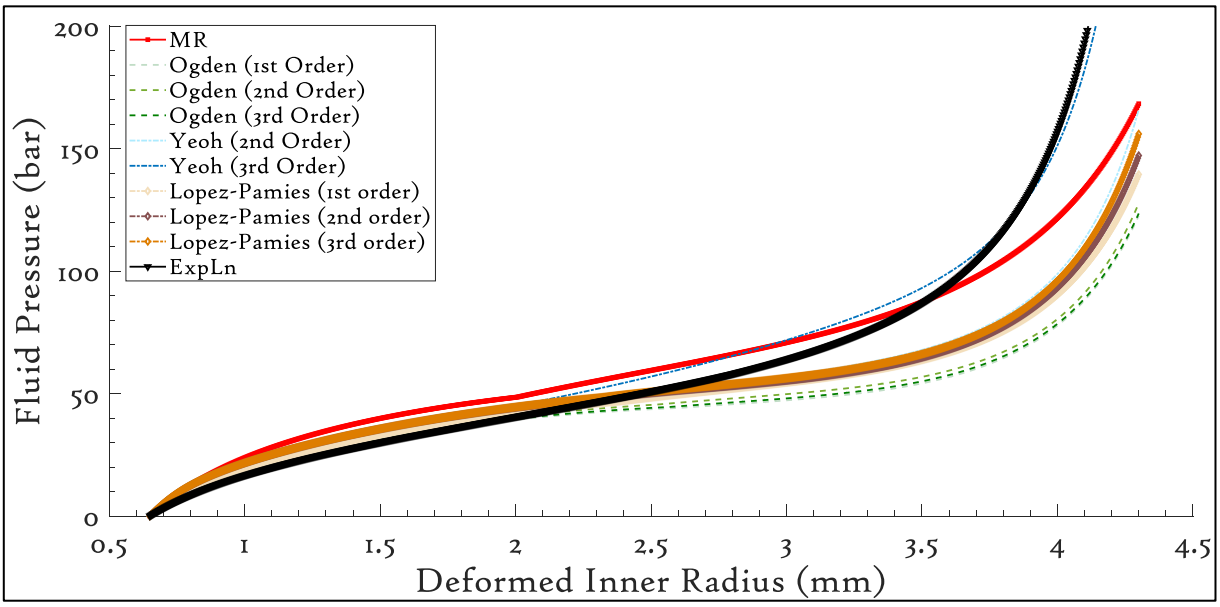

Figure IV.3.4: Evolution of fluid pressure (P) due to increasing deformed inner radius (v_0).

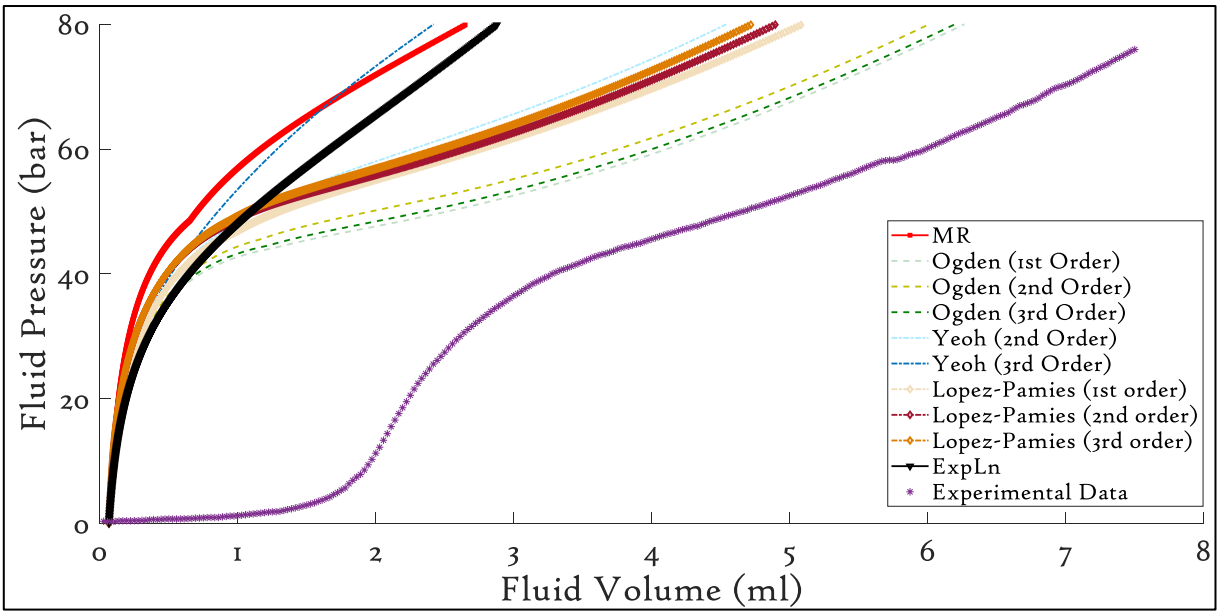

Figure IV.3.5: Fluid pressure evolution plotted for all 10 cases and compared with the experimental data.

multiaxial loading that the rubber cylinder undergoes in RCAIT. In addition, the presence of the confinement tube adds an extra boundary condition to the rubber inflation which, along with the incompressibility of the rubber, means that the rubber is forced to stretch more in the axial direction. For hyperelastic models showing higher strain hardening (ExpLn and Yeoh – 3rd order), the fluid pressure increases much more at large strains compared to the other models. These two phenomena together mean that the two models (ExpLn and Yeoh-3rd order) predict a larger amount of energy stored in the rubber. This is likely to result in a lower estimate of the SERR. In the forthcoming section, this effect is studied in detail.

A plot of the evolution of fluid pressure (*P*) due to the increasingly deformed inner radius (*v*) is shown in *Figure IV.3.4*. This plot is a direct outcome of the algorithm presented in *Figure IV.2.2*. The deformed inner radius and the axial stretch together accommodate for the injected volume. The trend seen in *Figure IV.3.3* is followed by each hyperelastic model in *Figure IV.3.4* as well. For fluid pressures greater than *60bar*, the models ExpLn and Yeoh- 3rd order show smaller deformations in axial as well as radial directions, thereby predicting a smaller injected volume during the test. This could mean that in *(II.4.15)* the fraction of ΔU_e^{rubber} will be smaller, hence the predicted SERR value could also be small.

Figure IV.3.3 and *Figure IV.3.4* can be combined to obtain the evolution of the fluid pressure, predicted for all 10 cases as shown in *Figure IV.3.5*. The plots are also compared with the experimental data shown in *Figure IV.2.1*. A clear disagreement between the prediction and the experimental data is seen. During the experiments, a small initial volume (approx. *1.5ml-2ml*) of liquid must be injected in order to occupy the empty space between the pre-crack

length of the steel cord and the rubber envelope. During this stage, the fluid pressure increases only slightly (*5bar-6bar*). The addition of this correction to the injected volume (*~1.5ml*) to the 10 cases shifts the curves to the right, and the pressure-volume evolution from the experimental data is virtually parallel to that predicted by the Ogden models, similar to the curves seen in *Figure IV.3.3*. Again, the confinement contact point of the experiment and the one predicted by the Ogden models do not match, indicating that the closeness of the curves is merely a coincidence.

IV.3.2. Effect of model on SERR calculation

Following the general relation of SERR with the test parameters and rubber material parameters described by *(IV.2.17)*, the SERR can now be calculated for the particular rubber in question – *Mix B*. For any given fluid pressure, the deformation state of the rubber cylinder and, as a result, the strain energy density can be calculated using the numerical algorithm described in *Figure IV.2.2*. Using *(IV.2.17)*, the *SERR vs Fluid Pressure* evolution can now be plotted, as seen in *Figure IV.3.6*. Similar to *Figure IV.3.3*, all the curves follow nearly the same path up to *50bar*. There is a large spread between the curves after that point, especially as the pressure increases. As predicted earlier, for large strains (or *pressure>120bar*) the models ExpLn and Yeoh (3rd order) show a lower estimation of G_c. The curves of the all three orders of the Lopez-Pamies model follow each other closely, even at pressures up to *140bar* (nearly twice that of the crack propagation pressure in *Figure IV.2.1*). Similar behaviour is observed for the Ogden models as well.

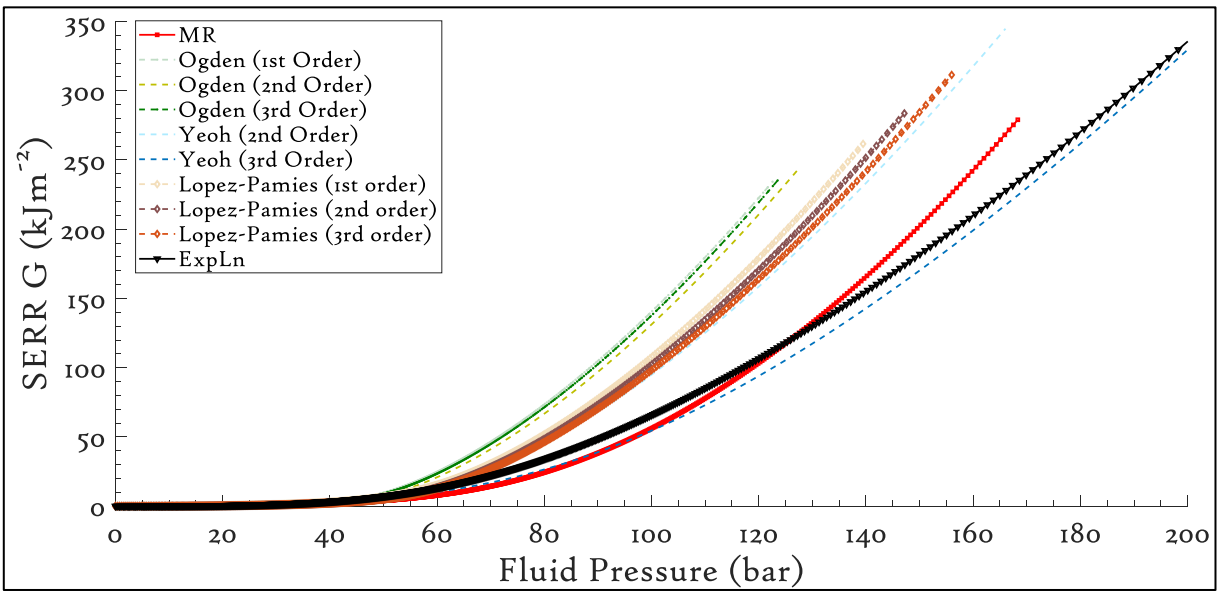

Figure IV.3.6: Evaluation of SERR for all 10 cases.

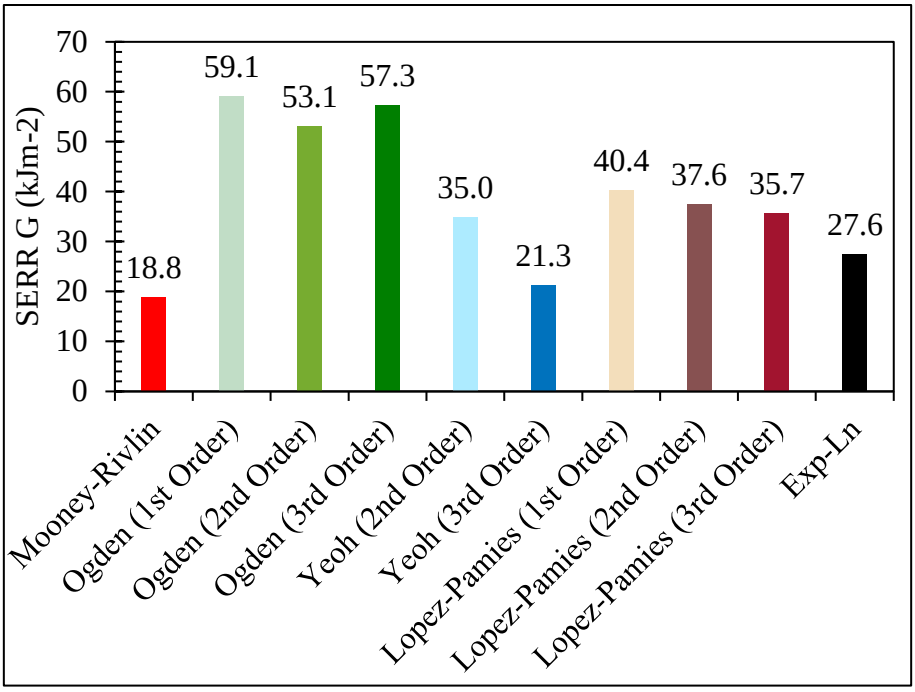

Figure IV.3.7: SERR values evaluated for the test case in Figure IV.2.1.

Using *Figure IV.3.6* the SERR values can be calculated for the test case shown in *Figure IV.2.1* at a fluid pressure of *74.9bar*. The results are presented in *Figure IV.3.7*. Between the five hyperelastic models the SERR value varies within a range of nearly $40kJm^{-2}$. To put this into perspective, a critical SERR value of $\sim 20kJm^{-2}$ was reported in [46] for rubber-steel cord composite fracture. This signifies that the rubber model significantly influences the evaluation of the critical SERR for RCAIT. The model parameters have been found using only uniaxial tensile test data. However, complex loading conditions such as pure shear and equi-biaxial tension in combination with the uniaxial tensile tests might produce more reliable rubber model fitting. Such a technique has been used in [78] and [79]. However, a limited availability of specimens resulted in relying on tensile test data only. Moreover, the planar tests (uniaxial, equi-biaxial and pure shear) carried out at a certain loading rate may not represent the volumetric multi-axial loading experienced by the rubber in RCAIT. It is possible that, the models used in this work may not be the best ones available in the literature. The algorithm presented in *Figure IV.2.2* can be applied to more recent models such as the *Shariff Model* [88], *Attard Model* [89] and *Extended Tube Model* [90]. Finally, for better data fitting, the volumetric data (*Figure IV.2.1*) can be used in conjunction with the theoretical model to predict the hyperelastic model parameters.

Nonetheless, the RCAIT has already proved to be a reliable and useful technical method for the comparative evaluation/selection of tyre cord/rubber interfaces and, clearly, when

sufficient attention is paid to the actual mechanical behaviour of the rubber, it constitutes a test capable of quantitative estimates of adhesion performance.

IV.4. Volumetric Data Fitting

Examining the results presented in the previous section, it is clear that quantitative analysis of how constitutive models affect SERR evaluation is important. However, it is also important to choose such a model wisely and fit the experimental data to obtain precise values of material properties. As explained above, due to a limited availability of the rubber samples for performing complex tests (bi-axial, pure shear etc.), fitting any rubber constitutive model to the data is not easy. However, as shown previously in *Chapter III*, there is a lot of information concealed in the *pressure vs injected volume* plot, such as *Figure IV.2.1*, which can be used to fit the rubber constitutive models. In *Chapter III*, volumetric data was used to fit to an Ogden model of the 1st order. It was shown that the model parameters calculated from the volumetric data give more accurate results than those calculated using planar test data.

Thus, this section focuses on the evaluation of strain energy density parameters for the 10 cases (or five hyperelastic models) using the volumetric data from *Figure IV.2.1*. Similar to the case with the Ogden model (1st order), the volumetric data from *Figure IV.2.1* can be used in conjunction with the theoretical model (§*IV.2*) expressed in a reverse order so that material parameters for all five hyperelastic models can be evaluated.

IV.4.1. Data fitting algorithm

The volumetric data fitting starts with a careful choice of the data from the CIS regime in the *pressure vs injected volume* plot. This ensures that the rubber tube is fully inflated and is in contact with the confinement tube. However, the fracture has yet not initiated. By choosing these specific data points, the number of variables in the system of equations to be solved is reduced to the number of material parameters to be evaluated. This is because, in the CIS, if the axial stretch ratio is known, the deformed inner radius of the rubber tube can be directly calculated using *(IV.2.6)*, *(IV.2.7)* and the condition $w=R$. On the contrary, if the volumetric data is chosen from the UIS regime, the deformed inner radius is unknown, and each data point will add an extra variable in the system of equations. For example, if the Mooney-Rivlin model is to be fitted to the UIS data with 40 data points, the number of variables to be found will be 2 material parameters (C_1 and C_2) and 40 deformed inner radii *i.e.* 42 variables in total. Each data point can only form one nonlinear equation. Hence, there will be 40 equations to be solved for 42 variables. Such a system of equations is indeterminate.

Care must be taken while choosing the data points, since often the confinement contact point is not distinctly visible in the *pressure vs volume* data. This poses a risk of mistakenly using UIS data points to solve equations of the CIS regime. It will result in erroneous results and the evaluation of SERR will not be reliable. To avoid this, an adequate number of data points should be chosen immediately before the fracture initiation. There is no rule to decide how many data points are adequate, though in principle every data point from the CIS regime can be used. Again, care should be taken so that these data points do not lie in the crack propagation regime.

Once the data points are chosen, the marker tracking technique should be used (as shown in §*III.3.3*) to calculate axial stretch ratio ($\lambda_{z_{exp}}$) at each data point (P_{exp}). Subsequently, a 4-step algorithm, as shown below, can be followed using *MATLAB*® (or another nonlinear curve fitting tool) to fit hyperelastic material parameters to the volumetric data:

A. Choose a hyperelastic model. Choose its material parameters as a first guess. Set upper and lower limits on those material parameters.

B. Calculate deformed inner radius at each data point using $v = \sqrt{\frac{v_0^2}{\lambda_{z_{exp}}} + \frac{R^2\lambda_{z_{exp}} - w_0^2}{\lambda_{z_{exp}}}}$

C. Using the Thick-Walled Cylinder Inflation Model, calculate P_{int}, σ_z and F_z for each data point.

D. Using *lsqnonlin* (or any other nonlinear least square fitting algorithm) calculate

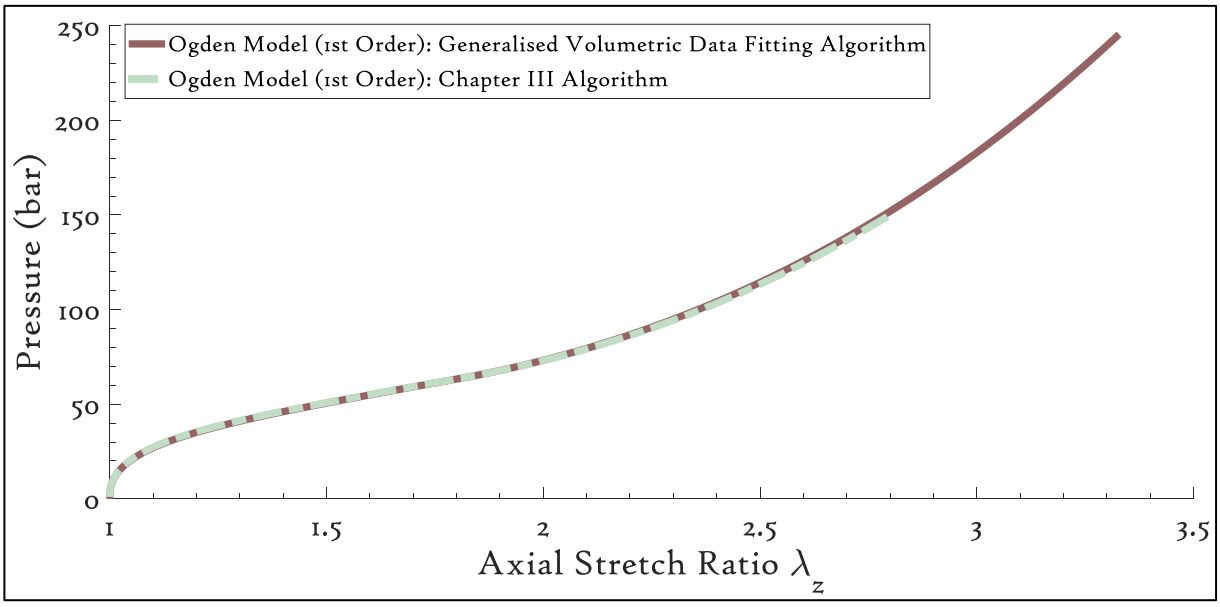

Figure IV.4.1: Comparison between Volumetric Data Fitting algorithms presented in current chapter and Chapter III.

hyperelastic material parameters of the chosen model in order to minimise the cost function $\{(P_{int} - P_{exp}) + (2\pi \sum_{v}^{R} \sigma_z(r) r \delta r - P_{int} \pi v^2)\}$

The algorithm presented here can be tested by comparing its performance with the one presented in *Chapter III*. In *Figure IV.4.1*, the volumetric data in *Figure IV.2.1* is treated using the two algorithms and *pressure vs axial stretch ratio* evolution is presented for both methods. Similar to the *Figure IV.2.3*, both of the curves follow the exact same path even at a strain value of *275%*. Thus, the generalised volumetric data fitting algorithm presented here can now be used to process the data and evaluate the critical SERR values for the five hyperelastic models.

For the test case shown in *Figure IV.2.1*, *36* consecutive data points (from *60bar* to *70bar*) are chosen just before the fracture starts. The axial stretch ratios at each data point are calculated using the image tracking technique. Subsequently, the volumetric data fitting algorithm presented above is followed to fit the material parameters of the five hyperelastic models.

The experimental data (P_{exp}) and the fitted data (P_{int}) are plotted against the injected fluid volume in *Figure IV.4.2*. Except for the 1st order Ogden model, all other hyperelastic models fit the data really well. Overall, the data fitting seems to be better compared to the one for tensile test data (*Figure IV.3.1*). The strain energy density parameters calculated using this fitting technique are tabulated in *Table B.II*. Clearly, the material parameter values calculated using volumetric data fitting are vastly different. At this stage, all hyperelastic models seem to show a very good fit. However, it is important to note that the raw data used to fit these

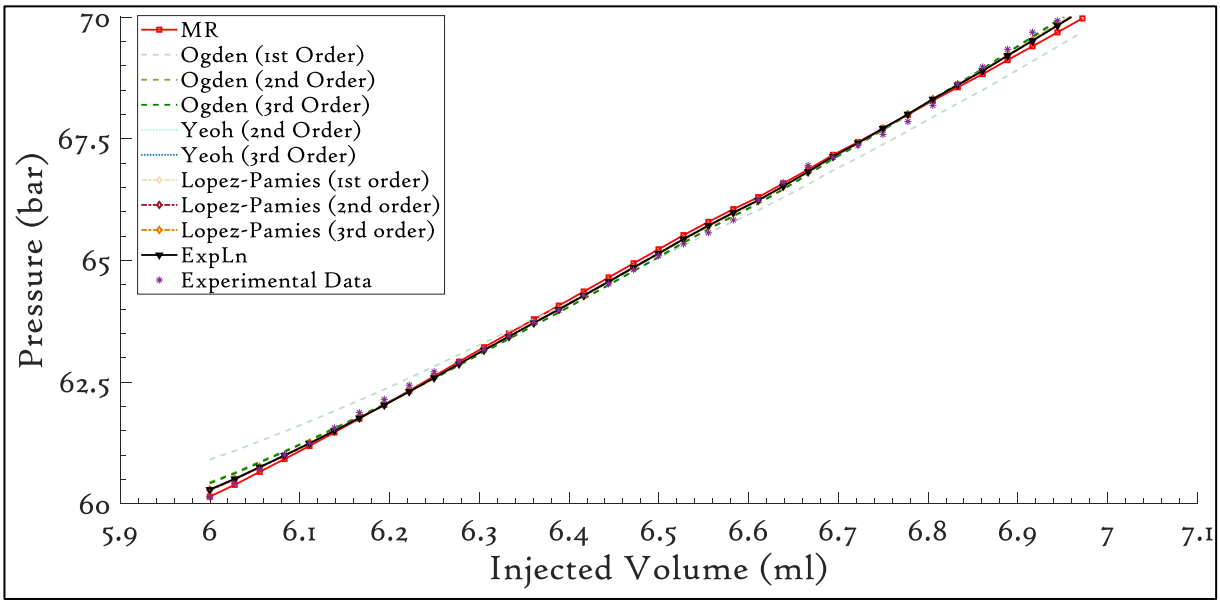

Figure IV.4.2: Volumetric data fitting for the specimen in Figure IV.2.1.

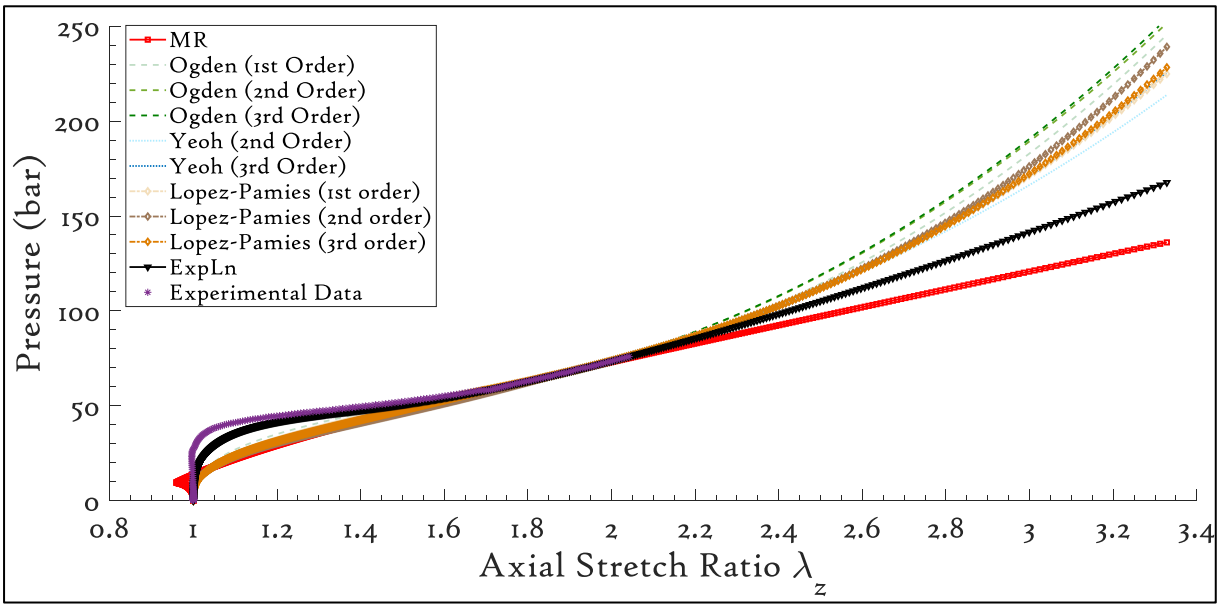

Figure IV.4.3: Pressure evolution for all 10 cases calculated using the volumetric data fitting.

models are only a small portion of the entire inflation experiment. It will now be interesting to see how this fitting predicts the volumetric evolution of the specimen.

Using the material parameters shown in *Table B.II* in conjunction with the Thick-Walled Cylinder Inflation Model (*Figure IV.2.2*), the evolution of *pressure vs axial stretch ratio* (λ_z) is plotted in *Figure IV.4.3*. As seen earlier, all hyperelastic models fit well to the data between *60bar* and *70bar*. In particular, the ExpLn model (black curve) seems to fit the volumetric data fairly well even in the UIS regime. The Mooney-Rivlin model, on the other hand, fits poorly in the UIS regime. This is believed to be due to a negative value of C_1 (see *Table B.II*). The rest of the models follow a very similar curve up to *80bar*, after which all of the curves

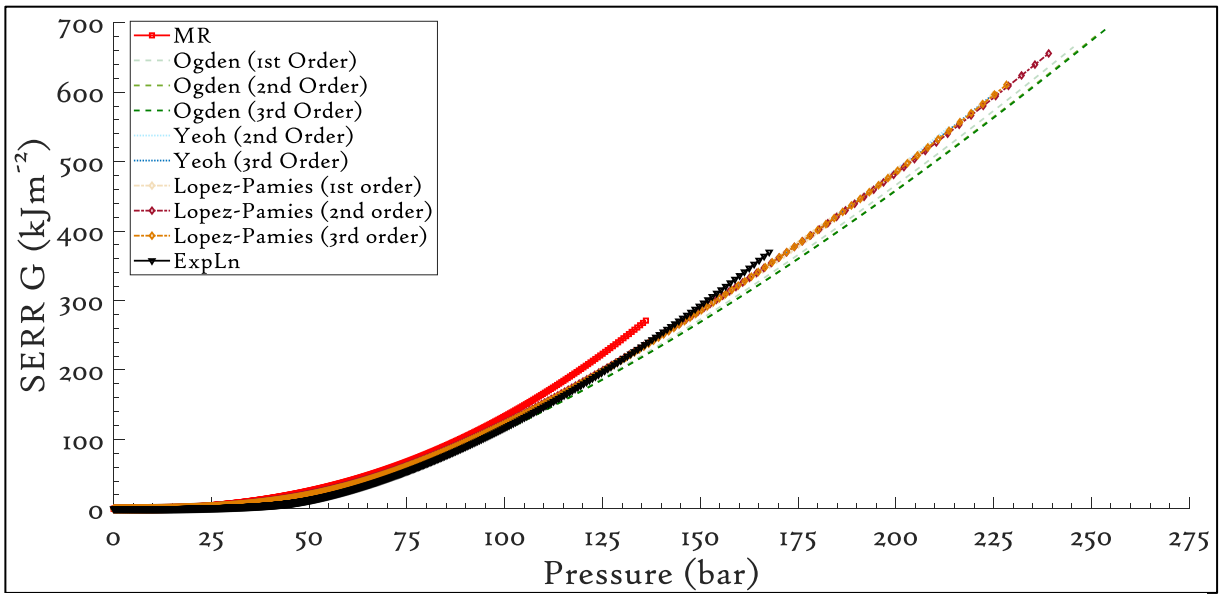

Figure IV.4.4: SERR values calculated for 10 cases using the volumetric data fitting.

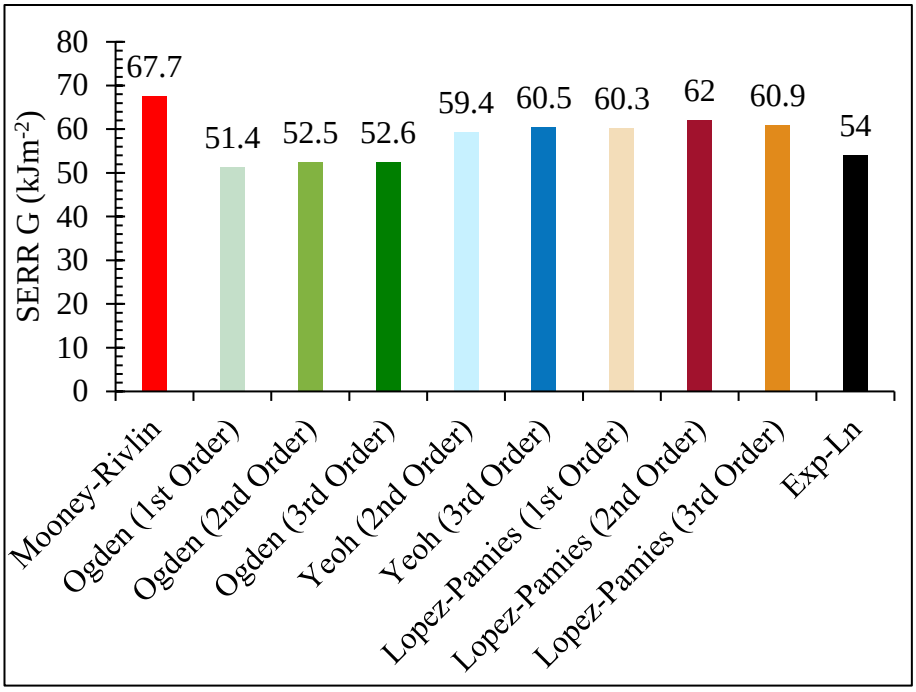

Figure IV.4.5: SERR values evaluated using the volumetric data fitting for the test case in Figure IV.2.1.

diverge. The Yeoh and Lopez-Pamies models show nearly identical behaviour up to *150bar*. This suggests that the SERR value predicted by these models could lie within a short range. Also, it can be predicted that the ExpLn model will show a very different critical SERR value.

The SERR values calculated using the material parameters from *Table B.II* and the algorithm in *Figure IV.2.2* are plotted against fluid pressure in *Figure IV.4.4*. Unlike the behaviour seen in *Figure IV.3.6*, the SERR curves in *Figure IV.4.4* do not show a spread even at *100bar*. Since the material parameters are calculated using the volumetric data, the hyperelastic models tend to show similar behaviour even at large strains (*~250%*). Except for the Mooney-Rivlin model, all other models show a moderate to high degree of strain hardening, resulting in variable values of SERR. This can be further investigated for the specimen in *Figure IV.2.1*.

Figure IV.4.5 shows the critical SERR values evaluated for *Figure IV.2.1* using *Figure IV.4.4*. As mentioned above, the spread between the values is much smaller, *~14kJm*$^{-2}$, compared to the *~40kJm*$^{-2}$ spread observed in *Figure IV.3.7*. Moreover, the critical SERR values calculated using the volumetric data fitting technique are different from those calculated using tensile test data.

IV.5. Chapter IV Summary & Further Discussion

In this chapter, numerical analysis of the Rubber Cord Adhesion Inflation Test (RCAIT) using five hyperelastic models has been presented. Firstly, a Thick-Walled Cylinder Inflation Model applicable for a broad range of hyperelastic models was discussed. The key equations required to construct the model along with the algorithm were also presented. The theoretical model was first applied to the Mooney-Rivlin model and the 1st order Ogden model, and the results were compared with those presented in *Chapter II*, as shown in *Figure IV.2.3*. The curves obtained from both models, above and from the previous chapter, follow very similar trends. This confirms the validity of the generalised Thick-Walled Cylinder Inflation Model.

The model was then applied to five different hyperelastic models (10 cases have been considered in total) and the effect of each model on RCAIT results was studied. It was found that although most of these models fit well with the uniaxial tensile test data of the rubber under consideration, their behaviour is drastically different when applied to RCAIT. The models predict vastly different strain values at large stresses (fluid pressures), resulting in a wide range (~$40kJm^{-2}$) of critical SERR for all 10 cases. This result can be attributed to several factors such as fitting of the models to the data, difference in loading conditions between tensile test and RCAIT as well as the inability of the models to predict the rubber's behaviour, etc.

To overcome the limitations related to the tensile test data fitting, a generalised volumetric data fitting technique was introduced. The *pressure vs axial stretch ratio* data obtained from the experimental results and image tracking technique can be used in the Thick-Walled Cylinder Inflation Model previously presented to get hyperelastic material parameters. A similar approach was presented in *Chapter III* in the case of the 1st order Ogden model. The results obtained by both algorithms, the volumetric fitting algorithm for Ogden model and the generalised volumetric fitting algorithm applied to the Ogden model, were compared as shown in *Figure IV.4.1*. It was found that the curves match extremely well even at large strains. This indicates that without any prior rubber testing, an RCAIT can be performed on a tyre rubber-steel cord specimen and the SERR can be evaluated. For a tyre designer this will prove to be very convenient as new elastomer-metal composites can be tested without having any prior knowledge about the rubber. However, care should be taken while choosing the lubricant if a different elastomer is being tested. The *CRC Silicone Grease* was found to be one of the better lubricants for *Mix B* only. This lubricant may not assist in the axial

deformation of other elastomers, thereby affecting the quality of the volumetric data fitting. There could be solvent effects occurring at the rubber-lubricant interface such as those discussed in [91] and [92]. Due to this, the axial stretch ratio calculated for a given pressure value will be lower than the ideal/maximum value. This will predict wrong material parameter values and the SERR evaluation will be unreliable.

The volumetric data fitting technique was applied to the five hyperelastic models previously chosen for the Thick-Walled Cylinder Inflation Model. It was found that the ExpLn model predicted the volumetric deformation more accurately than all other models. The rest of the models seem to predict similar behaviour to each other up to ca. *100bar*.

This technique of fitting volumetric data to the hyperelastic models is believed to be better than the usual planar test data fitting because of one more reason. The elastomer/rubber used in the specimen exhibits viscoelastic or perhaps visco-hyperelastic behaviour. The planar tests are performed at certain strain rates which will produce a certain amount of viscous dissipation. However, the inflation test is not planar and will operate at a completely different strain rate (volumetric strain rate) exhibiting a different amount of viscous dissipation. The crack propagation is of self-similar nature and therefore it is obvious to think that the viscoelastic dissipation should not affect the evaluation of the SERR. However, the material parameters used to calculate the critical SERR are directly influenced by the amount of viscous dissipation occurring during the inflation stages. Clearly, the planar tests (uniaxial, equi-biaxial, pure shear etc.) will allow estimation of the hyperelastic parameters associated with certain amount of viscous dissipation, which must be different from that exhibited during the inflation tests. On the contrary, by using the volumetric data to fit the material parameters, the viscous dissipation will already be accounted for and the critical SERR evaluation will be more reliable. This can be seen by comparing the *pressure vs axial stretch ratio* plots obtained by the two methods *viz*. *Figure IV.3.3* and *Figure IV.4.3*. Similar behaviour was observed in *Figure III.3.7*.

The theoretical work presented in this chapter can be extended in terms of fracture mechanics analysis for future study. From this point of view, it will be interesting to investigate how the rubber behaves under large circumferential strains present at the inner radius of the specimen. *Figure IV.5.1* shows the evolution of circumferential stretch ratio (λ_θ) at the specimen's inner radius as predicted using the 10 cases (five hyperelastic models). Using the data from *Figure IV.2.1*, λ_θ at the inner radius is found to be nearly *5.9* for all cases. A similar value was found

using FE modelling in *Figure II.2.6*. In [93], rubber specimens were tested under uniaxial loading until the fracture and the principal stretches at the fracture were presented. The maximum stretch before fracture was recorded as *3.8*. Therefore, the λ_θ values predicted by the five hyperelastic models indicate that the crack could be propagating not along the interface but parallel to the interface – inside the rubber envelope. In such an event, the geometry of the inflating rubber tube will change such that the inner radius is increased. The increase in the inner radius corresponds to the thin layer of rubber undergoing fracture when the crack is propagating and being deposited on the crack face. This in turn will change the evaluated fracture energy.

Figure IV.5.2 shows the evaluated critical SERR for the specimens in *Figure IV.2.1* with $v_0=1.15mm$ and $v_0=1.65mm$. In other words, respectively a *0.5mm* and *1mm* thick rubber layer remains on the steel cords during crack propagation. It can be seen that due to the reduction in the rubber thickness, the evaluated SERR values decrease, compared to those seen in *Figure IV.4.5*. This could be due to the fact that, with an increased inner radius, the rubber is more likely to behave like a thin membrane. Therefore, the energy stored in the rubber at any given pressure is likely to be similar for various hyperelastic models. Additionally, it indicates that the fracture is propagating through the rubber, thus explaining the lower values of G_c compared to *Figure IV.4.5* where fracture is assumed to have propagated along the interface.

In reference [57], 90° peel tests on rubber-steel adhesion showed a value of G_c of $\sim 30kJm^{-2}$. The values seen in *Figure IV.5.2 (b)* are closer to this value than those in *Figure IV.4.5*,

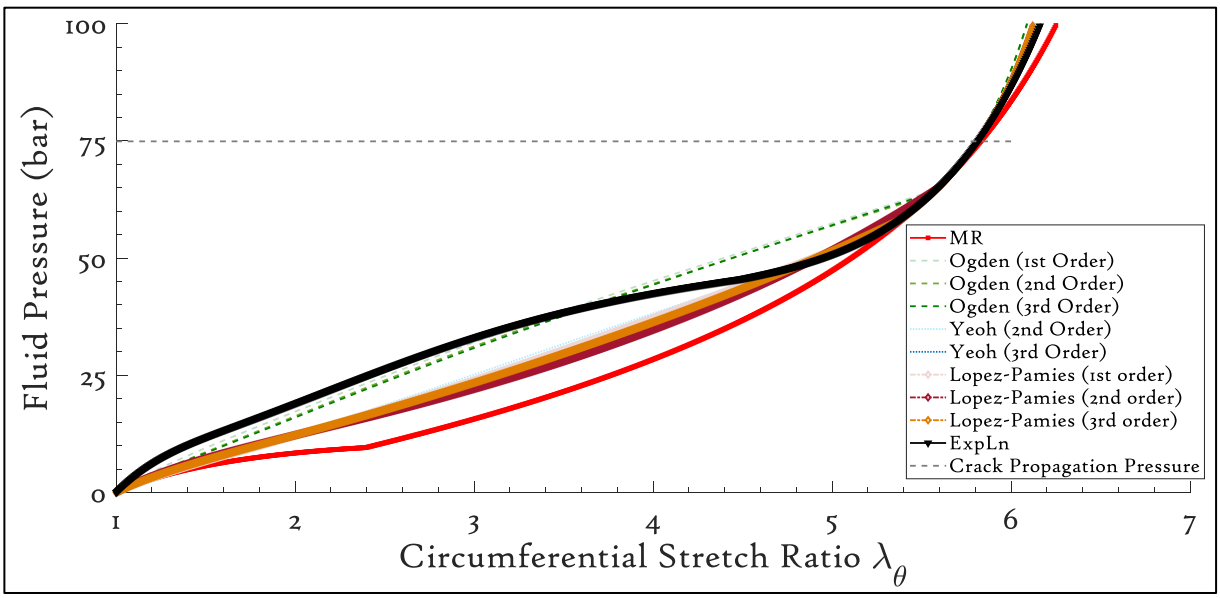

Figure IV.5.1: Evolution of circumferential stretch ratio at the inner radius of the inflated rubber tube. Crack propagation pressure for Figure IV.2.1 is shown as a grey dashed line.

especially for the ExpLn model which has already been seen to predict the volumetric evolution more accurately than other models. This is a promising result for the RCAIT and opens new avenues. A study of crack faces will reveal if the crack propagates along the interface or inside the rubber parallel to the interface. However, due to the axisymmetric geometry, the crack face and the inner radius of the specimen are hidden. As a future project,

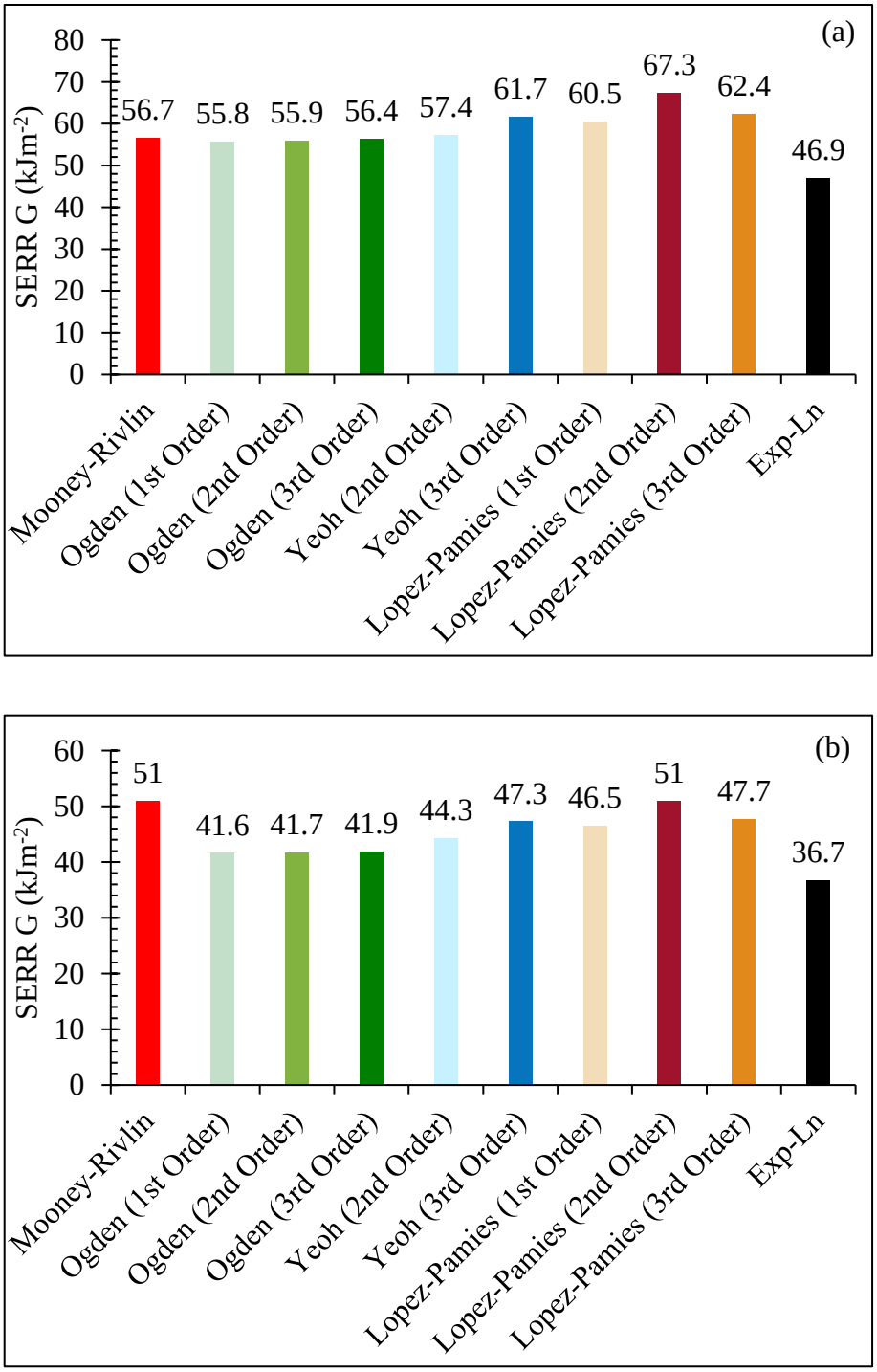

Figure IV.5.2: Effect of inner radius on evaluated SERR for five hyperelastic models (a) v_0=1.15mm (b) v_0=1.65mm.

a microscopic study of the failure faces or *in situ* X-ray tomography image analysis of the test could reveal more about this aspect. In such a case the critical SERR shown in *Figure IV.5.2* can be evaluated for the specimen based on a precise value of the inner radius measured during fracture propagation.

Chapter V: Perspectives and Conclusion

V.1. Some Future Applications of the RCAIT

Apart from the type of tests that have been presented in the previous chapters, the RCAIT protocol can potentially be used for many other applications. They include tests on various rubber composites discussed in *Chapter I* (rubber-steel cable, rubber-nylon, rubber-polyester etc.), tests performed under harsh conditions such as saline water or ethanol, and tests performed under cyclic loading to investigate viscoelastic dissipation mechanisms in the rubber and at the interface. In parallel to all the tests presented in this thesis so far, some additional tests were also performed to investigate the applicability of the test protocol to these test types. Below is a short summary of the tests and their results. No post-processing of the test data is presented here since the tests were performed solely with the purpose of exploring the capabilities of the RCAIT experimental arrangement. The detailed specifications of the materials (rubber, cables, cord etc.) and the loading rate are not discussed either. Regardless, the key here is to explore various ways the RCAIT can be applied to tyre rubber composites and not to study the material or interface behaviour – that in itself will be a new research path.

V.1.1. Tests on rubber-cables composites

Figure V.1.1: Steel cord used in commercial car tyres

Although the tests presented so far have been performed on rubber bonded to steel cords in the shape of a wire, in actual tyres the rubber is bonded to cables or cords made out of twisted filaments (see *Figure V.1.1*). If RCAIT were to be used in tyre industry as a standard fracture mechanical test on tyre rubber-steel cord adhesion, the specimens that would need to be tested must be made of such cables instead of wire cords. With this aim, two specimens with two types of cables, adhered to the same type of rubber, were tested. The specimen with cable type 1 is shown in *Figure V.1.2*.

During the first test it was found that the twisted geometry of the cables allowed the water to leak through the entire length of the specimen even before the specimen could inflate fully. Even at a pressure as low as *20bar*, the injected water leaked from the other end of the cable. Therefore, to avoid the leak, the adhered end of the specimen was sealed with an epoxy, as

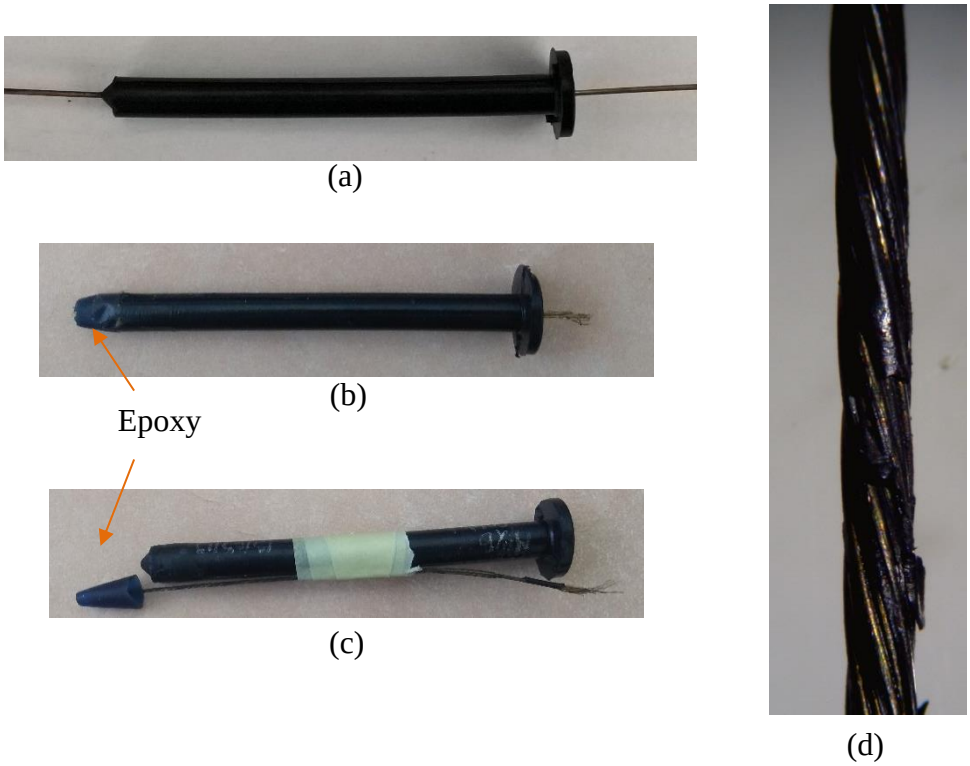

Figure V.1.2: (a) Test specimen with twisted cable strands bonded to rubber (b) test specimen sealed with epoxy at the end (c) fractured test specimen (d) fractured cable.

seen in *Figure V.1.2 (b)* and *(c)*. This experiment worked, and the specimens showed similar inflation behaviour to the one seen in previous chapters (see *Figure V.1.3*). The specimens showed nearly stable pressure during the crack propagation. The results are promising, since it shows that the tyre rubber-cable mesh adhesion can be tested using RCAIT. The results can be processed using the volumetric data fitting and marker tracking algorithm to calculate the critical SERR of the rubber-cable adhesion.

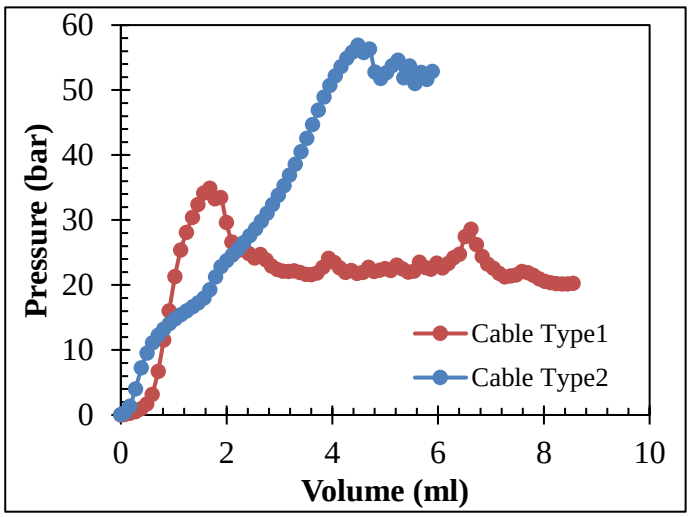

Figure V.1.3: RCAIT results for specimens with two types of cables bonded to the same type of rubber.

V.1.2. Tests using various injection fluids

While in operation, a vehicle tyre must withstand extreme environmental conditions such as high heat and humidity as well as various corrosive environments such as salt-water or other

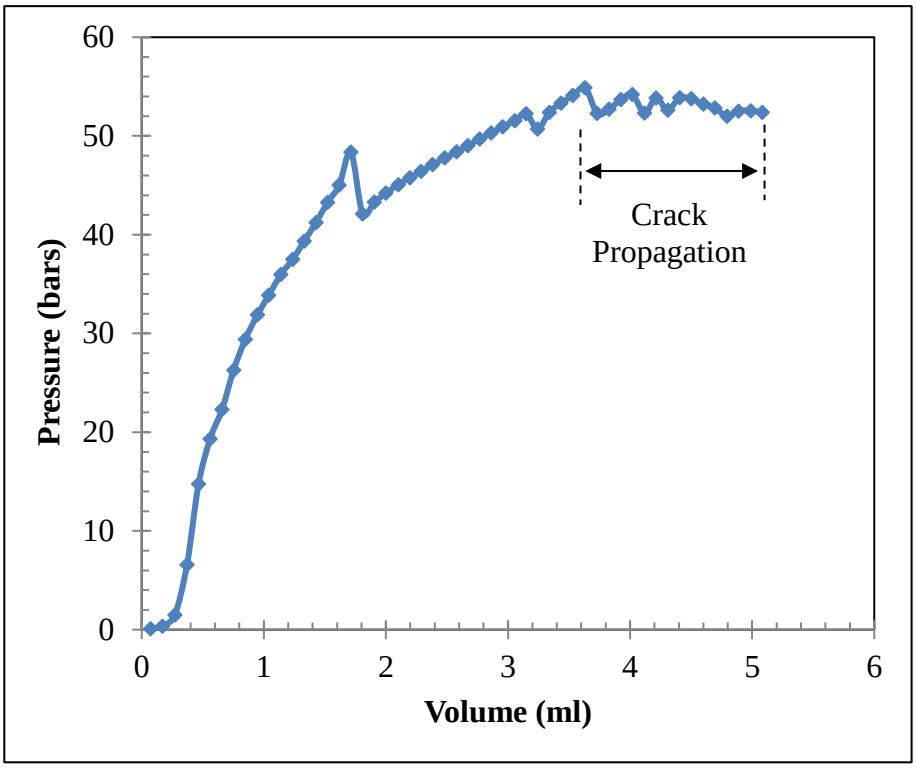

Figure V.1.4: RCAIT result for specimen injected with saline water.

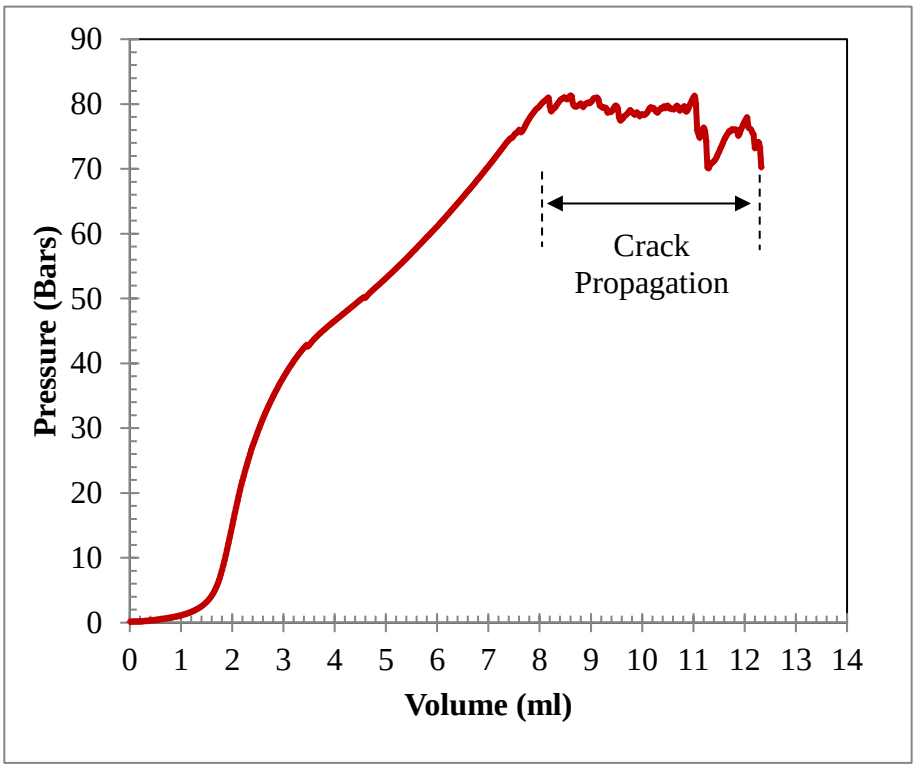

Figure V.1.5: RCAIT results for specimen injected with ethanol.

harsh fluid media. With this in mind, a few tests were performed on the specimens using saline water and ethanol as the injection fluid. The results for saline water are presented in *Figure V.1.4* and those for ethanol are presented in *Figure V.1.5*. In case of saline water, the behaviour is not exactly similar to the one seen in other tests, yet the fracture propagated at a nearly constant pressure of *55bar*. The specimen tested with ethanol showed similar behaviour to the specimens with water and the crack propagated at nearly *77bar*.

These results could be an outcome of the interaction between the injected fluid and the rubber or the interface. More detailed analysis could be done in the future using various other fluids such as Toluene, Acetone or Sulphate solutions which might interact with the interface under high pressure or cause considerable rubber uptake [94] - [97].

Another important reason to test the specimen with highly reactive and corrosive fluids is to separate the physical and chemical adhesive performance. By choosing such a fluid the chemical bonds at the interface can be broken leading to only physical adhesion or interlocking at the interface. At this stage, this is only a speculation. A detailed study of how various fluids affect the rubber and the interface will reveal interesting results.

V.1.3. Cyclic tests

Another interesting application of the RCAIT would be cyclic tests on the specimens under

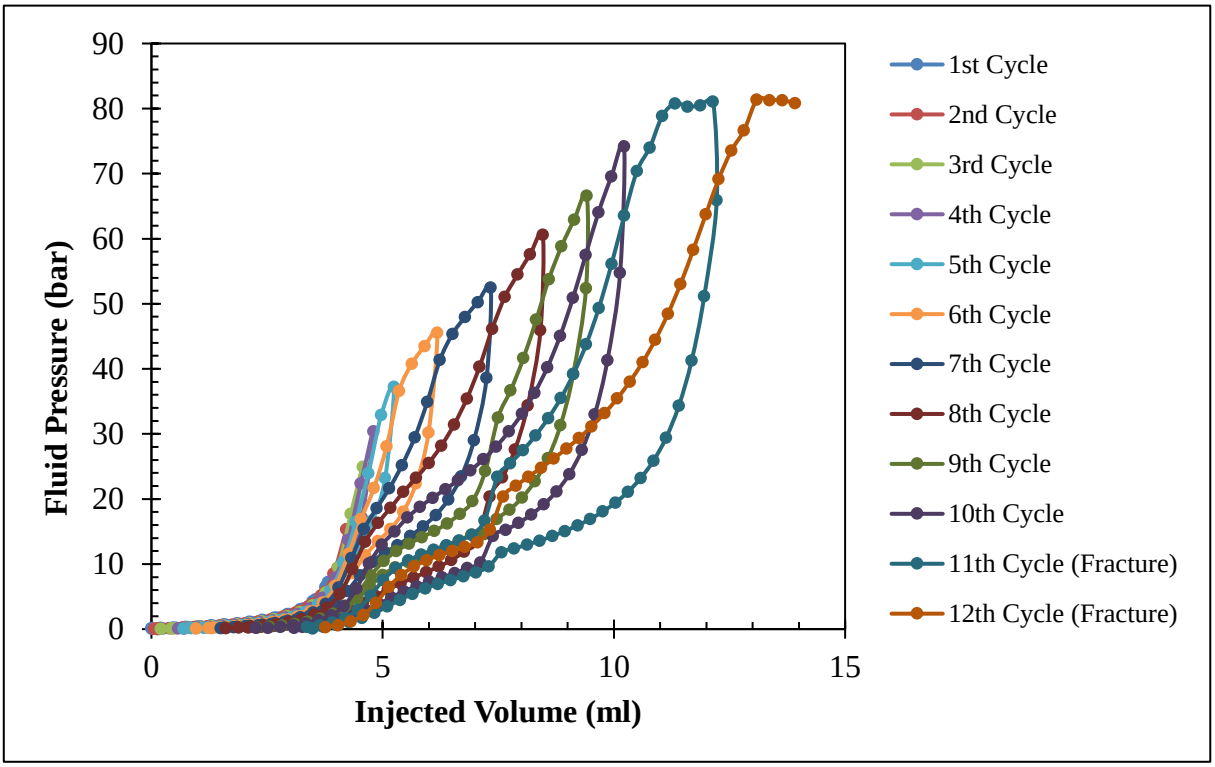

Figure V.1.6: Cyclic loading and unloading of an RCAIT specimen.

constant loading and unloading rates. This could include fatigue tests on the rubber or on the rubber-cord composite. Traditionally, hysteresis tests are performed on rubber samples to evaluate the Mullins effect [77] or other viscoelastic dissipation mechanisms. Similar tests can be performed on RCAIT specimens using volumetric loading and unloading until complete fracture. Results of one such test are shown in *Figure V.1.6*. The specimen was initially loaded at a constant volumetric injection rate up to a certain maximum pressure, much less than the expected crack propagation pressure. It was then unloaded at the same rate until the pressure dropped to zero. This constituted the 1st cycle. The cycle was repeated with increasing value of maximum pressure in the following cycles, until the specimen fractured completely. In the case of the specimen shown in *Figure V.1.6*, the crack propagated during the 11th and 12th cycle at nearly *82bar*.

The Mullins effect is clearly visible in the first few cycles as the curves do not line up to zero volume even though the pressure has dropped to zero. The remaining volume left in the specimen at zero pressure kept on increasing in each cycle. By calculating the energy stored in the specimen in each cycle ($\int PdV$) the energy dissipated in each cycle can be calculated. Subsequently, following the approaches presented in [98] and [99], the Mullins effect can be modelled for the rubber in question. If the dissipation in the rubber is modelled accurately, its effect on the critical SERR evaluation can be studied. In this way, the viscoelastic effects present in the rubber and at the interface can be separated with the use of one test only.

V.2. Conclusion

Rubber-cord composites form the skeleton of a modern pneumatic tyre. Strength and durability of the tyre depend on that of the rubber-cord adhesion. Various fracture mechanical tests are used in the tyre and rubber industry to test the adhesion performance of these rubber-cord composites. Those tests, however, suffer from various experimental artefacts. Therefore, a reliable evaluation of fracture energy of rubber-cord adhesion becomes a key issue for tyre designers.

This PhD thesis was aimed to develop a novel fracture mechanical test protocol referred to as *Rubber Cord Adhesion Inflation Test* (RCAIT) with one major goal – minimising the experimental artefacts associated with standard fracture mechanical tests. The test protocol was presented in detail in *Chapter II* along with initial theoretical, numerical and

experimental treatment of the fracture problem. The detailed experimental setup and post processing of the results was also presented. Initially, a semi-analytical model referred to as the *Thick Rubber Tube Inflation Model* was applied to Mooney-Rivlin type rubber. The model was then extended to Ogden type rubbers. The difference in evaluated fracture energy between the two modelling approaches was discussed, and it was found that precise evaluation of the rubber model parameters is key to reliable evaluation of fracture energy or critical Strain Energy Release Rate (SERR).

In *Chapter III*, the experimental study was extended to investigate the effect of lubrication between the specimen rubber and the confinement tube on the RCAIT results. Various commercially available lubricants were tested, and a suitable lubricant was chosen based on its performance as well as practicalities related to image processing. It was found that the chosen lubricant greatly affects the behaviour of the specimen during the test. The experimental study was then carried on to introduce a volumetric data fitting technique. The material parameters of the rubber were calculated using the *pressure vs axial stretch ratio* data (the volumetric data), and the specimen inflation behaviour was modelled using the previously introduced theoretical model to compare with the experimental results. It was found that the volumetric data fitting technique produces more accurate results than the conventional planar data fitting methods. The material parameters of the specimen rubber calculated using this technique were then used to calculate critical SERR of the interface in the case of lubricated and not-lubricated specimens. Following these results, the possible effect of lubrication on mode mixity was discussed. This study demands detailed analysis using a theoretical as well as finite element model. This could be a topic for future research work.

A repeatability study was also performed in this chapter for statistical analysis of the RCAIT results. The aim of this study was to test if the RCAIT can be used as a supplementary test to the conventional fracture mechanical tests. It was seen that the results varied within a small range, nonetheless, overall the specimen behaviour was repeatable. The results from this study will therefore be useful by the tyre designers at MFP Michelin for future rubber-metal adhesion tests.

The theoretical and numerical development presented in the previous chapters was explored further in *Chapter IV*. A generalised Thick-Walled Cylinder Inflation Model applicable to a broad range of phenomenological hyperelastic material models was presented. This model

was tested using the special cases of the Mooney-Rivlin model and the 1st order Ogden model which were previously studied in *Chapter II*. The results from *Chapter IV* and *Chapter II* matched almost exactly. Previously, it was shown that the results from *Chapter II* matched with the finite element results. This was strong evidence for the validity of the generalised theoretical model. The Thick-Walled Cylinder Inflation Model was then applied to the RCAIT to obtain results such as pressure *vs* volume evolution, axial stretch ratio evolution, as well as calculation of the interfacial critical SERR. The results obtained with the theoretical model were found to be mismatching with the experimental data. A generalised volumetric data fitting algorithm was proposed following the procedure used in *Chapter III* with the aim of reducing this mismatch. It was shown that the results obtained with this new technique were closer to the experimental results. Therefore, the critical SERR evaluated with this technique is believed to be more reliable.

One interesting topic discussed in *Chapter IV* was locating the path of the crack – either along the interface or along the rubber. Depending on this path, the calculation of the critical SERR needs to be changed. It was shown that by shifting the crack path radially by *0.5mm-1mm*, the critical SERR evaluation changes considerably. This topic can be studied further by performing a microscopic or XPS study of the crack faces.

The fracture mechanical study performed in this research work has been limited to a macroscopic LEFM approach using mainly semi-analytical as well as experimental approaches. Finite element modelling to study the effects of friction and lubrication on the specimen deformation, fracture modes and crack propagation has not been presented. Although the work was being performed during writing of this thesis, it was far from being presentable. The work presented in this thesis needs to be explored further along these lines.

During the repeatability study, a large number of specimens were tested. A comprehensive crack face analysis can be carried out in future to study the fracture in detail. The observations from such a study used in conjunction with an *in-situ* X-ray tomography analysis of the fracture propagation may lead to interesting conclusions for future research work. Following these results, the rubber-metal interface can be modelled in a finite element software using Cohesive Zone Modelling or similar approaches. This model can then be extended to include dissipation occurring at the crack process zone.

The possible future applications of RCAIT presented above show a promising picture. The test protocol can be regarded as versatile since several experimental conditions including

aggressive environmental and loading conditions can be tested on tyre components. This PhD thesis was part of a huge research project with goals that will have positive impact on sustainability targets of MFP Michelin. By utilising such a versatile test protocol, the costs involved in tyre material research can be reduced. Greener and sustainable rubber compounds can be tested for their strength and durability with better accuracy in shorter period of time. The severe environmental conditions can also be simulated during the test so that the reduced mass and increased rolling resistance goals can be achieved. Lowered mass of tyres will require lesser raw materials and it will also reduce the complexity in tyre production. This will positively impact the cost of production as well as the environmental effects of tyre production. The reduced tyre mass will help reduce the rate of deforestation as well as ocean pollution. This thesis work will therefore be a stepping-stone towards a green and sustainable mobility.

References

[1] S. Bertman, Handbook to Life in Ancient Mesopotamia, Oxford University Press, p.35, 2005.

[2] R. W. Thomson.Patent US5104A, 08 May 1847.

[3] B. E. Lindemuth, "An overview of tire technology," in *The Pneumatic Tire*, US Department of Transportation, NHTSA, 2006, pp. 2-27.

[4] A. Lechtenboehmer, H. G. Moneypenny and F. Mersch, "A review of polymer interfaces in tyre technology," *Polymer International, 22(4), 265-301,* 1990.

[5] L. R. G. Treloar, "The elasticity and related properties of rubbers," *Rep. Prog. Phys. 36 (1973), 755-826.*

[6] M. Akiba and A. S. Hashim, "Vulcunization and Crosslinking in Elastomers," *Prog. Polym. Sci. 22 (1997), 475-521.*

[7] T. Takeyama and J. Matsui, "Recent Developments with Tire Cords and Cord-to-Rubber Bonding," *Rubber Chem. Technol. 42(1) (1969), 159-256.*

[8] F. J. Kovac and T. M. Kersker, "The Development of the Polyester Tire," *Text. Res. J. 34 (1) (1964), 69-79.*

[9] Y. Iyengar, "Adhesion of Kevlar Aramid Cords to Rubber," *J. Appl. Poly. Sci. 22(3), (1978), 801-812.*

[10] R. E. Wilfong and J. Zimmerman, "Future Organic Tire Fibers," *J. Appl. Polym. Sci. 17 (1973), 2039-2051.*

[11] E. T. McDonel, "Tire Cord and Cord-to-Rubber Bonding," in *The Pneumatic Tire*, US Department of Transportation, NHTSA, 2006, pp. 80-104.

[12] T. S. Solomon, "Systems for tire cord-rubber adhesion," *Rubber Chem. Technol. 58 (1985), 561-576.*

[13] C. J. Shoaf, “Shaped structures treated with polyepoxide and polyisocyanate for improving adherence to rubbers”. USA Patent 3,307,966, 07 March 1967.

[14] W. B. Wennekes and J. W. M. Noordermeer, “Mechanistic Investigations into The Adhesion Between Rfl-Treated Cords And Rubber. Part I: The Influence of Rubber Curatives,” *Rubber Chem. Technol. 80 (2007),545-564.*

[15] K. Kirihara, “Production Technology of Wire Rod for High Tensile Strength Steel Cord,” Kobelco Technology Review No.30, Dec 2011.

[16] W. J. van Ooij, “The role of XPS in the study and understanding of Rubber-to-metal bonding,” *Surf. Sci. 68 (1977) 1-9.*

[17] W. J. van Ooij, “Fundamental aspects of rubber adhesion to brass plated steel tire cords,” Rubber Chem. Technol. 52 (1979), 605-675.

[18] W. J. van Ooij, “Mechanism and Theories of Rubber Adhesion to Steel Tire Cords—An Overview,” *Rubbber Chem. Technol. 57(3) (1984), 421-456.*

[19] W. J. van Ooij and P. B. Harakuni, “Adhesion of steel tire cord to rubber,” Rubber Chem. Technol. 82 (2009), 315-339.

[20] G. Haemers and J. Mollet, “The role of the brass surface composition with regard to steel cord rubber adhesion,” J. Elast. Plast. 10 (1978), 241-261.

[21] S. Chang, C. Lee and S. Jeon, “Measurement of rock fracture toughness under modes I and II and mixed-mode conditions by using disc-type specimens,” Eng. Geo. 66 (2002), 79-97.

[22] H. Bueckner, “The propagation of cracks and the energy of elastic deformation,” Trans. Amer. Soc. Mech. Eng. 80 (1958), 1225-1230.

[23] D. Leguillon, “Strength or toughness ? A criterion for crack onset at a notch,” *Eur. J. Mech. A/Solids 21 (2002), 61-72.*

[24] J. D. Clayton, “Nonlinear Fracture Mechanics,” in *Altenbach H., Öchsner A. (eds) Encyclopedia of Continuum Mechanics. Springer, Berlin, Heidelberg (2018).*

[25] B. N. J. Persson, O. Albohr, G. Heinrich and H. Ueba, “Crack propagation in rubber-like materials,” *J. Phys. Condens. Matter 17 (2005), 1071-1142.*

[26] P. Charrier, E. Ostoja-Kuczynsky, E. Verron, G. Marckmann, L. Gornet and G. Chagnon, “Theoretical and numerical limitations for the simulation of crack propagation in natural rubber components,” *3rd European Conference on Constitutive Models for Rubber (ECCMR), Sep 2003, Londres, United Kingdom. hal-01004689.*

[27] G. Legrain, N. Moës and E. Verron, “Stress analysis around crack tips in finite strain problems using the eXtended finite element method,” *Int. J. Numer. Meth. Engng. 63 (2005), 290-314.*

[28] K. M. Liechti, E. B. Becker, C. Lin and T. H. Miller, “A fracture-analysis of cathodic delamination in rubber to metal bonds,” *Int. J. Fract. 39(1-3) (1989), 217-234.*

[29] K. M. Liechti and W. Adamjee, “Mixed-mode cathodic delamination of rubber from steel,” *J. Adhes., 40(1) (1992), 27-45.*

[30] K. M. Liechti and W. Jeng-Dah, “Mixed-mode, time-dependent rubber/metal debonding,” *J. Mech. Phys. Solid. 49 (2001) 1039-1072.*

[31] Liechti, K M and Wu, J D, “Mixed-mode, time-dependent rubber/metal debonding,” *J. Mech. Phy. Solids, 49(5) (2001), 1039-1072.*

[32] J. H. Chang and J. B. Yeh, “Energy flux associated with a plane crack along an (hyper)elastic bimaterial interface,” *Int. J. Fract. 85 (1997) 211-229.*

[33] P. H. Geubelle and W. G. Knauss, “Finite strains at the tip of a crack in a sheet of hyperelastic material: II. Special bimaterial cases,” *J. Elast. 35 (1994) 99-137.*

[34] M. Methia, H. Bechir, A. Frachon and N. A. Hocine, “An asymptotic finite plane deformation analysis of the elastostatic fields at a crack tip in the framework of hyperelastic, isotropic, and nearly incompressible neo-Hookean materials under mode-I loading,” *Acta Mech. 239 (2020) 929-946.*

[35] K. N. Morman Jr., K. A. Mazich, F. G. Oblinger, F. Zhang and P. C. Killgoar Jr, “Critical tearing energy in a circumferentially-cracked circular cylinder of rubber under

finite deformation," *Int. J. Fract. 53 (1992) 129-157.*

[36] R. Nahta and B. Moran, "Domain Integrals for Axisymmetric Crack Porblems," *Int. J. Solid. Struct. 30(15) (1993) 2027-2040.*

[37] R. M. V. Pidaparti and G. Pontula, "Three-dimensional analysis of interface cracks in rubber materials," *Int. J. Fract. 68 (1995) 315-332.*

[38] C. J. Quigley and D. M. Parks, "The finite deformation field surrounding a mode I plane strain crack in a hyperelastic incompressible material under small-scale nonlinearity," *Int. J. Fract. 65 (1994) 75-96.*

[39] J. Scheel and A. Ricouer, "A comprehensive interpretation of the J-integral for cohesive interface cracks and interactions with matrix cracks," *Theor. Appl. Fract. Mech. 100 (2019) 281-288.*

[40] C. F. Shih, B. Moran and T. Nakamura, "Energy release rate along a three-dimensional crack front in a thermally stressed body," *Int. J. Fract. 30 (1986) 79-102.*

[41] R. A. Stephenson, "The equilibrium field near the tip of a crack for finite plane strain of incompressible elastic materials," *J. Elast. 12(1) (1982).*

[42] X. A. Zhong, "On the Stability of Phase Separation in a Finite Solid with Interfaces," *Mech. Compos. Mat. Struct. 7:1 (2010) 35-53.*

[43] A. N. Gent, "Fracture mechanics applied to elastomeric composites," *Rubber Chem. Technol. 56 (5) (1983), 1011-1018.*

[44] W. J. Lyons, M. L. Nelson and C. M. Conrad, "Study of the H Test for Evaluating the Adhesive Properties of Tire Cord in Natural and GR-S Rubbers," *Rubber Chem. Technol. 20 (1947), 268-280.*

[45] D. W. Nicholson, D. I. Livingston and G. S. Fielding-Russell, "A New Tire Cord Adhesion Test," *Tire Sci. Technol. 6 (1978), 114-124.*

[46] G. S. Fielding-Russell, D. W. Nicholson and D. L. Livingston, "Physical Factors in Cord-to-Rubber Adhesion by a New Tire Cord Adhesion Test," *Tire Reinforcement and*

Tire Performance, ed. R. Fleming and D. Livingston (West Conshohocken, PA: ASTM International, 1979), 153-162.

[47] A. N. Gent, G. S. Fielding-Russell, D. I. Livingston and D. W. Nicholson, "Failure of cord-rubber composites by pull-out or transverse fracture," *J. Mat. Sci. 16 (1981), 949-956.*

[48] A. N. Gent and O. H. Yeoh, "Failure loads for model adhesive joints subjected to tension, compression or torsion," *J. Mater. Sci. 17 (1982), 1713-1722.*

[49] M. D. Ellul and R. J. Emerson, "A new pull-out test for tire cord adhesion- Part I. Hot Bonding," Rubber Division Meeting, American Chemical Society, October 6-9, Cleveland, Ohio, 1987.

[50] A. N. Gent and S. Y. Kaang, "Pull-Out and Push-Out Tests for Rubber-to Metal Adhesion," *Rubber Chem. Technol. 62(4) (1989) 757-766.*

[51] M. Jamshidi, F. Afshar, N. Mohammadi and S. Pourmahdian, "Study on cord/rubber interface at elevated temperatures by H-pull test method," *Appl. Surf. Sci., 249(1-4) (2005) 208-215.*

[52] F. Teklal, A. Djebbar, S. Allaoui, G. Hivet, Y. Joliff and B. Kacimi, "A review of analytical models to describe pull-out behavior–Fiber/matrix adhesion," *Compos. Struct. 201 (2018), 791-815.*

[53] L.-M. Zhou, Y.-W. Mai, L. Ye and J.-K. Kim, "Techniques for Evaluating Interfacial Properties of Fibre-Matrix Composites," *Key. Eng. Mater. 104-107 (1995), 549-600.*

[54] R. S. Rivlin, "The Effective work of adhesion," *Paint Technol. 9 (1944), 2611-2614.*

[55] A. K. Graham, "Notes on Cleaning Cycles for Plating," *Transactions of the IMF 31 (1954), 259-266.*

[56] A. N. Gent and G. R. Hamed, "Peel mechanics," *J. Adhes. 7 (1975), 91-95.*

[57] J. W. Cook, S. Edge and D. E. Packham, "The adhesion of natural rubber to steel and the use of the peel test to study its nature," *Intl. J. Adhes. Adhes. 17(4) (1997) 333-337.*

[58] A. H. Muhr, A. G. Thomas and J. K. Varkey, "A fracture mechanics study of natural rubber-to-metal bond failure," *J. Adhes. Sci. Technol. 10 (7) (1996), 593-616.*

[59] ASTM D1781-98(2012), Standard Test Method for Climbing Drum Peel for Adhesives, ASTM International, West Conshohocken, PA, 2012, www.astm.org.

[60] ASTM D1871-04(2014), Standard Test Method for Adhesion Between Tire Bead Wire and Rubber, ASTM International, West Conshohocken, PA, 2014, www.astm.org.

[61] ASTM D2229-10(2014), Standard Test Method for Adhesion Between Steel Tire Cords and Rubber, ASTM International, West Conshohocken, PA, 2014, www.astm.org.

[62] ASTM D429-14(2014), Standard test methods for rubber property – adhesion to rigid substrates, ASTM International, West Conshohocken, PA, 2014, www.astm.org.

[63] ASTM D4776 / D4776M-18, "Standard Test Method for Adhesion of Tire Cords and Other Reinforcing Cords to Rubber Compounds by H-Test Procedure," *ASTM International, West Conshohocken, PA, 2018, www.astm.org.*

[64] H. Dannenberg, "Measurement of Adhesion by a Blister Method," *Journal of Applied Polymer Science, 5 (14), 125-134,* 1961.

[65] Y. S. Chang, Y. H. Lai and D. A. Dillard, "The constrained blister—a nearly constant strain energy release rate test for adhesives," *J. Adhes. 27(4) (1989), 197-211.*

[66] M. J. Napolitano, A. Chudnovsky and A. Moet, "The constrained blister test for the energy of interfacial adhesion," *J Adhes Sci Technol, 2(1), 311-323,* 1988.

[67] Y. S. Chang, Y. H. Lai and D. A. Dillard, "The constrained blister—a nearly constant strain energy release rate test for adhesives," *J. Adhes. 27(4) (1989), 197-211.*

[68] W. S. Fulton, G. C. Smith and K. J. Titchener, "Interfacial microanalysis of rubber–tyre-cord adhesion and the influence of cobalt," *Appl. Surf. Sci. 221 (2004), 69-86* .

[69] D. P. Skala, "Modified Equations of Rubber Elasticity Applied to The Inflation Mechanics of A Thick-Walled Rubber Cylinder," *Rubber Chem. Technol. 43(4) (1970), 745-757.*

[70] M. Mooney, “A Theory of Large Elastic Deformation,” *J. Appl. Phys. 11 (1940), 582.*

[71] A. N. Gent, “Elastic Instabilities in Rubber,” *Int. J. NonLin. Mech. 40(2-3) (2004), 165-175.*

[72] M. J. Napolitano, A. Chudnovsky and A. Moet, “The constrained blister test for the energy of interfacial adhesion,” *J. Adhes. Sci. Technol. 2:1 (1988), 311-323.*

[73] E. F. Rybicki and M. F. Kanninen, “A finite element calculation of stress intensity factors by a modified crack closure integral,” *Eng. Fract. Mech. 9 (1977), 931-938.*

[74] C. A. Schneider, W. S. Rasband and K. W. Eliceiri, “NIH Image to ImageJ: 25 years of image analysis,” *Nat. Methods 9(7) (2012), 671-675.*

[75] A. N. Gent and R. P. Petrich, “Adhesion of viscoelastic materials to rigid substrates,” *Proc. R. Soc. Lond. A 310 (1997), 433–448.*

[76] Liechti, K M and Wu, J D, “Mixed-mode, time-dependent rubber/metal debonding,” *J. Mech. Phy. Solids, 49(5), 1039-1072,* 2001.

[77] L. Mullins, “Softening of Rubber by Deformation,” *Rubber Chem. Technol. 42(1) (1969), 339-362.*

[78] G. Marckmann and E. Verron, “Comparison of hyperelastic models for rubber-like materials,” *Rubber Chem. Technol. 79(5) (2006), 835-858.*

[79] M. Hossain and P. Steinmann, “More hyperelastic models for rubber-like materials: consistent tangent operators and comparative study,” *J. Mech. Behav. Mater. 22 (2012), 1-2.*

[80] H. Darijani and R. Naghdabadi, “Hyperelastic materials behavior modeling using consistent strain energy density functions,” *Acta Mech. 213 (2010), 235-254.*

[81] H. Dal, Y. Badienia, K. Acikgoz and F. A. Denli, “A comparative study on hyperelastic constitutive models on rubber: State of the art after 2006,” in *Proceedings of the 11th European Conference on Constitutive Models for Rubber (ECCMR 2019), June 25-27, 2019*, Nantes, France.

[82] T. Beda, “An approach for hyperelastic model-building and parameters estimation a review of constitutive models,” *Eur. Polym. J. , 50 (2014), 97-108.*

[83] L. R. G. Treloar, “Stress-strain data for vulcanised rubber under various types of deformation,” *Trans. Faraday Soc. 40 (1944), 59-70.*

[84] R. W. Ogden, “Large deformation isotropic elasticity – on the correlation of theory and experiment for incompressible rubberlike solids,” *Proc. R. Soc. Lond. A 326 (1997), 565-584.*

[85] O. H. Yeoh, “Some forms of the strain energy function for rubber,” *Rubber Chem. Technol. 66(5) (1993), 754-771.*

[86] O. Lopez-Pamies, “A new I1-based hyperelastic model for rubber elastic materials,” *C. R. Mec. 338 (2010), 3-11.*

[87] H. Khajehsaeid, J. Arghavani and R. Naghdabadi, “A hyperelastic constitutive model for rubber-like materials,” *Eur. J. Mech. A-Solid. 38 (2013), 144-151.*

[88] M. H. B. M. Shariff, “Strain Energy Function for Filled and Unfilled Rubberlike Material,” *Rubber Chem. Technol. 73 (1) (2000), 1-18 .*

[89] M. M. Attard and G. W. Hunt, “Hyperelastic constitutive modeling under finite strain,” *Int. J. Solid. Struct. 41 (2004), 5327-5350.*

[90] M. Kaliske and G. Heinrich, “An Extended Tube-Model for Rubber Elasticity: Statistical-Mechanical Theory and Finite Element Implementation,” *Rubber Chem. Technol. 72 (4) (1999), 602-632.*

[91] P. J. Flory, “Thermodynamics of High Polymer Solutions,” *J. Chem. Phys. 9 (1941), 660.*

[92] M. L. Huggins, “Solutions of Long Chain Compounds,” *J. Chem. Phys. 9 (1941), 440.*

[93] P. L. Rosendahl, M. Drass, J. Felger, J. Schneider and W. Becker, “Equivalent strain failure criterion for multiaxially loaded incompressible hyperelastic elastomers,” *Int. J. Solids. Struct. 166 (2019), 32-46.*

[94] A. P. Mathew, S. Packirisamy, R. Stephen and S. Thomas, "Transport of aromatic solvents through natural rubber/polystyrene (NR/PS) interpenetrating polymer network membranes," *J. Membrane Sci. 201(2002), 213-227.*

[95] N. Sombatsompop and K. J. Christodoulou, "Penetration of natural hydrocarbons into natural rubbers," *Polyms. Polym. Compos. 5(5), 1997, 377-386.*

[96] H. A. Daynes, "The absorption and diffusion of water in rubber," *Trans. Faraday Soc. 33(1937), 531-544.*

[97] G. J. Van Amerongen, "Diffusion in Elastomers," *Rubber Chem. Technol. 37(1964), 1065-1152.*

[98] R. W. Ogden and D. G. Roxburgh, "A pseudo–elastic model for the Mullins effect in filled rubber," *Proc. R. Soc. Lond. A. 455 (1999), 2861-2877.*

[99] A. Dorfmann and R. W. Ogden, "A constitutive model for the Mullins effect with permanent set in particle-reinforced rubber," *Int. J. Solid. Struct. 41 (2004), 1855-1878.*

Appendix A

In §*IV.3* the Thick-Walled Rubber Cylinder Inflation problem was solved for five hyperelastic models. The algorithm to solve the problem is already described in *Figure IV.2.2* along with generalised stress-elongation equations to be solved. However, these equations need to be solved for each hyperelastic model. In this Appendix, a list of strain energy density equations for the chosen hyperelastic models and their corresponding deviatoric Cauchy stress equations are given.

Mooney-Rivlin [70]:

Strain energy density	$W = C_1(I_1 - 3) + C_2(I_1 - 3)$
Stress elongation relation	$\sigma_i{}^{dev} = 2C_1\lambda_i^2 - 2\dfrac{C_2}{\lambda_i^2}$

Ogden [84]:

Strain energy density	$W = \sum_{p=1}^{N} \dfrac{\mu_p}{\alpha_p}(\lambda_1{}^{\alpha_p} + \lambda_2{}^{\alpha_p} + \lambda_3{}^{\alpha_p} - 3)$
Stress elongation relation	$\sigma_i{}^{dev} = \sum_{p=1}^{N} \mu_p\, \lambda_i{}^{\alpha_p}$

Yeoh [85]:

Strain energy density	$W = \sum_{n=1}^{3} C_n(I_1 - 1)^n$
Stress elongation relation	$\sigma_i{}^{dev} = \left(\sum_{n=1}^{3} nC_n(I_1 - 1)^{n-1}\right)\lambda_i^2$

Lopez-Pamies [86]:

Strain energy density	$$W = \sum_{r=1}^{M} \frac{3^{1-\alpha_r}}{2\alpha_r} \mu_r (I_1^{\alpha_r} - 3^{\alpha_r})$$
Stress elongation relation	$$\sigma_i{}^{dev} = \left(\sum_{r=1}^{M} 3^{1-\alpha_r} \mu_r I_1^{\alpha_r - 1} \right) \lambda_i^2$$

ExpLn [87]:

Strain energy density	$$W = A \left[\frac{1}{a} \exp(a(I_1 - 3)) + b(I_1 - 2)(1 - \ln(I_1 - 2)) - \frac{1}{a} - b \right]$$
Stress elongation relation	$$\sigma_i{}^{dev} = 2A\left[\exp\left(a(I_1 - 3)\right) - bln(I_1 - 2)\right]\lambda_i^2$$

Appendix B

In *Chapter IV*, material parameters of specimen rubber were calculated by fitting experimental data to five hyperelastic models. *Table B.I* shows the results from the uniaxial data fitting described in detail in §*IV.3.1*.

The material parameters were calculated again using a volumetric data fitting technique in §*IV.4*. The results obtained are tabulated in *Table B.II*.

Hyperelastic Model	**Parameter Fit from Uniaxial Tests**	
Mooney-Rivlin	C_1=1.34 MPa	C_2=0.37MPa
Ogden Model (1st order)	α=2.64	μ=1.89MPa
Ogden Model (2nd order)	α_1=0.175	μ_1=4.97MPa
	α_2=2.81	μ_2=1.52MPa
Ogden Model (3rd order)	α_1=0.0075	μ_1=8.4MPa
	α_2=2.67	μ_2=1.81MPa
	α_2=0.0074	μ_2=23MPa
Yeoh Model (2nd order)	C_1=1.33MPa	C_2=0.059MPa
Yeoh Model (3rd order)	C_1=1.39MPa	C_2=0.024MPa
	C_3=0.006MPa	
Lopez-Pamies Model (1st rder)	α=1.36	μ=2.62MPa
Lopez-Pamies Model (2nd order)	α_1=1.41	μ_1=2.54MPa
	α_2=-16.26	μ_2=1.11MPa
Lopez-Pamies Model (3rd order)	α_1=1.06	μ_1=1.31MPa
	α_2=1.68	μ_2=1.26MPa
	α_2=-17.7	μ_2=1.12MPa
ExpLn	A=1.16MPa a=0.102	b=-0.02

Table B.I: Uniaxial test data fit to 10 Cauchy stress equations (5 hyperelastic models)

Hyperelastic Model	Parameter Fit from Volumetric Data	
Mooney-Rivlin	C_1=-0.18 MPa	C_2=0.62MPa
Ogden Model (1st order)	α=4.12	μ=0.63MPa
Ogden Model (2nd order)	α_1=3.79	μ_1=1.07MPa
	α_2=2.1	μ_2=-0.87MPa
Ogden Model (3rd order)	α_1=3.85	μ_1=0.97MPa
	α_2=1.78	μ_2=-0.87MPa
	α_2=-1.03	μ_2=3.55Pa
Yeoh Model (2nd order)	C_1=0.45MPa	C_2=0.13MPa
Yeoh Model (3rd order)	C_1=0.49MPa	C_2=0.091MPa
	C_3=0.002MPa	
Lopez-Pamies Model (1st order)	α=2.27	μ=0.93MPa
Lopez-Pamies Model (2nd order)	α_1=1.11	μ_1=0.76MPa
	α_2=2.89	μ_2=0.29MPa
Lopez-Pamies Model (3rd order)	α_1=1.8	μ_1=0.67MPa
	α_2=2.72	μ_2=0.29MPa
	α_2=0.5369	μ_2=-0.64Pa
ExpLn	A=0.97MPa a=-1.9	b=-1.13

Table B.II: Volumetric data fit for 10 strain energy density equations (5 hyperelastic models).

Appendix C

Research Output

- Kane K, Jumel J, Lallet F, Mbiakop-Ngassa A, Vacherand J-M, Shanahan MER. *A novel inflation adhesion test for elastomeric matrix/steel cord*. Int. J. Solid. Struct. 2019;160: 40–50
- Kane K, Jumel J, Lallet F, Mbiakop-Ngassa A, Vacherand J-M, Shanahan MER. *Experimental study of the rubber cord adhesion inflation test*. Eng. Fract. Mech. Volume 224, 2020, 106783.
- Kane K, Jumel J, Lallet F, Mbiakop-Ngassa A, Vacherand J-M, Shanahan MER. *RCAIT Analysis: Crack Propagation Monitoring and Influence of Confinement Tube Lubrication*. Polym. Test., Under Review.
- Kane K, Jumel J, Lallet F, Mbiakop-Ngassa A, Vacherand J-M, Shanahan MER. *Rubber Cord Adhesion Inflation Test: Effect of constitutive rubber model on evaluation of* G_c. Eng. Fract. Mech., Under Review.
- EURADH/CLBA 2018 Conference, Portugal 5-7 September 2018- Oral presentation on '*Fracture Mechanics of a Rubber Tube – Metal Cord Inflation Test*'